People's Democratic Republic of Algeria
Ministry of Higher Education and Scientific Research

Abdelhamid Ibn Badis University of Mostaganem
Faculty of Exact Sciences and Computer Science

Department of Physics

Thesis

to obtain the degree of

Doctor of Physics

Specialty: **Condensed Matter Physics**

Presented by:

Abdesamed Benbedra

Thesis directed by: **Said Meskine**
Co-directed by: **Hamza Abbassa**

Prepared within the **Laboratory of Elaboration and characterization Physico-Mechanical and Metallurgical of Materials (ECP3M)**

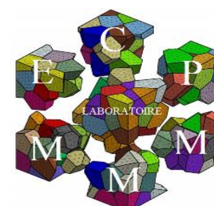

Ab-initio investigation of electric polarization in wurtzite crystals

Defended publically on 18/12/2025 in front of the following jury:

Pr. Zoubir Aziz (University of Mostaganem)	President
Dr. Charef Abbes (University of Mostaganem)	Examiner
Pr. Bachir Bouhafs (University of Sidi Bel Abbès)	Examiner
Pr. Boucif Abbar (University of Sidi Bel Abbès)	Invited
Pr. Said Meskine (University of Mostaganem)	Director
Pr. Hamza Abbassa (University of Mostaganem)	Co-director

“It is said with truth that every building is constructed stone by stone, and the same may be said of knowledge, extracted and compiled by many learned men, each of whom builds upon the works of those who preceded him. What one of them does not know is known to another, and little remains truly unknown if one seeks far enough. Now I take my turn as mason, carving what I know to place one more stone in the great bastion of knowledge that has been built over the centuries. A bastion raised by countless hands that came before, and which will, no doubt, continue to rise with the aid of countless hands yet to come.”

— The World of Ice and Fire, George R. R. Martin

"يُقالُ في الحقيقةِ أنَّ كُلّ بِناءٍ يُبنى حجرًا على حجَر، ويُمكنُ قَولُ الشّيءِ نفسِه عنِ المَعرفة التي استخرَجَها وجمَعَها كثيرٌ من الرِّجال المُتعلِّمين، كلٌّ مِنهُم بنَى على أعمالِ مَن سبقوه، وما لا يعرِفُه أحَدٌ منهُم يعرِفُه آخر، ويبقى القليلُ لِمعرفَتِهِ حقًّا إذا سَعى المرءُ بما فيه الكِفاية. والآن أنا أتَّخِذُ دَوري كبَنّاء، لِأنحَتَ ما أعرِفُهُ لِوَضعِ حجَرٍ آخر في مَعقَلِ المعرفَة العظيم الذي تمَّ بِناؤُه على مرِّ القُرون. ذلِكَ المعقَلُ الذي أعلَتهُ أيادٍ لا حَصر لها مِمَن جاءَ قبلَنا، وسيستمرّ، بِلا شَكّ، في العُلُوّ بِمُساعدة ما لا يُحصَى من الأَيدي التي لم تَأتِ بَعد."

ـــ عالَمُ الجليدِ وَالنّار، جورج ر.ر. مارتن

Abstract

The prevalence of electric polarization in modern technology makes it important to study its effects. The present PhD thesis covers the topic of electric polarization in hexagonal wurtzite crystals. We focus our attention on the technologically important group III-nitrides and II-oxides. Different types of systems are investigated, including pure binaries, ternary and quaternary alloys and one particular kind of crystalline defects named stacking faults. For these systems, we provide many polarization properties, such as spontaneous polarization, Born effective charge, piezoelectric coefficient and interface polarization charge. These quantities serve as input for the modelling of optoelectronic, power electronic and piezoelectric nitride- and oxide-based devices. Our study is done by means of direct simulations with the WIEN2k code, which is based on density-functional theory, in combination with the BerryPI code to calculate the polarization-related quantities mentioned above. The theoretical framework of BerryPI is the Berry-phase theory, which is thoroughly explained in this manuscript. The work presented in this thesis is divided into four research projects, each project corresponds to a peer-reviewed article. In the first project, we propose the trigonal crystal structure as a reference to access the spontaneous polarization of wurtzite materials. In addition, we demonstrate the equivalence between the trigonal and the already-established zincblende structures in determining this quantity for wurtzite binary III-nitrides AlN, GaN and InN and II-oxides BeO and ZnO. The second project is dedicated to using the layered-hexagonal structure as a reference for wurtzite alloys in order to compute their spontaneous polarization. The piezoelectric polarization and the interface polarization charge are also studied for biaxially-strained ternary (AlGaN, InGaN and InAlN) and quaternary (AlInGaN) nitride alloys. The third project deals with the influence of compressive uniaxial strain on the structural and piezoelectric properties of the binary wurtzite compounds studied here. Finally, in the fourth project, we show how the presence of basal stacking faults affects the physical properties of wurtzite GaN and ZnO. The investigated properties are the atomic structure (lattice parameters and Stacking-fault formation energy), the electronic structure (band gap, band offsets and effective mass) and polarization quantities (spontaneous polarization, interface charge and piezoelectric constant).

Key words: electric polarization, Berry phase, piezoelectricity, wurtzite crystals, alloys, stacking faults, density-functional theory, augmented plane wave method, WIEN2k, BerryPI.

Résumé

La prévalence de la polarisation électrique dans la technologie moderne rend l'étude de ses effets particulièrement importante. La présente thèse de doctorat porte sur la polarisation électrique dans les cristaux hexagonaux wurtzite. Nous concentrons notre attention sur les nitrures du groupe III et les oxydes du groupe II qui revêtent une grande importance technologique. Différents types de systèmes sont étudiés, notamment les composés binaires purs, les alliages ternaires et quaternaires ainsi qu'un type particulier de défaut cristallin appelé défaut d'empilement. Pour ces systèmes, nous fournissons de nombreuses propriétés de polarisation telles que la polarisation spontanée, la charge effective de Born, le coefficient piézoélectrique et la charge de polarisation d'interface. Ces grandeurs servent de données d'entrée pour la modélisation de dispositifs optoélectroniques, microélectroniques et piézoélectriques à base de nitrures et d'oxydes. Notre étude est réalisée au moyen de simulations directes avec le code WIEN2k, qui est basé sur la théorie de la fonctionnelle de la densité, en combinaison avec le code BerryPI pour calculer les grandeurs liées à la polarisation mentionnées ci-dessus. Le cadre théorique de BerryPI est la théorie de la phase de Berry, qui est expliquée en détail dans ce manuscrit. Le travail présenté dans cette thèse est divisé en quatre projets de recherche, chacun correspondant à un article évalué par des pairs. Dans le premier projet, nous proposons la structure cristalline trigonale comme référence pour accéder à la polarisation spontanée des matériaux wurtzite. De plus, nous démontrons l'équivalence entre la structure trigonale et la structure zincblende pour la détermination de cette quantité pour les nitrures du groupe III AlN, GaN et InN et les oxydes du groupe II BeO et ZnO. Le deuxième projet est consacré à l'utilisation de la structure hexagonale compacte comme référence pour les alliages wurtzite afin de calculer leur polarisation spontanée. La polarisation piézoélectrique et la charge de polarisation d'interface sont également étudiées pour les alliages nitrures ternaires (AlGaN, InGaN et InAlN) et quaternaires (AlInGaN) sous une contrainte biaxiale. Le troisième projet traite de l'influence de la contrainte compressive uniaxiale sur les propriétés structurales et piézoélectriques des composés binaires wurtzite étudiés ici. Finalement, dans le quatrième projet, nous montrons comment la présence de défauts d'empilement basaux affecte les propriétés physiques du GaN et ZnO. Les propriétés investiguées incluent la structure atomique (paramètres de maille et énergie de formation des défauts d'empilement), la structure électronique (largeur de la bande interdite, décalages de bande et masse effective), ainsi que les grandeurs de polarisation (polarisation spontanée, charge d'interface et constante piézoélectrique).

Mots clés: polarisation électrique, phase de Berry, piézoélectricité, cristaux wurtzite, alliages, défauts d'empilement, théorie de la fonctionnelle de la densité, méthode des ondes planes augmentées, WIEN2k, BerryPI.

مُلَخَّص

إنّ شيوع الاستقطاب الكهربائي في التكنولوجيا الحديثة يجعل دراسةَ تأثيراتِه أمرًا بالغ الأهمية. تتناول أطروحة الدكتوراة الحالية موضوع الاستقطاب الكهربائي في البلّورات السداسية من نوع وارتزيت، بحيث ركّزنا اهتمامنا على النيتريدات والأكاسيد ذات الأهمية التكنولوجية. تمّت دراسة أنواع مختلفة من الأنظمة، بما في ذلك المواد الثنائية النقية، السبائك الثلاثية والرباعية ونوع معين من العيوب البلّوية يُعرَف باسم عيوب التراص. درسنا العديد من المقادير الفيزيائية للاستقطاب لهذه الأنظمة، مثل الاستقطاب التلقائي، شحنة بورن الفعّالة، المعامل الكهروضغطي و شحنة الاستقاطب السطحية. تُستخدم هذه الكميات عادةً كمُدخلات لنمذجة الأجهزة الكهروضوئية، أجهزة الطاقة الإلكترونية والأجهزة الكهروضغطية المصنوعة من النيتريدات والأكاسيد. أُجرِيَت دراستنا عن طريق المحاكاة المباشرة باستخدام كود WIEN2k المعتمد على نظرية الكثافة الوظيفية، بالإضافة للكود BerryPI لحساب كميات الاستقطاب المذكورة أعلاه. الإطار النظري لبرنامج BerryPI هو نظرية طور بيري، والتي تمّ شرحها بالتفصيل في هذه الرسالة. ينقسم العمل المقدم في هذه الأطروحة إلى أربعة مشاريع بحثية، كل مشروع منها يقابل مقالا علميا تمّت مراجعته من طرف الأقران. في المشروع الأول، نقترح الهيكل البلّوري ثلاثي الزوايا كمرجع لحساب الاستقطاب التلقائي لمواد الوارتزيت. بالإضافة إلى ذلك، نوضّح التكافؤ بين الهيكل الثلاثي وهيكل بلند الزنك في تحديد هذه الكمية في مواد الوارتزيت الثنائية كالنيتريدات AlN، GaN و InN والأكاسيد BeO و ZnO. المشروع الثاني مُكرّس لاستخدام الهيكل البلوي السداسي الطبقي كمرجع لحساب الاستقطاب التلقائي في سبائك الوارتزيت. كما يتم دراسة الاستقطاب الانضغاطي وشحنة الاستطاب السطحية لكل من سبائك النيتريد الثلاثية (AlGaN، InGaN و InAlN) والرباعية (AlInGaN) الخاضعة للإجهاد ثنائيّ المحور. يتناول المشروع الثالث تأثير الإجهاد الضغطي أحادي المحور على الخصائص البنيوية والكهروضغطية لمركّبات الوارتزيت الثنائية المدروسة هنا. وأخيرا، في المشروع الرابع، نوضّح كيف تؤثر عيوب التراص القاعدية على الخصائص الفيزيائية لكل من GaN و ZnO. تشمل الخصائص المدروسة البنية الذريّة (ثوابت الشبكة البلوية و طاقة تكوين عيوب التراص)، البنية الإلكترونية (فجوة النطاق، إزاحات النطاق والكتلة الفعالة) وكميات الاستقطاب الكهربائي (الاستقطاب التلقائي، شحنة الاستقطاب السطحية والثابت الكهروضغطي).

الكلمات المفتاحية: الاستقطاب الكهربائي، طور بيري، الكهرباء الانضغاطية، بلّورات الوارتزيت، السبائك، عيوب التراص، نظرية الكثافة الوظيفية، طريقة الموجة المستوية والمُعززة، WIEN2k، BerryPI.

Acknowledgements

This thesis has only been possible through the support of many people, to whom I am indebted for their help, encouragement, guidance and company over the six years of my PhD journey. Since this is a scientific work, I will start the acknowledgement by thanking the scientists.

I did not realize it at first, but now I am aware that I am incredibly lucky to had Prof. Said Meskine as my supervisor. His strength and intuition in theoretical physics is unmatched, and he has an unshakable attitude in the face of tough problems. It was him who introduced me, for the first time, to polarization research and advanced condensed-matter concepts such the Berry phase. He also taught me how to use the WIEN2k code, from constructing *struct* files to running BerryPI calculations. The best times in my PhD have been performing WIEN2k simulations together while indulging in deep and lengthy discussions, not only about physics related-topics, but also about science-fiction novels, movies, series and even animes. I thank him for the valuable insights and guidance that help me grow as a scientist. But most of all I want to thank him for, since day one, providing a unique environment of academic freedom, by letting me propose and follow my naïve ideas, rather than forcing me to specific directions as is the case with most PhD students. Thank you for accompanying me in this journey, and I look forward to the rest of the road.

Next, I thank my second supervisor, Prof. Hamza Abbassa, for his constant support and encouragement, especially at the final stages of my doctoral journey. I especially thank him for the thoughtful reading of the initial draft of my thesis, where he spotted and corrected many mistakes, and explaining to me the difference between British and American English. He also showed me, among many other things, how to conduct elasticity calculations “manually”, or “point by point”. I am grateful to you, thank you so much.

I would also like to thank the director of our lab, Prof. Abdelkader Boukortt, for many reasons. First, he opened the (LMD) doctoral training in physics within our faculty for the very first time, which was very important to me because otherwise I would have done my PhD in another city far away from home. Second, he provided to me a new computer (Poste 6) to conduct my simulations. Third, he included me in a very fruitful collaboration with other physicists from abroad, which resulted in three papers and one internship. My deepest thanks to him for all these things and for his gentle guidance and valuable pieces of advice. Thank you of being a Great Boss.

A special thanks to Prof. Roland Hayn, professor of physics at the University of Marseille (France), with whom I wrote and published my first ever papers. It was actually him who proposed the topics of piezoelectricity and stacking faults as research projects many years ago, which were assign to me (among other projects) by my supervisor when I applied for my PhD. Furthermore, he invited me for an internship during which we finalized our joint article on stacking faults. It was truly valuable working with him, learning a lot of new things, such as topological materials and the quantum Hall effects, which I decided to be one of my future axes of research. I am sincerely thankful for your hospitality and expert-level insights. My thanks are also due to Michael Texier, Oliver Thomas and Thomas Cornelius for their helpful contribution to the stacking-fault paper.

Acknowledgements

I would like to express my deepest and warmest gratitude to my committee members: Prof. Zoubir Aziz, Prof. Bachir Bouhafs, Prof. Boucif Abbar and Dr. Charef Abbes for agreeing to be my thesis examiners. I thank them because they spared some of their time and expertise to read and judge the manuscript despite its unusually extreme length (more than 200 pages). Thanks again to Dr. Charef Abbes for teaching me electromagnetism and Maxwell's equations when I was a physics student, and for explaining the difference between the gradient, divergence and curl differential operators many times.

I was very fortunate to have been mentored by many great professors throughout my years in university. As such I want to thank my quantum-mechanics teacher, Prof. Aissa Belhouari, who, via his competence and enthusiasm, turned this formidable module to a comprehensible and enjoyable one (at least for me), and Prof. Wassila Leila Rahal for being a fantastic instructor and for her kind words of support and encouragement before and during I pursue my PhD.

To all my colleagues at the ECP3M laboratory who made my PhD a fun and memorable experience, thank you for everything. I have a huge debt of gratitude to my best mate El Habib Abbes, for being a trusted friend (since 2014) and for all the "adventures" we have been on, the last of which is a collaboration about a wurtzite polarized half-Heusler compound. I hope that many more strong collaborations grow between us in the future. Thanks go to the many candidates I met over the last six years, particularly to Khadidja Missoum, who showed me how to work with the Phonopy code, as well as to Ahlam Benaouad for her many shared insights about thermoelectricity.

Many thanks as well to the previous PhD students (now doctors) for including me in their works: El Habib Abbes, Ahlam Benaouad, Imen Bouhamou, Fatima Zohra Behar, Nour El Houda Habibes and Yousra Mamouni. I feel privileged for having the opportunity to be a co-author in your papers, thank you. My gratitude goes to Abdelhadi Hammou, the lab engineer, for his efforts to make the lab a cool and interesting place to work and for his amazing skills at making problems go away. I also thank him for letting me use the lab's resources whenever I need them.

Outside the lab, I want to thank Mohammed Amin Bezzekhami and Mohammed Amine Boudjeltia for continuous moral assistance. Although they are both chemists, we had some really fruitful discussions. Thanks to the people who made some of the codes and softwares I have used during my research, including Windows, Ubuntu, Office, OriginPro, matlab, Photoshop, VESTA and WIEN2k. Special thanks to Sheikh Jamil Ahmed for developing BerryPI. My work on electric polarization would not have been possible without this code.

Finally but most importantly, a warm thank you to my parents, my father Abdelkader Benbedra (a.k.a. Hadj) and my mother Zenaini Fatiha, who have supported my academic pursuits my entire life. I have to thank my father for calling me "doctor" since my first day in college, and for letting me worry only about science, and I thank my mother for her unconditional love and never-ending support. I do not believe in "dedication", but if I have to dedicate this thesis to some individuals, those individuals would be indeed my parents (even though they cannot understand a word of what their son wrote here). I am thankful to my brothers Salah dine (the chemist), Tareq, Mohamed Taha and Youcef, and my sister Israa for their love and warm support. I'm also deeply grateful to my dear cousin Yasser Mebrek (who is also a chemist) for his constant support even from afar. Thank you all.

Scientific output

Published articles

This is a complete list of all the (international) publications performed during this thesis as first author:

- **A. Benbedra**, S. Meskine, A. Boukortt, R. Hayn and H. Abbassa, "Influence of compressive uniaxial strain on the piezoelectric response of wurtzite crystals", J. Phys. D: Appl. Phys. 56, 385304 (2023).
- **A. Benbedra**, H. Abbassa, A. Boukortt, R. Hayn, S. Meskine, and E. H. Abbes, "The trigonal structure as a reference to access the spontaneous polarization of wurtzite crystals", Physica B 667, 415183 (2023).
- **A. Benbedra**, S. Meskine, A. Boukortt, H. Abbassa and E. H. Abbes, "Polarization properties of wurtzite III-nitride alloys using the hexagonal reference structure", ECS J. Solid State Sci. Technol. 12, 103008 (2023).

- **A. Benbedra**, S. Meskine, A. Boukortt, R. Hayn, M. Texier, O. Thomas and T. W. Cornelius, "Energetics, electronic structure and electric polarization of basal stacking faults in wurtzite GaN and ZnO", Comput. Condens. Matter 43, e01033 (2025).

The list also includes the peer-reviewed papers to which we contributed as collaborating author. Our contribution is mainly proofreading the manuscript, improving the figures quality, answering the comments of the reviewers, and in some cases contributing to the simulation procedure:

- E. H. Abbes, H. Abbassa, S. Meskine, **A. Benbedra** and A. Boukortt, "The effect of uniaxial stress on magneto-electronic properties and band Jahn-Teller distortion of Ni_2MnGa Heusler alloy: an ab initio study", Phil. Mag. 102, 844-859 (2021).
- A. Benaouad, S. Meskine, A. Boukortt, **A. Benbedra** and H. L. Beklaouz, "Thermoelectric performance of n-type filled skutterudites $RECo_4Sb_{12}$ using rare earths as filler atoms (RE=Nd,Sm,Eu,Yb)", ECS J. Solid State Sci. Technol. 12, 033006 (2023).
- I. Bouhamou, H. Abbassa, C. Abbes, A. Boukortt, E. H. Abbes and **A. Benbedra**, "Electronic, magnetic properties and pressure-induced phase transition of new $D0_{19}$ Fe_2MnSn Heusler alloy", Mater. Phys. Mech. 51, 65-75 (2023).
- F.Z. Behar, S. Meskine, A. Boukortt and **A. Benbedra**, "Response of Mg_2X (X = Si, Ge and Sn) compounds to extreme uniaxial compression: first-principles calculations", Modelling Simul. Mater. Sci. Eng. 32, 025003 (2024).
- N. E. H. Habibes, A. Boukortt, S. Meskine, **A. Benbedra**, Y. Mamouni and H. Bennacer, "Electronic and optical properties of Mn-doped HgSe topological insulator for spintronic devices", ECS J. Solid State Sci. Technol. 13, 013013 (2024).
- Y. Mamouni, H. Bennacer, A. Boukortt, **A. Benbedra**, A. H. Denawi, N.E.H. Habibes, "Investigating the optoelectronic properties of Mn and Fe doped $CuAlS_2$ for intermediate band solar cell applications", Mater. Today Commun. 41, 110508 (2024).

Unpublished articles

The thesis contains work that will appear in the following paper:

● **A. Benbedra**, “Review of the Berry-phase theory of electric polarization: application to wurtzite III-nitrides” (not submitted yet).

Conference posters

There are four international and national communications in the form of conference posters:

● **A. Benbedra**, S. Meskine, H. Abbassa and A. Boukortt, “Spontaneous polarization of II-VI oxides: ab-initio calculation”. 1st International Conference on Sustainable Energy and Advanced Materials (ICSEAM’21), April 27st-28nd 2021, Ouargla, Algeria.
● **A. Benbedra**, S. Meskine, H. Abbassa and A. Boukortt, “Ab-initio study of electric polarization of the wurtzite alloy $Al_xGa_{1-x}N$”. 2ème Conférence Internationale sur les Sciences et Génie des Matériaux (ICMSE21), July 3rd-4th 2022, Sidi Bel-Abbès, Algeria.
● **A. Benbedra**, S. Meskine, H. Abbassa and A. Boukortt, “Electric polarization field reduction in wurtzite InGaN ternary alloy”. 1st National Conference on Photovoltaic Materials and Devices (1NCPVMD21), December 14th-15th 2021, Bechar, Algeria.
● **A. Benbedra**, S. Meskine, H. Abbassa and A. Boukortt, “Mechanical behaviour of the wurtzite alloys InGaN and CdZnO”. 1st National Conference on Science & Technology (NCST22), June 27th-28th 2022, Mascara, Algeria.

Internship

Our doctoral internship took place at Institut Matériaux Microélectronique Nanoscience de Provence (IM2NP) of the Saint Jérôme faculty, Marseille (France). We were invited by Pr. Hayn Roland, the head of the Quantum Matter Theory research unit, for a working stay between 16th and 26th May 2023. The work we did during this internship is part of the efforts undertaken to understand the influence of stacking faults on the physical properties of wurtzite materials, and the discussions were used to finalize our paper on the basal stacking faults in GaN and ZnO. This research project is a collaboration between the two laboratories ECP3M and IM2NP. As a perspective, we briefly studied the quantum Hall effect in topological materials. In particular, there was a discussion on the Hall electrical conductivity and its relation to the concept of the Berry phase.

Contents

General introduction **1**

Part I: Theoretical background **4**

Chapter I: Electric polarization of crystalline solids **5**

I.1 Introduction 5
I.2 Definition of polarization 5
I.2.1 Microscopic origin 5
I.2.2 Electronic and ionic polarizations 7
I.2.3 Polarization of metals 8
I.3 Polarization-induced charge 8
I.3.1 Volume and surface charges 8
I.3.2 Interface charges 9
I.4 Polarization effects 10
I.4.1 Piezoelectricity 10
I.4.2 Pyroelectricity 11
I.4.3 Ferroelectricity 12
I.5 Wurtzite crystals 15
I.5.1 Crystalline structure 16
I.5.2 Polarization in wurtzite crystals 17
I.5.3 Properties and applications 20
A. Optoelectronics 29
B. Electronics 23
C. Piezoelectronics 24

Chapter II: Review of density-functional theory **27**

II.1 Introduction 27
II.2 Quantum many-body problem 28
II.3 Theorems of Hohenberg and Kohn 29
II.4 Khon-Sham equation 30
II.5 Exchange and correlation functionals 32
II.5.1 Generalized gradient approximation 32
II.5.2 Modified Becke-Johnson approximation 33
II.6 Augmented plane-wave methods 35
II.6.1 APW 35
II.6.2 LAPW 36
II.6.3 LAPW+LO 37
II.6.4 LAPW+LO+lo 37
II.7 WIEN2k 38
II.7.1 Iterative process 38
II.7.2 Convergence parameters 39
II.7.3 Supercell geometry 40

II.8 Conclusion 41

Chapter III: Review of the Berry-phase theory: Application to wurtzite crystals 44

III.1 Introduction 44
III.2 Difference in polarization 44
III.3 Polarization as a Berry phase 47
III.3.1 Dipole-moment picture 47
III.3.2 Adiabatic-current picture 49
III.3.3 Berry-phase picture 51
III.3.4 Formal and effective polarizations 53
III.4 Polarization lattice 54
III.5 Polarization branch 55
III.6 Examples 57
III.6.1 Ionic-displacement-induced polarization 58
III.6.2 Strain-induced-polarization 63
III.6.3 Interface polarization-induced charge 65
III.7 BerryPI 65
III.8 Conclusion 69

Part II: Simulation results and discussion 72

Chapter IV: Spontaneous polarization of wurtzite III-nitrides and II-oxides: The trigonal structure as a reference 73

IV.1 Introduction 73
IV.2 Theoretical approach 74
IV.2.1 Wurtzite and trigonal structures 74
IV.2.2 Computational details 76
IV.3 Results and discussion 76
IV.3.1 Structural optimization of the wurtzite structure 76
A. Lattice constants and the internal parameter 76
B. Bond lengths and interbond angles 79
IV.3.2 Structural optimization of the trigonal structure 80
IV.3.3 Formal polarization 81
A. Components of the formal-polarization vector 81
B. Full formal-polarization vector 82
C. Relation between the zincblende and trigonal polarizations 82
D. Formal polarization of ideal wurtzite 84
E. Wurtzite polarity 84
IV.3.4 Spontaneous polarization 85
A. Comparison between the trigonal and zincblende references 87
B. Spontaneous polarization of ideal wurtzite 87
C. Failure of WIEN2k when using the zincblende reference.................................... 87
IV.3.5 Electronic and ionic polarizations 88
IV.3.6 Dependence of polarization on the internal parameter 89
IV.4 Conclusion 90

Chapter V: Polarization properties of wurtzite III-nitride alloys **92**
V.1 Introduction 92
V.2 Theoretical approach 93
V.2.1 Supercells structure 93
V.2.2 Calculation details 94
V.3 Results for the strain-free ternary alloys 95
V.3.1 Lattice constants 95
V.3.2 Average internal parameter 97
V.3.3 Polarization discontinuity 99
V.3.4 Spontaneous polarization 101
V.3.5 Effect of the exchange-correlation functional on polarization 102
V.3.6 Effect of the supercell dimension on polarization 102
V.3.7 Comparison between the hexagonal and trigonal references 107
V.3.8 Refined understanding of the wurtzite spontaneous polarization 109
V.4 Results for the ternary alloys lattice-matched to GaN 110
V.4.1 Mismatch-induced strain 110
V.4.2 Elastic constants 112
V.4.3 Poisson effect 114
V.4.4 Lattice parameters 116
V.4.5 Piezoelectric polarization 117
V.4.6 Effect of the supercell dimension on polarization 119
V.5 Results for the quaternary alloy AlInGaN/GaN 121
V.5.1 Structural optimization 121
V.5.2 Interface polarization charge 122
V.6 Comparison to other theoretical and experimental data 125
V.6.1 Evaluation of polarization charge in wurtzite ternary alloys 125
V.6.1 Accuracy of the theoretical calculations 125
A. AlGaN/GaN 126
B. InGaN/GaN 126
C. InAlN/GaN 126
D. Summary 128
V.7 Conclusion 128

Chapter VI: Influence of compressive uniaxial strain on the piezoelectric response of wurtzite III-nitrides and II-oxides **130**
VI.1 Introduction 130
VI.2 Computational details 131
VI.3 Results 131
VI.3.1 Lattice constants 131
VI.3.2 Internal parameter and phase transition 134
VI.3.3 Piezoelectric polarization 136
VI.3.4 Piezoelectric coefficient 138
VI.4 Discussion 139
VI.4.1 Born effective charge 140
VI.4.2 Strain sensitivity of the internal parameter 142

VI.5 Conclusion 143

Chapter VII: Energetics, electronic structure and electric polarization of basal-stacking faults in wurtzite GaN and ZnO **144**

VII.1 Introduction 144
VII.2 Theoretical methodology 145
VII.2.1 Basal-stacking faults in hexagonal crystals 145
VII.2.2 Supercells choice 146
VII.2.3 Simulation settings 147
VII.3 Results and discussion 147
VII.3.1 Energetics and structural optimization 147
A. Structural parameters 147
B. Formation energy 148
VII.3.2 Electronic structure 151
A. Band gap 151
B. Band offsets 153
C. Stacking faults as quantum wells 154
D. Effective mass 156
E. Unfolded band structure 159
VII.3.3 Electric polarization 161
A. Spontaneous polarization 161
B. Interface polarization charge 163
C. Piezoelectric coefficient 165
D. Spontaneous polarization of stacking faults in GaN 166
VII.4 Conclusion 168

General conclusion **171**

Perspectives **174**

References **180**

General introduction

It is hard to overestimate the importance of electric polarization for a deeper understanding of various modern day technologies. A typical example can be seen from piezoelectric applications, such as acoustic transducers, whose operation is only possible through the mutual conversion of polarization and mechanical strain [1]. Piezoelectric materials and the associated devices are the basis of a multi-billion dollar worldwide market [2]. Another multi-billion industry are optoelectronic devices, where polarization also plays a major role. Specifically, the optical efficiency of lasers and light emitting diodes can be further improved by simply minimizing the electric fields that originate from polarization discontinuities in heterostructure layers [3,4]. If we look at another field of applications, namely power electronics, the polarization-induced fields allow the confinement of free charge carriers at interfaces, forming a dense two-dimensional electron gas used in the fabrication of high-electron-mobility transistors [5]. Therefore, since the commercial applications mentioned above are made from polarized materials, their device performance and properties (and even their lifetime) are significantly modified under the influence of polarization.

The research in electric polarization consists mainly in studying certain physical phenomena, including the piezoelectric effect, ferroelectric switching and some aspects of lattice dynamics [6–8]. A considerable amount of research is dedicated to determining the values of polarization properties via theory and experiment. Examples of experimental techniques used in the measurements are bulk and acoustic wave resonator setups, which have been successfully applied to extract the values of the piezoelectric coefficients [9]. Furthermore, the polarization-induced interface charges and electrostatic fields that build up in quantum wells and dots are measured by a combination of capacitance-voltage profiling and Hall effect [10,11]. Given the complex setup needed to curry out most of these measurements, direct investigation of polarization properties is not straightforward, and many researchers rely on ab-initio simulations instead.

Surprisingly, a rigorous quantum mechanical definition of the polarization of crystalline solids was not available until the early 1990s, after the formal development of the Berry-phase theory by Vanderbilt, King-Smith and Resta [12,13]. The theory got its name from the fact that the polarization is related to a geometric phase acquired by the crystal wave functions called the Berry phase [14]. This approach has been extremely successful in predicting polarization values, and is routinely employed for device modelling and analysis.

Several low-symmetry crystallographic structures allow a non-vanishing polarization vector. Perhaps the most popular materials that exhibit polarization behaviour are the ones crystallizing in the hexagonal wurtzite structure. The reasons why wurtzite crystals gained so much popularity in polarization research are that: (i) They are accessible numerically due to their symmetry and simple geometry. In fact, the wurtzite phase has the highest symmetry compatible with the existence of the spontaneous polarization [15]. (ii) They can be grown as thin films in the laboratory with a relatively high quality, using growth techniques such as plasma-assisted molecular beam epitaxy [16]. (iii) They enable the study of the three fundamental polarization effects: piezoelectricity (polarization induced by strain),

pyroelectricity (polarization induced by temperature) and even ferroelectricity in special cases [17] (polarization induced by electric field).

Among all wurtzite materials, the III-nitrides and II-oxides are the ones that have allowed the emergence of the most promising and useful technologies in the domains of optoelectronics, microelectronics and piezoelectric devices [18–22]. The III-nitrides, e.g. aluminium nitride (AlN), gallium nitride (GaN) and indium nitride (InN), are compounds which involve nitrogen (N) and a group-III metal of the periodic table (Al, Ga and In). The II-oxides, on the other hand, comprise oxygen (O) and a group-II metal (Be and Zn). Examples of oxides include beryllium oxide (BeO) and zinc oxide (ZnO). The wurtzite phase is the most thermodynamically stable structure of these crystals at ambient conditions [23]. There are other III-nitride and II-oxide materials whose ground-state structure is not wurtzite, such as boron nitride (BN, layered-hexagonal [24]) and cadmium oxide (CdO, rocksalt [25]). Both groups have been studied intensively during the past three decades. However, and despite their technological relevance, there are still dark areas and missing details surrounding the field of polarization research for this material system. This work addresses several aspects of the description of polarization in wurtzite crystals that, in our opinion, need more elaboration. While our theoretical study can in principle be done for any wurtzite system, the nitride binaries AlN, GaN and InN, the nitride ternaries AlGaN, InGaN and InAlN, the nitride quaternary AlInGaN as well as the oxide binaries BeO and ZnO have been chosen as examples to illustrate our findings.

The present thesis is based on a collection of published and unpublished papers that have been the subject of our doctoral research in ECP3M, Laboratory of Elaboration et Caractérisation Physico Mécanique et Métallurgique des Matériaux, from 2019 to 2025, under the supervision of Pr. Said Meskine and Pr. Hamza Abbassa. Initially, our research included two different projects that have some points in common. They started in 2017 as a collaboration with Institut Matériaux Microélectronique Nanoscience de Provence (IM2NP), specifically with the Quantum Matter Theory Group headed by Pr. Roland Hayn. One of the projects was about the direct piezoelectric effect in wurtzite compounds. The results of this study are given in Chapter VI, where we propose uniaxial pressure as a way to enhance the piezoelectric response of nitride and oxide materials. The other project consisted of determining the influence of the crystalline defects known as stacking faults on the properties of GaN and ZnO. We present in Chapter VII, for the first time, the electronic structure and polarization properties of both wurtzite GaN and ZnO in the presence of basal-plane stacking faults.

During the time in which the work on piezoelectricity was performed, we considered the equilibrium situation where no strain is applied. This led to the study of the spontaneous polarization of wurtzite crystals, the results of which are outlined in Chapter IV. Chapter V on the polarization of wurtzite alloys was motivated by the seminal paper by Dryer et *al.* [26]. The work included here is basically an extension of Dryer's results from pure binary III-nitrides to their ternary and quaternary alloys.

In addition to the article-based chapters, there are also introductory chapters of the concepts, theories and methods used throughout the rest of the thesis: introduction to electric polarization in crystals (Chapter I), review of density-functional theory (Chapter II) and review of the Berry-phase theory and its application to the study of polarization in wurtzite materials (Chapter III). In the latter chapter, we will showcase the basic framework of our understanding

of the Berry-phase method, and we will lay the foundation for the polarization calculation presented in Chapters IV-VII. Also, Chapter III will be submitted for journal publication as a topical review paper that will eventually include some of the results on the polarization of alloys and stacking faults.

Remarks about the thesis:

This thesis contains seven chapters. Although these chapters are closely related to each other, they are rather self-contained and can be read on their own. However, it is highly recommended to read them in the order presented here, i.e. from Chapter I to Chapter II and so on. The first three chapters provide the necessary theoretical background. Of particular importance is Chapter III on the Berry-phase theory. We cannot stress too strongly how important this chapter is. It suffices to say that a full and proper understanding of the simulation results reported in Chapters IV-VII hinges on a careful reading of Chapter III. In particular, the reader should be comfortable with the concepts of formal polarization, effective polarization, polarization quantum, polarization lattice and polarization branch, all explained in detail via the definitions and examples of Chapter III.

Chapters IV, V, VI and VII present the findings reported in our papers. We add in these chapters many details and results that are not included in the journal versions. This includes, but limited to, formal-polarization values of different crystalline structures (Chapter IV), structural optimization of biaxially strained heterostructures (Chapter V), and electronic effective masses and band-structure unfolding of stacking faults (Chapter VII). In Chapter V, the approach for calculating the piezoelectric polarization of the nitride alloys is quite different from the one followed in the corresponding paper. We think that the method of the thesis is more consistent with the spirit of the Berry-phase formalism.

Throughout this thesis, the electric polarization is always given in the unit C/m^2 (some authors use $\mu C/cm^2$). We express energies and distances in eV and Å, respectively, unless otherwise stated. Vector quantities are denoted by bold letters such as **P** for the polarization vector (instead of $\vec{P}$). On the other hand, vector magnitudes and components, as well as scalars, are represented by a letter in italic type, e.g. the z-component of polarization is P_z. Over 75 graphs are given in the text, all of them are plotted using the software OriginPro. The only exceptions are Figures V.20, VII.9 (*c*) and VII.10 (*b*), which are made by the scripts of matlab. We design the schematic figures, such as Figures I.2 and III.4, via Adobe Photoshop, and we make use of VESTA to visualize all the crystalline structures studied here.

This is our humble contribution to science. As in the words of George Martin quoted a couple of pages back, we hope that this work constitutes an additional *stone in the great bastion of knowledge*. The formal citation of this thesis is the following: A. Benbedra, “ab-initio investigation of electric polarization in wurtzite crystals”, PhD thesis, University of Mostaganem, Algeria (2025).

Part I
Theoretical background

Chapter I

Electric polarization of crystalline solids

I.1 Introduction

Electric polarization is one of the fundamental quantities in condensed-matter physics. On the theoretical side, it is essential to any proper description of electromagnetic phenomena of matter. Indeed, when studying electric fields inside material media, the polarization vector enters Maxwell's equations (specifically Gauss's law) in order to quantify the interaction between the material and the applied field [27]. Put in other terms, polarization answers the question: how do the microscopic charges within the system response toward an electric field? (More generally toward any perturbation that causes a charge separation, such as strain and temperature). On the practical side, the concept of polarization is basic as well, as it directly affects the performance and functionality of various electronic devices. This effect can be advantageous or not, depending on the specific application in mind. In light emitters, for instance, polarization can severely deteriorate the optical efficiency of the device [28].

The scope of this chapter is to establish the theoretical background to some of the concepts, principles and theories pertaining to the polarization of dielectric crystals. We start in Section I.2 with the classical definition, shared by many old textbooks, that relates polarization to dipole moments, and we discuss the electronic and ionic contributions to polarization as well as the polarization of metallic compounds. In Section I.3, we explain the two types of electric charge that accumulates due to the presence of polarization: surface/volume and interface charges. We then give in Section I.4 an overview of three polarization phenomena that are often encountered in both theory and experiment. These are the piezoelectric, pyroelectric and ferroelectric effects. The discussion on ferroelectricity is complemented by some own simulation results for the ferroelectric perovskite $BaTiO_3$. This thesis concerns the study of electric polarization in wurtzite crystals. Therefore, in Section I.5 we outline an in-depth description of the crystalline structure, polarization and real-life applications of wurtzite materials. We pay special attention to group III-nitrides and II-oxides, which are the only materials studied in the present work.

I.2 Definition of polarization

I.2.1 Microscopic origin

When oppositely charged particles are separated within an insulating object we say that the object is *electrically polarized* [27,29]; that is, it has an excess of positive charge on one side (positive pole) and an excess of negative charge on the other side (negative pole). Such separation can be achieved by different methods. Consider for example what happens when we apply an external electric field $\boldsymbol{E}$ to an insulator. As Figure I.1 shows, the electron cloud of atoms is deformed and displaced with respect to the nuclei in the direction opposite to the

field [27,29]. The negative electrons shift only slightly from their initial configuration, because the positive nuclei exert a restoring force to pull them back. This microscopic charge redistribution gives rise to a macroscopic polarized state of the system. It is important to note that the charged particles responsible for polarization (electrons in this case) are tightly bound to their respective atoms, and cannot move freely in response to the applied field. This is to be expected since we are dealing with insulators, which by definition do not have free charges. An insulator that is polarized when placed in an electric field is referred to as *a dielectric* [27,29].

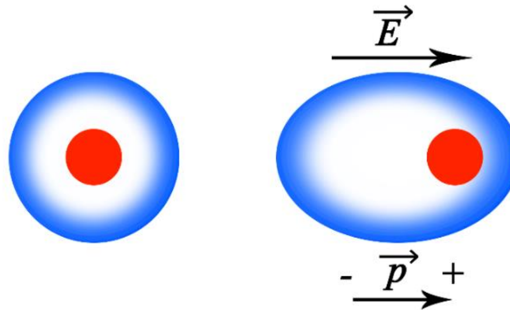

Figure I.1 On the left: a neutral atom in the absence of an electric field. In this case the center of the negative charge (in blue) and that of the positive charge (in red) coincide, which means that the atom is not polarized. On the right: applying an external electric field **E** separates the centers of negative and positive charges, so that the atom is polarized and consequently an electric dipole **p** is formed. The deformation of the electron cloud is exaggerated to dramatize the effect of the electric field.

Two equal but opposite charges separated by a small distance form an electric dipole, which is characterized by its dipole moment **p**. The latter is a vector oriented from the negative charge to the positive one, and its magnitude is given by the product qd [27,29], where q is the absolute value of one of the charges and d is the distance between them. An electric dipole can be either permanent or induced. In a permanent dipole, such as the water molecule, the oppositely charged particles maintain a permanent separation. A dipole can also be created by shifting the electrons of a neutral atom with an electric field. This is an induced dipole, in which the charge separation disappears when the field is switched-off. However, electric dipoles can be induced by other means, for instance mechanical strain (see Sec. I.4). In both cases (permanent and induced dipoles), the dipole moment is a measure of the system's polarity. Note that even though the dipole contain charges and hence sets up an electric field, it remains electrically neutral.

In macroscopic systems, such as crystalline solids, it is customary to define physical properties in terms of densities. In order to describe the charge separation in solid samples, one should use the density of dipole moments, or *electric polarization* **P** (*cf.* Fig. I.2), defined as the dipole moment per unit volume (measured in C/m²) [27,29]:

$$\mathbf{P} = \frac{d\mathbf{p}}{dV}, \tag{I.1}$$

where V in this context is the volume of one unit cell, which is the building block of any crystalline solid.

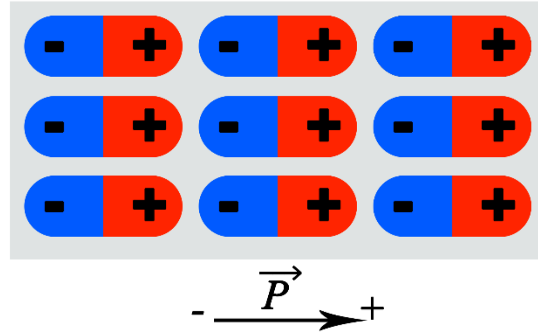

Figure I.2 Sample of a dielectric material contains nine electric dipoles (− +), each has a microscopic dipole moment. The macroscopic polarization vector **P** is defined as the density of these dipole moments and points from the negative pole in the left side to the positive pole in the right side.

I.2.2 Electronic and ionic polarizations

The polarization caused by the deformation of the electron cloud as discussed above is known as *electronic* polarization [30]. In some ionic crystals, the applied electric field does not only shift the electrons, but the ions as well, causing a relative displacement of cations and anions in opposite directions. This results in another type of polarization, namely *ionic* polarization [30]. The ions are generally considered as point-like electric charges located at specific positions in the unit cell according to the symmetry of the host crystal. The ionic polarization $\mathbf{P_{ion}}$ can be obtained as the sum of the dipole moments of all the ions divided by the unit-cell volume [30]:

$$\mathbf{P_{ion}} = \frac{1}{V}\sum_i eZ_i\mathbf{r}_i. \tag{I.2}$$

The summation index i runs over all ions in the unit cell each with charge eZ_i (e is the electron charge and Z_i is the atomic number of ion i) and position vector $\mathbf{r}_i$ relative to a fixed origin. The polarization is independent of the choice of origin provided that the ionic charges sum up to zero [29].

The electronic contribution is calculated in a similar manner, except that electrons are not confined to specific positions, they are instead distributed continuously in the bulk region of the solid. In such a case one works with electronic charge density $\mathrm{n}(\mathbf{r})$ (i.e. charge per unit volume), and the summation in Eq. (I.2) turns into an integral over one unit cell. The electronic polarization $\mathbf{P_{ele}}$ then reads [30]:

$$\mathbf{P_{ele}} = \frac{1}{V}\int en(\mathbf{r})\mathbf{r}d\mathbf{r}. \tag{I.3}$$

The total polarization of the condensed system is simply computed as the sum of equations (I.2) and (I.3). It turns out, however, that the electronic polarization as given by Eq. (I.3) is poorly defined. In fact it is not possible, even in principle, to derive a physically meaningful value of $\mathbf{P_{ele}}$ from the electronic density $\mathrm{n}(\mathbf{r})$ [31]. We will explain the reasons of this ambiguity and how to solve it later in Chapter III. For now we state that electrons are quantum particles

described by wave functions, and any treatment of their polarization must rely on quantum-mechanical concepts that go beyond the classical picture of dipole moments.

I.2.3 Polarisation of metals

There are two classes of materials as defined by their electrical properties: insulators and conductors. The electrons in insulators are tightly bound to the nuclei and not free to move around. In metallic conductors, the outer electrons (called valence electrons in chemistry) are only weakly bound to the nuclei, so that they can become detached from their parent atoms are free to wander through the entire solid. The metal as a whole remains electrically neutral, because we have not added or removed any electrons, but the electrons are now rather like a negatively charged gas or liquid, sometimes called the electron sea, permeating an array of positively charged ion cores.

We have discussed in the previous two subsections the electric polarization of insulators. Metals can also be polarized, but with a mechanism somehow different from that for insulators. When a metal is placed in an externally applied electric field, the sea of electrons shifts slightly, polarizing the metal to have an excess and deficit of electrons on opposite sides. Because the electric force from the positive nuclei, the electron sea shifts only slightly. In practice, the shift or displacement of the electron sea is usually less than 10^{-15} m [32]! An insulator has no free electrons to shift if an external electric field is applied to it. Instead, as shown in Fig. I.1, the electrons bound to all atoms become polarized.

In this thesis, we restrict our interest to the polarization of insulators. All the definitions, concepts, notions, theories (including the Berry-phase theory of Chap. III) and simulation results apply to insulating and semiconducting compounds, specifically III-nitride and II-oxide semiconductors crystallizing in the wurtzite structure.

I.3 Polarization-induced charge

I.3.1 Volume and surface charges

Suppose we have a piece of a polarized material, i.e. an object having a non-zero electric polarization. A standard problem in electrostatics is to calculate the electric field produced by this object (not the field that caused the polarization, but the field the polarization itself causes). If we perform this calculation and drives the expression of the field (as done in Refs. [27,33]), we notice that the field of a polarized object is the same as that generated by a volume charge density ρ plus a surface charge density σ. A rigorous analysis shows that these charge densities can be written as [27,33]:

$$\begin{aligned} \rho &= -\boldsymbol{\nabla}.\mathbf{P}, \\ \sigma &= \mathbf{P}.\mathbf{n}. \end{aligned} \tag{I.4}$$

The volume charge is computed as the divergence of the spatially varying polarization vector $\mathbf{P}$. Recall that the divergence of a vector is the dot product of the gradient operator $\boldsymbol{\nabla}$ and that

same vector. The surface charge is given by the dot product of polarization and the outward unit vector **n** normal to the material boundary.

Equation (I.4) reveals that where polarization occurs, an equivalent electric charge is formed at the bulk and surface regions. We refer to ρ and σ as bound (or polarization) charges, as opposed to free charges. Bound charges are those that are attached to specific atoms or molecules, they are caused by the shifting of electrons and nuclei that occurs as a response to an external electric field. The total bound charge ($\rho + \sigma$) is always zero because no charges are genuinely added to or removed from the neutral sample.

I.3.2 Interface charges

The polarization charge we are interested in here is the one that appears at the interface between two layers having different polarizations [34,35]. These layers can be two polarized materials (e.g. $Al_xGa_{1-x}N$ and GaN) or a crystalline defect in a single material (e.g. basal stacking fault in GaN). We consider the realistic situation illustrated in Figure I.3 that occurs in heterostructure systems, such as quantum wells and quantum dots. In this case we assume the two layers to be on top of each other and the interface between them is perpendicular to their polar axis. The polarization of the top layer is $\mathbf{P}_t$ and that of the bottom layer is $\mathbf{P}_t$, with $\mathbf{P}_t \neq \mathbf{P}_b$. At the interface there is a discontinuous sudden change in polarization, which manifests itself as a net pileup of charge at that interface [34,35].

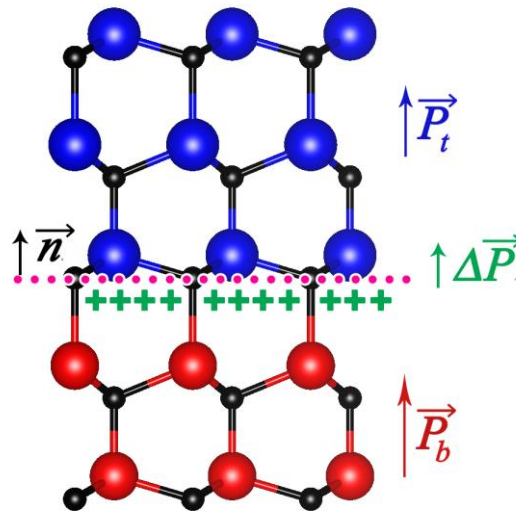

Figure I.3 Interface between two wurtzite materials. This is a very common case where the interface (represented by a pink dotted line in the middle) lies on the horizontal basal plane, and the polar axis coincides with the *c*-axis which is perpendicular to the interface (see Sec. I.5 for a description of wurtzite crystals). The bottom layer is the substrate, it is composed of cations (red spheres) and anions (black spheres), and its polarization is $\mathbf{P}_b$. The top layer also contains cations (blue spheres) and the same anions as the bottom layer, with polarization $\mathbf{P}_t$. The polarization difference $\Delta\mathbf{P}$ equals the polarization charge that bounds at the interface (plus signs). Note that **n**, $\mathbf{P}_\mathrm{b}$, $\mathbf{P}_t$ and $\Delta\mathbf{P}$ are along the vertical polar axis. Note also that the polarization charge is positive because $\mathbf{P}_t > \mathbf{P}_b$. Similar interfaces were used to compute the polarization charge of wurtzite-rocksalt interfaces such as ZnO/MgO [36] and GaN/ScN [37].

Our goal is to determine the bound polarization charge at such an interface. For this purpose, we use the *interface theorem* developed by Vanderbilt and King-Smith [38], which states that the interface polarization charge is the difference between the polarization of the bottom layer and the polarization of the top layer, projected along the normal of the interface:

$$\sigma = \Delta\mathbf{P}.\mathbf{n} = (\mathbf{P}_b - \mathbf{P}_t).\mathbf{n}, \tag{I.5}$$

where **n** is the normal vector of the interface. The interface theorem is only valid if both layers are insulating with a non-zero band gap. From Fig. I.3, we see that the polarization vectors are perpendicular to the interface (i.e. parallel to **n**), indicating that the dot product in Eq. (I.5) reduces to:

$$\sigma = \Delta P = P_b - P_t. \tag{I.6}$$

This is the case of an interface between two wurtzite layers studied in detail in Chapters V and VII.

I.4 Polarization effects

Electric polarization is usually used to describe the response of a dielectric material (i.e. how the charges will shift) to an externally applied perturbation. Examples of such perturbations include mechanical deformations, temperature changes, electric fields and lattice vibrations. This diversity results in a plethora of phenomena, or effects, such as piezoelectricity, pyroelectricity and ferroelectricity. In the following we give for each effect an overview of the polarization mechanism. We also discuss the quantities that relate the induced polarization to the respective perturbation.

I.4.1 Piezoelectricity

Piezoelectricity is the property of some materials to exhibit an electric polarization upon the application of a mechanical stress (force per area) [39]. This is often referred to as the *direct* piezoelectric effect. The applied stress deforms the material, generating a mechanical strain (relative change of length). As previously explained, the dipole moments are created within the material because the shift of electrons and ions, but in this case the charge separation is a response to a mechanical distortion rather than to an electric field. The reverse process, labeled as the *converse* piezoelectric effect, refers to the internal strain induced by an applied electric field [39].

Whether or not a crystal is piezoelectric depends on its symmetry. Specifically, crystals whose symmetry allows an inversion center cannot display this effect. Only insulating ionic materials belonging to one of the twenty non-centrosymmetric crystal classes can exhibit piezoelectricity [40]. The mathematical description of this electromechanical phenomenon is given in terms of two sets of parameters. The piezoelectric coefficient e_{ij} links the polarization-vector component P_i and strain ϵ_j via [41]:

$$e_{ij} = \frac{dP_i}{d\epsilon_j}. \tag{I.7}$$

The piezoelectric modulus d_{ij}, on the other hand, gives the evolution of polarization as a function of stress σ_j [41]:

$$d_{ij} = \frac{dP_i}{d\sigma_j}. \tag{I.8}$$

Both e_{ij} and d_{ij} are actually third-order tensors, i.e. they are labeled by three indices. However in this work we employ the so-called Voigt notation for brevity, so that the piezoelectric tensors are labeled by only two indices. The experimental data on the piezoelectric response are most often given in terms of d_{ij} [9]. Of particular interest to this work are the piezoelectric coefficients e_{ij} because they are easily accessible to simulation. The relation between e_{ij} and d_{ij} can readily be obtained from the elastic tensor C_{ij} [41].

Different deformations result in different piezoelectric polarizations. For example, the response of a piezoelectric material to a compressive stress would be different from that to a shear stress. This means that the piezoelectric tensor contains different constants, each one of them corresponds to a specific type of mechanical strain. In the most general case, the tensor has 18 independent components. This number is reduced significantly by the symmetry operations of the crystal. For hexagonal lattices (such as wurtzite), which are the most relevant to the work of this thesis, the piezoelectric tensor $\mathbb{e}$ in Voigt notation has the following matrix form [42]:

$$\mathbb{e} = \begin{pmatrix} 0 & 0 & 0 & 0 & e_{15} & 0 \\ 0 & 0 & 0 & e_{15} & 0 & 0 \\ e_{31} & e_{31} & e_{33} & 0 & 0 & 0 \end{pmatrix}. \tag{I.9}$$

So hexagonal crystals are characterized by just three unique non-zero piezoelectric coefficients. These are e_{33}, e_{31} and e_{15}. The number indices refer to Cartesian axes (1=x, 2=y and 3=z), with the first (second) number corresponding to the direction of the polarization vector (applied strain). With this in mind, e_{33} measures the polarization induced parallel to the z-axis by a uniaxial strain applied along that same axis, whereas e_{31} measures the polarization induced along the z-axis by a biaxial strain on the xy-plane [42]. The third component e_{15} describes the polarization induced by a shear strain perpendicular to the z-axis. We will not compute the complete piezoelectric tensor here, and limit ourselves to the dominant coefficient e_{33} which always has the largest value.

I.4.2 Pyroelectricity

Among the twenty crystal classes of piezoelectric materials, ten classes are compatible with the existence of permanent dipole moments, and thus possess a polarization in the absence of strain and electric field or any other external perturbation [43]. Such polarization is known as *spontaneous polarization* $\mathbf{P_{sp}}$, and its vector is always parallel to a specific direction in the

crystal lattice called the polar axis. Charge separation in this case maintains itself due to an intrinsic broken-symmetry. The latter statement needs some elaboration.

The ions are located at well-defined positions in the unit cell. These positions are usually (fractional) Cartesian coordinates (x,y,z) that can be either ideal or non-ideal. Ideal positions are those whose all coordinates can be written as simple ratios: 1/2, 2/3, etc., otherwise the positions are said to be non-ideal, also referred to as *internal parameters*. We have observed that crystalline structures that are spontaneously polarized always have one or more internal parameters, which indicates that the broken-symmetry responsible for the existence of the spontaneous polarization manifests itself as non-ideal ionic positions [44]. The simplest structure where $\mathbf{P_{sp}}$ is allowed is wurtzite, which only has one internal parameter. As will be shown later on by explicit calculations, the magnitude of the spontaneous polarization is found to be proportional to the value of the internal parameter. Notice that the converse is not necessarily true; that is, not all crystals with internal parameters can exhibit a spontaneous polarization.

The spontaneous polarization is temperature dependent: changes in temperature either shorten or elongate the already existing dipoles, altering the positions of ions and deforming electron clouds within the sample, which results in a corresponding change of polarization. This phenomenon is the pyroelectric effect [43]. This effect is one of the mechanisms used to convert heat into usable electricity. When a pyroelectric material is heated or cooled, its polarization changes according to this expression [43]:,

$$\Pi_i = \frac{dP_i}{dT}, \tag{I.10}$$

where Π_i is the vector component of the pyroelectric coefficient and T is the temperature. As explained in the two previous sections, the spontaneous polarization produces opposite electric charges on the material surfaces, and if electrodes and conducting wires are attached to the surfaces the generated charges can be collected and used as an electric current. It should be emphasized that all pyroelectric compounds are also piezoelectric. In the present work, we will study how the spontaneous polarization of wurtzite crystals changes with respect to the internal strain (Chap. IV), alloy composition (Chap. V) and basal stacking faults (Chap. VII). However, we will not address the temperature dependence of $\mathbf{P_{sp}}$ in this thesis.

I.4.3 Ferroelectricity

A condensed system is ferroelectric if it is polar like pyroelectric materials, with the additional property that the spontaneous-polarization vector can be reversed under the application of an external electric field [44]. Pyroelectrics do not display the latter property, as their spontaneous polarization is always fixed in a specific direction. The polarization of a ferroelectric material is linked to the applied field E_j through the relation [44]:

$$\chi_{ij} = \frac{dP_i}{dE_j}, \tag{I.11}$$

where χ_{ij} is a material-dependent parameter known as the electric susceptibility, which describes how the polarization is changed in response to the electric field. The greater the susceptibility, the greater the ability of the system to polarize.

Above a certain temperature called the Curie temperature T_C, a ferroelectric crystal adopts a paraelectric configuration: a centrosymmetric structure with zero polarization. Below T_C, the crystal undergoes a series of structural phase transitions to non-centrosymmetric structures depending on temperature. Each structure is characterized by the value and orientation of its ferroelectric polarization [44]. To better illustrate this phenomenon, we consider the prototypical ferroelectric material barium titanate $BaTiO_3$, which crystallizes in the perovskite structure [45]. In the paraelectric state $BaTiO_3$ has a cubic symmetry, which can be described with Ba at the corners, Ti at the cube center and O at the center of the faces. The cubic symmetry reduces to the tetragonal one at T_C= 393 K (corresponding to 120 °C) [46]. Below this temperature, the central Ti and O atoms deviate slightly along the tetragonal *c*-axis. This relative displacement of atoms turns the ideal atomic positions into non-ideal ones (or internal parameters) and develops a spontaneous polarization, making the structure polar [46]. Reducing the temperature even further, the tetragonal structure of $BaTiO_3$ transforms into the orthorhombic (at 278 K) and finally into the rhombohedral (at 183 K) phases [46].

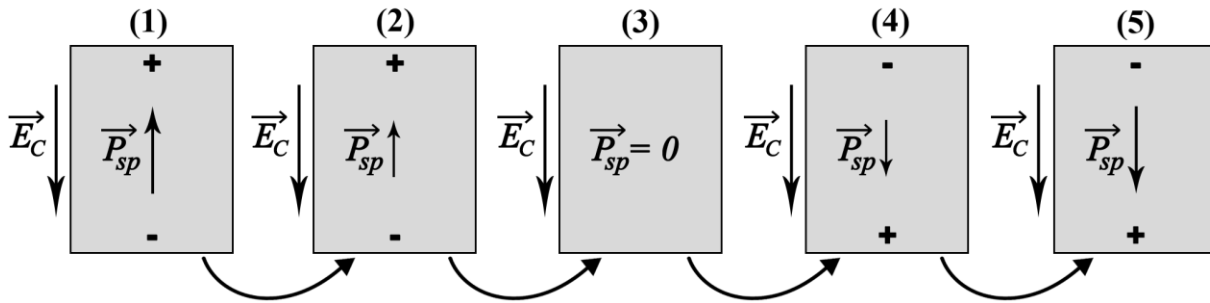

Figure I.4 Schematic of the Ising-type ferroelectric switching path in $BaTiO_3$. The path starts at structure (1), which is the polar tetragonal structure where the polarization points “up” and equals the spontaneous polarization $\mathbf{P_{sp}}$. Upon applying the coercive electric field $\mathbf{E_C}$, the polarization decreases as shown in structure (2), and eventually vanishes in structure (3). The latter is the non-polar paraelectric state. In structure (4), the polarization increases but in the opposite direction compared to structures (1) and (2) (the same direction as the field). The increase in polarization continues until its magnitude is equal to the spontaneous polarization of the first structure. Structure (5) is the end of the switching path and corresponds to the anti-polar configuration with “down” polarization. Looking at the first and last structures, we see that the polarization vector changes its orientation by 180°.

Next we describe the mechanism of polarization reversal. In order to switch the spontaneous polarization of ferroelectric compounds, one has to apply a strong enough electric field in the opposite direction of $\mathbf{P_{sp}}$. As a response to the applied field, the magnitude of the polarization vector decreases gradually until it vanishes, then the vector flips with its magnitude increasing in the same orientation as the field [7,47]. This process is depicted schematically in Figure I.4. We define the coercive field $\mathbf{E_C}$ to be the minimum field at which the switching occurs [48]. The process just explained is known as *Ising*-type switching and corresponds to a

180° flip of polarization [49,50]. There exists other ferroelectric switching mechanisms such as the *Bloch*- and *Néel*-types, in which the polarization vector does not vanish but rather rotates by an angle. A more detailed account can be found in the paper by Lee et *al.* [51]. As shown in Fig. I.4, three key structures are required in the Ising-type polarization reversal: a ferroelectric polar [structure (1) in Fig. I.4], paraelectric non-polar [structure (3)] and ferroelectric anti-polar [structure (5)] states. These structures (and the other structures between them) form what is called a switching path. The polar and anti-polar states are crystallographically equivalent in the sense they have the same energy. In addition, their polarizations are equal but have opposite signs.

Ferroelectricity in $BaTiO_3$:

In what follows, we present some of our results concerning the ferroelectric properties of $BaTiO_3$, which is one of the most well-characterized perovskite compounds. The total energy of a ferroelectric crystal as a function of polarization is given by the Landau-Devonshire phenomenological model [47,52], which describes the energy-polarization variation as a fourth order polynomial:

$$E(P) = E_0 + \alpha P^2 + \beta P^4, \qquad \text{(I.12)}$$

where E_0 is the energy of the paraelectric structure. The coefficients α and β are the model constant parameters. Both energy and polarization are correlated to the structural degrees of freedom of the crystal. We generate a set of structures that map the Ising switching path of $BaTiO_3$ by shifting the positions of Ti and O atoms between the two ferroelectric and paraelectric states and compute their energies and polarizations as described in Part II of the thesis [49]. We assume that the tetragonality of the system remains unchanged during the polarization switching; in other words, the lattice parameters a and c are held constant throughout the calculation.

The results of fitting the energy-polarization data to equation (I.12) are represented in Figure I.5. We observe two minima which correspond to the polar and anti-polar ferroelectric structures with opposite polarization. The paraelectric state connecting the two ferroelectric minima is positioned at the saddle point (zero polarization). In this case, the paraelectric configuration is a tetragonal structure where all atomic positions are ideal, i.e. without any atomic distortions. This energy profile is a double-well potential [44,53]: two symmetrical adjacent wells having the same height and length.

One can extract important information from Fig. I.5. The best fit corresponds to the following parameters of Eq. (I.12): α= 357 meVm²/C² and β= −2120 meVm^4/C^4. The height of the potential well is the energy barrier U_S for polarization switching, which is equal to the difference in energy between the ferroelectric and paraelectric configurations [7]. U_S is found to be 15 meV per unit cell, which lies within the range of previously reported values 5-56 meV [53]. This barrier between the two opposite ferroelectric states is weak enough so that an applied electric field can induce flipping. The polarization of the two minima coincides with the spontaneous polarization of $BaTiO_3$. Our value of P_{sp} is 0.29 C/m², in excellent

agreement with the experimental value 0.26 C/m² [54]. Knowing U_S and P_{sp} we can estimate the strength of the coercive field defined above via [47]:

$$E_C = \frac{8}{3^{3/2}} \frac{U_s}{V P_{sp}}, \tag{I.13}$$

with V being the volume of one unit cell. We find that the switching of polarization by 180° requires a moderate coercive field of 6.37 MV/cm.

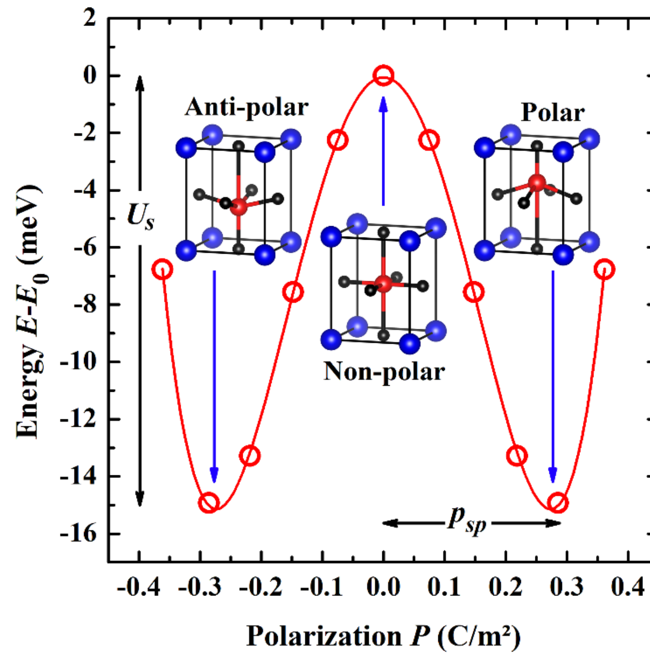

Figure I.5 Energy-polarization profile calculated from first-principles for the 180° polarization reversal of $BaTiO_3$. The vertical scale is the total energy of the unit cell, whereas the horizontal scale represents polarization values. Note that the energy is referenced to the energy of the paraelectric (non-polar) configuration E_0. Each data point corresponds to a structure generated by linearly interpolating the positions of O and Ti atoms from the polar to the anti-polar states (passing by the non-polar structure). The curve is obtained by fitting the data to the Landau-Devonshire parameterization, Eq. (I.12). The switching energy barrier U_S and the spontaneous polarization P_{sp} are shown. Also shown are the tetragonal unit cells corresponding to the polar, non-polar and anti-polar structures.

Here, we investigate the polarization of materials crystallizing in the wurtzite phase such as GaN and ZnO. Because the polarization of this material system is not switchable, the ferroelectric effect is out of the scope of the present study. However, wurtzite crystals can become ferroelectric under certain circumstances. We will further explain this point in the perspectives at the end of the thesis.

I.5 Wurtzite crystals

Among the 26 structures of hexagonal crystals, we focus on studying one particular structure, namely *wurtzite*. In this section, we describe the crystalline geometry of the wurtzite phase in detail, defining the different structural parameters. Next we explain the physical origin of polarization and its relation to symmetry reduction and structural distortions. Finally, we present some applications of wurtzite materials in the fields of electronics, optoelectronics and piezoelectronics.

I.5.1 Crystalline structure

The space group of the wurtzite structure is $P6_3mc$ or 186, which contains 12 symmetry operations that left the crystal unchanged (for comparison, cubic crystals have 24 operations). These operations include two 120° rotation around a six-fold axis (6_3), three reflections with respect to mirror planes (m), six reflections each followed by a translation with respect to a glide plane (c) and the identity [55]. Figure I.6 (*a*) shows the primitive (Wigner-Seitz) unit cell that captures the full symmetry of the wurtzite phase. Even though such a cell is defined by three lattice vectors **a**, **b** and **c**, the crystallographic directions and planes are described by four Miller indices, not three like the other crystal lattices. One complete hexagonal base is shown in Fig. I.6 (*b*).

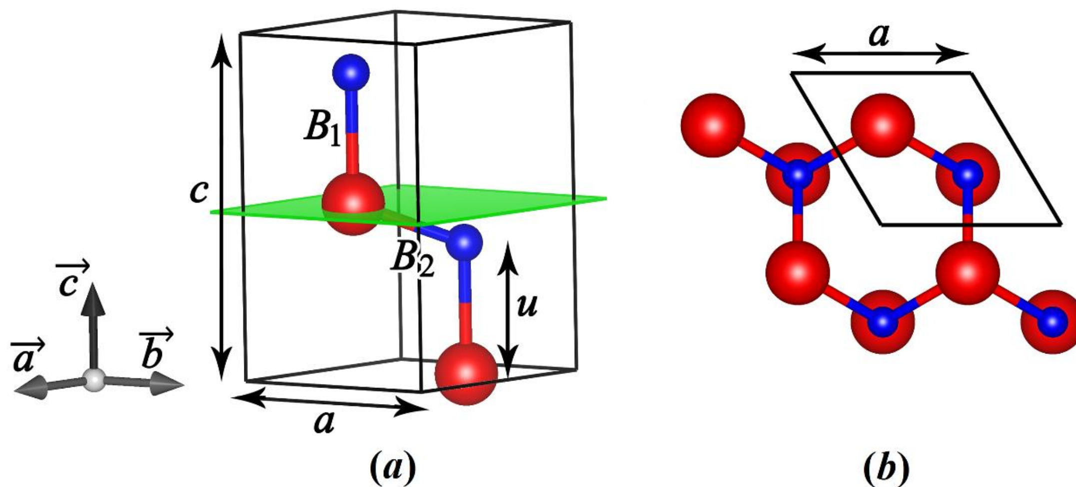

Figure I.6 (*a*) Side view of the standard 4-atom unit cell of wurtzite crystals illustrating the structural parameters a, c and u described in the text. The lattice vectors **a**, **b** and **c** are shown to the left, with the vertical **c** vector being normal to both **a** and **b**. These two vectors define the horizontal green plane known as the basal or c-plane. Red and blue spheres correspond to cations and anions, respectively. The label B_1 refers to the bond linking the cation and anion along the c-axis, whereas B_2 is the bond in the basal plane. (*b*) Top view of the full hexagonal base and the borders of the unit-cell base shown in (*a*). This structure is actually a 32-atom supercell. Further information about supercells, including their uses and generation, are provided in Section II.7. These crystalline structures are constructed using the software VESTA [56].

Any unit cell is completely described by the lattice constants a, b and c, the lattice angles α, β and γ as well as the atomic positions x, y and z. Within the Cartesian system of coordinates, the hexagonal lattice vectors $\mathbf{a}$, $\mathbf{b}$ and $\mathbf{c}$ are related to the lattice constants a and c by these relations: $\mathbf{a} = \frac{a\mathbf{i}}{2} + \frac{a\sqrt{3}\mathbf{j}}{2}$, $\mathbf{b} = -\frac{a\mathbf{i}}{2} + \frac{a\sqrt{3}\mathbf{j}}{2}$ and $\mathbf{c} = c\mathbf{k}$, where $\mathbf{i}$, $\mathbf{j}$ and $\mathbf{k}$ are the Cartesian unit vectors along the x-, y- and z-axes, respectively. The hexagonal symmetry dictates the equality of the lattice constants a and b [57]. We call a the basal or in-plane lattice constant because it lies on the basal (0001) plane [the green plane in Fig. I.6 (a)]. The other lattice constant c is the axial or out-of-plane lattice constant [57]. It is longer than a and parallel to the [0001] direction (the hexagonal c-axis). When wurtzite heterostructures are grown, the most common growth direction coincides with the c-axis. It is extremely difficult to construct heterostructures of high crystal quality along other directions [58]. The angle between the vectors **a** and **c** (**b** and **c**) is α= 90° (β= 90°) and that between **a** and **b** is γ= 120° [57].

Wurtzite crystals are usually binary ionic compounds, their unit cell contains two cations and two anions. The Cartesian coordinates of the cations are (0,0,0) and (a/2,$a\sqrt{3}$/6,c/2). For the anions we have (0,0,uc) and (a/2,$a\sqrt{3}$/6,(1/2+u)c) [59]. The z-coordinate of the anion contains an internal parameter u whose value depends on the material at hand. The internal parameter is defined as the ratio of the cation-anion bond length along the c-axis and the lattice constant c [37]. In practice, however, it is more convenient to use the coordinate system attached to the unit cell, i.e. the non-orthogonal coordinate system whose axes are the a-, b- and c-axes, rather than the Cartesian axes x, y and z. In this case, the positions of the two cations are (a/3,2a/3,0) and (2a/3,a/3,c/2), and the two anions are situated at (a/3,2a/3,cu) and (2a/3,a/3,(1/2+u)c) [60]. It is also costmary to write the atomic positions as fractional coordinates (x/a,y/a,z/c), e.g. (1/3,2/3,u) instead of (a/3,2a/3,cu). Finally, there exists two types of chemical bonds between the cation and anion: one bond labeled B_1 along the c-axis and three bonds B_2 in the basal plane [61] [only one bond is shown in Fig. I.6 (a)].

Multinary wurtzite crystals:

The crystalline structure explained above describes the traditional binary wurtzite materials, such as GaN, ZnO and SiC, etc., which have two types of elements: one cation and one anion. By mixing two or more such binaries, we can make ternary and quaternary alloys which also adopt the wurtzite phase. For instance, the ternary alloy AlGaN is a mixture of AlN and GaN. There are however pure wurtzite materials (i.e. not alloys) that contain more than two atomic species. Examples of such mutinary (beyond binary) compounds include NaMgAs, Mg_3MoN_4 and $MgSiN_2$. The wurtzite structure of these crystals is somehow different from that of the binaries. Take NaMgAs as an example, which belongs the half-Heusler group. Since NaMgAs has one anion (As) and two cations (Na and Mg), its wurtzite phase is characterized by two different internal parameters u and v [62], which measure the fractional coordinate along the c-axis of Mg and As, respectively. Herein, we are solely interested in binary wurtzite compounds (namely III-nitrides and II-oxides) and their alloys.

I.5.2 Polarization in wurtzite crystals

The wurtzite structure has a tetrahedral geometry [63]: each atom is surrounded by four atoms of the other type at the corners of a tetrahedron, and vice versa, implying that the coordination number, or the number of closest neighbours, is $N = 4$. We present in Figure I.7 the cation- and anion-centered tetrahedrons, where we can see that each tetrahedron contains four bonds. The three bonds B_2 in the basal plane are equivalent, while the bond B_1 along the c-axis is a little bit longer [63]. This makes the wurtzite structure non-centrosymmetric, i.e. it lacks a center of inversion. Recall that a crystallographic structure is said to be centrosymmetric if the mapping of every lattice point (x,y,z) onto the point $(-x, -y, -z)$ leaves the structure indistinguishable, otherwise the structure is non-centrosymmetric. This intrinsic symmetry reduction, in addition to the ionic nature of the bonding, are the physical origin of polarization [63]. A mechanical strain applied to a wurtzite crystal induces a piezoelectric polarization, but even in the absence of strain the material still has a spontaneous polarization in the c-direction [42], meaning the polar axis coincides with the c-axis. We will study both kinds of polarization of pure and alloyed wurtzite compounds throughout this thesis.

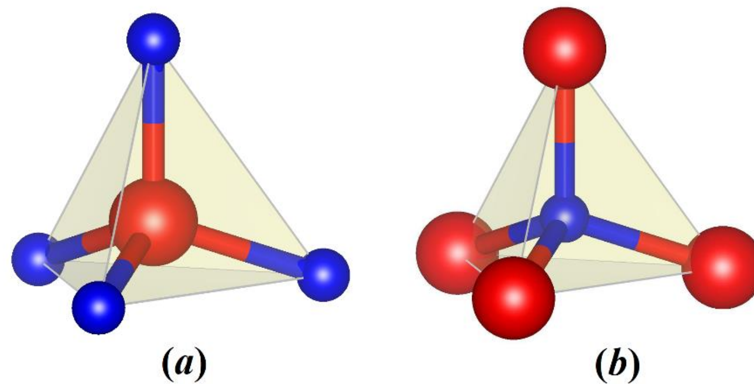

Figure I.7 Tow tetrahedral building blocks. In (a), the anions (in blue) form the corners of the tetrahedron, whilst the cation (in red) sits at its center. The situation in (b) is reversed. The vertical bond is labeled B_1 in Fig. I.6 (a), and the three (near) horizontal bonds are labeled B_2. In the wurtzite structure the bonds B_1 and B_2 have different lengths. The bond lengths are equal only in the ideal wurtzite structure.

When the internal parameter u of the wurtzite structure is fixed at 3/8 and the ratio of the lattice constants c/a at $\sqrt{8/3}$, it follows that all bond lengths and the interbond angles are equal [23,61]. The equivalence of the bonds can be inferred by the tetrahedral cage being regular; that is, its geometric center coincides with the location of the central atom. The resulting structure is known as *ideal* wurtzite, which is also non-centrosymmetric.

There is another structure that can be derived from wurtzite, which is the *layered-hexagonal* structure. It is obtained by setting the wurtzite internal parameter to 1/2, so that the cation and anion are located on the same atomic plane. Figure I.8 pictures the unit cell of the real wurtzite (in the middle), ideal wurtzite (left) and layered-hexagonal (right) structures. Contrary to the real and ideal wurtzite phases, the layered-hexagonal structure is centrosymmetric.

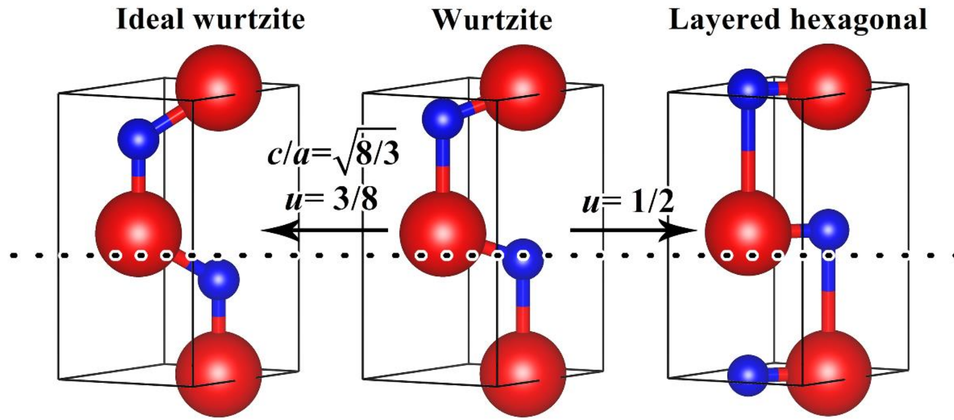

Figure I.8 The ideal wurtzite structure (on the left) is obtained from the wurtzite phase (in the middle) by setting the internal parameter u and the lattice-constant ratio c/a to 3/8 and $\sqrt{8/3}$, respectively. The wurtzite phase transforms into the layered-hexagonal structure (on the right) when u= 1/2. The dotted horizontal line that passes by the first anion of wurtzite highlights the difference between the values of the internal parameter for the three structures.

Model of polarization:

Previous studies have reported a simple model to evaluate the spontaneous polarization of wurtzite compounds. This model is based on the definition of a polarization-related quantity called the *Born effective charge* Z_{33}^*, which is the amount of charge that a displacing ion effectively contributes to the polarization. We will study the effective charge later in Chapter VI. The spontaneous polarization P_{sp} within this model is written as [64,65]:

$$P_{sp} = -\frac{4e}{a^2\sqrt{3}} Z_{33}^* \left(u - \frac{3}{8}\right), \tag{I.14}$$

where a and u represent the in-plane lattice constant and the internal parameter, respectively. These structural parameters for wurtzite materials are measured with sufficient accuracy by using X-ray diffraction. At a classical level, we can think of $Z_{33}^*(u - 3/8)$ (charge multiplied by displacement) as a permanent dipole moment in the unit cell, which is responsible for the occurrence of spontaneous polarization in the macroscopic sample.

The results of Eq. (I.14) show a level of agreement with the reported literature values. In the case of wurtzite GaN, for which a= 3.19 Å, u= 0.377 and Z_{33}^*= 2.82, the spontaneous polarization is calculated to be −0.020 C/m², which is in line with the experimental value −0.022 C/m² and with the theoretical (first-principles) value −0.034 C/m² [66]. Some authors used similar models to estimate the spontaneous polarization of perovskite oxides [67]. Equation (I.14) suggests that the magnitude of the spontaneous polarization is determined by the deviation from the ideal tetrahedral coordination of atoms. Stated differently, P_{sp} critically depends on the difference between the internal parameter u and its ideal value 3/8. Our results presented in Chapter IV are in favour to this reasoning. Even though the proposed model is highly simplified it still captures the essence of polarization in the wurtzite structure. However, it incorrectly predicts a vanishing spontaneous polarization of the ideal wurtzite lattice [setting

u= 3/8 in Eq. (I.14) yields P_{sp}= 0]. As we will show in Chapter IV, this is not the case as both the real and ideal wurtzite structures are spontaneously polarized.

In recent years, theoretical and experimental discoveries have pointed out that the relative ionic displacement of Eq. (I.14) should be $u - 1/2$ rather than $u - 3/8$, which gives:

$$P_{sp} = -\frac{4e}{a^2\sqrt{3}} Z_{33}^* \left(u - \frac{1}{2}\right). \qquad \text{(I.15)}$$

Using this formula, the spontaneous polarization of wurtzite GaN is 1.26 C/m², very close to the measured and calculated values 1.29 C/m² and 1.31 C/m², respectively [68]. If we want to compute the spontaneous polarization of the layered-hexagonal structure via Eq. (I.15), we equate u to 0.5, resulting in zero polarization, fully consistent with the fact that this crystal structure has a centre of inversion as a symmetry operation. But how wurtzite GaN has two different values of P_{sp}? One of the major findings of our thesis is that the predictions of Eq. (I.15) are more appropriate than those of Eq. (I.14) for modelling the spontaneous polarization of wurtzite crystals. More details and insights about this point are provided in Chapter V, specifically in Section V.3.7.

I.5.3 Properties and applications

Among the compounds that have the wurtzite structure in their ground state are the group III-nitrides: aluminium nitride (AlN), gallium nitride (GaN) and indium nitride (InN), and the group II-oxides: beryllium oxide (BeO) and zinc oxide (ZnO). These materials are the ones that we are going to explore in the present work. Both groups have been demonstrated as technologically exciting materials for a variety of domains, including optoelectronics, microelectronics and piezoelectronics.

A. Optoelectronics:

The most widespread application of the nitrides AlN, GaN and InN is for optoelectronic devices, such as laser diodes (LDs), light-emitting diodes (LEDs) and photovoltaic solar cells. This is mainly due to the fact that these materials are semiconductors with direct band gaps [69], which prefer radiative transitions. The band-gap values of the pure binaries are limited, which causes a problem when looking for a particular wavelength not compatible with the gap of any binary. Solving this and other limitations may require the use of alloys (solid solutions), where two or three different materials are mixed together to form one material. One can adjust the chemical composition of the alloy to obtain the desired band gap [70]. This method of alloying different compounds can be applied to control other physical properties as well, for instance elasticity and electric polarization [65,71].

In order to make an optoelectronic device, for example a LED, two materials with different band gaps are assembled together to form a junction [72]. A commonly used material combination is shown on Figure I.9 (a): a layer of GaN with smaller band gap is inserted between two layers of $Al_xGa_{1-x}N$ which has a larger gap. The alloy $Al_xGa_{1-x}N$ is produced when some fraction x of Ga atoms in the GaN lattice is replaced by In atoms. The resulting

heterostructure is a quantum well grown along the vertical c-axis which we notate as $Al_xGa_{1-x}N/GaN/Al_xGa_{1-x}N$ (or simply $Al_xGa_{1-x}N/GaN$) [73]. These structures can be grown by molecular beam epitaxy or chemical vapour deposition. The band diagram of such a quantum well is given in Figure I.9 (b). Two parameters are needed to characterize the quantum well, these are the height (or depth) and the length. In our case, the height of the quantum well is determined by the conduction-band offset ΔE_C and the valence-band offset ΔE_V (more details about these offsets can be found in Chapter VII). As for the length of the well, it is simply equal to the thickness L of the middle GaN layer.

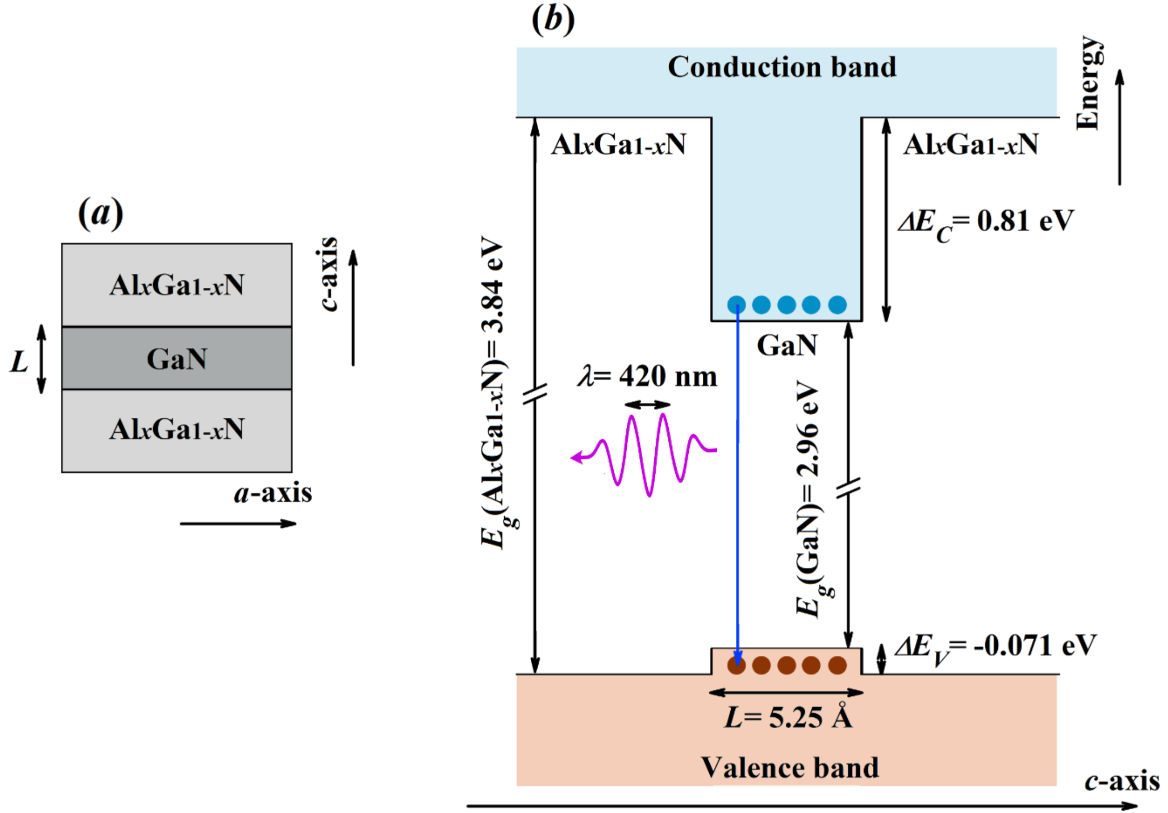

Figure I.9 (a) $Al_xGa_{1-x}N/GaN$ heterostructure (for x= 0.5) in a quantum-well configuration grown along the c-axis. Because the band gap of the GaN layer is lower than the gap of the $Al_xGa_{1-x}N$ layer, electrons and holes are trapped in the middle GaN region which has a thickness L. In this case both layers are lattice-matched, i.e. the lattice constant a of GaN is equal to that of $Al_xGa_{1-x}N$. In practice, this is accomplished via applying compressive or tensile biaxial strain. (b) Band diagram of the quantum well shown in (a). The electrons (●) and holes (●) are trapped in the conduction and valence bands of GaN, respectively. We compute the gap value of the GaN and $Al_xGa_{1-x}N$ regions using the modified Becky-Jonson exchange-correlation functional (see Sec. II.5.2). The band offsets ΔE_C and ΔE_V, which give the height of the quantum well, are calculated using the gap and Fermi energies (see Sec. VII.3.2). Here, the length of the quantum well L is equal to the lattice constant c of GaN. The blue vertical arrow is an electronic transition, and the purple wave packet is the photon emitted from the transition.

The band gap is lower in the GaN region (2.96 eV) than in the $Al_xGa_{1-x}N$ region (3.84 eV). This difference in energy can be thought of as a potential that an electron or hole would feel. As a consequence, an electron in the conduction band with low energy will be trapped in the quantum-well region (the GaN layer) [72]. Similarly, holes in the valence band are also trapped. When an electron from the bottom of the conduction band falls and recombines with a hole at the top of the valence band, an energy equal to the band gap E_g is released. In many semiconductors, including GaN and $Al_xGa_{1-x}N$, the energy can be emitted as a photon of wavelength λ:

$$\lambda = \frac{hc}{E_g}, \tag{I.16}$$

where h and c are Planck constant and the speed of light in vacuum, respectively. In our example of $Al_xGa_{1-x}N$/GaN (for x= 0.5), Eq. (I.16) predicts a photon wavelength of 420 nm, which belongs the purple region of the spectrum. To emit enough light to be useful as a LED, the heterostructure must have a suitably large number of electron-hole transitions. This can be achieved by connecting the quantum well to a strong external voltage. The important point here is that by tuning the composition x of the $Al_xGa_{1-x}N$ layers, one can tune the energy of the gap and therefore the optical wavelength of the light emitted by the LED [70,72].

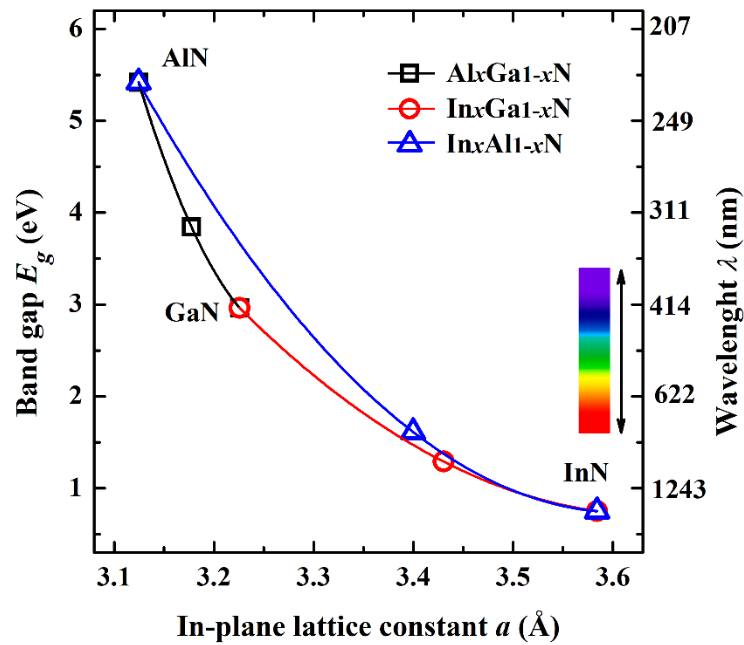

Figure I.10 Direct band gap of the technologically important III-V wurtzite materials as a function of their in-plane lattice constant a. The symbols indicate the gap values of the ternary alloys $Al_xGa_{1-x}N$, $In_xGa_{1-x}N$ and $In_xAl_{1-x}N$ for x= 0, 0.5 and 1. The data for the gaps and lattice constants for each alloy composition x is obtained by direct total-energy calculation (see Chaps. V and VII). The curves result from a quadratic polynomial fit of the calculated data. The y-axis to the right is for the optical wavelength [Eq. (I.16)] corresponding to each band gap: 1 eV corresponds to 1243 nm, 2 eV to 622 nm and so on. The double arrow and the colorful strip represent the visible spectrum, which is confined between 3.3 (380) and 1.65 eV (750 nm).

The above discussion clarifies that for the design of alloy-based optoelectronic devices, it is imperative to know the behaviour of the fundamental band gap with composition. The variations of the band gap and the corresponding wavelengths as a function of the in-plane lattice constant are depicted in Figure I.10 for the wurtzite ternary alloys $Al_xGa_{1-x}N$, $In_xGa_{1-x}N$ and $In_xAl_{1-x}N$. The details of how the band gap is calculated are expanded upon in Chapter VII. Based on these results, we point out that the III-nitride alloys have a set of band gaps that cover the visible part of the electromagnetic spectrum. As such, one can access any wavelength in between simply by tuning the alloy composition (in this case In and Al content x). $In_xGa_{1-x}N$ has been already used in the fabrication of violet and blue light-emitting diodes [74], and further inspection of Fig. I.10 indicates the possibility to extend its application to longer wavelengths (near infrared). In practice, however, the large lattice mismatch between the parent materials AlN, GaN and InN causes several challenges that impose severe limitations on the experimentally achievable alloys [75]. The strain-induced lattice mismatch results in poor crystal quality due to the formation of structural defects (e.g. dislocations) [76]. Furthermore, these defects stimulate non-radiative transitions, which attenuates the light emission and degrades the performance of quantum-well devices [77]. As a consequence, the range of the possible wavelengths is reduced significantly compared to the one expected from the band gaps.

One of the main problems that are encountered when dealing with nitride-based optoelectronic devices is the existence of built-in electrostatic fields [78]. These fields can be very large (of the order of 1 MV/cm for $Al_xGa_{1-x}N$/GaN [79]), and are induced by polarization discontinuities between different layers. We refer to Ref. [78] for more details including the formulas that relate polarization and the resulting fields in different situations. Experimentally, one can confirm the existence of such fields via measurements of the quantum-confined Stark effect [80], which reduces radiative recombination rates through the separation of electrons and holes [3]. This effect is the physical origin of the efficiency drop of light emitters. In solar cells, the internal fields act as a barrier that opposes the carrier collection, and therefore leads to a dramatic reduction in the light-generated current [81,82]. In order to overcome this problem, composition engineering in alloys has been proposed as a route toward suppression (or screening) of the strong electric fields present in III-N quantum-well devices [83,84]. We will apply this strategy to cancel the polarization interface charge and field of the quaternary-alloy heterostructure $Al_xIn_yGa_{1-x-y}N$/GaN in Chapter V.

ZnO is also exploited in optoelectronic applications owing to its direct wide gap which is almost equal to that of GaN [21]. However, ZnO and its alloys have some advantages over GaN and the other III-nitrides. An example of such advantages is the much higher quality of ZnO films [85], which circumvents the problems associated with the formation of dislocations that plagues the growth of nitride films. This high quality results in efficient and lower cost ZnO-based devices.

B. Electronics:

Transistors are perhaps the most important application of III-nitride and II-oxide materials in electronics. Generally, a transistor is a three-terminal semiconducting device that is used to amplify or switch input electrical signals (currents or voltages) [86]. There are many types of

modern transistors, we will discuss here only one particular type. Like LEDs, the design of a transistor also incorporates a quantum-well-like structure such as the one shown in Fig. I.9 [87]. Initially, the trapped charge carriers are coming from the host materials $Al_xGa_{1-x}N$ and GaN. To add more electrons and holes to the quantum well, one typically has to include n- and p-dopants respectively. Electrons that are trapped in the quantum-well region are free to move in two dimensions (the basal *c*-plane), but they are tightly confined in the third dimension (denoted as *c*-axis in Figs I.9). If such confined electrons do not have enough energy to jump out of the well, their motion is strictly two-dimensional [72]. This system of electrons is termed two-dimensional electron gas (2DEG) [88]. The analogous system for holes is called two-dimensional hole gas (2DHG).

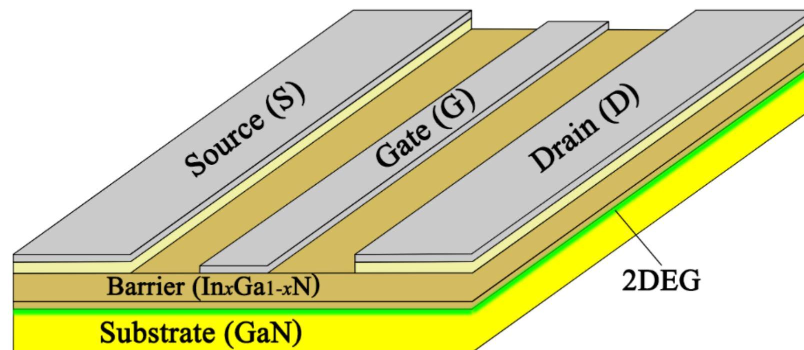

Figure I.11 Generalized HEMT through which electrons flow from the source terminal S to the drain terminal D. Note that the electron current flows in the opposite direction. The magnitude of the current is controlled by the electric field set up by the voltage applied to the gate terminal G and by the electric field generated by the polarization charge at the interface of the quantum well. There is a fourth electrical contact not shown here, namely the ground. The 2DEG is indicated by the bright green layer between GaN and $Al_xGa_{1-x}N$. Source of the image: downloaded from Wikipedia.

When the quantum well is built from the junction of two wurtzite layers, such as $Al_xGaA_{1-x}N$/GaN, there is another mechanism to confine charge carriers and thus to generate a 2DEG. As we have already emphasized, the wurtzite structure can have both spontaneous and piezoelectric polarization. Since the polarization differ between the $Al_xGaA_{1-x}N$ and GaN layers, an uncompensated electric charge of about 0.02-0.08 C/m² is induced according to the interface theorem (see Sec. V.6.2). This positive polarization charge sets up an electric field which contributes to the carriers confinement by attracting electrons to the interface, causing a 2DEG to be formed with a density of the order of 10^{13} electrons per cm² [89].

A transistor whose operation relies on the formation of a 2DEG is called HEMT, which stands for high-electron mobility transistor [90]. The electric current in the HEMT is caused by the planner motion of the 2DEG, which happens at the interface between two layers of differing band gaps and polarizations. Figure I.11 displays a generalized HEMT in which the flow of current can be controlled by an electric field, both an external bias and polarization-induced field. HEMT forms the basis of many modern electronics. They can be found in integrated circuits as digital on-off switches, current amplifiers as well as in high frequency and high power devices such cell phones, satellite receivers and radar equipment.

C. Piezoelectronics:

In addition to electronics and optoelectronics, another promising application of wurtzite crystals is based on piezoelectricity. Today, piezoelectric materials are integral to numerous devices that exploit this effect. Examples are found in various transducers, sensors, motors, actuators, transformers, and surface/bulk acoustic wave resonators. These technologies all rely on the mutual conversion of electric polarization and mechanical deformation. The direct piezoelectric effect is essential for energy harvesting systems where ordinary human activities like walking, running, finger tapping and even breathing can be used to generate electrical power for electronic devices [91]. An example of a piezoelectric-powered system that employs biomechanical energy is illustrated in Figure I.12.

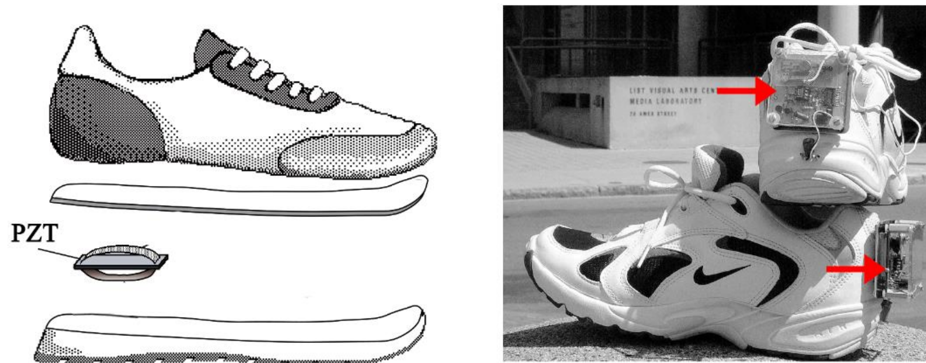

Figure I.12 (*a*) Sketch of a piezoelectric energy harvester integrated in shoes. When a person walks or run, the heels exercise a pressure on the piezoelectric material PZT ($PbZr_{1-x}Ti_xO_3$), which is an alloy made form PTO ($PbTiO_3$) and PZO ($PbZrO_3$). PZT converts the applied pressure to an electrical signal that can be used to power an electronic device attached to the shoes. (*b*) Photograph of the piezoelectric shoes. The official name of this system is Piezoelectric-Powered Radio Frequency Identification. The red arrows point to the mounted electronic device. Figure taken from Ref. [92].

Due to their excellent electromechanical properties, lead (Pb)-based piezoelectric materials, such as lead zirconate titanate (PZT), are one of the most widely exploited materials in the piezoelectric industry [93]. However, these compounds have a critical drawback: lead is highly toxic, which poses severe problems for the environment and human health. Research on piezoelectricity nowadays focuses on the development of environmental friendly lead-free piezoelectric materials [94,95]. Systems crystallizing in the wurtzite structure, such as GaN, AlN and ZnO, exhibit interesting piezoelectric properties and are considered as potential alternatives to PZT-like materials. Although wurtzite crystals have several advantages, their piezoelectric response is too low compared to Pb-based piezoelectrics. For example, the piezoelectric modulus d_{33} of ZnO is 12.4 pC/N [96], while for PZT d_{33} is in the range 200-600 pC/N. It is therefore preferable to develop effective ways to improve the piezoelectric properties of ZnO and other wurtzite materials. One strategy to do this is the process of doping. Indeed, transition-metal-doped ZnO has a giant piezoresponse as high as 170 pC/N [97]. Some studies have demonstrated that alloying can also be used to enhance the overall piezoelectric performance [98].

In our work we highlight two other methods to optimize the piezoelectric response of wurtzite nitrides and oxides. The first method is detailed in Chapter VI and consists in using compressive uniaxial strain as a tuning mechanism to increase the value of the axial piezoelectric coefficient e_{33}. In Chapter VII, it is found that the presence of planar defects, namely basal-plane stacking faults, degrades the piezoelectric performance of GaN and ZnO, meaning that better electromechanical coupling can be achieved by reducing the density of these defects in the material samples.

Chapter II

Review of density-functional theory

II.1 Introduction

Almost all modern technological applications incorporate electronic components made from different types of materials, most notably semiconductors. By exploiting these materials, many applications can be fabricated, ranging from daily ones such as mobile phones and computers, to more specialized equipment used in the fields of medicine, weaponry and heavy industrial machinery. The functionality of the applications relies crucially on the physical properties of the underlying compounds. As an example, current uses of III-nitride thin films include commercial light-emitting diodes and solar cells. These optoelectronic devices exploit the unique electronic and optical parameters of nitride materials, for instance the band gap and absorption coefficient.

Accurate knowledge of the properties of matter is indispensable for a reliable modelling of material-based devices. Because of the obstacles associated with experimental measurements, direct investigation in many cases remains difficult to carry out. Such obstacles may be the lack of material samples, the lack of characterization-technique instruments, and the complexity of the measurement procedure itself. Many properties, such as electric polarization, are not easily accessible in the laboratory [66]. In the cases where the experimental determination is available (e.g. elasticity), the obtained values are accompanied by large uncertainties [99], which limits their usefulness in interpreting the results of experiments and in device analysis.

Theoretical calculations are commonly used to complement (and sometimes to replace) experimental determination of material properties. Such calculations, which are based on quantum mechanics, are referred to as first-principles or ab-initio, meaning they can be performed without empirical input. From a theoretical viewpoint, all the physical and chemical properties of any system (solid, surface, molecule, etc.) can be obtained from the wave functions and energies that constitute the solution of the Schrödinger equation. Thus, the primary goal of first-principles calculations is to provide the solution of this equation and the subsequent evaluation of material properties. In the past couple of decades, many computational simulation techniques have been devised to do this task. The most popular method used today is density-functional theory (DFT) [100]. Indeed, DFT have been very successful at predicting the properties of condensed matter with a high degree of accuracy, which have offered an unprecedented understanding of the atomic and electronic structure of crystalline solids (the only systems that will be studied here).

In this chapter we lay the groundwork of DFT that we will use throughout Part II of this thesis. We present the basic framework of the theory in Sections II.2 and II.3, where we discuss the general quantum many-body problem and the two theories of Hohenberg and Kohn that provide the formal proof of DFT. Section II.4 is devoted to the practical scheme of Kohn and

Sham that enables DFT to efficiently solve the many-body problem. Next, we introduce the fundamental approximations involved with Khon-Sham DFT: functionals of exchange and correlation (Section II.5), including the generalized gradient approximation and the modified Becky-Jonson functional to overcome the band-gap problem for semiconductors, and the different variants of the augmented plane-wave formalism (Section II.6) used in the numerical integration of the Khon-Sham equation. Finally in Section II.7, we give a brief overview of the computer code WIEN2k that we have used to conduct our ab-initio study, focusing on the iterative algorithm for calculating the Khon-Sham orbitals and the convergence parameters that one needs to set up before running realistic calculations with WIEN2k.

II.2 Quantum many-body problem

A crystalline solid is a collection of heavy positively charged nuclei and light negatively charged electrons. If the unit cell of the solid contains N atomic nuclei, we are dealing with a problem of $N + NZ$ interacting particles, where Z is the atomic number. This is a many-body problem [101]. The starting point for solving such a problem is to write down the total energy. For a system of electrons and nuclei, the Hamiltonian operator $\hat{H}$ can be written as [101]:

$$\begin{aligned}\hat{H} = -\frac{\hbar^2}{2m_e}\sum_i \Delta_i - \frac{\hbar^2}{2M_n}\sum_I \Delta_I + \frac{e^2}{8\pi\varepsilon_0}\sum_{i\neq j}\frac{1}{|\mathbf{r}_i - \mathbf{r}_j|} \\ + \frac{e^2}{8\pi\varepsilon_0}\sum_{I\neq J}\frac{Z_I Z_J}{|\mathbf{R}_I - \mathbf{R}_J|} - \frac{e^2}{4\pi\varepsilon_0}\sum_{i,J}\frac{Z_I}{|\mathbf{r}_i - \mathbf{R}_J|},\end{aligned} \tag{II.1}$$

where lower-case and upper-case summation subscripts denote electrons and nuclei, respectively. The electrons have mass m_e with coordinates $\mathbf{r}_i$, the mass of the nuclei at positions $\mathbf{R}_i$ is M_n. The symbol Δ is the Laplacian operator. The other symbols represent atomic constants: e is the electron charge, $\hbar$ is the reduced Planck constant, and ε_0 is the permittivity of free space. We can rewrite Eq. (II.1) in a more compact form as follows:

$$\hat{H} = \hat{T}_e + \hat{T}_n + \hat{V}_{ee} + \hat{V}_{nn} + \hat{V}_{en}. \tag{II.2}$$

The first term is the kinetic energy operator for the electrons, the second for the nuclei. The last three terms describe respectively the electrostatic interaction between electrons, between nuclei, and between electrons and nuclei.

The motion of the nuclei is restraint, as they vibrate around their equilibrium positions. The electrons move in orbitals around the nuclei and/or propagate in the bulk-region of the unit cell. The more massive nuclei move rather slowly compared to the fast motion of the electrons, hence we can freeze them at fixed positions. In this case, Eqs. (II.1) and (II.2) become purely electronic, since the kinetic energy T_n of the nuclei vanishes, and the nuclear interaction term V_{nn} becomes a constant. In the end we are left with NZ interacting electrons moving in the external potential V_{en} created by the nuclei. Focusing only on the behaviour of the electrons is known as the Born-Oppenheimer approximation [102]. Once the electronic Hamiltonian is established, the next step is to solve the non-relativistic time-independent Schrödinger equation, which reads [101]:

$$\hat{H}\Psi(\mathbf{r}) = E\Psi(\mathbf{r}), \tag{II.3}$$

where $\Psi(\boldsymbol{r})$ is the multi-electron wave function and E is the total energy. Given the fact that electrons are fermions, the wave function must be antisymmetric under the exchange operator.

The solution of Eq. (II.3) will allow us to answer basic questions about the condensed system: is it a metal? Is it a semiconductor? What happens if it gets squeezed, pulled, or heated up? Is it polarized or not? And so on. In fact, all physical properties of the material can in principle be deduced from the Schrödinger equation, and indeed if it were possible to integrate it directly, quickly and efficiently, then much of this chapter would be unnecessary. However, this is far from the case, and the numerical integration of the Schrödinger equation faces formidable challenges. The main difficulty is due to the repulsive electron-electron interaction V_{ee}, for which the number of terms increases exponentially with the number of electrons, resulting in coupled differential equations that cannot be solved exactly, and even a numerical solution is computationally intractable [103]. This problem is sometimes referred to as "the curse of dimensionality" [104].There are several methods to reduce Eq. (II.3) to an approximate but tractable form. Among them, the so-called density-functional theory is one of the most used methods in the solid-state-physics community [100]. DFT is based on two theorems due to Hohenberg and Kohn, to which we now turn.

II.3 Theorems of Hohenberg and Kohn

The core idea behind DFT is to treat the electron density $\mathrm{n}(\mathbf{r})$, instead of the wave function, as the defining variable of the system. The electronic density bears the meaning of the number of electrons per unit volume, and is equal to the module squared of the many-electron wave function:

$$n(\mathbf{r}) = \Psi(\mathbf{r})^*\Psi(\mathbf{r}) = |\Psi(\mathbf{r})|^2, \tag{II.4}$$

where the asterisk (*) denotes the complex conjugate of $\Psi(\mathbf{r})$. At the heart of DFT is the Hohenberg-Kohn (HK) theorems. The first theorem states that for a given external potential [e.g. V_{en} in Eq. (II.2)], any observable of the system, including total energy, is a unique functional of the ground-state density $\mathrm{n}_0(\mathbf{r})$ [105]. Also, Hohenberg and Kohn proved the additional theorem that there exists an energy functional of density, $E[n(\mathrm{r})]$, whose minimum is the ground-state energy of the system, and the density that results in this functional being minimized is the exact ground-state density [105].

So in essence, the electronic density is sufficient to determine all properties of the system. Switching from wave functions to densities has proved to be very useful in electronic-structure calculations. The wave function depends on the positions of all electrons in the system, meaning for N electrons, it has $3\mathrm{N}$ variables. Therefore, solving for such a wave function becomes prohibitively expensive for a handful of electrons. If we consider the density, however, it has only three spacial variables for any number of electrons, significantly reducing the computational cost.

The total energy is given after Eq. (II.2) by the expectation value of the Hamiltonian, then we can write it as a functional of the density:

$$\begin{aligned} E[n(\mathbf{r})] &= T_e[n(\mathbf{r})] + E_{ee}[n(\mathbf{r})] + E_{en}[n(\mathbf{r})] \\ &= F_{HK}[n(\mathbf{r})] + E_{en}[n(\mathbf{r})] \end{aligned} \tag{II.5}$$

where $F_{HK}[n(\mathbf{r})]$ is the Hohenberg-Kohn functional, which is defined as the sum of the expectation value of the electron kinetic T_e and interaction E_{ee} energies. Since it does not contain information on the nuclei and their position (given by E_{en}), F_{HK} is a universal functional of any many-electron system. Recall that the kinetic T_e and interaction E_{nn} energies of the nuclei are not taken into account due to applying the Born-Oppenheimer approximation. In theory it should be possible to calculate $E[n(\mathbf{r})]$, since the first HK theorem guarantees that it is a functional of the ground-state density. In practice, one does not know how to do this explicitly. It is far from obvious how to cast Eq. (II.5) in terms of densities. In the next section, on the Khon-Sham equation, we will outline one widely used approach for dealing with this issue.

II.4 Khon-Sham equation

In the Kohn-Sham (KS) approach to density-functional theory, the many-body-interacting system of electrons is replaced by a fictitious system of non-interacting particles in an effective potential chosen such that it reproduces the ground-state density of the actual many-body system [106]. In other words, this is an independent-particle approach where the density is given by a set of single-particle wave functions (or orbitals) $\psi_i(\mathbf{r})$:

$$n(\mathbf{r}) = \sum_{i=1}^{N} |\psi_i(\mathbf{r})|^2, \tag{II.6}$$

where i runs over all occupied states. We will show in the following how this procedure turns DFT into a practical tool.

An explicit expression for the kinetic energy $T_e[n(\mathbf{r})]$ and the mutual repulsive interaction energy $E_{ee}[n(\mathbf{r})]$ of a system of interacting electrons are not known. An accurate treatment of $T_e[n(\mathbf{r})]$ Is based on decomposing it into one part that represents the kinetic energy of non-interacting particles $T_e^s[n(\mathbf{r})]$, where the superscript s stands for 'single-particle', and one that represents the correlation energy $E_C[n(\mathbf{r})]$ [101]:

$$T_e[n(\mathbf{r})] = T_e^s[n(\mathbf{r})] + E_C[n(\mathbf{r})], \tag{II.7}$$

$T_e^s[n(\mathbf{r})]$ is not known exactly as a functional of $n(\mathbf{r})$, but it can easily be expressed in terms of the single-particle wave functions just introduced:

$$T_e^s[n(\mathbf{r})] = -\frac{\hbar^2}{2m_e}\sum_i \int \psi_i(\mathbf{r})^* \Delta\psi_i(\mathbf{r}) d\mathbf{r}, \tag{II.8}$$

the total kinetic energy for non-interacting particles is just the sum of the individual kinetic energies, and hence the summation in Eq. (II.8). Next, we turn our attention to $E_{ee}[n(\mathbf{r})]$. While

in a classical picture it corresponds only to the electrostatic electron-electron repulsion (called Hartree energy E_H), in a quantum-mechanical frame one must pay attention to the quantum nature of electrons. Specifically, this term should account for the exchange energy $E_X[n(\mathbf{r})]$ describing the repulsive effect due to the Pauli exclusion principle. Therefore, $E_{ee}[n(\mathbf{r})]$ is the sum of the classical electrostatic and the quantum exchange energies [101]:

$$E_{ee}[n(\mathbf{r})] = E_H[n(\mathbf{r})] + E_X[n(\mathbf{r})]. \tag{II.9}$$

With this knowledge, we can rewrite the total-energy functional in the following way:

$$E[n(\mathbf{r})] = T_e^s[n(\mathbf{r})] + E_H[n(\mathbf{r})] + E_{en}[n(\mathbf{r})] + E_{XC}[n(\mathbf{r})], \tag{II.10}$$

where $E_C[n(\mathbf{r})] + E_X[n(\mathbf{r})]$ is the exchange-correlation functional, which we denote $E_{XC}[n(\mathbf{r})]$. We point out that Eqs. (II.5) and (II.10) are basically the same. One can use the second HK theorem to minimize $E[n(\mathbf{r})]$ with respect to $n(\mathbf{r})$. The minimizing function $n_0(\mathbf{r})$ is the system's ground-state density and the value $E[n_0(\mathbf{r})]$ is the ground-state energy. But then we won nothing from introducing the mono-particle orbitals. A fruitful alternative is to minimize $E[n(\mathbf{r})]$ with respect to $\psi_i(\mathbf{r})$. In order to do so, we take the functional derivative of $E[n(\mathbf{r})]$ with respect to the complex conjugate of the ith single-particle wave function, i.e. $\delta E[(\mathbf{r})]/\delta\psi_i^*(\mathbf{r})$ [101]. This converts the energies in Eq. (II.10) to potentials, resulting in the Kohn-Sham eigenvalue equation [106]:

$$\hat{H}_{KS}\psi_i(\mathbf{r}) = \epsilon_i\psi_i(\mathbf{r}), \tag{II.11}$$

where the Kohn-Sham Hamiltonian $\hat{H}_{KS}$ is given by the kinetic energy operator of non-interacting particles and a KS effective potential $\hat{V}_{KS}$:

$$\hat{H}_{KS} = -\frac{\hbar^2}{2m_e}\Delta + \hat{V}_{KS} = -\frac{\hbar^2}{2m_e}\Delta + \hat{V}_H + \hat{V}_{en} + \hat{V}_{XC}, \tag{II.12}$$

where H, en and XC denote the Hartree, electron-nuclei attraction, and exchange-correlation potentials, respectively. The main point exploited here is that we can solve Eq. (II.11) to find the wave functions $\psi_i(\mathbf{r})$, then the ground-state density is calculated directly using Eq. (II.6) [which is equal to the density of Eq. (II.4)]. It is worth emphasizing that the single-particle wave functions $\psi_i(\mathbf{r})$ are not the wave functions of electrons! They describe mathematical quasi-particles, without direct physical meaning. Only the overall density of these quasi-particles is guaranteed to be equal to the true (interacting) electron density, which is the essence of the Kohn-Sham formalism. Also the single-particle energies ϵ_i are not single-electron energies.

All many-body effects are contained within the exchange-correlation potential V_{XC}. One may argue that the Hartree potential V_H is also a many-body interaction, since it describes the mutual electrostatic repulsion of electrons. In this approach, however, each electron is moving in the potential due to all other electrons, so that V_H can be considered to be an external potential, just as the electron-nuclei potential V_{en}. Because each particle is treated independently of the other particles, the Khon-Sham approach allows the Schrödinger equation, (Eq. II.3), to be broken into Z separate Khon-Sham equations, Eqs. (II.11), one for each particle.

The Kohn-Sham scheme described above is formally exact, in the sense that the different terms of the KS Hamiltonian are known exactly. The only exception is the exchange-correlation term, for which no general exact expression is known (although the HK theorem guarantees that it is a density functional). It is here that approximations enter the theory. The use of the KS equation for determining the orbitals $\psi_i(\mathbf{r})$, and hence the density $n(\mathbf{r})$, requires at least an approximate functional of the exchange-correlation energy and potential.

II.5 Exchange and correlation functionals

The choice of an appropriate functional to model the exchange-correlation (XC) interactions is of central importance in order to obtain reliable results [107]. Several different functionals are available in the literature, and many of them are implemented in standard DFT packages. We provide below an overview of two exchange-correlation functionals used in this work, namely the generalized gradient approximation (GGA) and the modified Becke-Johnson (mBJ) potential.

II.5.1 Generalized gradient approximation

The GGA approximation is one widely used functional for modelling the XC potential. Before looking at that, however, it is worthwhile to recall an older, but equally useful, alternative: the local density approximation (LDA) [108]. This approximation, originally proposed by Kohn and Sham, is based on using the exchange and correlation energies corresponding to the homogeneous electron gas (HEG), i.e. a system of constant density *n*. For such a homogeneous system, the exchange energy per electron is:

$$\epsilon_X^{HEG} = -\frac{3e^2}{4}\left(\frac{3}{\pi}\right)^{\frac{1}{3}} n^{\frac{4}{3}}. \qquad \text{(II.13)}$$

The LDA treatment of the exchange part is realized by substituting the constant charge density *n* of the HEG by the local density $n(\mathbf{r})$ of the KS system. The total contribution E_X^{LDA} is obtained by multiplying ϵ_X^{HEG} by $n(\mathbf{r})$ and integrating this product with respect to volume:

$$E_X^{LDA}[n(\mathbf{r})] = -\frac{3e^2}{4}\left(\frac{3}{\pi}\right)^{\frac{1}{3}} \int n(\mathbf{r})^{\frac{5}{3}} d\mathbf{r}. \qquad \text{(II.14)}$$

For the correlation part the situation is more complicated, because there is no law of nature for the per-electron correlation energy ϵ_C^{HEG}. One must employ parameterized formulas relying on auxiliary numerical data, e.g. the Perdew and Zunger parameterization [109]. The total exchange-correlation energy in the LDA is expressed as:

$$E_{XC}^{LDA}[n(\mathbf{r})] = \int n(\mathbf{r})\epsilon_{XC}^{HEG}(n(\mathbf{r}))d\mathbf{r}, \qquad \text{(II.15)}$$

where $\epsilon_{XC}^{HEG}$is the exchange-correlation energy density of the HEG. The corresponding XC potential is given by the functional derivative $V_{XC} = \delta E_{XC}[n(\mathbf{r})]/\delta n(\mathbf{r})$.

While LDA considers the exchange-correlation energy for a system where the density remains constant, in real systems the density changes with position. It is then natural to expect that the value of ϵ_{XC} depends not only on the density itself but on its spacial derivative, that is, its gradient. The simplest approximation within this gradient picture is to assume that ϵ_{XC} is a function, in addition to $n(\mathbf{r})$, of the magnitude of the density gradient $|\nabla n(\mathbf{r})|$:

$$E_{XC}^{GGA}[n(\mathbf{r})] = \int n(\mathbf{r})\epsilon_{XC}^{GGA}(n(\mathbf{r}), |\nabla n(\mathbf{r})|)d\mathbf{r}. \tag{II.16}$$

The approximation implied by Eq. (II.16) is referred to as the generalized gradient approximation [110]. Many GGAs exist that slightly improve the predictions of LDA. One of the most widely used GGA parameterizations, and the one employed for the results obtained in the present work, is that of Perdew, Burke and Ernzerholf (PBE) [110].

The LDA and GGA functionals are found to be quite accurate for the calculation of properties depending on total energy, such as structural parameters, cohesive and formation energies, and elastic constants. However, both functionals tend to equally deviate from the experimental bond lengths and lattice constants. In particular, LDA underestimates the values while GGA overestimates them. One of the most significant problems with GGA and LDA is related to the prediction of the band gap of semiconductors and insulators. Thus, one has to resort to other exchange-correlation functionals to get reliable results for the band gap.

II.5.2 Modified Becke-Johnson approximation

It is well known that GGA and LDA provide band gaps that are much smaller than experiment [111], often by 50% or more. This underestimation leads to the incorrect theoretical prediction of conducting states (i.e. vanishing gaps) for materials that are insulating or semiconducting in reality, which is a considerable problem in the case of narrow-gap semiconductors, such as InN-containing systems, preventing the calculation of their polarization. As we will see in Chapter III, electric polarization is only defined for semiconductors and insulators. There have been many attempts to solve the band-gap problem. Hybrid functionals, such as the Heyd-Scuseria-Ernzerhof (HSE) implementation [112], can lead to much accurate values, but they are computationally very demanding and therefore can only be applied to systems containing a small number of atoms.

The modified Becke-Johnson (mBJ) functional was designed to counterreact the band-gap underestimation [113]. Successful prediction of band gaps for a wide range of materials has been demonstrated using this functional [114]. The run times of mBJ calculations are on the order of those of conventional LDA and GGA calculations, making mBJ easily applicable to large systems in an efficient way (e.g. supercells). Here, in addition to standard GGA-PBE, we use the mBJ functional as our approximation for the exchange-correlation potential to get more precise band structures. There are many variants of the mBJ potential, the one that we employ is the Tran-Blaha modified Becke-Johnson (TB-mBJ) functional [113], which consists of a modified version of the Becke-Johnson potential [115] for exchange and LDA for correlation. The exchange part is given by:

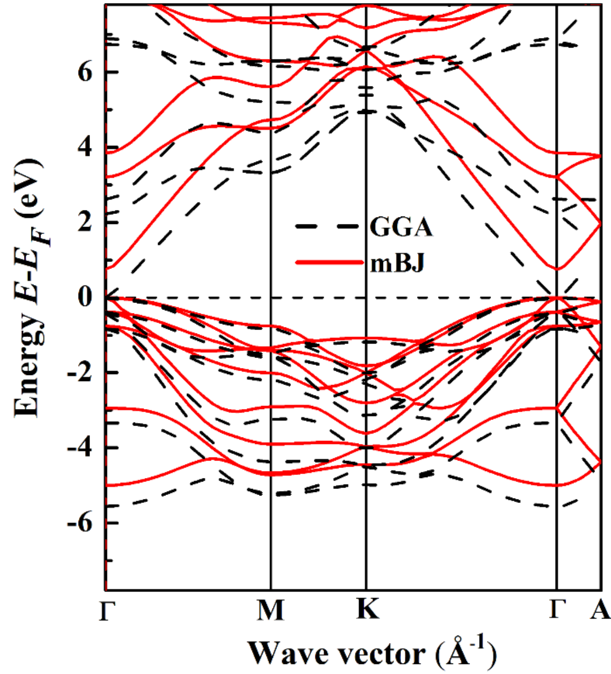

Figure II.1 Band structure of InN in the wurtzite phase obtained using GGA (black discontinuous curves) and mBJ (red continuous curves) XC functionals. The vertical scale is the energy of charge carriers: electrons (positive energies) and holes (negative energies). The horizontal scale is the points of high symmetry in the Brillouin zone of the wurtzite structure, physically they are related to the norm of the wave vectors associated with charge carriers. The origin of energies is the Fermi level E_F (dashed horizontal line).

$$V_X^{mBJ}(\mathbf{r}) = cV_X^{BR}(\mathbf{r}) + \frac{(3c-2)}{\pi}\left[\frac{5t(\mathbf{r})}{6n(\mathbf{r})}\right]^{\frac{1}{2}}, \tag{II.17}$$

where $V_X^{BR}(\mathbf{r})$ is the Becke-Roussel potential [116], $t(\mathbf{r})$ is the kinetic-energy density, and $c = \alpha + \beta g^p$ with α, β and p being numerical factors and g is the average of $|\nabla n(\mathbf{r})|/n(\mathbf{r})$. The reader can find a detailed description of several XC functionals, including mBJ, in Ref. [114].

For the sake of comparison, our band structure calculated by both GGA-PBE and TB-mBJ approximations is shown in Figure II.1 for wurtzite InN. It can be observed that for GGA, the conduction-band minimum crosses the Fermi level E_F, resulting in a vanishing gap. This is in opposition with practice, since InN does have a gap, albeit a very narrow one. On the other hand, the mBJ functional gives a non-zero direct gap of 0.75 eV, in excellent agreement with the experimental value of 0.70 eV [117].

So far we have studied the KS equation and the different approximations made to simplify the calculation of the electron-electron interaction. We turn now to the procedure curried out to solve this equation numerically.

II.6 Augmented plane-wave methods

In KS-DFT, the determination of the physical properties of a condensed system boils down to solving the following KS differential equation [101,118]:

$$\left[-\frac{\hbar^2}{2m_e}\Delta + \hat{V}_H + \hat{V}_{XC} + \hat{V}_{en}\right]\psi_i(\mathbf{r}) = \epsilon_i\psi_i(\mathbf{r}). \tag{II.18}$$

The operator on the left-hand side of Eq. (II.18) is the KS Hamiltonian $\hat{H}_{KS}$, which is defined as the sum of the non-interacting kinetic-energy operator, the Hartree potential (generated by the electrons), the external potential (generated by the nuclei) and the exchange-correlation potential. The latter is treated approximately using the GGA, mBJ or other approximations. The goal is to solve for the single-particle wave functions $\psi_i(\mathbf{r})$ and energies ϵ_i associated with the Hamiltonian $\hat{H}_{KS}$.

Mathematically speaking, solving the KS equation means we want to find the coefficients c_p^i needed to expand the functions $\psi_i(\mathbf{r})$ in a given basis set $\varphi_p(\mathbf{r})$ [118]:

$$\psi_i(\mathbf{r}) = \sum_p c_p^i\, \varphi_p(\mathbf{r}), \tag{II.19}$$

The choice of the basis wave functions $\varphi_p(\mathbf{r})$ depends on the computational method used to solve Eq. (II.18). The work of this thesis is based on an all-electron approach known as the augmented plane-wave (APW) method. The term "all-electrons" means that all electrons (core and valence) are included in the calculations. This is at variance with the pseudopotential scheme, which treats only valence electrons. The APW method was originally introduced by Slater as a technique to solve the periodic-potential problem [119], and it was adapted in DFT to obtain the solutions of the KS equation.

II.6.1 APW

The main idea underlying the APW method is the separation of space into an inner region and an outer one by a spherical boundary, which enables one to apply, in the two different regions, different approximations, where they are relevant. In our numerical context, this affords us the use of different basis functions in either region. Close to the nuclei the electrons behave quite as they are in an isolated atom (the potential is spherically symmetric), and they can be described by atomic-like orbitals. Away from the nuclei, on the other hand, the electrons are more or less free (the potential is constant), so that they are described by plane waves [101,118]. Each nuclear site is therefore surrounded by a sphere of radius R_{MT}, as shown schematically in Figure II.2. Such a sphere is often called a muffin-tin (MT) sphere. The remaining of the unit cell outside the spheres is called the interstitial region. The searched KS wave functions can be expanded in terms of localized atomic orbitals in the MT nuclei-centered region, and in terms of non-localized plane waves in the interstitial region. Putting all this together, the augmented plane-wave $\varphi_{\boldsymbol{k}+\boldsymbol{G}}^{APW}(\mathbf{r})$ used in the expansion of $\psi_i(\mathbf{r})$ is defined as [118] :

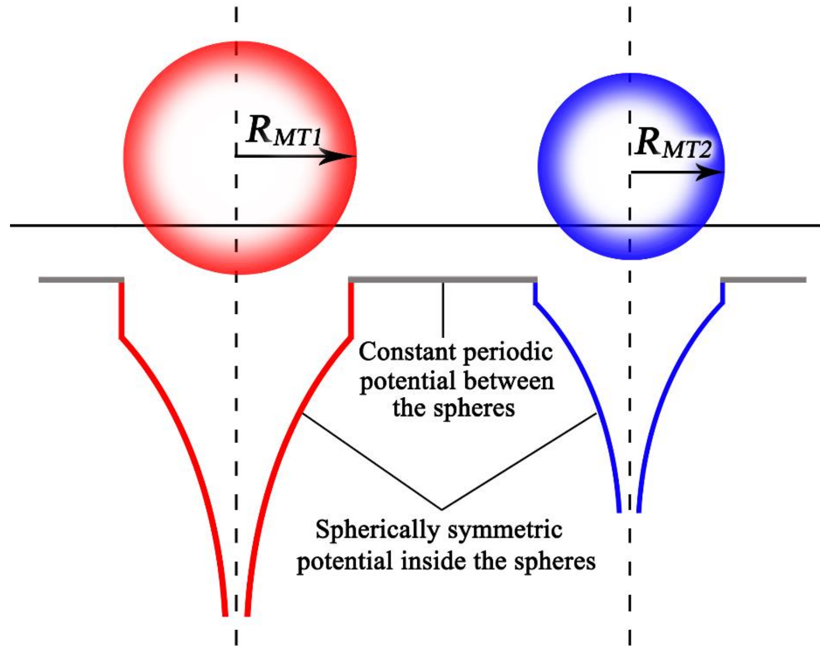

Figure II.2 APW division of a unit cell into two muffin-tin spheres of radius R_{MT1} (red) and R_{MT2} (blue) and an interstitial region in between. As described in the text, inside the spheres the actual potential of the crystal is approximated by a spherically symmetric potential where the wave functions are atomic orbitals (i.e. a combination of radial functions and spherical harmonics), and in the interstitial region the potential is constant and periodic with the wave functions being plane waves. The MT radii increase with the size of atoms. The MT spheres should not overlap. Figure based on the lecture notes of Terry Loucks [120].

$$\varphi_{\mathbf{k}+\mathbf{G}}^{APW}(\mathbf{r}) = \begin{cases} \sum_{l,m} A_{lm,\alpha} u_{l,\alpha}(r, E_{l,\alpha}) Y_m^l(\hat{\mathbf{r}}), & r < R_{MT} \\ \frac{1}{\sqrt{V}} \sum_{G} C_G e^{i(\mathbf{k}+\mathbf{G}).\mathbf{r}}, & r > R_{MT} \end{cases} \tag{II.20}$$

where $\mathbf{k}$ is a vector in the first Brillouin zone (BZ) of the crystal, $\mathbf{G}$ is a reciprocal lattice vector (outside the BZ), V is the volume of the unit cell, $Y_m^l(\hat{\mathbf{r}})$ are spherical harmonics, $u_{l,\alpha}(r, E_{l,\alpha})$ are the solutions of the radial part of the Schrödinger equation for a free atom, and $E_{l,\alpha}$ is an energy parameter associated with $u_{l,\alpha}$. Since the wave function must be continuous everywhere, the expansion coefficients $A_{lm,\alpha}$ and C_G are chosen such that the sphere and interstitial parts of the APW match over the surface of the MT sphere, i.e. at $r = R_{MT}$. As for the indices, l and m are the usual angular quantum numbers, and α is the atom index.

II.6.2 LAPW

We can use the APW basis set and proceed in order to determine the coefficients c_p^i in the expansion of the KS solutions [Eq. (II.19)] by, for instance, the Rayleigh-Ritz variational principle. However, this does not work: the radial functions $u_{l,\alpha}$ are still unknown because we did not settle their energy $E_{l,\alpha}$. The procedure carried out to find $E_{l,\alpha}$ turns out to be a non-linear eigenvalue problem, the resolution of which is a time-consuming process. This makes the APW

approach inherently slow. Many modifications have been proposed and implemented to make the original APW basis set more efficient. We refer the reader interested in the conceptual and mathematical details to the literature for further information. We present below a sketch of the fundamentals.

The problem with the APW method lies in the non-linearity associated with the energy-dependent basis functions. To overcome this difficulty, Anderson proposed a linearization of this energy dependency [121]. This can be done by introducing the derivative of the radial wave functions in the MT expansion [122], which is the core of the linearized augmented plane-wave (LAPW) method. In this case, the basis set functions are [118]:

$$\varphi_{\boldsymbol{k+G}}^{LAPW}(\mathbf{r}) = \begin{cases} \sum_{l,m} \left[A_{lm,\alpha} u_{l,\alpha}(r, E_{l,\alpha}) + B_{lm,\alpha} \dot{u}_{l,\alpha}(r, E_{l,\alpha})\right] Y_m^l(\hat{\mathbf{r}}), & r < R_{MT} \\ \frac{1}{\sqrt{V}} \sum_{G} C_G e^{i(\mathbf{k}+\mathbf{G}).\mathbf{r}}, & r > R_{MT}, \end{cases} \quad \text{(II.21)}$$

where $\dot{u}_{l,\alpha}$ is the first energy derivative of $u_{l,\alpha}$, the other symbols keep their usual meaning. Both $A_{lm,\alpha}$ and $B_{lm,\alpha}$ are uniquely determined by requiring that $\varphi_{\boldsymbol{k+G}}^{LAPW}(\mathbf{r})$ and its first position derivative to be continuous at the boundary of the two regions.

II.6.3 LAPW+LO

The LAPW method has proved to be an efficient computational tool, but it falls short in describing accurately the semi-core states. This problem is solved by adding the so-called local orbitals (LO) to the LAPW basis set [123], which are non-zero only inside the MT sphere, and given by [118]:

$$\varphi_{\boldsymbol{lm,\alpha}}^{LO}(\mathbf{r}) = \begin{cases} \sum_{l,m} \left[A_{lm,\alpha}^{LO} u_{l,\alpha}(r, E_{l,\alpha}) + C_{lm,\alpha}^{LO} u_{l,\alpha}(r, E_{l,\alpha}^{LO})\right] Y_m^l(\hat{\mathbf{r}}), & r < R_{MT} \\ 0. & r > R_{MT}. \end{cases} \quad \text{(II.22)}$$

The two coefficients $A_{lm,\alpha}^{LO}$ and $C_{lm,\alpha}^{LO}$ are chosen such that $\varphi_{\boldsymbol{lm,\alpha}}^{LO}(\mathbf{r})$ is normalized and has zero value at the MT boundary. The linearization energy $E_{l,\alpha}$ is suitable for the highest valence states, while $E_{l,\alpha}^{LO}$ is used for the lower semi-core state. Thus by adding LOs, a consistent and accurate description of both valence and semi-core electrons is possible. This accuracy does come at a cost in the form of a slightly increased computational time.

II.6.4 LAPW+LO+lo

Finally, the linearization of the energy-dependent radial wave functions can be facilitated even further by introducing another type of local orbitals labeled lo (not to be confused with LO), which have the effect of improving the systematic convergence compared to the typical LAPW basis set [124]. In the next section we deal with the issue of convergence that influences the accuracy of realistic calculations.

The results presented in the remainder of this thesis are obtained using the (linear) augmented plane-wave with local orbitals [(L)APW+LO+lo] method, which we simply call LAPW [118]. This method has gained popularity due to providing further computational advantages compared to, for instance, pseudopotential and projector augmented-wave (PAW) methods. Technical details about running electronic-structure calculations using the code WIEN2k will be introduced next.

II.7 WIEN2k

II.7.1 Iterative process

Our theoretical simulation is performed with the *WIEN2k* package [125], which is a powerful computational tool for first-principles total-energy calculations using the LAPW basis set. In WIEN2k, and most DFT codes, the KS equation is solved self-consistently by an iterative process [126]. To understand why this is the case, note that the Hartree and exchange-correlation potentials depend on the density $n(\mathbf{r})$, which in turn depends on the wave functions $\psi_i(\mathbf{r})$. So in order to construct the KS Hamiltonian and solve the corresponding KS equation, one has to evaluate these potentials using the electronic density. But the density is exactly what we are trying to determine in the first place! Hence, we end up with a contradiction and an iterative process is needed to escape from it.

In practice, one starts with a trial density $n^{(0)}$ derived from trial orbitals $\psi_i^{(0)}$, that allows to construct the initial Hamiltonian $H_{KS}^{(0)}$. A clever choice of $n^{(0)}$ is essential for speeding up the calculation. For a solid-state system it is convenient to obtain $n^{(0)}$ from a combination of atomic orbitals that constitute the system. Using $H_{KS}^{(0)}$, the KS equation can be solved yielding the orbitals $\psi_i^{(1)}$ from which the new density $n^{(1)}$ is derived. Most probably our guessed $n^{(0)}$ will be different from $n^{(1)}$, we therefore have to try a second guess, or in the language of numerical analysis we have to start a second iteration (the first iteration being the one resulted in $n^{(1)}$). The density $n^{(1)}$ serves as input to generate the new Hamiltonian $H_{KS}^{(1)}$, which gives the density $n^{(2)}$, and then the whole procedure starts over again, etc [126].

Within each iteration, we compute both the density and total energy via the LAPW mrthod. The calculation cycle comes to an end when some convergence criterion is reached. When this happens we say that convergence (and thus self-consistency) is achieved [126]. The most common criterion is based on the difference of energy between two consecutive iterations i and $i-1$. This difference will progressively decrease, and the cycle is stopped when $E^{(i)} - E^{(i-1)} < \varepsilon_E$, where $E^{(i)}$ [$E^{(i-1)}$] is the total energy at iteration i ($i-1$), and ε_E is a user-defined tolerance. One can rely on additional criteria based on the difference of other parameters, depending on the problem at hand, e.g. electric charge and atomic forces. If the convergence condition is not fulfilled, we restart the calculation with a new density $n^{(i+1)}$. In most cases, the latter is a linear combination of the output and input densities of the previous iteration $n_{out}^{(i)}$ and $n_{in}^{(i)}$:

$$n^{(i+1)} = \beta n_{out}^{(i)} + (1-\beta) n_{in}^{(i)}\,, \tag{II.23}$$

where β is a mixing parameter with $0 < \beta < 1$. This mixing is nessesary in order to avoid numerical instabilities. More sophisticated mixing schemes can also be used [127]. The computational procedure described above is referred to mathematically as "the fixed-point problem", and is ideally suited to computer codes such as WIEN2k. The solutions for the densities will therefore be numerical, i.e. they cannot be expressed by analytical formulae. The iterative process for obtaining the density and energy, called self-consistent field (SCF) cycle, is implemented very efficiently in WIEN2k [127]. The SCF cycle is performed using several different programs: lapw$n$ (n= 0,1,2), lcore and mixer. We present in Figure II.3 a simplified flux diagram showing the essentials of WIEN2k's self-consistency loop for convergence to the electronic ground state. Further information is to be found in the WIEN2k manual and the paper by Blaha et *al.* [125].

II.7.2 Convergence parameters

We now make a few comments on important aspects of running practical calculations that will be mentioned in the numerical-detail sections in the upcoming chapters. The KS wave functions $\psi_i(\mathbf{r})$ belong to a function space, meaning that the expansions in Eqs (II.19)-(II.22) run in principle to infinity, but in practice they have to be stopped as some point. In other words, we have to work with a limited number of basis functions $\varphi_p(\mathbf{r})$. This is called the expansion cutoff. For the APW or LAPW method, the size of the basis set is determined by the product $R_{MT}^{min}K_{max}$ of the smallest muffin-tin atomic radius R_{MT}^{min} and the highest wave vector K_{max} in the reciprocal lattice (i.e. $k + G < K_{max}$) [118]. The value of $R_{MT}^{min}K_{max}$ is chosen such that a relatively small number of basis functions gives a reasonably accurate results. In a typical WIEN2k calculation, one usually sets $R_{MT}^{min}K_{max}$= 7.

Because of the periodic nature of crystals, and according to the Bloch theorem, the KS equation can be solved efficiently in reciprocal space (or k-space) [101]. Many quantities of importance, such as the system's total-energy, therefore, can be expressed as an integral over k-space. Such an integral is restricted to the first Brillouin zone (BZ) of the unit cell where bands are occupied. For an energy $E_i(\mathbf{k})$ at point **k** and band i, the corresponding integral giving its total value E is:

$$E = \frac{V}{(2\pi)^3}\sum_i \int f_{i,\mathbf{k}}\, E_i(\mathbf{k})d\mathbf{k}, \qquad \text{(II.24)}$$

where V is the unit-cell volume. The summation over bands involves occupancies $f_{i,\mathbf{k}}$, which in the zero-temperature limit are 1 (occupied band) or 0 (unoccupied band). We need to solve the KS equation [Eq. (II.18)] (i.e. iterate self-consistently) everywhere in the BZ. In realistic calculation, however, we do it for a limited account of k-points, and replace the continuous integral in Eq. (II.23) by a summation over k [128]. The computation time scales with the number of k-points (or k-vectors) at which the wave functions and energies need to be calculated. Thus, it is important to find the lowest number of k-points that gives the required accuracy. To obtain the curves in Fig. II.1, we have calculated the band energies at each point **k**. The calculation is performed along the highest symmetry points of the hexagonal crystalline structure: Γ, A and W, etc. The number of k-points that we used is the WIEN2k default value of

1000. Note that for some properties, in particular thermoelectric and optical properties, a greater number of k-points, which corresponds to a denser k-mesh, is needed.

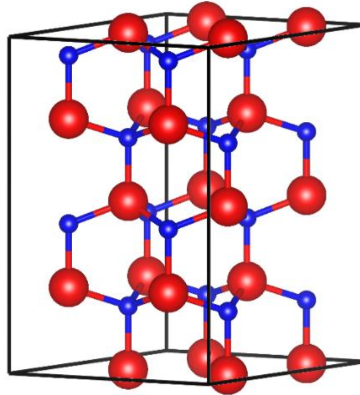

Figure II.4 Wurtzite supercell containing 32 atoms. In terms of atomic layers, it has a 2×2×2 arrangement, that is, the 4 atoms of the unit cell double along the a-direction to become 8 atoms, then these 8 atoms also double along the b-direction to become 16 atoms; finally, along the c-axis the 16 atoms double again to form 32-atom supercell.

II.7.3 Supercell geometry

All of our calculations are performed under periodic (Born–von-Kàrmàn) boundary conditions, where the unit cell of the solid is repeated in all three directions. However, many important aspects cannot be studied using conventional unit cells. This includes, but not limited to, alloyed compounds, crystalline defects, ferroelectric domains, and phonon frequencies. To handle these systems one must use larger cells known as *supercells*, which can be perturbed in such a way to determine the required properties. For example, phonon frequencies are calculated using force values on slightly displaced atoms in the supercell [129]. Herein, we use supercells in order to simulate ternary and quaternary alloys as well as basal-stacking faults. Figure II.4 shows a 32-atom wurtzite supercell generated by doubling the periodicity of the wurtzite unit cell along the three lattice directions.

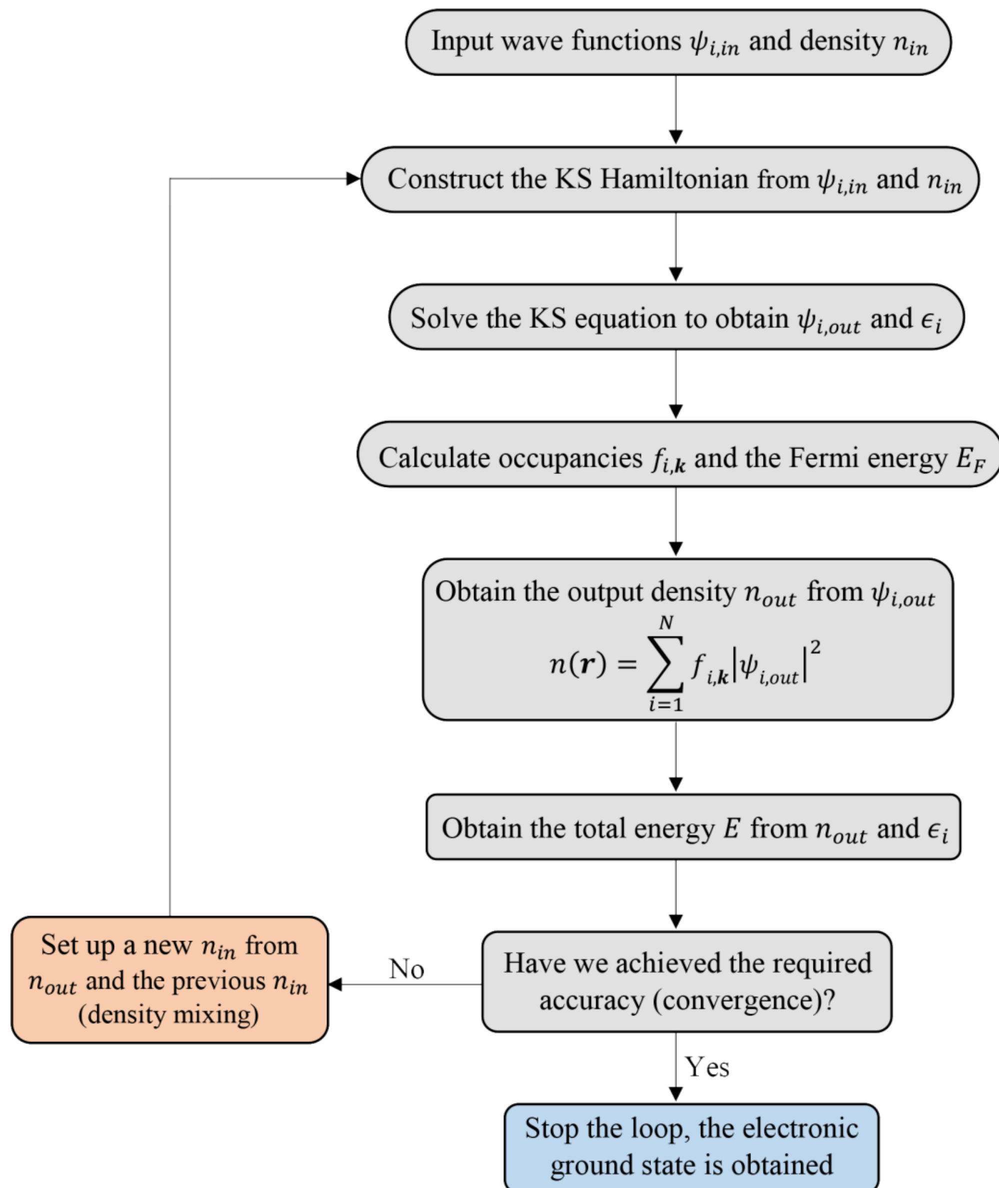

Figure. II.3 Flowchart depicting the basic procedure that WIEN2k performs towards solving the Kohn-Sham equation and obtaining the ground-state electronic density and energy.

II.8 Conclusion

We reviewed in this chapter the fundamentals of density-functional theory as it applies to the specific case of crystalline solids, which is the theory upon which our simulations are based. We started by describing the problem at hand: a system of interacting electrons and nuclei. We showed that it is not possible to solve this problem via a direct integration of the Schrödinger equation, and an alternative approach is needed to do that. This approach is provided by DFT through the Hohenberg and Kohn two theorems, which postulate that all the properties of a system can in principle be deduced from its electronic density.

Then we showed how the Khon-Sham equation (a modified version of the Schrödinger equation) simplifies the problem by replacing the real interacting system of electrons with a

non-interacting one, with the constraint that both systems have the same electron density. For the Khon-Sham procedure to be useful in practice, approximate functionals of the exchange-correlation interactions are required. We discussed two such functionals, namely the generalized gradient and the modified Becky-Jonson approximations. The latter is used to correct the band-gap underestimation predicted by the former.

As a next step, we explained the augmented plane wave method employed to solve the Khon-Sham equation. Within this method, abbreviated as LAPW, one splits the space of the crystal cell into spherical regions (muffin-tin spheres) and the region between the spheres (interstitial region). This allows the use of different ansatz of the wave functions in each region, which in turns facilitates the integration of the Kohn-Sham algorithm. Finally, we presented the WIEN2k code, a solver of the Khon-Sham equation, and explained the iterative process followed by it in order to find the Khon-Sham (and hence the real) electronic density. We also described some technicalities usually encountered when running calculations with WIEN2k, such as the cutoff parameter, the number of k-points and supercells.

For a more detailed presentation the reader is directed to the literature cited throughout this chapter. In this conclusive paragraphs we shed some light on other topics of DFT that are not usually discussed. The techniques of DFT are not only used to explain the behaviour of experimentally known materials, but also to model materials that have not been grown in the laboratory. By computing the formation energy, one can show if the system at hand can be synthesized or not. Further, the calculation of the elastic tensor and phonon modes can be used as a filter to check the mechanical and dynamical stability. Note that the evaluation of many properties often involves theories beyond the standard framework of DFT. This is the case for example of polarization-related quantities and thermoelectric transport parameters, where one must rely respectively on the Berry-phase theory (see Chap. III) and the semi-classical Boltzmann theory to account for these properties.

There is a class of DFT-computations that employs the so-called high-throughput methods to conduct a large scale simulation involving thousands or even ten thousands of compounds [130]. This allows the construction of databases of calculated properties that are beneficial for both theorists and experimentalists for materials discovery and design. Working in a high-throughput environment, de Jon et *al.* [131] computed the full piezoelectric tensor for nearly a thousand inorganic crystals, which resulted in the largest database of the piezoelectric response. This scheme can also be used to search for new materials for targeted fields of applications. An example of this kind of research is the work of Garrity [132], who employed high-throughput DFT combined with symmetry analysis to identify candidate ferroelectric compounds with improved functionalities.

While DFT was initially formulated to deal with crystalline solids, the case of disordered (or amorphous) solids can also be handled despite their very complex atomic structure. The ability of DFT to describe disordered materials has only been possible thanks to machine learning approaches to atomistic modelling [133]. The exact role of DFT here is to provide the training data, which is a set of atomic observables such as total energies, forces between atoms and their separations, and the like. These values are stored in a database from which a machine-

learning algorithm can learn how to model the system of interest. The two main methodologies for learning from DFT-data are artificial neural networks and Gaussian process regression. The emergence of machine leaning in material science have enabled for the first time an accurate description of disordered systems at affordable computational cost compared to DFT alone. A complete summary of this subject and its application to amorphous carbon and silicon has been recently given by Caro [133].

Chapter III

Review of the Berry-phase theory: Application to wurtzite crystals

III.1 Introduction

Contrary to the ionic polarization, the polarization due to electrons is a quantum phenomenon and cannot be treated by a classical model. Our aim in this chapter is to lay a firm foundation for the Berry-phase theory of electronic polarization that will be employed in the subsequent chapters. In doing so, we thoroughly discuss the main postulates upon which this theory is laid: (1) focusing only on polarization differences between two different states, and (2) computing the polarization of each state as a Berry phase of the corresponding wave functions. We then introduce and explain the formal notions of adiabatic current, Berry phase, formal polarization, effective polarization, polarization quantum, polarization lattice and polarization branch. To take a pedagogical approach, the introduction of these concepts is followed by an application with three concrete examples that showcases the theory in action. At last, we show how the Berry-phase theory is implemented in BerryPI. The latter is a software that enables an accurate modelling of polarized materials by allowing the calculation of numerous polarization quantities, including spontaneous polarization, piezoelectric coefficients and Born effect charges.

We stress that the Berry-phase formalism is the basis of our results presented in Part II of this dissertation. For this reason, Chapter III should be regarded as the heart of Part I. Take note that many of the results and practicalities included here may not be found in other standard introductions to the subject. This chapter is written with a wide audience in mind, i.e. the reader is not assumed to have familiarity with the Berry-phase theory. The only perquisites are a basic knowledge of quantum mechanics and crystallography. The material presented in this chapter will be gathered in a review paper for future publication.

III.2 Difference in polarization

The major step towards the Berry-phase method has been the realization that there is a fundamental ambiguity in defining the polarization of a crystalline solid. To understand why this is the case we follow the reasoning of Spaldin [134] and consider Figure III.1, where a simple model of a one-dimensional ionic crystal is shown. The model crystal is composed of alternating anions and cations of charge $-e$ and $+e$ respectively (where e is the elementary charge) separated by a distance d. Our task is to calculate the electric polarization using three different choices of the crystal cell shown as dashed rectangles in the figure. It is vital to note that all these cells are equivalent, in the sense that repeating one of them along the x-axis produces the same crystal.

We begin with the cell on the left (the red rectangle). Since the vector of dipole moment is always directed from the negative to the positive charge, we can see that the polarization vector is oriented to the right (positive x-axis). In other words, the polarization has a positive value. As stated in Sec. I.2, the dipole moment of two charges is given by the absolute value of one of the charges multiplied by their separation [27,29]. Dividing this by the cell volume V results in polarization P_1:

$$P_1 = \frac{ed}{V}. \tag{III.1}$$

We do the same calculation for the second cell (the blue rectangle). In this case the polarization vector points to the left (negative x-axis) with a value $P_2 = -P_1$. Finally, the remaining cell (green rectangle) can be divided into two sub-cells with opposite polarizations $0.5ed/V$ and $-0.5ed/V$, which means that the net polarization vanishes ($P_3 = 0$). So despite the three cells are equally valid, we have obtained different values of polarization! We say that the polarization of a periodic crystal is a *multivalued* quantity, as both its value and orientation depend on the choice of the crystal cell used in the calculation. Two more subtleties to note: first, the polarization calculated here is the ionic one, as we have ignored the effect of electrons. Second, the volume of the cells V is actually one-dimensional, and is given by the lattice constant a (i.e. $P_1 = ed/a$).

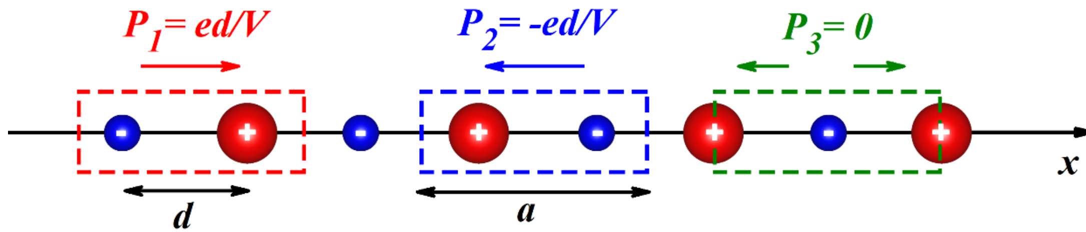

Figure III.1 Schematic illustration of a one dimensional infinite crystal along the x-axis. The crystal is constituted by alternating cations and anions (red and blue spheres, respectively). Comparing to Fig. I. 6, this linear ionic chain mimics the vertical c-axis of a wurtzite crystal. Three representative cells are indicated by coloured dashed rectangles. The lattice constant of the cells is a, and each cell has two ions spaced a distance d apart. As explained in the text, the cells all have different polarization values. These polarizations are due to the separation of ions, so they are ionic polarizations (the electronic polarizations are neglected).

This feature of polarization being not uniquely defined raises significant problems. After all, polarization causes observable and measurable effects such as electric fields which can be exploited in real-life applications, so it should be single-valued. Further, electric polarization is, by definition, an intrinsic bulk property of solids, insensitive to the shape, location and volume of the crystal cell. To clarify the latter point we calculate for the crystal in Fig. III.1 another intrinsic property, namely the mass density ρ_m. Assuming that the two ions have masses m_1 and m_2, then the three cells give the same value of the mass density, which is $\rho_m = m_1 + m_2/V$. It would be absurd to obtain multiple values of ρ_m for the same physical system.

Interestingly, this "non-uniqueness" problem can be solved by looking closely at how polarization is measured. Most experiments of polarization effects discussed earlier in Sec. I.4 access *changes* in polarization rather than polarization itself [135,136]. Indeed, the well-known polarization-related quantities such as the piezoelectric coefficient, the paraelectric coefficient, the electrical susceptibility and the Born effective charge are derivatives (i.e. a change) of polarization with respect to suitable perturbations [see Eqs. (I.7-I.11)]. In the case of the ferroelectric effect, the spontaneous polarization is measured as a finite difference between two opposite polarities. Motivated by this experimental fact, it seems that one should abandon the concept of absolute polarization and regards the difference in polarization as the key quantity under consideration.

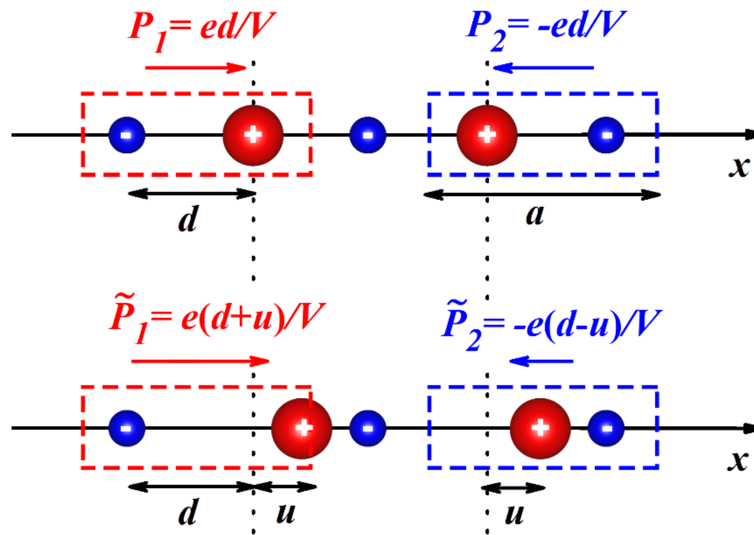

Figure III.2 Upper panel: the same 1D ionic crystal presented in Fig. III.1. Lower panel: A distorted version of the previous crystal, where the cations are moved by a distance u to the left/right of the anions. The vertical dotted lines mark the initial equilibrium positions of the cations. This ionic displacement u changes the value of polarization for both cells (the red and blue ones). The ionic separation is $d+u$ for the red cell and $d-u$ for the blue cell. Contrary to the absolute polarizations, the polarization difference is unique as long as the difference is taken for the same cell.

Now we go back to our one-dimensional ionic crystal and try to extract a single value of its polarization. The upper panel of Figure III.2 is basically the same as Fig. III.1. In the lower panel we introduce a structural distortion by displacing the cation by a distance u relative to the anion. This relative displacement might be a response to an applied strain or electric field. Following the same approach as before, we calculate the absolute polarization of the distorted crystal using two different cells. For the left cell (in red), the separation between ions is $d+u$, and the polarization $\tilde{P}_1$ is computed as:

$$\tilde{P}_1 = \frac{e(d+u)}{V}. \tag{III.2}$$

Similarly, the polarization $\tilde{P}_2$ for the right cell (in blue), where the separation is $d-u$, is:

$$\tilde{P}_2 = -\frac{e(d-u)}{V}. \tag{III.3}$$

Again, we obtain different results, but consider what happens if we calculate the difference in polarization ΔP between the equilibrium and distorted configurations for each cell:

$$\begin{aligned} \Delta P = \tilde{P}_1 - P_1 &= \frac{e(d+u)}{V} - \frac{ed}{V} = \frac{eu}{V}, \\ \Delta P = \tilde{P}_2 - P_2 &= -\frac{e(d-u)}{V} - \left(-\frac{ed}{V}\right) = \frac{eu}{V}, \end{aligned} \tag{III.4}$$

we notice that the difference in polarization is the same in both cases. For ΔP to be physically meaningful, one must substrate absolute polarizations of the same cell (e.g. the difference $\tilde{P}_1 - P_2$ has no sense). Quoting Spaldin [134]: "…So, while the absolute value of polarization in a bulk periodic system is multi-valued, the change in polarization (which is the quantity that can be measured in an experiment) is single-valued and well defined, provided that we stick with the same choice of unit cell and basis throughout the analysis".

We have just established the first postulate of the Berry-phase theory of polarization: only differences in polarization between two different states have physical meaning and correspond to measurable quantities [135,136]. These two states could be, for instance, the unstrained and strained structures of a piezoelectric crystal. The corresponding polarization difference in this case coincides with the piezoelectric polarization. In the context of ferroelectricity, the two states correspond to the two ferroelectric structures with opposite polarizations. Switching the polarization induces a difference ΔP equals twice the value of the spontaneous polarization. It is not necessary for the two states to belong to the same material, they can be different materials altogether. This allows to compute the polarization charge that accumulates at the interface between two polar solids using the interface theorem [38]. Note that the latter is already consistent with the Berry-phase theory, as the interface bound charge is defined as a difference in polarization between the upper and lower layers [see Eq. (I.5)]. The second postulate, which will be discussed in the next section, relates the polarization of a particular state to the Berry phase of the crystal wave function corresponding to that same state.

III.3 Polarization as a Berry phase

III.3.1 Dipole-moment picture

Most elementary textbooks define electric polarization as the dipole moment per unit-volume. For an arbitrary charge density $n(\mathbf{r})$ due to electrons and ions, the polarization of the system is formally given via the relation [134]:

$$\mathbf{P} = \frac{1}{V}\int en(\mathbf{r})\mathbf{r}d\mathbf{r}. \tag{III.5}$$

According to the neutrality condition, the charge distribution averages to zero within any unit volume, as well as within the whole sample. As it turned out, however, this definition is only valid for well-localized charge densities, such as atoms and molecules and other finite systems, and completely fails for infinite crystalline solids [31]. The difficulties can be summarized in two main points: (i) the electronic charge in a polarized crystal is distributed in a periodic delocalized manner, for which the dipole moment is ill defined, and (ii) within this approach the polarization cannot be regarded as a bulk property.

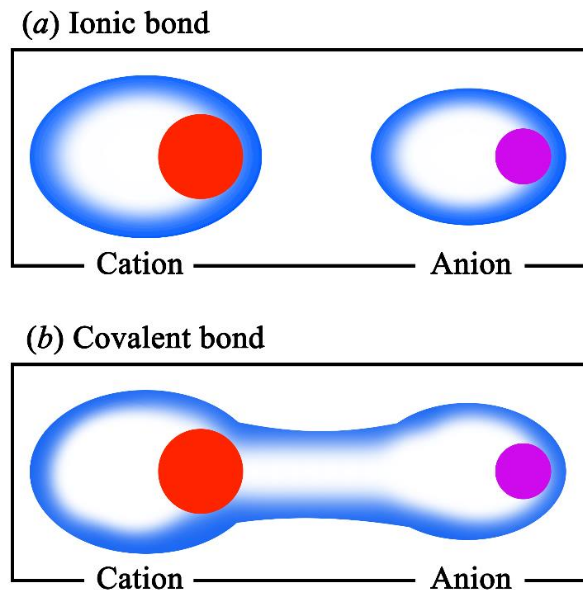

Figure III.3 (*a*) Unit cell of a purely ionic crystal where the cation and anion are linked by an ionic bond (electrical attraction). Because electrons (blue shaded aria) are localized around the nuclei (orange and purple spheres), they do not overlap, which makes the electrons-nuclei separation and thus the electronic polarization well defined. (*b*) Unit cell of an ionic/covalent crystal, in which an important part of the electronic charge is overlapped and shared among the ions in a delocalized manner. In this case, the electron-nuclei separation is largely arbitrary, resulting in the electronic polarization being ill defined if calculated via the electronic charge density [Eq. (III.5)].

The first difficulty concerns the polarization of electrons. In Figure III.3 a simple illustration is given to understand why the electronic polarization, if evaluated by Eq. (III.5), is not well defined. A unit cell of a polarized ionic crystal is sketched in Fig. III.3 (*a*). The valence electrons are strongly localized around the nucleus of both the cation and anion. Remember that the electronic polarization is induced by the separation between the nuclei and the electron clouds. This charge separation is quite clear in Fig. III.3 (*a*), where we can unambiguously extract the value of the electronic polarization using the formal expression of Eq. (III.5). However, most real materials exhibit a mixed ionic/covalent character, where some chemical bonds involve the sharing of electrons between ions. Fig. III.3 (*b*) shows a typical covalent bond linking two ions together. Because the shared valence electrons are delocalized in the space between the ions, there is no way of unambiguously determining the separation between the electrons and nuclei as we did in the previous case [136]. As such, the electronic polarization

calculated with this method is ill defined, with an array of possible values arising from different choices of charge separation. So aside from the extreme ionic case, Eq. (III.5) fails at giving a unique value of electronic polarization.

We now address the second difficulty, which is about the bulk nature of polarization (more precisely the polarization difference). We have stated in Sec. I.3 that the polarization induced in a system appears as an accumulation of charge in the bulk region. An important part of this polarization charge also piles up at the sample surfaces. The problem is that the surface contribution cannot in principle be accessed. In practice, the polarization surface charge is generally neutralized by electrically active defects and external charges [15], which makes its measurement extremely difficult. Even at the theoretical level the surface charge is inaccessible. In condensed-matter physics one usually uses periodic boundary conditions, originally proposed by Born and von Karman. Here, instead of considering a three-dimensional sample with actual ends, we imagine that the ends are connected together making the sample a hyper-ring. A polarized system under such boundary conditions has no surfaces, implying it is not possible to compute the surface contribution of its polarization [136]. The key point is that polarization is phenomenologically known to be a bulk observable, i.e. independent of surface conditions and determined only by what happens inside the volume of the system under investigation [135,136]. Therefore, the polarization vector as given by Eq. (III.5) does not represent a genuine bulk property of the material.

III.3.2 Adiabatic-current picture

The conclusion that can be drawn from this analysis is that the concept of the dipole moment, and by extension the charge density, does not lead to a useful definition of electronic polarization of crystals. These and other problems led to immense efforts in the late 20th century, resulting in a new theoretical framework for understanding the phenomenon: the so-called Berry-phase theory of polarization [135,136]. The breakthrough that led to the development of the theory was made by Resta [13], who showed that the difference in polarization $\Delta\mathbf{P}$ is equivalent to an electrical *current* produced by the flow of charge (electrons and ions) within the sample as it is gradually changed during some perturbation. This statement parallels the way polarization is experimentally accessed: the raw output of a typical measurement is the amount of current flowing through the sample while the external perturbation is applied.

Figure III.4 (*a*) presents a typical setup of an experiment where a piezoelectric material is sandwiched between two conducting electrodes. When the strain is applied, the induced piezoelectric polarization $\mathbf{P}_{\mathbf{pz}}$ gives origin to an electric charge at the sample surfaces. If both electrodes are wired, the accumulated surface charges flow through the wires to form an electric current. This current is used to measure the piezoelectric polarization. For practical purposes, the current can be harvested to charge electronic devices or to be used as an electrical signal in pressure sensors. Another example is depicted in Figure III.4 (*b*). Assuming the piezoelectric crystal to be also ferroelectric, then putting it in an external electric field reverses the polarization along the polar axis. Even though the magnitude of the spontaneous polarization $\mathbf{P}_{\mathbf{sp}}$ stays the same, its orientation varies by 180° (from “up” to “down”). This polarization

reversal is accompanied by a charge redistribution between the two opposite faces of the sample, and the change in polarization is once again measured by the resulting current.

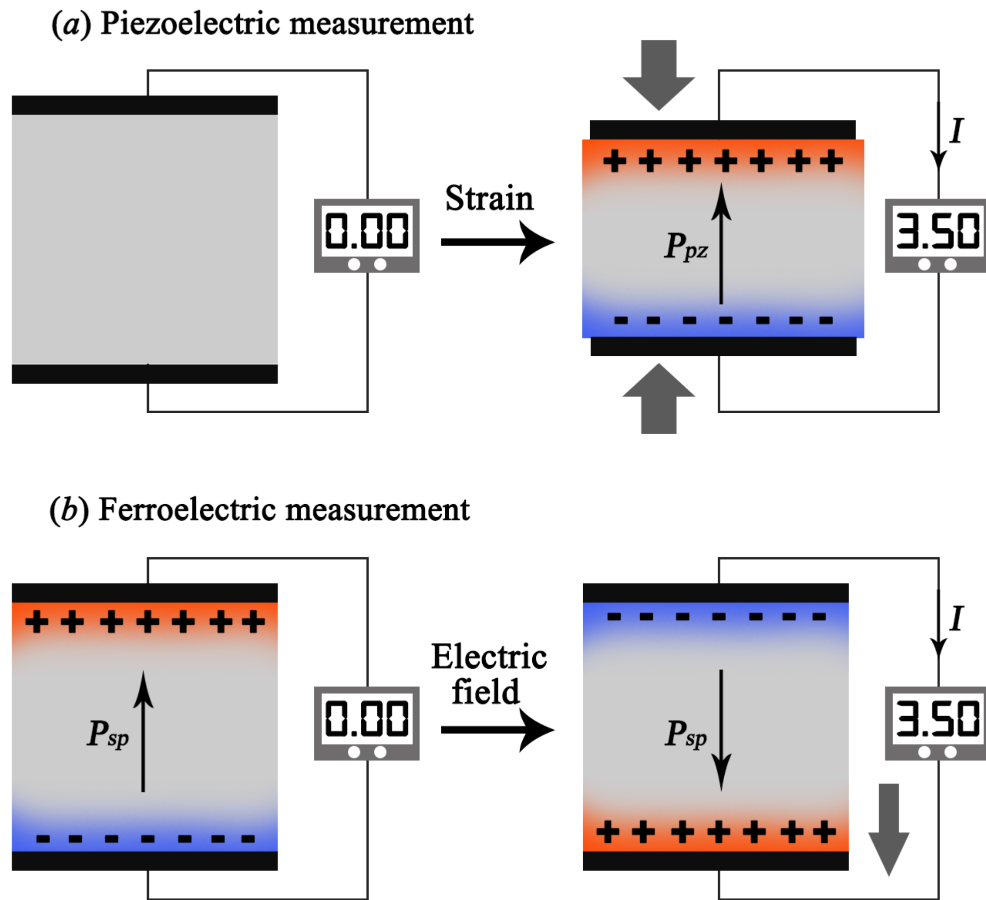

Figure III.4 (a) Sketch of a piezoelectric material (grey rectangle) placed between two electrodes. When the strain state of the material is changed, induced opposite charges pile up at its surfaces, and the change in polarization between the strained and unstrained structures is given by the piezoelectric polarization P_{pz}. Connecting the strained crystal to an external circuit makes the charges flow through the wires and an electric current I is measured, which can be used to access the value of the induced polarization. (b) The same situation as in (a) except that the material is ferroelectric with switchable polarization. The applied field switches the spontaneous polarization from P_{sp} to -P_{sp}, causing the surface charges to flow in opposite directions through the wires. As in the piezoelectric case, the current that flows during the switching is directly related to the difference in polarization between the up- and down-polarized states. Figure inspired by Ref. [136].

In both situations discussed above, the induced current is time-dependent, and is described by a current density $\mathbf{J}(t)$, which is related to the polarization vector via [136]:

$$\mathbf{J}(t) = \frac{d\mathbf{P}}{dt}. \tag{III.6}$$

This implies that the difference in polarization is the time-integral of the current density that flows during a time interval Δt:

$$\Delta \mathbf{P} = \mathbf{P}(\Delta t) - \mathbf{P}(0) = \int_0^{\Delta t} \mathbf{J}(t) dt. \quad \text{(III.7)}$$

A proof of Eqs. (III.6) and (III.7) based on elementary electrostatics can be found in Ref. [137]. Quite generally, the polarization-related current is rigorously defined if two different states of the polarized crystal are connected by an *adiabatic* transformation. It is customary to characterize such a transformation by a continuous parameter λ, whose values are in the interval [0,1]. The term "adiabatic" is essential, in this context it means that the said transformation is a slowly varying perturbation [138]. According to Resta, the value of $\Delta\mathbf{P}$ is obtained via the following integral [13,136]:

$$\Delta \mathbf{P} = \mathbf{P}(1) - \mathbf{P}(0) = \int_0^1 \frac{d\mathbf{P}}{d\lambda} d\lambda, \quad \text{(III.8)}$$

where $d\mathbf{P}/d\lambda$ denotes the generalized current-density. Strictly speaking, the above equation states that the polarization difference between two states is given by the integrated current as the system adiabatically (slowly) evolves from the initial state at λ= 0 to the final state at λ= 1 [136]. Basically, λ has the meaning of time, but its physical nature is much broader. In real modelling of the piezoelectric and ferroelectric effects, one can identify λ as atomic positions, whose change is caused by strain or electric field. For Eq. (III.8) to hold, the system is assumed to remain insulating or semiconducting at any intermediate value of λ (i.e. its gap does not close).

Thinking in terms of currents instead of charges and dipole moments results in a bulk definition of polarization, because the current has no surface component by construction, as it flows entirely in the interior of the polarized system. Indeed, from the continuity equation $\mathbf{\nabla}.\mathbf{J} = \partial\rho/\partial t$ [27], one can see clearly that the current density **J** is related the flow of the volume charge density ρ, i.e. a charge that exists in the bulk, not on the surface. From a quantum-mechanical viewpoint, the current is a property of the phase of the wave function [139]. In a milestone paper, Vanderbilt and King-Smith [12] proved the quantum nature of polarization. They achieved this by linking the associated polarization current to a quantum phase of the electronic wave functions known as the *Berry phase*. Once these concepts were adopted and understood, all the issues were solved, and the development of the new framework was complete. Physicists finally had a successful theory of electric polarization in crystals.

III.3.3 Berry-phase picture

A deeper account of the mathematics of the Berry-phase theory is beyond the scope of this review, and the interested reader is oriented to external references for detailed information. These references include the pioneering papers by Resta [13], Vanderbilt and King-Smith [12], the early review by Resta [135], the pedagogical book chapter by Resta and Vanderbilt [136], and the pedagogical paper by Spaldin [134]. We give below only a brief sketch of the central formula of the theory, namely the expression of the electronic polarization $\mathbf{P}_{\mathbf{ele}}$. The ions are dealt with as classical pointwise charges, whose contribution to polarization $\mathbf{P}_{\mathbf{ion}}$ is trivial and given by the ionic dipole moment [see Eq. (I.2)]. Due to their quantum wave-like nature,

electrons propagate through the unit cell of the crystalline solid. The electronic wave function $\psi_{n\mathbf{k}}(\mathbf{r})$ for such a periodic system takes the Bloch form [29,72], i.e. a plane wave modulated by a function having the periodicity of the crystal lattice:

$$\psi_{n\mathbf{k}}(\mathbf{r}) = u_{n\mathbf{k}}(\mathbf{r})e^{i\mathbf{k}.\mathbf{r}}, \tag{III.9}$$

where $\mathbf{k}$ is the wave vector of the propagating electrons, n is the band index, and $u_{n\mathbf{k}}(\mathbf{r})$ is a cell-periodic function that satisfies $u_{n\mathbf{k}}(\mathbf{r}+\mathbf{R}) = u_{n\mathbf{k}}(\mathbf{r})$, with $\mathbf{R}$ being any real-space lattice vector. The dot product **k.r** is the phase of the wave function, which is a dynamical phase related to the energy of the electronic system, and has nothing to do with polarization. Next, we assume that we can continuously (and adiabatically) transform the polarized crystal from one state to another by switching the aforementioned parameter λ. In this case the Bloch wave functions, now denoted $\psi_{n\mathbf{k}}^{(\lambda)}(\mathbf{r})$ as they depend on λ, acquire an additional phase [14,138]. This is a geometric phase which bears connection to the electronic current traversing the crystal cell during the transformation. Such an integrated current is directly related to the difference in electronic polarization $\Delta\mathbf{P}_{\mathbf{ele}}$ between the final and initial states.

Without going through the details, the geometric phase, which we call the Berry phase φ, can be cast as [140]:

$$\varphi = -\,i \oint \left\langle u_{n\mathbf{k}}^{(\lambda)} \middle| \nabla_{\mathbf{k}} \middle| u_{n\mathbf{k}}^{(\lambda)} \right\rangle . d\mathbf{k}. \tag{III.10}$$

This formula is a *line* integral around a closed loop in parameter space, which is a four dimensional space: three dimensions due to the three components of the wave vector $\mathbf{k}$ and one extra dimension due to the adiabatic parameter λ. The operator $\nabla_{\mathbf{k}} = -i\partial/\partial\mathbf{k}$ is the position operator in k-space, and the bra-ket notation gives the expected value of this operator with respect to the eigenstates $u_{n\mathbf{k}}^{(\lambda)}$. Within the Berry-phase formulation, $\left\langle u_{n\mathbf{k}}^{(\lambda)} \middle| \nabla_{\mathbf{k}} \middle| u_{n\mathbf{k}}^{(\lambda)} \right\rangle$ is known as the Berry connection. Being a phase, φ is a dimensionless angular quantity; let us check this out. Because of the normalization condition $\int \psi_{n\mathbf{k}}^{(\lambda)*}\psi_{n\mathbf{k}}^{(\lambda)} d\mathbf{r} = \int u_{n\mathbf{k}}^{(\lambda)*}u_{n\mathbf{k}}^{(\lambda)} d\mathbf{r} = 1$, the dimension of the function $u_{n\mathbf{k}}^{(\lambda)}$ is $L^{-3/2}$ (where L is the dimension of length). The dimension of $\nabla_{\mathbf{k}}$ is L because that of $\mathbf{k}$ is L^{-1}. From basic quantum mechanics, the position representation of the Berry connection is $\int u_{n\mathbf{k}}^{(\lambda)*}\nabla_{\mathbf{k}} u_{n\mathbf{k}}^{(\lambda)} d\mathbf{r}$. Written in this form, we can see that it has the dimension of length L. Therefore, the dimension of the Berry phase is L (from the Berry connection) multiplied by L^{-1} (from the differential "k-space length" element $d\mathbf{k}$), meaning that the Berry phase has no dimension as expected. We can express the polarization due to electrons as an explicit sum over occupied bands n of the Berry connection:

$$\mathbf{P}_{\mathbf{ele}} = -\frac{ie}{(2\pi)^3}\sum_{n} \int \left\langle u_{n\mathbf{k}}^{(\lambda)} \middle| \nabla_{\mathbf{k}} \middle| u_{n\mathbf{k}}^{(\lambda)} \right\rangle d\mathbf{k}, \tag{III.11}$$

where the integral is taken over the volume of the Brillouin zone of the solid (here $d\mathbf{k}$ is the differential "k-space volume" element). This is the Berry-phase formula for the electronic polarization obtained by Vanderbilt and King-Smith [12]. The significance of the Berry phase

in physics has been recognized after the publication by Berry [14], where he demonstrated that the adiabatic evolution of some systems in the parameter space generates an extra phase in the wave functions. This phase can have a profound effect on material properties. Here, the parameter space is the Brillouin zone, and the property of interest in the electric (electronic) polarization. Other phenomena that can be described in terms of the Berry phase are orbital magnetism, quantum Hall effects and quantum charge pumping, etc. We refer to a nice review [137] which summarizes the Berry-phase effects in a variety of solid-state phenomena.

III.3.4 Formal and effective polarizations

We establish here the distinction between the formal polarization and the effective polarization. Each of the quantities $\mathbf{P}(0)$ and $\mathbf{P}(1)$ in Eq. (III.8) is identified as the *formal* polarization $\mathbf{P_f}$ of a single state [136]. The same thing can be said about the electronic polarization defined in Eq. (III.11). In general, the formal polarization of a given state consists of electronic and ionic contributions:

$$\mathbf{P_f} = \mathbf{P_{ele}} + \mathbf{P_{ion}}, \qquad \text{(III.12)}$$

As we have previously mentioned, the calculation of the ionic polarization is straightforward, whereas the electronic polarization is computed as a Berry phase of the Bloch orbitals. Physically observable quantities result only from differences in formal polarization. We refer to such a difference as the *effective* polarization $\mathbf{P_{eff}}$ [136]. Hence, if the system is taken from an initial state ($\lambda = 0$) to a final state ($\lambda = 1$) the effective polarization reads:

$$\mathbf{P_{eff}} = \mathbf{P_f^{(1)}} - \mathbf{P_f^{(0)}}, \qquad \text{(III.13)}$$

where $\mathbf{P_f^{(0)}}$ and $\mathbf{P_f^{(1)}}$ are the formal polarizations of the states 0 and 1, respectively.

So far our discussion has been rather abstract. As a concrete example we consider the application of the Berry-phase theory to wurtzite crystals. In the context of piezoelectricity, in which the material is strained, the scalar parameter λ controls the lattice constants a and c and the internal parameter u of the wurtzite phase. The case $\lambda = 0$ corresponds to the equilibrium situation, while the case $\lambda = 1$ corresponds to the final strained structure. The difference between the formal polarization of the two configurations provides the (effective) piezoelectric polarization $\mathbf{P_{pz}}$.

For the calculation of the spontaneous polarization $\mathbf{P_{sp}}$, one of the structures has a higher symmetry compared to that of wurtzite [136]. This *reference* structure is characterized by $\lambda = 0$, and in the case of wurtzite materials it could be the zincblende, trigonal or layered-hexagonal polytypes. The effective polarization is interpreted as the spontaneous polarization of the crystal in the low-symmetry structure (wurtzite here, for which $\lambda = 1$). Detailed simulations show that the spontaneous polarization of traditional wurtzite III-nitrides (AlN, GaN and InN) and II-oxides (BeO and ZnO) falls in two ranges: from −0.02 to −0.09 C/m² and from 0.81 to 1.34 C/m², depending on the choice of the reference structure. We will explain

how to deal with the spontaneous polarization of wurtzite compounds in the second part of the thesis (Chapters IV and V).

III.4. Polarization lattice

A central concept in the Berry-phase theory, which is essential in practical calculations of polarization, is the quantum of polarization. It is easiest to describe this first in one dimension. To do so we reconsider once again the toy model of the 1D ionic crystal. There are in principle infinite choices of the unit cell. Three such cells are indicated as coloured rectangles in Figure III.5. Despite the fact that these unit cells are different, making periodic replica of them over the *x*-axis results in the same crystalline chain. We have already calculated the equilibrium formal polarization of the red and blue unit cells in Sec. III.1, we have found the values *ed/V* and 0, respectively, where *d* is the ionic separation and *V* is the cell volume. The larger pink unit cell contains four ions with two dipole moments pointing to the right, which implies that the polarization is 2*ed/V*. These results are in agreement with the general concept that the formal (or absolute) polarization is a multivalued vector quantity. One can repeat this analysis with many other choices of the unit cell to obtain many values of polarization: ..., -2*ed/V*, -*ed/V*, 0, *ed/V*, *2ed/V*, … [134]. This spectrum of polarization values is called the polarization *lattice*. It can be seen that the allowed successive values are equally spaced by *ed/V* [134]. This is referred to as the *quantum* of polarization P_q [135,136].

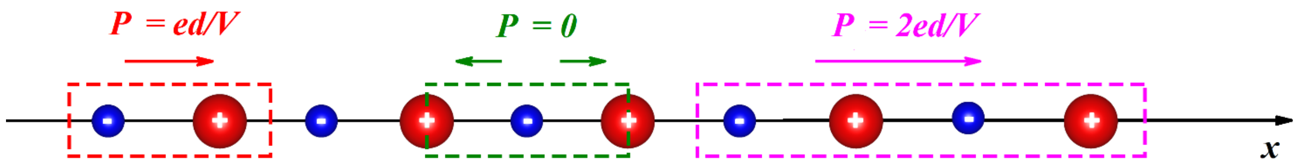

Figure III.5 One dimensional ionic crystal used to explain the concepts of the polarization lattice and polarization quantum. Three different ways to choose the unit cell are shown. The pink cell is two times larger than the red and green ones. Each cell has its own polarization. These values constitute the polarization lattice, and the difference between any two adjacent values is the quantum of polarization.

The discussion about the polarization lattice and quantum leads to a very important result within the Berry-phase formalism: the formal polarization, defined via Eq. (III.12), is only well-defined *modulo* a polarization quantum [135,136]. That is, if the formal polarization of a system is P_f, the polarizations P_f+nP_q (n is an integer) are also equally valid values. This result is really a restatement of the idea, strongly emphasized above, that the formal polarization is a multivalued quantity. This multivaluedness is consistent with the nature of the Berry phase. Indeed, the Berry phase, being an angular variable measured in radians, is well-defined modulo 2π, i.e. the phases φ and $\varphi + 2n\pi$ correspond to the same angle on the unit circle. The values of the integer n accounts for the choice of the unit cell, for instance $n= 0$ corresponds to the red cell in Fig. III.5 (for which $P_f= ed/V$), $n= -1$ corresponds to the green cell ($P_f= 0$), the larger pink cell is characterized by $n= 1$ ($P_f= 2ed/V$), etc.

III.5. Polarization branch

The next step is to address the influence of the polarization quantum on the effective polarization, but first we need to formalize our results concerning the polarization lattice. Note that the formal polarization of a system is always labeled by the state and the cell for which it is evaluated. For this reason we introduce the notation $P_{f,n_i}^{(\lambda)}$, which refers to the formal polarization calculated at the state λ and for the cell n_i. For the 1D crystal of Fig. III.5, the state may correspond to the unstrained equilibrium structure (λ= 0) of the red cell (n_i = 0), or it is the strained structure (λ= 1) of the green cell (n_i= -1).

For a given adiabatic gap-preserving transformation scaled by the state parameter λ, the formal polarizations evaluated for the start and end states (λ= 0 and 1) and for the cells n_i and n_j are, respectively, $P_{f,n_i}^{(0)}$ and $P_{f,n_j}^{(1)}$. The effective polarization is defined as the difference between the two formal polarizations:

$$P_{eff} = P_{f,n_j}^{(1)} - P_{f,n_i}^{(0)}. \qquad \text{(III.14)}$$

The collection of formal polarizations $P_{f,n_i}^{(\lambda)}$ for the same cell n_i and for different states λ, including the initial and final states and all the states in between, form what we call a polarization *branch* [134,136]. It should not confuse the concept of the polarization lattice, discussed above, with the polarization branch just introduced. While the former is a set of polarization values associated with the same state but different unit cells (fixed λ and varying n_i), the latter contains formal polarizations of different states belonging to one unit cell (varying λ and fixed n_i).

Each polarization branch corresponds to a single choice of the system cell. Since we assign an integer n for each cell, the branches are also labeled by this same integer, so that we can write branch -1, 0, 1, 2 and so on. The formal polarization $P_{f,n_i}^{(\lambda)}$ is therefore labeled by the state λ and the branch n_i. For the effective polarization of Eq. (III.14) to be physically meaningful, the formal polarizations $P_{f,n_i}^{(\lambda)}$ and $P_{f,n_j}^{(\lambda)}$ must be computed for the same unit cell. In other words, one has to make sure that the polarization values belong to the same polarization brunch [134], implying that the integers n_i and n_j must be equal: $n_i = n_j = n$. Equation (III.14) can then be rewritten as:

$$P_{eff} = P_{f,n}^{(1)} - P_{f,n}^{(0)}. \qquad \text{(III.15)}$$

We have mentioned earlier in Sec. III.2 that the change in polarization, as defined by Eq. (III.13), is a single-valued vector quantity. However, the polarization concepts explained above make the effective polarization multivalued! Indeed, there is no guarantee that the difference between the formal polarizations $P_{f,n}^{(1)}$ and $P_{f,n}^{(0)}$ is equal for all the branches n. For example, for the branch n= 1 the polarization difference in Eq. (III.15) is $P_{f,1}^{(1)} - P_{f,1}^{(0)}$, and for the branch n= 2 the difference is $P_{f,2}^{(1)} - P_{f,2}^{(0)}$. Our statement here is that in general, $P_{f,1}^{(1)} - P_{f,1}^{(0)}$ is not

always equal to $P_{f,2}^{(1)} - P_{f,2}^{(0)}$, resulting in different effective polarizations for the same system (see the second example of Sec. III.6.2 about the piezoelectric polarization).

The quote by Spaldin [134] at the end of Sec. III.2 stresses that one must stick to a single choice of the crystal cell for the polarization difference (or P_{eff}) to be single-valued. But based on our treatment we see that this statement is quite inaccurate: even if we stick to the same cell (i.e. for the same branch n_i), we would still obtain in general different values of the effective polarization. Resta and Vanderbilt, two founders of the present theory, have arrived at the same conclusion in their excellent review [136]. The effective polarization calculated using equation (III.15) is well-defined and corresponds to the quantity measured in experiments. The problematic multivaluedness of P_{eff} can be removed using different techniques, we will mention briefly in Sec. III.6.2 how to deal with this issue in the important case of the piezoelectric response. Also, we will discuss the conditions for P_{eff} to be single-valued for the specific case of wurtzite crystals.

Most real systems are three-dimensional, for which the different polarization quantities $\mathbf{P_f}$, $\mathbf{P_q}$ and $\mathbf{P_{eff}}$ are vectors with three Cartesian components. The extension of the previous conclusions to three dimensions is straightforward. The vector of the quantum of polarization reads [134,136]:

$$\mathbf{P_q} = \frac{e\mathbf{R}}{V}, \tag{III.16}$$

where e is the usual electron charge, V is the (3D) cell volume and $\mathbf{R}$ is any Bravais lattice vector. The latter is given by the primitive lattice vectors $\mathbf{a}$, $\mathbf{b}$ and $\mathbf{c}$ via $\mathbf{R} = \mathbf{a} + \mathbf{b} + \mathbf{c}$. Using this expression for $\mathbf{R}$, we can cast the quantum as three components $P_{q,i}$ ($i = x,y,z$) as:

$$\begin{aligned} P_{q,x} &= \frac{ea}{V}, \\ P_{q,y} &= \frac{eb}{V}, \\ P_{q,z} &= \frac{ec}{V}, \end{aligned} \tag{III.17}$$

where a, b and c represent the lattice constants obtained by taking the norm of the primitive lattice vectors $\mathbf{a}$, $\mathbf{b}$ and $\mathbf{c}$ within the coordinate system of the lattice. The 3D version of equation (III.15) is simply:

$$\mathbf{P_{eff}} = \mathbf{P}_{\mathbf{f},n}^{(1)} - \mathbf{P}_{\mathbf{f},n}^{(0)}. \tag{III.18}$$

Remember that the difference $\mathbf{P}_{\mathbf{f},n}^{(1)} - \mathbf{P}_{\mathbf{f},n}^{(0)}$ must be taken along the same branch of polarization n for Eq. (III.18) to make sense.

Implicit in the above analysis is that the states 0 and 1 describe the same crystal (e.g. GaN), as otherwise they are not connected by an adiabatic transformation. As an example, if λ is taken to be ionic positions, the transformation is a relative displacement of ions within the same material. This example is relevant to the polarization switching (ferroelectricity) and the

polarization induced by optic phonons (lattice vibration). In some cases the states 0 and 1 describe different materials (such as GaN and InN), and therefore are not linked by an adiabatic deformation path. This is most exemplified in the calculation of the polarization charge that builds up at an insulating interface. In this case, λ describes the evolution of the structural parameters of two different materials: λ= 0 for the state of one material and λ= 1 for the state of the other one. Consequently, one is left dealing with two sets of integers n labelling two sets of polarization branches, one for each crystal (in the first case we have one material, so there is one set of integers and correspondingly one set of branches). The bound polarization charge σ at the interface of two different materials can be accessed provided that the difference between the formal polarizations of the two compounds is taken along the same branch:

$$\sigma = \left(\mathbf{P}_{\mathbf{f},n}^{(1)} - \mathbf{P}_{\mathbf{f},n}^{(0)}\right).\mathbf{n}, \tag{III.19}$$

where $\mathbf{n}$ is the unit vector normal to the interface. This formula is the interface theorem (Eq. I.5) in the light of the Berry-phase approach.

There is an interesting situation in which the polarization charge appears at the interface of two different atomic structures of the same system, such as the crystalline defects of stacking faults in GaN studied in detail in Chapter VIII. There, and unlike the different-materials case, the states 0 and 1 can be connected adiabatically via atomic displacements. To determine the interface charge we also use Eq. (III.19). Finally, sometimes we may have a single crystal whose states cannot be linked adiabatically. This is the case of different polymorphs of the same material, e.g. wurtzite and zincblende GaN. We will encounter this case in Chapter IV when studying the spontaneous polarization of wurtzite crystals referenced to the trigonal structure.

III.6 Examples

Since all the discussion in the previous two sections may seem a bit (or a lot) cumbersome, we resort in the following to three practical examples to clarify the concepts of the polarization quantum, lattice and branch, as well as the formal and effective polarizations. We take wurtzite GaN as a case-study, whose typical structure is represented in Fig. I.6. Let us start by calculating the quantum of polarization for the unit cell. Symmetry arguments suggest and first-principles calculations confirm that the polarization vector of the wurtzite phase has only one component along the [0001] direction (the c-axis in the convention of Fig. I.6). Since the horizontal (basal) components are zero in all of our calculations, from now on we indicate the polarization value only through its vertical (axial) component, which renders the problem effectively one dimensional. As a result, the components $P_{q,x}$ and $P_{q,y}$ in Eq. (III.17), which lie in the basal plane perpendicular to the c-axis, vanish, and only $P_{q,z}$ remains. The magnitude of the polarization-quantum vector for wurtzite unit cells is:

$$P_q = \frac{ec}{V}, \tag{III.20}$$

where c is the out-of-plane lattice constant. Given that the volume of the wurtzite unit cell is $V = \sqrt{3}a^2\, c/2$, we can write:

$$P_q = \frac{2e}{\sqrt{3}a^2}. \qquad \text{(III.21)}$$

This is the polarization quantum associated with the standard 4-atom wurtzite unit cell of Fig. I.6. Notice that P_q only depends on the in-plane lattice constant a. We will use this and similar expressions many times throughout this work, in particular for linking formal polarizations of different cells and for calculating the spontaneous polarization of wurtzite compounds. Using the reported value of the lattice constant a for GaN (3.23 Å), Eq. (III.21) yields a polarization quantum equal to 1.771 C/m².

III.6.1 Ionic-displacement-induced polarization

In order to calculate the formal and effective polarizations of wurtzite GaN, one must devise a transformation that links different states λ ($0 \le \lambda \le 1$) of the crystal. In this first example we define the transformation to be a displacement of the anion N relative to the cation Ga along the c-axis, without changing the lattice constants a and c. The adiabatic parameter λ scales the internal parameter u, or more precisely the internal strain ε_u. Details on how such a strain is defined are found at the end of Chapter IV. The electronic and ionic polarizations are provided by the BerryPI [141] module of WIEN2k [125], which we explore in detail in the next section. The results are summarized in Figure III.6, which displays the variation of the wurtzite formal polarization P_f as a function of the percentage displacement of the anion ε_u. For zero displacement (i.e. at 0%), the formal polarization of the 4-atom unit cell is calculated to be -0.480 C/m². The minus sign indicates that the polarization vector points to the negative c-axis or the $[000\bar{1}]$ crystalline direction.

The polarization lattice associated with the state 0% can be constructed via calculating the formal polarization of other wurtzite cells. These cells are referred to in the jargon of ab-initio simulations as supercells (see Sec. II.7 C). Starting from the wurtzite unit cell, which contains 4 atoms, we create a supercell of 32 atoms. This is done by multiplying the lattice constants a and c of the unit cell by 2. The resulting supercell is shown in a 2D representation on the right side of Fig. III.6. Supercells are usually labeled by their dimensions: for our 32-atom supercell the dimension labelling is 2×2×2, meaning that the lattice constants a and c of the supercell are two times those of the unit cell. If we evaluate the formal polarization of this supercell we find it equal to -0.0373 C/m², which is different from the value obtained using the conventional unit cell (-0.480 C/m²).

This finding may seem counterintuitive and disturbing, since one expects that the physical properties of materials are dictated by the microscopic interactions between atoms and electrons, and are not modified by the sample size. For instance, the value of the band gap is 1.68 eV for both the unit cell and supercell. Remember from our discussion in the one-dimensional case that the value of the formal polarization depends on the choice of the crystal cell. This conclusion is valid in three dimensions as well, so the formal polarization of the 4-atom cell and its 32-atom version must be different, as predicted by our calculation.

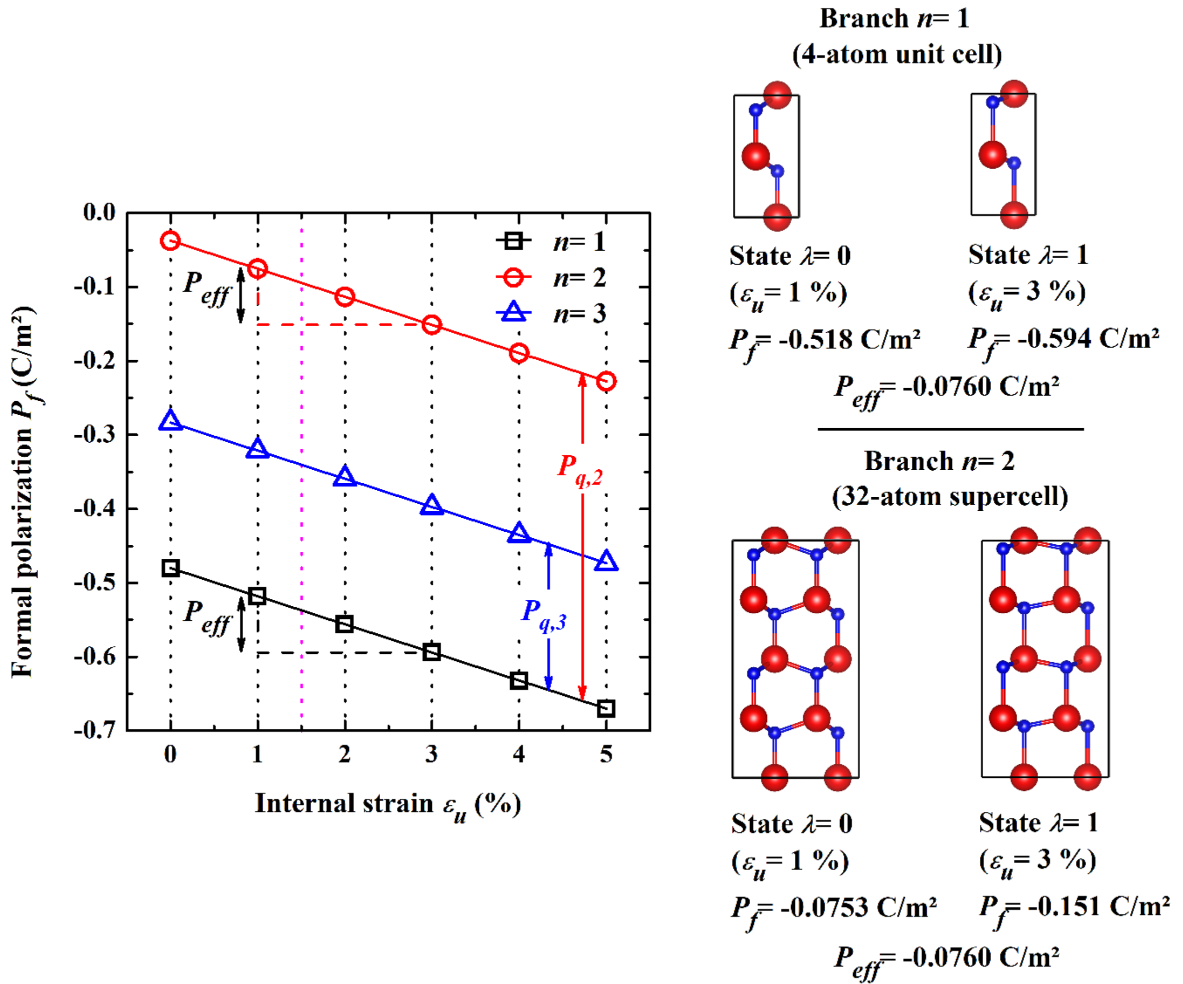

Figure III.6 Variation of the formal polarization of wurtzite GaN as a function of the internal strain. The calculation is performed in a first-principles framework using the BerryPI implementation of the Berry-phase theory. The states λ are crystalline structures with different ionic displacements of N with respect to Ga. In this example we employ six such displacements, from 0% to 5%. Consequently six polarization lattices are shown (in fact there are infinitely many lattices), which are indicated by the data points along the dotted vertical lines. Each lattice contains three formal-polarization values because three different wurtzite cells are used in the simulation. These are the 4-atom unit cell, the 32-atom supercell and the 108-atom supercell. Since there are three choices of the crystal cell, we count three polarization branches. The branches correspond to the three linear curves, each labeled by the integer n that gives the dimensionality of the cells along the a- and b-axes: n= 1 for the 4-atom unit cell, n= 2 for the 32-atom supercell and n= 3 for the 108-atom supercell. The coloured double arrows represent the polarization quanta of the supercells $P_{q,2}$ (in red) and $P_{q,3}$ (in blue) that separates the n= 2 and n= 3 branches from the n= 1 branch, respectively. To the left of the graph we show the details of computing the effective polarization P_{eff} for two setups. In the first case, the polarization difference is evaluated using two structures of the wurtzite unit cell, where the structures correspond to an ionic displacement of 1% (the initial state λ= 0) and 3% (the final state λ= 1). In the second case, the 32-atom wurtzite supercell is employed for the same displacements. The value of the effective polarization is the same in both cases because the quantum of polarization is a constant quantity (see the text for an explication). The effective polarization is indicated by a black double arrow along the branches n=1 and 2.

Relating the formal polarization of the unit cell and supercells:

A follow up question would be: what is the relation between the unit cell and supercell polarizations? Once again we turn to our treatment of the ionic chain, where we have stated that the difference between two values of the polarization lattice coincides with the polarization quantum. Motivated by this, we compute the difference $P_{f,2} - P_{f,1}$, where $P_{f,1}$ is the formal polarization of the 4-atom unit cell and $P_{f,2}$ is that of the 32-atom supercell. We denote the formal polarization of the unit cell with $P_{f,1}$ throughout the examples. The same thing applies to the other properties, namely the lattice constants a_1 and c_1 and the polarization quantum $P_{q,1}$. The reason for this will be described shortly. As for the supercell, its corresponding properties are denoted as $P_{f,2}$, a_2, c_2 and $P_{q,2}$.

The subscripts 1 and 2 indicate that the polarization branches are n= 1 and 2, which characterize the unit cell and supercell, respectively. Also for simplicity, we refrain from explicitly including the state λ in the formal polarization, since the polarization lattice contains formal polarizations of a single state. The formal-polarization difference $P_{f,2} - P_{f,1}$ yields a value of 0.443 C/m². This is not the value of the polarization quantum for the unit cell $P_{q,1}$ calculated previously, so it must be the quantum for the supercell $P_{q,2}$. Indeed, one can use Eq. (III.20) to obtain this value of $P_{q,2}$ by using the lattice parameters of the supercell: $a_2 = 2a_1$, $c_2 = 2c_1$ and $V_{22} = \sqrt{2}(a_2)^2\, c_2/2 = \sqrt{3}(2a_1)^2\, 2c_1/2$:

$$P_{q,2} = \frac{ec_2}{V_{22}} = \frac{2e}{2^2\sqrt{3}{a_1}^2} = \frac{P_{q,1}}{2^2}. \tag{III.22}$$

The polarization quantum of the 32-atom supercell is one fourth the quantum of the unit cell. The formal polarizations are then related by:

$$\begin{aligned} P_{f,2} &= P_{f,1} + P_{q,2} \\ &= P_{f,1} + \frac{P_{q,1}}{2^2}. \end{aligned} \tag{III.23}$$

The number 2 in the denominator indicates that the length of the lattice constant of the unit cell a_1 has increased two times. In general, the lattice constants a_1 and c_1 can be increased n and m times, respectively, resulting in supercells of dimension $n\times n\times m$. In this case $a_n = na_1$, $c_m = mc_1$ and $V_{nm} = \sqrt{3}a_n^2\, c_m/2 = \sqrt{3}(na_1)^2\, mc_1/2$. Then we have:

$$P_{q,n} = \frac{2ec_m}{V_{nm}} = \frac{2e}{n^2\sqrt{3}{a_1}^2} = \frac{P_{q,1}}{n^2}, \tag{III.24}$$

and:

$$\begin{aligned} P_{f,n} &= P_{f,1} + P_{q,n} \\ &= P_{f,1} + \frac{P_{q,1}}{n^2}. \end{aligned} \tag{III.25}$$

Substituting n= 1 in Eq. (III.24) gives the polarization quantum of the unit cell $P_{q,1}$, and this is the reason why the value of n for the unit cell is 1. Eq. (III.25), which gives the lattice of polarization for wurtzite crystals, is a key result of our work. It states that the formal polarization of a wurtzite supercell $P_{f,n}$ is equal to the sum of the formal polarization of the wurtzite unit cell $P_{f,1}$ and the polarization quantum of the supercell $P_{q,n}$ (which is given by the unit-cell quantum $P_{q,1}$ divided by n^2). However, it is crucial to point out that Eq. (III.25) is only true for $n \geq 2$, and does not apply for n= 1. Put in another way, this expression holds for wurtzite supercells, not for the unit cell, and we can write:

$$P_{f,n} = \begin{cases} P_{f,1} & \text{for } n = 1 \\ P_{f,1} + \dfrac{P_{q,1}}{n^2} & \text{for } n \geq 2 \end{cases}. \qquad \text{(III.26)}$$

Nevertheless, we will use Eq. (III.25) in the case of n= 1 in Chapter V to make a correction regarding the spontaneous polarization of wurtzite materials.

We test the validity of Eq. (III.25) once again by computing the polarization of a wurtzite supercell of GaN with dimensions 3×3×3, which corresponds to 108 atoms. Substituting in Eq. (III.25) the unit-cell values of P_f (−0.480 C/m²) and P_q (1.771 C/m²) and setting n= 3, we find that the formal polarization of the 108-atom supercell amounts to −0.283 C/m². Our polarization code (BerryPI, see Sec. III.7) reproduces almost the exact same value, which confirms the validity of equation (III.25). There are two important points worth noting. Firstly, notice that Eq. (III.25) only depends on the dimension of the supercell along the a- and b-directions, i.e. on the integer n. The dimension along the c-direction (or the integer m) has no effect at all. We conclude that different supercells whose lattice constants a_n are enlarged by the same integer n have the same polarization. Consider for example 2×2×2 (32-atom) and 2×2×1 (16-atom) supercells. Even though these supercells are different, their formal polarizations are equal because their dimension in the a-direction is the same [n= 2 in both cases, see Eq. (III.25)]. Secondly, supercells with dimensions 1×1×m (i.e. n= 1), that is, their lattice constant satisfies $a_n = a_1$, have a formal polarization equal to that of the corresponding unit cell ($P_{f,n} = P_{f,1}$). We make use of such supercells in order to model the polarization of wurtzite alloys in Chapter V.

Polarization lattices:

Here, we determine the formal polarization of three wurtzite cells of GaN: the 4-atom unit cell (n=1), the 32-atom supercell (n=2) and the 108-atom supercell (n=3). In Fig. III.6, the first polarization lattice is represented by the data points along the vertical dotted line that passes through ε_u= 0%. In the spirit of Eq. (III.26), and using the values of $P_{f,1}$ and $P_{q,1}$ for $\lambda = \varepsilon_u$= 0%, this lattice is given by −0.480 C/m² for n= 1 and −0.480+1.771/n^2 (in C/m²) for n=2 and 3. Next, the formal polarization of the three wurtzite cells is calculated for ionic displacements from 1% to 5%. The polarization lattices for each displacement state are obtained with the same procedure as for 0%, and correspond to the five vertical lines passing through the respective displacements. For instance, the lattice for $\lambda = \varepsilon_u$= 5 % is −0.670 C/m² for n= 1 and −0.670+1.771/n^2 for n=2 and 3.

Polarization branches:

We now turn our attention towards the polarization branch. In the context of the graphical representation of Fig. III.6, each branch is obtained by fitting the calculated data points for the same cell at different ionic displacements. In the present case the three polarization branches are straight inclined lines, where the branch corresponding to the unit cell (i.e. *n*= 1) is spaced by one polarization quantum from the branches associated with the supercells (*n*= 2 and 3). The polarization quanta of the supercells $P_{q,2}$ and $P_{q,3}$ are represented by double arrows in the figure. It is worth emphasizing that the integer n that specifies the polarization branch also specifies the dimensionality of the wurtzite cell along the a- and b-direction, i.e. a supercell whose dimension is n×n×m corresponds to the polarization branch n.

Care must be taken when computing the effective polarization: the two values of P_f needed to find P_{eff} must be extracted from the same branch. For instance, consider the two data points in the branch *n*= 1 connected by the dashed lines. The displacement between the points is 3%−1%= 2%. The formal polarization changes from −0.518 C/m² to −0.594 C/m², and so the difference in polarization is −0.0760 C/m². This value of the effective polarization is perfectly well-defined because we stick to the same branch (or to the same cell, namely the unit cell). If the point that corresponds to 3% it taken from the branch *n*= 2, the ionic-displacement difference is also 2%, but the polarization difference equals −0.367 C/m². The result of this calculation differs from the previous one and is completely wrong (without physical meaning) because different branches (or different cells) are employed.

It is important to note that differences in polarization along each branch for the same displacements are identical. When displacing the anion from the cation, the lattice parameter a is kept unchanged, implying that the quantum of polarization is constant during the transformation. Graphically, this means that the polarization branches are parallel and are always separated from the first branch by the same amount, namely the polarization quantum, which is equal to 0.443 C/m² for the 32-atom supercell (the red double arrow) and 0.197 C/m² for the 108-atom supercell (the blue double arrow). This finding, that the effective polarization is single-valued and independent from the choice of branch, can be expected from Eqs. (III.18) and (III.25). For wurtzite materials, these two equations are expressed collectively as:

$$\begin{aligned} P_{eff} &= P_{f,n}^{(1)} - P_{f,n}^{(0)} \\ &= P_{f,1}^{(1)} - P_{f,1}^{(0)} + \frac{1}{n^2}\left[P_{q,1}^{(1)} - P_{q,1}^{(0)}\right]. \end{aligned} \tag{III.27}$$

Because the polarization quantum is the same for any initial and final states, $P_{q,1}^{(0)} = P_{q,1}^{(1)}$, and consequently Eq. (III.27) becomes:

$$P_{eff} = P_{f,1}^{(1)} - P_{f,1}^{(0)}, \tag{III.28}$$

for any branch n, where $P_{f,1}^{(0)}$ and $P_{f,1}^{(1)}$ are the formal polarizations of the unit cell that are taken from the first branch. In fact, since the polarization varies linearly with the ionic displacement,

the formal polarization of the initial and final states can be taken from any other branch as long as the displacement variation $\Delta\varepsilon_u$ is the same. That is to say, the effective polarization is -0.0760 C/m² for any ionic-displacement difference of 2 % along any branch. Finally, we emphasize that only six polarization lattices are shown in Fig. III.6, but due to the fitting curves (or the polarization branches) one can draw vertical lines that pass through any displacement state ε_u (e.g. ε_u= 1.5 %, the vertical pink dotted line in Fig. III.6). Hence, while there are only three branches, there are actually an infinite number of lattices.

III.6.2 Strain-induced-polarization

In the second example, we tackle the situation where the polarization quantum varies between states. For that to happen the adiabatic transformation must change not only the ionic positions but also the basal lattice constant a. This is the case of the direct piezoelectric effect. We model this effect by reducing the axial lattice constant c of the wurtzite cells to mimic a compressive uniaxial strain ε_c applied along the c-axis. The lattice parameter a of GaN varies in response to this strain, resulting in a corresponding change in the quantum of polarization [see Eq. (III.21)]. The variation of a is due to a physical phenomenon known as the Poisson effect. For simplicity, we overlook the technical details of the simulation, which can be found in Chapter VI for both the structural and polarization properties.

At equilibrium or zero strain, the polarization quantum as well as the polarization lattice are the same as in the first example for zero ionic displacement. For a compressive strain of -1%, the lattice constant a is 3.24 Å and the quantum equals 1.768 C/m². The lattice is computed to be -0.483 C/m² for n= 1 and $-0.483+1.768/n^2$ for n= 2 and 3. For ε_c= -5%: a= 3.26 Å, P_q= 1.736 C/m² and P_f= -0.532 C/m² for n= 1 and $-0.532+1.736/n^2$ for n= 2 and 3. Notice that since the lattice parameter a changes with strain, the polarization quantum for ε_c= -1% differs from that for ε_c= -5%. In Figure III.7 we show how the formal polarization of wurtzite GaN varies as the strain is applied along the c-axis. As in Fig. III.6, we observe the polarization lattices (vertical dotted lines) and the polarization branches (fitted non-linear curves). A major difference as compared to Fig. III.6 is that the different branches are not equally spaced, which is a natural consequence of the fact that the polarization quantum is not a constant quantity. What can we say about the effective polarization? We take two values of the formal polarization from the same branch and subtract them to obtain P_{eff}. Upon direct inspection of Fig. III.7, we note that different branches result in different polarization differences for the same strains. For this specific case, the effective polarization is given by an expression identical to Eq. (III.27):

$$P_{eff} = P_{f,1}^{(1)} - P_{f,1}^{(0)} + \frac{1}{n^2}\left[P_{q,1}^{(1)} - P_{q,1}^{(0)}\right]. \tag{III.29}$$

Contrary to the first example, $P_{q,1}^{(0)} \neq P_{q,1}^{(1)}$, so that the strain-induced effective (or piezoelectric) polarization depends on the choice of branch n [140]. If we fix the initial and final strain states to 0 and -5%, we find for the branches n= 1, 2 and 3 effective polarizations of -0.0525, -0.0622 and -0.0568 C/m², respectively. These are all equally valid values.

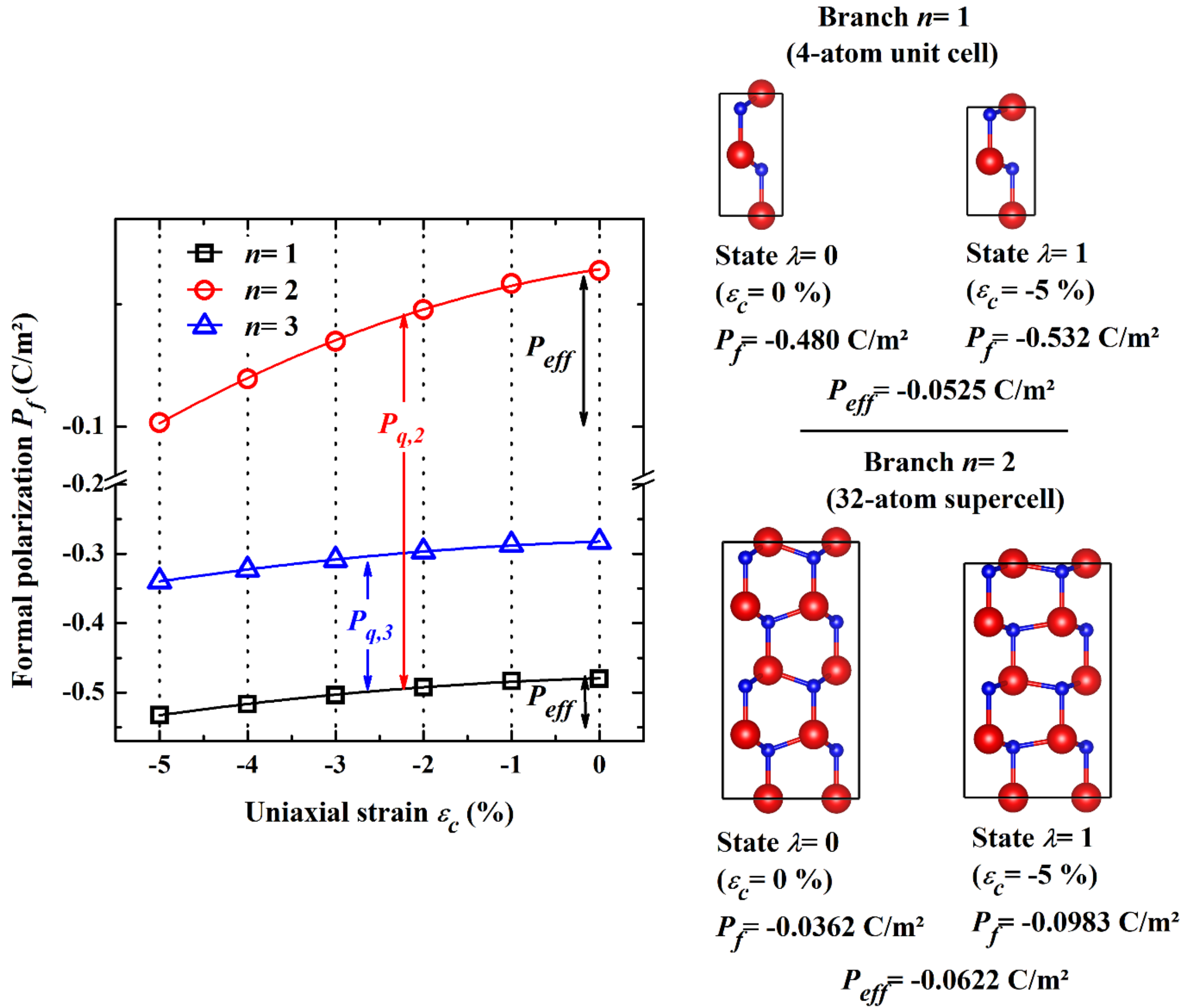

Figure III.7 Formal polarization versus uniaxial compressive strain for wurtzite GaN. Here, the states λ are identified as mechanically distorted structures having different ionic positions and lattice constants a and c. As in the previous example, we distinguish six lattices and three branches, there are however noticeable differences. The polarization branches are non-linear curves obtained by a quadratic interpolation of the data. Due to the fact that the polarization quantum varies with strain, the branches are not parallel as in Fig. III.6. As a result of this, the effective polarization in this case is branch-dependent or multivalued. This is illustrated in the right-side calculation, where the unit cell (branch n= 1) and the 32-atom supercell (branch n= 2) give different values of P_{eff}. According to the Berry-phase formulation, both values are physically true. We set a “break” on the y-axis in order to highlight the inequality of P_{eff} obtained from the first and second branches.

This branch-dependence of the piezoelectric polarization suggests that it is not adequate to use this quantity to quantify the observed piezoelectric behaviour. In practice, the piezoelectric response of materials is usually expressed in terms of the piezoelectric coefficients e_{ij}. The piezoelectric constant defined by Eq. (I.7), which relates polarization and strain, is the *improper* coefficient [140]. There is also the *proper* coefficient, which links the polarization current to an adiabatic (slow) mechanical deformation [140]. Because of this relation with the flow of current, it is the proper piezoelectric constant, not the improper one, that should be compared

to experimental measurements. Thus, while the improper piezoelectric coefficient depends on the polarization branch (i.e. the crystal cell), its proper counterpart has some sort of branch-invariance [140]: it has a single value regardless of the choice of the crystal cell, as expected from a bulk well-defined quantity. A more detailed discussion is available in Refs. [9,26,140].

III.6.3 Interface polarization-induced charge

The third and final example is about the polarization-induced charge at the interface of the wurtzite materials InN (λ= 0) and GaN (λ= 1). We consider the very common situation where the interface lies on the basal (0001) plane. We assume GaN to be the substrate upon which InN is grown along the hexagonal c-axis. Such an interface is shown in Fig. I.3. Furthermore, we assume that the InN layer is strained coherently to the GaN layer, so that both layers have the same lattice constant a. To use the interface theorem [Eq. (I.6)] we need to calculate the formal polarization of relaxed GaN and strained InN with our implementation of the Berry-phase technique. In order to obtain the correct result, we make sure to use the same cell for both crystals. If GaN is modelled by a 2×2×2 supercell, then InN must be modelled by a 2×2×2 supercell as well (or by a 2×2×1 supercell, since both have the same dimensionality along the a-axis, which is 2). This guarantees that we stay on the same polarization branch. Notice that the two material layers have the same quantum of polarization because they are lattice-matched, i.e.$\mathrm{a_{GaN}} = \mathrm{a_{InN}}$. The polarization charge is given by:

$$\sigma = P_{f,1}^{(1)} - P_{f,1}^{(0)}, \tag{III.30}$$

where $P_{f,1}^{(1)}$= -0.480 C/m² is the unit-cell formal polarization of the bottom layer of GaN, and $P_{f,1}^{(0)}$= -0.263 C/m² is the unit-cell formal polarization of the top layer of InN. The predicted polarization charge at the interface of wurtzite InN/GaN is $\sigma = 0.211$ C/m², which corresponds to a charge-carrier concentration of 13.2×10^{13} electrons per cm^2. This value is independent of the choice of polarization branch n due to the cancelation of the polarization quanta.

III.7 BerryPI

The Berry-phase method has offered conclusive insights into polarization phenomena, both as a matter of description and as a powerful computational tool for studying real materials. The theory is now implemented in several popular electronic-structure codes, such as VASP, ABINIT and PWSCF (Quantum ESPRESSO). The package that we use to perform our simulations is WIEN2k [125]. The theoretical background of this code was reviewed in Chapter II, alongside some practicalities of running actual quantum simulations. WIEN2k enables the calculation of the electronic (Berry-phase) and ionic parts of polarization via the software *BerryPI* [141]: a Python-based code developed by Ahmed et *al.* to expand the functionality of WIEN2k.The Berry-phase approach is implemented very efficiently in BerryPI, since the user can evaluate the formal polarization of all kinds of deformed structures. As an example, we use this program to obtain polarization values of mechanically strained crystal structures, which allows the determination of the piezoelectric coefficients.

Figure III.8 illustrates the general scheme used for the computation of polarization in BerryPI. Before running any BerryPI calculation, the studied structures must be first relaxed using WIEN2k. Usually, the structural relaxation is applied to the lattice constants as well as to the atomic positions. Once the relaxed structures are available, we use them as input for BerryPI to evaluate the Berry phase and the corresponding electronic polarization. As we have already explained is Sec. III.3.3, the Berry phase is extracted from the periodic part $u_{n\mathbf{k}}$ of the Bloch-like orbitals. BerryPI accesses the value of the electronic Berry phase φ_{ele} via a discrete version of Eq. (III.10) [12]:

$$\varphi_{ele} = iln \prod_{j} det \left\langle u_{n,\mathbf{k}_j}^{(\lambda)} \middle| u_{m,\mathbf{k}_{j+1}}^{(\lambda)} \right\rangle. \tag{III.31}$$

The integral over the wave vector **k** in Eq. (III.10) is replaced by a multiplication. The number of **k**-vectors in the multiplication is specified by the number of *k*-points, which is the only convergence parameter required to run the calculation. The bra-ket of $u_{n,\mathbf{k}_j}^{(\lambda)}$ and $u_{m,\mathbf{k}_{j+1}}^{(\lambda)}$ is the overlap matrix that mixes the Bloch states at a given **k**. It is sometimes denoted as $\mathbb{S}_{\mathrm{mn}}(\mathbf{k}_j, \mathbf{k}_{j+1})$ where *m* and *n* are two indices referring to occupied bands. The determinant (*det*) of the overlap matrix is calculated by the wien2wannier code [142] integrated in WIEN2k. Note that the result of the product of determinants in Eq. (III.31) is in general a complex number of the form e^{ib}, and the logarithmic function *i ln* extracts its phase *b* which contributes to the total Berry phase φ_{ele} [136]. As for the ionic polarization, it is computed by using the charges and positions of the ions constituting the crystal cell as available in the structure files of WIEN2k [141].

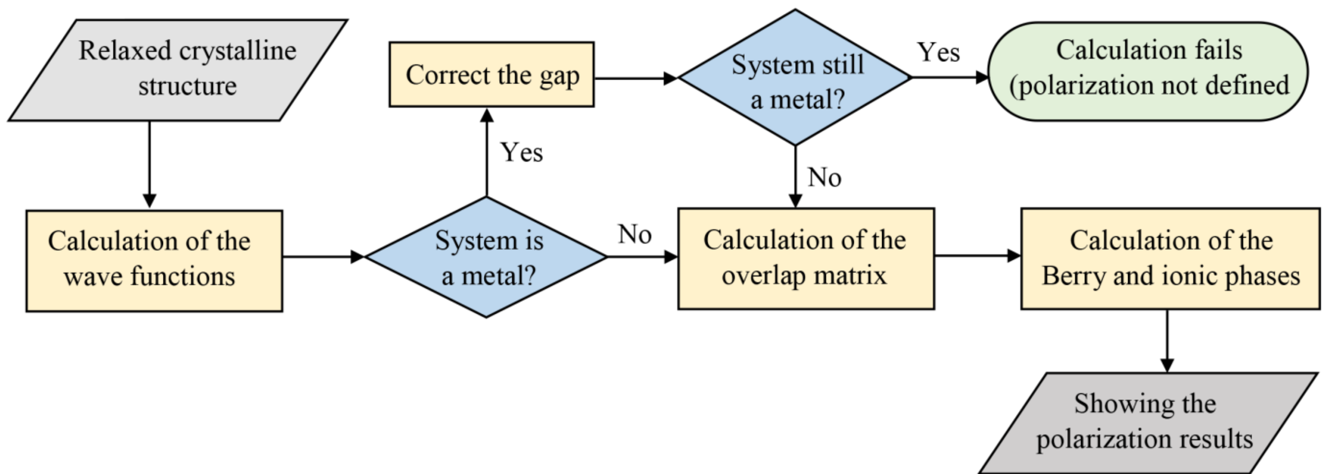

Figure III.8 Flowchart describing the workflow of BerryPI. The workflow includes an error-checking step to detect whether or not the simulated material is a metal. The band gap can be opened via for example the mBJ functional. Not all the steps are performed by BerryPI. The calculation of the crystal wave functions and the gap correction are done using WIEN2k. Also, the calculation of the overlap matrices $\mathbb{S}_{\mathrm{mn}}(\mathbf{k}_j, \mathbf{k}_{j+1})$ are provided by wien2wannier. BerryPI is used to compute the Berry and ionic phases and the corresponding polarizations. The final results are gathered in a single text document.

Materials can only exhibit a dielectric polarization behaviour if they have an electronic band gap [135,136]. If the gap is zero, BerryPI displays a message error notifying a metallic character and the calculation fails. In some cases, when the studied material is suspected to be an insulator or semiconductor, an additional calculation is run by WIEN2k with more sophisticated exchange-correlation functionals to correct for the gap (such as the mBJ functional [113], more details in Sec. II.5.2). If the system is still gapless after this calculation, the material is tagged as metal whose polarization is not defined (in the sense of the Berry-phase method).

Table III.1 Example of an output of a BerryPI calculation obtained following the workflow of Fig. III.8. The case-study is GaN in its equilibrium wurtzite structure. The first table presents the results concerning the electronic phases and polarizations. The results of the ionic phases and polarizations are in the second table. The last table summarizes the final polarization results. To understand the meaning of the coloured highlighted values and how to obtain them we refer the reader to the text.

```
CALCULATION OF ELECTRONIC POLARIZATION
===========================================================================================
Value                             | spin  |    dir(1)     |    dir(2)     |    dir(3)
-------------------------------------------------------------------------------------------
Berry phase (rad)                   sp(1)  [ 4.809741e-07, -1.687360e-07,  3.023780e+00]
Berry phase (rad)                   up+dn  [ 9.619482e-07, -3.374721e-07,  6.047560e+00]
Berry phase wrapped (rad)           up+dn  [ 9.619482e-07, -3.374721e-07, -2.356258e-01]
Electronic polarization (C/m2)      sp(1)  [ 1.671980e-07, -5.865663e-08, -6.666930e-02]
===========================================================================================

CALCULATION OF IONIC POLARIZATION
===========================================================================================
Elem.| Fractional coord.  | spin | Zion |    dir(1)     |    dir(2)     |    dir(3)
-------------------------------------------------------------------------------------------
                                         +------------ Ionic phase (rad) ------------+
Ga  (0.3333, 0.6667, 0.0000)  sp(1) 13.00 [ 2.722714e+01,  5.445427e+01,  0.000000e+00]
Ga  (0.6667, 0.3333, 0.5000)  sp(1) 13.00 [ 5.445427e+01,  2.722714e+01,  4.084070e+01]
 N  (0.3333, 0.6667, 0.3768)  sp(1)  5.00 [ 1.047198e+01,  2.094395e+01,  1.183614e+01]
 N  (0.6667, 0.3333, 0.8768)  sp(1)  5.00 [ 2.094395e+01,  1.047198e+01,  2.754410e+01]
-------------------------------------------------------------------------------------------
Total ionic phase (rad)       sp(1)       [ 1.130973e+02,  1.130973e+02,  8.022095e+01]
Total ionic phase wrap. (rad) sp(1)       [-1.130973e-06, -1.065814e-14, -1.460462e+00]
Ionic polarization (C/m2)     sp(1)       [-1.965765e-07, -1.852511e-15, -4.132313e-01]
===========================================================================================

SUMMARY OF POLARIZATION CALCULATION
===========================================================================================
Value                             | spin  |       X       |       Y       |       Z
-------------------------------------------------------------------------------------------
Electronic polarization (C/m2)      sp(1)  [ 1.447977e-07, -1.422556e-07, -6.666930e-02]
Ionic polarization (C/m2)           sp(1)  [-1.702403e-07,  9.828827e-08, -4.132313e-01]
-------------------------------------------------------------------------------------------
TOTAL POLARIZATION (C/m2)           both   [-2.544260e-08, -4.396735e-08, -4.799006e-01]
===========================================================================================
```

Example of a BerryPI output:

A BerryPI output for a typical calculation of the polarization of wurtzite GaN is shown in Table III.1. First of all, the calculation is done for the ground-state of GaN, which corresponds to the equilibrium values of the lattice constants a and c and the internal parameter u. We start our analysis with the results of the electronic polarization represented in the first table entitled "`CALCULATION OF ELECTRONIC POLARIZATION`". These results are the values of the Berry phase and the corresponding electronic polarization along the three crystallographic directions, i.e. the a-, b- and c-axes.

The first line is the Berry phase as obtained using Eq. (III.31), whose value along the c-axis [dir (3)] is 3.02378 rad (highlighted in yellow). The phase values are always given in terms of 2π [the Berry phase equals $(3.02378/2\pi)$ rad]. The second line gives the spin contribution. Since GaN is non-magnetic, up- and down-spin electrons have the same contribution to the Berry phase. To accounts for the spin degeneracy, the first value of the phase is multiplied by a factor of 2, which yields a value of 6.04756 rad (in blue). The third line is another value of the Berry phase obtained by *wrapping* the second phase value in the range $[-\pi, \pi]$ [141]. Here, wrapping means finding the smallest phase. This can be achieved by taking the tangent of the second phase value, tan(6.04756), which results in -0.24008, and then taking the inverse tangent $\tan^{-1}(-0.24008)$. The new phase of -0.235626 rad (in green) is labeled "Berry phase wrapped" and it is the phase used to calculate the polarization. There is also another wrapping range which is $[0, 2\pi]$. In this case, the second phase value (in blue) does not change and it is the one that is used to compute the electronic polarization. The components of the electronic-polarization vector are given in the last line. The component along the c-axis $P_{ele,z}$ is expressed in terms of the (wrapped) Berry phase $\varphi_{ele,z}$ as [140]:

$$P_{ele,z} = \frac{\varphi_{ele,z}}{2\pi}\frac{ec}{V}, \tag{III.32}$$

In order to find the x- and y-components (respectively $P_{ele,x}$ and $P_{ele,y}$) we use the lattice constant a instead of c and the phases $\varphi_{ele,x}$ and $\varphi_{ele,y}$. By substituting the formula of the cell volume V we obtain:

$$P_{ele,z} = \frac{\varphi_{ele,z}}{2\pi}\frac{2e}{\sqrt{3}a^2}, \tag{III.33}$$

We observe that $P_{ele,z}$ is basically the quantum of polarization multiplied by the Berry phase, that is, $P_{ele,z} = (\varphi_{ele,z}/2\pi)P_q$. From Eq. (III.33), the polarization value (in pink) is found to be -0.0666693 C/m².

The results of BerryPI concerning the ionic polarization of GaN are represented in the second table "`CALCULATION OF IONIC POLARIZATION`". The two cations (Ga) and two anions (N) are listed with their fractional coordinates (x,y,z) and ionic charges Z_{ion}. Next to them is the ionic phase of each ion. It is essential to understand that this phase is not a Berry phase! Ions are treated as classical particles and are not described by wave functions. This ionic phase is rather a "fictitious" phase used to access the ionic part of polarization in analogy with the

electronic part. The ionic phase of an individual ion $\varphi^1_{ion,i}$ along a given direction i is defined as [140]:

$$\varphi^1_{ion,i} = 2\pi Z_{ion}\rho_i, \tag{III.34}$$

where ρ_i is the fractional coordinate of the ion along the studied direction and Z_{ion} is the charge of the ion. The superscript 1 in $\varphi^1_{ion,i}$ indicates that this is the phase of a single ion. The charge is not the atomic number Z, it is given by the number of valence electrons. Thus, the ionic charge of N is 5 rather than of 7, because the outermost shell of this atom contains 5 electrons. The case of Ga is a bit tricky. The Ga atom has 3 valence electrons; however, one usually treats the semicore electrons of the *d* orbitals as valence ones, so that there are 13 valence electrons, not 3, which means that the charge of Ga is 13. For the first N ion, for which $\rho_3 = 0.3768$, Eq.(III.34) gives an ionic phase of 11.83614 rad in the *c*-direction (in yellow). To find the total ionic phase φ_{ion} along a specific direction, we simply sum up the phases of all the ions in that direction. As in the case of the electronic phase, the total ionic phase must be wrapped in the interval $[-\pi, \pi]$. For instance, wrapping the total ionic phase along the *c*-direction (using the tangent function and its inverse) turns 80.22095 rad (in blue) to -1.460462 rad (in green). Finally, the ionic polarization is computed by a formula similar to the one used for the electronic polarization, namely:

$$P_{ion,z} = \frac{\varphi_{ion,z}}{2\pi}\frac{2e}{\sqrt{3}a^2}, \tag{III.35}$$

and its value is -0.413231 C/m² (highlighted in pink). The final polarization data, including the electronic, ionic and total polarization, is summarized in the third table "`SUMMARY OF POLARIZATION CALCULATION`". Each Cartesian component of the total polarization is the sum of the electronic and ionic contributions. Note that all the polarizations shown in the tables are formal ones, as they have been calculated for a single state, namely the equilibrium wurtzite structure of GaN. In order to determine the effective polarization, another BerryPI calculation is performed for a different state of the same cell of GaN to ensure that we stay on the same polarization branch. These results are obtained for the wrapping range $[-\pi, \pi]$. If we work within the other range of $[0, 2\pi]$, we would obtain different phases and formal polarizations, but of course we would find the same effective polarizations. In other words, the effective polarization is independent of the choice of wrapping range. For more information about the execution and workflow of BerryPI, see the original paper By Ahmed et *al.* [125] where the code was introduced for the first time. There is also a GitHub repository (online site) that contains useful tutorials on running basic calculations using both WIEN2k and BerryPI.

III.8 Conclusion

We have devoted this chapter to give a comprehensive account of the Berry-phase theory, which is relevant for defining and calculating the electric polarization of crystalline solids. We first used a one-dimensional model of an ionic crystal to highlight the importance of polarization differences in providing a unique and well-defined value of polarization. Then we demonstrated that when the electronic polarization in concerned, the charge density of electrons (and by

extension their dipole moment) is insufficient to give a bulk definition of the polarization vector (which is by convention a bulk quantity). The Berry-phase formulation solves this issue by shifting from charge to current, because the electric current flows entirely in the bulk of the crystal cell, without any surface contribution.

The concept of current is central in the present theory. As a matter of definition, polarization can be defined in terms of the flow of current when the polarized system evolves between two states under an adiabatic transformation. As a matter of computation, the current is related the phase of the wave function (e.g. if the wave function is real, i.e. without a phase, the associated current is identically zero), which indicates that polarization is also related to the phase. More concretely, the calculation of the components of the polarization vector for a particular state is curried out via the evaluation of the so-called Berry phase of the Bloch orbitals.

A full treatment of polarization properties of solids is only possible via understanding the following terms: polarization lattice, polarization quantum, polarization branch, as well as the formal and effective polarizations. We explained each term separately, first within the simple 1D situation and then within the general case of 3D crystals. This chapter was written in the form of a tutorial, where the theoretical concepts were clarified by specific numerical examples. We emphasized the relevance of the above-mentioned terms in three examples: the polarization induced by an ionic displacement or lattice dynamics, the polarization induced by mechanical strain or piezoelectricity and the electric charge induced by the polarization discontinuity at an interface. Furthermore, we outlined the implementation of the Berry-phase theory, the BerryPI code, used throughout this thesis to simulate the polarized materials. We described the basic workflow and one example of the output of the software. The studied output concerns the formal polarization of the wurtzite unit cell of GaN.

As a closing remark, an alternative approach to study the polarization of solids is based on the concept of the Wannier functions. For each Bloch state $\psi_{n\mathbf{k}}(\mathbf{r})$, there is a corresponding Wannier function $w_{n\mathbf{R}}(\mathbf{r})$ related to it by a Fourier-like transform:

$$
\begin{aligned}
w_{n\mathbf{R}}(\mathbf{r}) &= \frac{V}{(2\pi)^3}\int e^{-i\mathbf{k}.\mathbf{R}}\psi_{n\mathbf{k}}(\mathbf{r})d\mathbf{k} \\
&= \frac{V}{(2\pi)^3}\int e^{i\mathbf{k}.(\mathbf{r}-\mathbf{R})}u_{n\mathbf{k}}(\mathbf{r})d\mathbf{k},
\end{aligned}
\tag{III.36}
$$

where we used Eq. (III.9) to express $w_{n\mathbf{R}}(\mathbf{r})$ in terms of the periodic part $u_{n\mathbf{k}}(\mathbf{r})$. Note that the Wannier function is labeled by an energy band n and real-space lattice vector $\boldsymbol{R}$. Contrary to the Bloch functions which are delocalized plane waves, the Wannier functions are localized in space. This locality is a direct consequence of the Fourier transform. Because of their localized nature, the Wannier wave functions can be used to map the continuous electronic charge density into single point charges located at specific positions in the unit cell, provided that these positions are evaluated as the expectation value of the position operator $\mathbf{r}$ with respect to the Wannier functions. The resulting positions are called the *Wannier centers* $\bar{\mathbf{r}}_{n\mathbf{R}}$ and are given by [136]:

$$\bar{\mathbf{r}}_{n\mathbf{R}} = \int w^*_{n\mathbf{R}}(\mathbf{r})\mathbf{r}w_{n\mathbf{R}}(\mathbf{r})d\mathbf{r}. \qquad \text{(III.37)}$$

The integral is curried out over the unit cell, and the asterisk symbol (*) refers to the complex conjugate. Eq. (III.37) is written within the position representation; we can equally rewrite it in the momentum (or wave vector) representation by setting the position operator to be equal to $\mathbf{r} = \nabla_{\mathbf{k}} = -i\partial/\partial\mathbf{k}$ (notice that the dimension of $\nabla_{\mathbf{k}}$ is length). Doing this and substituting the expression of $w_{n\mathbf{R}}(\mathbf{r})$ [Eq. (I.36)] we obtain [134]:

$$\bar{\mathbf{r}}_{n\mathbf{R}} = \frac{iV}{(2\pi)^3}\int e^{-i\mathbf{k}.\mathbf{R}}\langle u_{n\mathbf{k}}|\nabla_{\mathbf{k}}|u_{n\mathbf{k}}\rangle d\mathbf{k}, \qquad \text{(III.38)}$$

where in this case we calculate the integral within the first Brillouin zone. For a rigorous proof of the transition from Eq. (III.37) to Eq. (III.38) see Ref. [143]. The reader will remark the striking similarity between the expression of the Wannier center, equation (III.38), and the Berry-phase formula, equation (III.11)! In fact, The Berry phase φ can be regarded as giving the position of the Wannier center $\bar{\mathbf{r}}$ [140]. Once we have the Wannier centers in the unit cell, which are a set of positions locating the "point" electronic charge, we can compute the (formal) electronic polarization in the same fashion used for the ionic one; that is, as a sum over charges times their positions (where the positions are $\bar{\mathbf{r}}_{n\mathbf{R}}$) [134]:

$$\mathbf{P}_{\mathrm{ele}} = \frac{1}{V}\sum_n e\bar{\mathbf{r}}_{n\mathbf{R}}. \qquad \text{(III.39)}$$

The sum is taken over all occupied bands n since the electrons in each band contribute to the polarization. The subtleties concerning the multivaluedness of the formal and effective polarizations are also present in the Wannier-functions formulation, where the counterpart of the polarization quantum $e\boldsymbol{R}/V$ is the Wannier-center quantum $\boldsymbol{R}$. In other words, the Wannier center is only defined modulo a Bravais lattice vector $\boldsymbol{R}$ [136]. To summarize, the polarization of an insulating or semiconducting crystal is calculated through the Berry phase of the Bloch orbitals, or through the Wannier centers of the localized Wannier functions. The question is then whether these two alternative strategies give the same computational results. The answer to this question is a resounding yes. Noel et *al.* [144] implemented both schemes to calculate polarization properties of wurtzite ZnO and BeO, they obtained essentially the same values and the same level of agreement with the experimental data. As we have stated previously, our work here is based entirely on the Berry-phase method, without any reference to the Wannier functions.

Part II

Simulation results and discussion

Chapter IV

Spontaneous polarization of wurtzite III-nitrides and II-oxides: The trigonal structure as a reference

IV.1 Introduction

Due to their intrinsic low symmetry, wurtzite crystals are characterized by the existence of a built-in electric polarization, called spontaneous polarization, which persists even in equilibrium [42]. The spontaneous polarization manifests itself as bound charges and internal electric fields in the layers of heterostructures, significantly affecting the properties and performance of semiconductor devices [145], such as light-emitting diodes, lasers, high-mobility transistors and other nanostructured systems [146]. Experimental measurements of the spontaneous polarization are very limited, simply because such measurements are too challenging [66]. Part of this difficulty is due to the fact that ordinary wurtzite crystals are pyroelectrics: the orientation of their polarization is fixed and cannot be reversed. In ferroelectrics, on the other hand, application of a sufficiently intense electric field switches the polarization vector. This polarization-reversal effect allows an accurate measurement of the spontaneous polarization and is the basis of many important applications [63]. Except for some III-nitrides and II-oxides, no direct determination for the spontaneous polarization is available, and the experimental values for the majority of wurtzite materials are still unknown. Because of this, theoretical calculations are currently used to provide polarization values in order to interpret the results of experiments and for device modelling.

The theoretical framework in which the polarization of solids is studied is the Berry-phase method, developed in the 90s by Resta, Vanderbilt and King-Smith [12,13]. This method is based on two fundamental insights. First, only polarization differences between two states are accessible and rigorously defined, experimentally as well as theoretically. Second, the difference in polarization is directly related to a quantum geometric phase of the electronic wavefunctions known as the Berry phase [102]. In the specific case of the spontaneous polarization, the two states correspond to a non-centrosymmetric structure (wurtzite in the present case) and its high-symmetry counterpart, also referred to as the *reference* structure [135,136]. For materials crystallizing in the wurtzite phase, the cubic zincblende structure (space group $F\bar{4}3m$ or 216) has been used in the literature as a reference to calculate the spontaneous polarization [15,144,147,148]. Some authors have employed the ideal wurtzite structure as a reference [9,149], and recent studies show that the layered-hexagonal structure should be used instead of zincblende to compute the spontaneous polarization differences between different wurtzite materials [26]. This is outside the scope of the present chapter and will be addressed in Chapter V.

In this chapter, we propose the *trigonal* structure as another reference in terms of which the spontaneous polarization of wurtzite crystals is defined. We show that the values that result using this reference are extremely close to those obtained by zincblende. Because of their importance in modern technology, the binary III-nitrides AlN, GaN and InN and II oxides BeO

and ZnO are chosen as case studies to elucidate the equivalence between the two reference structures in determining the spontaneous polarization of wurtzite compounds. In addition, we decompose the polarization into purely electronic and ionic components, and find that the first component is dominant. The rest of the chapter is organized as follows. In Section IV.2, we describe the wurtzite and trigonal structures, and provide the numerical details of the simulation. Section IV.3 presents the results of the chapter: Sections IV.3.1 and IV.3.2 deal with the structural optimization needed to perform the polarization calculations. In Section IV.3.3, the formal polarization of the zincblende, trigonal, wurtzite and ideal wurtzite structures is studied. Section IV.3.4 gives the spontaneous polarization values referenced to the trigonal structure and compares them with the values obtained by zincblende. In Section IV.3.5 we discuss the electronic and ionic contributions to polarization. We explore in Section IV.3.6 how the spontaneous polarization varies with the internal strain. Finally, in section IV.4 a conclusion is drawn which summarizes our main results. The material in this chapter is based on our paper: Benbedra et *al.*, Physica B 667, 415183 (2023).

IV.2 Theoretical approach

IV.2.1 Wurtzite and trigonal structures

The wurtzite structure has a hexagonal Bravais lattice (space group $P6_3mc$ or 186) with four atoms per unit cell and two lattice constants: the edge length *a* of the hexagon base and the height *c* of the hexagonal prism. Furthermore, there is a third structural degree of freedom, a dimensionless internal parameter *u* that characterizes the cation-anion bond length parallel to the *c*-axis [148]. The wurtzite unit cell is illustrated in Figure IV.1 (*a*). The cations occupy (1/3,2/3,0) and (2/3,1/3,1/2) positions, while the anions are located at (1/3,2/3,*u*) and (2/3,1/3,*u*+1/2).

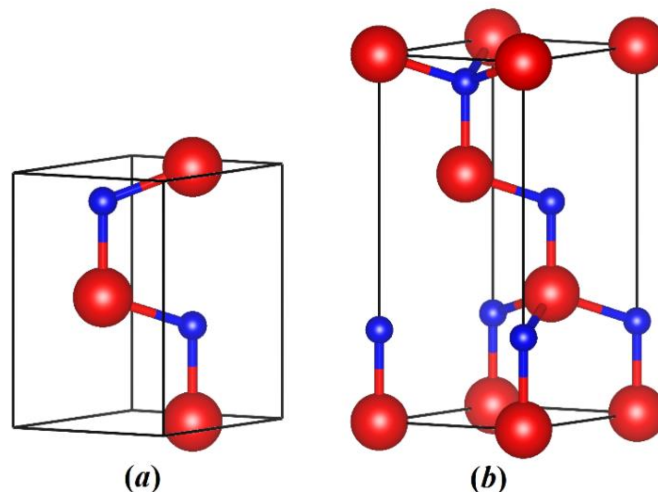

Figure IV.1 Unit cell of the (*a*) wurtzite and (*b*) trigonal structures. Both structures are tetrahedrally bonded, but they differ in the stacking sequence of atomic planes: AB for wurtzite and ABC for trigonal. Red and blue spheres correspond to cations and anions, respectively. More than 6 atoms (4 atoms) are shown in the trigonal (wurtzite) unit cell due to periodic boundary conditions.

Figure IV.1 (*b*) shows the unit cell of the trigonal structure (*P*3*m*1 or 156). It has a hexagonal-like unit cell (i.e. the lattice angle γ= 120°) containing six atoms. The positions of the cations are (0,0,0), (1/3,2/3,1/3) and (2/3,1/3,2/3), and those of the anions are (0,0,1/4), (1/3,2/3,7/12) and (2/3,1/3,11/12). We point out that the trigonal crystal structure is similar to zincblende in two different ways: (i) the bonding is tetrahedral with the four bonds having the same length, and (ii) the stacking of atomic planes is in the sequence ABC along the [111] (for zincblende) or [001] (for trigonal) direction, which is in opposition to the wurtzite system, where the stacking is AB along [0001]. Because of these similarities, the trigonal structure is said to be identical to zincblende but with a different space group, and is sometimes referred to as the six-atom [111]-oriented zincblende structure [55]. In fact, one can obtain the trigonal structure by rotating the zincblende unit cell around its diagonal [111] axis as shown in Figure IV.2 [55]. The corresponding rotation matrix $\mathbb{M}$ is:

$$\mathbb{M} = \begin{pmatrix} 0.5 & 0 & 1 \\ 0 & 0.5 & 1 \\ -0.5 & -0.5 & 1 \end{pmatrix}. \tag{IV.1}$$

This rotation matrix can be implemented in the software VESTA [56] and is used to transform the lattice vectors $\mathbf{R}^{\mathrm{ZB}}$ and atomic positions $\mathbf{P}^{\mathrm{ZB}}$ of zincblende to those of the trigonal structure $\mathbf{R}^{\mathrm{T}}$ and $\mathbf{P}^{\mathrm{T}}$ via the expressions:

$$\begin{aligned} R_i^T &= \sum\nolimits_j M_{ij} R_j^{ZB}, \\ P_i^T &= \sum\nolimits_j M_{ij} P_j^{ZB}. \end{aligned} \tag{IV.2}$$

Our major finding is that the trigonal structure is well suited for the derivation of the spontaneous polarization of wurtzite materials, yielding similar values as the ordinary zincblende phase.

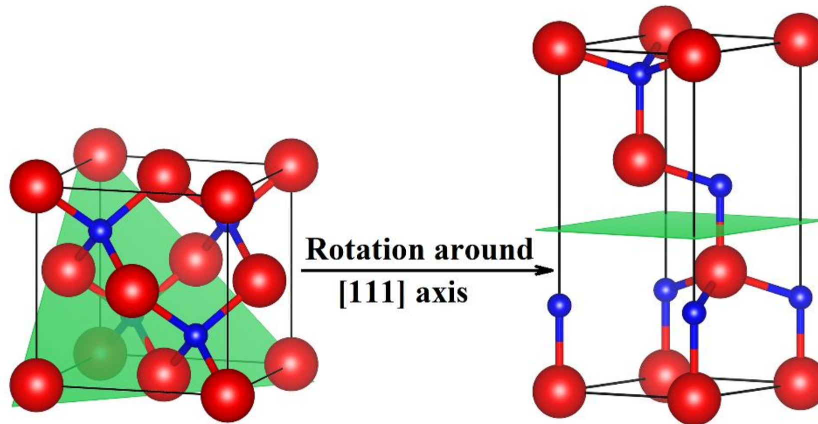

Figure IV.2 Unit cell of the zincblende (left) and trigonal (right) structures. The trigonal cell is obtained by rotating the zincblende one around the main cubic diagonal [111] by the matrix of Eq. (VI.1). The said rotation transforms the (111) plane of zincblende to the (001) plane of the trigonal system (both planes are shown in green in their respective cells).

IV.2.2 Computational details

The first-principles results presented in this work are obtained using density functional theory (DFT) [100,105] within the framework of the Kohn-Sham (KS) algorithm [106] as incorporated in the code WIEN2k [125]. The exchange-correlation contribution to the total energy is described by the combination of the generalized gradient approximation [110] and the modified Becke-Johnson approach [113] (GGA+mBJ). To solve the KS equations we rely on the full-potential linearized augmented plane wave (FP-LAPW) method [150], which is explained in detail in Chapter II.

In our study the development on atomic orbitals is up to a maximum angular momentum l_{max}= 10, and a cutoff of $R_{MT}^{min}K_{max}$= 8.5 is used for the plane wave expansion [118], where R_{MT}^{min} is the radius of the smallest muffin-tin sphere (that of Be, see below), and K_{max} represents the norm of largest wave vector. Our value of $R_{MT}^{min}K_{max}$ corresponds to an expansion cutoff of 500 eV. For energy calculations, the tetrahedron method is employed to perform the integration of the KS equations over the Brillouin zone by taking a dense mesh of 1000 k-points (a uniform sampling of 10×10×10) [128]. These values of the expansion cutoff and k-points are found to be enough for the convergence of the total energy, electric charge and atomic forces to an accuracy of about 10^{-4} Ry, $10^{-3}e$ (where e is the electron charge) and 10^{-4} Ry/Bohr, respectively.

The FP-LAPW method is an all-electron technique, meaning it considers all electrons self consistently in a full-potential treatment. The core electrons are fully confined within the muffin-tin spheres while valence electrons are not. The radii R_{MT} of these atomic spheres for different elements are chosen as follows: 1.5, 1.8, 2, 2.1, 1.6, 1.4, and 2.05 Bohr for N, Al, Ga, In, O, Be and Zn, respectively. We take the borderline to distinguish between core and valence electrons to be −6 Ry, i.e. all orbitals with an energy more negative than this value are core states.

The computation of polarization properties is carried out via the code BerryPI [141], which allows to calculate the electronic and ionic contributions to polarization. The electronic part is evaluated as a Berry phase of the cell-periodic Bloch-like functions [135,136]. For the sake of consistency and maintaining the same degree of convergence, we kept the number of k-points in BerryPI the same as in total-energy calculations.

IV.3 Results and discussion

IV.3.1 Structural optimization of the wurtzite structure

A. Lattice constants and the internal parameter:

In order to determine the spontaneous polarization for each material, two structures must be carefully prepared. These are the wurtzite and the trigonal reference structures. The determination of the structural properties is done by means of a total-energy minimization process [151]. As mentioned previously, hexagonal wurtzite unit cells have three degrees of freedom (a, c and u), so three energy calculations should be performed, one for each structural

parameter. To evaluate the equilibrium values of the lattice constants a and c, a self-consistent calculation of the total energy for several cell volumes $V\,(= \sqrt{3}a^2\,c/2)$ and lattice constant ratios c/a is performed. Such calculations are initialized and repeated until the convergence criteria mentioned in Sec. IV.2.2 are verified. For the purpose of illustration, we plot in Figure IV.3 the volume- and c/a-variations of energy for GaN, our prototype of a nitride, and for ZnO, our prototype of an oxide. The curve of $E(V)$ [Fig. IV.3 (1)] is obtained by fitting the calculated data to the Murnaghan equation of state [152]:

$$E(V) = E_0 + \frac{BV}{B'}\left[\frac{1}{B'-1}\left(\frac{V}{V_0}\right)^{B'} + 1\right] - \frac{BV_0}{B'-1}, \tag{IV.3}$$

where V_0 and E_0 are the volume and energy of the unit cell at equilibrium, respectively. B represents the bulk modulus and B' is the first derivative of B with respect to hydrostatic pressure. On the other hand, the curve of $E(c/a)$ [Fig. IV.3 (2)] is obtained from a fit to a fourth order polynomial of the form:

$$E\left(\frac{c}{a}\right) = k_0 + k_1\left(\frac{c}{a}\right) + k_2\left(\frac{c}{a}\right)^2 + k_3\left(\frac{c}{a}\right)^3 + k_4\left(\frac{c}{a}\right)^4, \tag{IV.4}$$

with the k's being fitting parameters representing the numerical coefficients of the polynomial. In order to determine both lattice constants one extracts the volume V_0 and ratio $(c/a)_0$ that minimize the total energy, then uses the following formulae:

$$a = \left[\frac{2V_0}{\sqrt{3}(c/a)_0}\right]^{1/3}, \qquad c = a(c/a)_0. \tag{IV.5}$$

The internal parameter u is obtained by the relaxation of atomic sites according to the Hellman-Feynman theorem [153], which involves computing the derivative of total energy with respect to the z-coordinate of the anion (N for the nitrides and O for the oxides).

Table IV.1 Calculated equilibrium lattice constants a and c, the internal parameter u (in units of c) and the bulk modulus pressure derivative B' within the GGA functional for wurtzite AlN, GaN, InN, BeO and ZnO.

Material	a (Å)		c (Å)		u		B'	
	Our work	Exp.	Our work	Exp.	Our work	Exp.	Our work	Exp.
AlN	3.13	3.11[a]	5.02	4.50[a]	0.381	0.382[a]	4.01	-
GaN	3.23	3.19[a]	5.25	5.19[a]	0.376	0.377[a]	4.55	-
InN	3.59	3.54[a]	5.79	5.70[a]	0.379	-	4.60	-
BeO	2.72	2.70[b]	4.41	4.38[b]	0.378	0.378[b]	4.31	-
ZnO	3.29	3.25[c]	5.28	5.21[c]	0.381	0.383[c]	4.45	-

[a] Ref. [154], [b] Ref. [155], [c] Ref. [156]

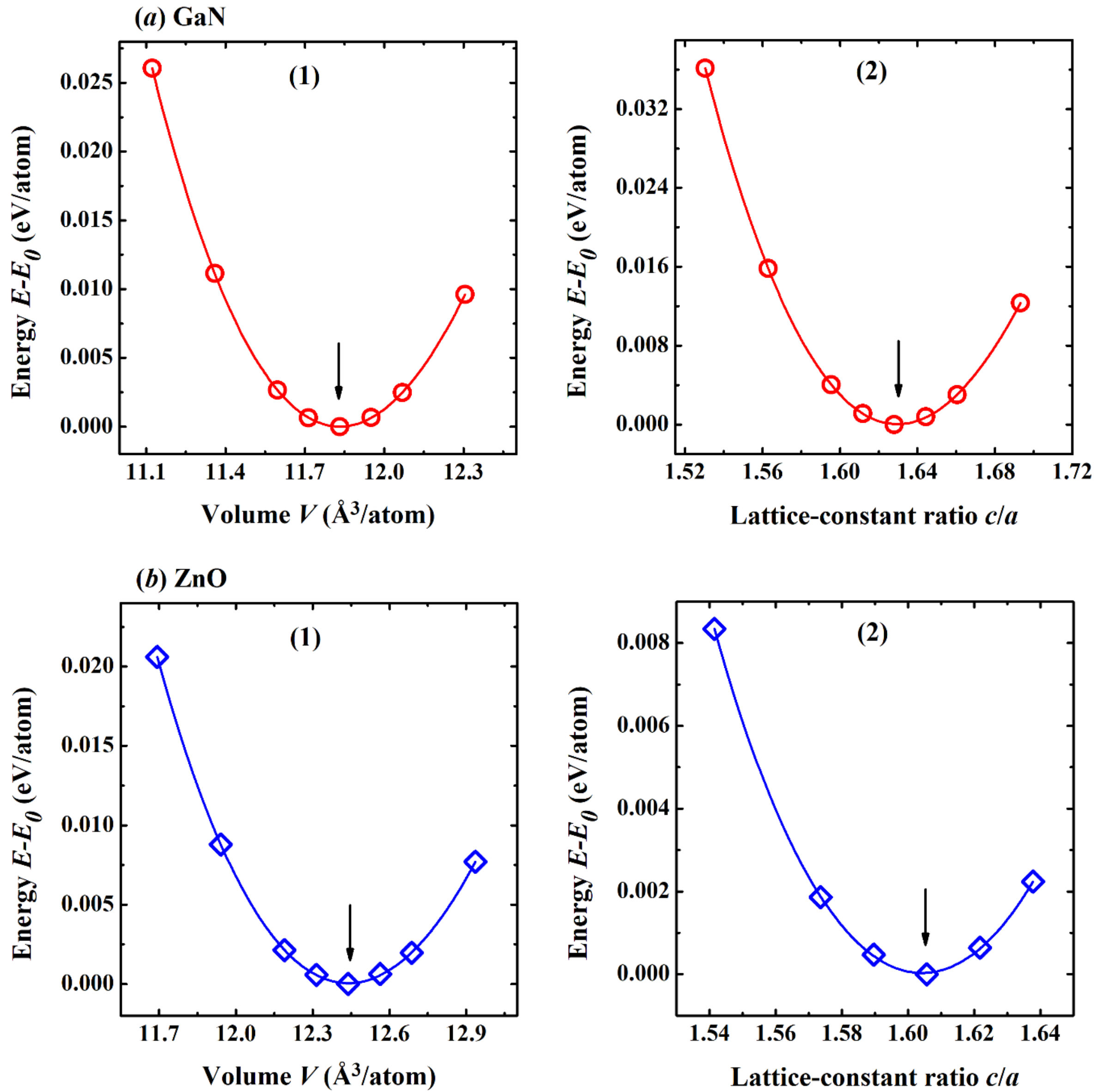

Figure IV.3 Total energy of wurtzite (*a*) GaN and (*b*) ZnO as a function of (1) unit-cell volume and (2) lattice-constant ratio *c/a*. For each case, the energy scale is shifted by the minimum value E_0 (indicated by an arrow). The curves in (1) are a fit to the Murnaghan equation and those in (2) are a fit to a 4th order polynomial.

The results of the structural optimization are shown in Table IV.1 for each wurtzite compound. We find an overall agreement between our calculated values and those obtained by experiment. As expected, the values of the lattice constants a and c obtained by GGA tend to be higher than those obtained experimentally [154–156]. The relative differences are only about 1%, which is typical for well-converged DFT calculations. Our theoretical internal parameters agree very well with the experimental ones. For all wurtzite crystals, u is slightly greater than the ideal value 0.375. The calculated B' are found to be around 4, which is in accordance with the general rule that the values of B' remain lesser than 5 for most crystals studied so far [157].

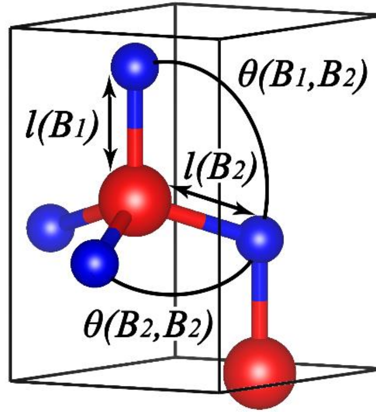

Figure IV.4 Wurtzite unit cell illustrating the lengths of the different bonds connecting the cations (in red) and anions (in blue) and the angles between them. The length of the single bond B_1 along the c-axis is $l(B_1)$, and that of the three bonds B_2 in the basal or c-plane is $l(B_2)$. The angle between the bonds B_1 and B_2 and that between the two bonds B_2 is $\theta(B_1, B_2)$ and $\theta(B_2, B_2)$, respectively.

B. Bond lengths and interbond angles:

There are two other important (and often overlooked) structural parameters of crystalline solids, namely the bond lengths and the interbond angles. As we have mentioned previously in Sec. I.5.1, the wurtzite structure has two types of first-neighbour anion-cation bonds [61]. As shown in Figure IV.4, one bond B_1 along the c-axis with a length $l(B_1)$ given by:

$$l(B_1) = uc, \tag{IV.6}$$

and three bonds B_2 in the basal plane whose length $l(B_2)$ is:

$$l(B_2) = \sqrt{\frac{1}{3}a^2 + \left(\frac{1}{2} - u\right)^2 c^2}. \tag{IV.7}$$

In addition to the first-neighbour bonds, there exists three types of second-neighbour cation-anion bonds which we choose to ignore in this study. The angle between the bonds B_1 and B_2 is denoted as $\theta(B_1, B_2)$ and the angle between two basal bonds B_2 is $\theta(B_2, B_2)$ [158] (see Fig. IV.4):

$$\theta(B_1, B_2) = \frac{\pi}{2} + arccos\left\{\left[1 + 3\left(\frac{c}{a}\right)^2\left(\frac{1}{2} - u\right)^2\right]^{-\frac{1}{2}}\right\}, \tag{IV.8}$$

$$\theta(B_2, B_2) = 2arcsin\left\{\left[\frac{4}{3} + 4\left(\frac{c}{a}\right)^2\left(\frac{1}{2} - u\right)^2\right]^{-\frac{1}{2}}\right\}. \tag{IV.9}$$

The values of the bond lengths and angles of our wurtzite crystals calculated using equations (IV.6-IV.9) are listed in Table IV.2. We also provide the values of these quantities from the literature for comparison. Our results are consistent with those of Ref. [158]. For both nitrides and oxides (and apparently any binary wurtzite crystal), the bond linking the cation and anion

along the c-axis (B_1) is just a little bit longer than the bonds in the basal plane (B_2). If we put in Eqs. (IV.6) and (IV.7) the ideal values of the internal parameters u= 3/8= 0.375 and the lattice constant ratio c/a= $\sqrt{8/3} \approx 1.633$, we find that the two types of bonds are of the same length, i.e. $l(B_1) = l(B_2)$. It also follows from Eqs. (IV.8) and (IV.9) that for the ideal values of u and c/a, the interbond angles are equal and independent of the lattice parameters a, c and u. Hence, for the ideal wurtzite structure $\theta(B_1, B_2) = \theta(B_2, B_2) = 109.5°$.

Table IV.2 First-neighbour bond length $l(B_1)$ and $l(B_2)$ as well as bond angles $\theta(B_1, B_2)$ and $\theta(B_2, B_2)$ for AlN, GaN, InN, BeO and ZnO in the (real) wurtzite structure.

Material	$l(B_1)$ (Å)		$l(B_2)$ (Å)		$\theta(B_1, B_2)$ (°)		$\theta(B_2, B_2)$ (°)	
	Our work	Exp.	Our work	Exp.	Our work	Exp.	Our work	Exp.
AlN	1.913	1.907[a]	1.903	1.890[a]	108.30	108.19[a]	110.68	110.73[a]
GaN	1.975	1.971[a]	1.974	1.955[a]	109.25	109.17[a]	109.75	109.78[a]
InN	2.194	2.00[a]	2.188	2.185[a]	108.69	108.69[a]	110.31	110.24[a]
BeO	1.667	-	1.660	-	108.92	-	110.08	-
ZnO	2.012	-	2.001	-	108.31	-	110.67	-

[a] Ref. [158]

IV.3.2 Structural optimization of the trigonal structure

It is not necessary to fully optimize the geometry of the trigonal structure, because its lattice constants are related to those of the relaxed wurtzite structure. According to the zincblende-trigonal transformation matrix discussed above, the in-plane and out-of-plane lattice constants for the trigonal system are, respectively, a and $a\sqrt{6}$, with a being the wurtzite in-plane lattice constant.

The trigonal lattice constant c can also be obtained from the lattice constant ratio as follows. The ideal hexagonal ratio c/a equals $\sqrt{8/3}$. Since the trigonal phase has three atomic layers [see Fig. IV.1 (b)], and the thickness of one layer is $0.5c$ [159], the trigonal ratio c/a is simply $1.5\sqrt{8/3}$. With a bit of algebra, the trigonal lattice constant c is given by c= $a\sqrt{6}$ (where a is again the wurtzite in-plane lattice constant). We report in Table IV.3 the values of the trigonal lattice parameters. Note that the internal parameter of the trigonal structure becomes an "ideal" position and is fixed to 0.25 for all the materials studied.

Table IV.3 Lattice constants a and c and the internal parameter u (in units of c) of AlN, GaN, InN, BeO and ZnO in the trigonal structure. The values of the trigonal lattice constants are obtained from the wurtzite in-plane lattice constant a as explained in the text.

Material	a (Å)	c (Å)	u
AlN	3.13	7.67	0.25
GaN	3.23	7.91	0.25
InN	3.59	8.79	0.25
BeO	2.72	6.65	0.25
ZnO	3.29	8.06	0.25

IV.3.3 Formal polarization

Conceptually, we distinguish two types of polarization within the Berry-phase scheme. First we have the formal polarization P_f, which is the polarization of a single structure. The other type is the effective polarization P_{eff} defined as the difference, on the same polarization branch n, between the formal polarization of two different structures [136]. For initial (0) and final (1) structures with formal polarizations $P_{f,n}^{(0)}$ and $P_{f,n}^{(1)}$, P_{eff} is given by:

$$P_{eff} = P_{f,n}^{(1)} - P_{f,n}^{(0)}. \qquad \text{(IV.10)}$$

We stress that this difference, not the formal polarizations by themselves, is the quantity of interest [135,136]. The effective polarization coincides with the spontaneous or piezoelectric polarizations, or it can be related to quantities such as the piezoelectric coefficient, the Born effective charge or the interface bound charge, which are all measurable quantities.

A. Components of the formal polarization vector:

In this section we study the formal polarization of the zincblende, trigonal and wurtzite structures. We deal with the effective (spontaneous) polarization of the wurtzite phase in the next section. A crystalline structure is said to be centrosymmetric (that is, it has a centre of inversion) if its formal polarization is zero. At first sight, zincblende may seem centrosymmetric because of its cubic symmetry. However, there are alternating layers of positive and negative ions along the [111] axis, which give rise to a dipole moment in that direction. The symmetry operations (such as rotations and reflections) constrain the formal polarization of zincblende P_{ZB} to be calculated by the following expression [38]:

$$P_{ZB} = \frac{\sqrt{3}ea_{ZB}}{4V_{ZB}}, \qquad \text{(IV.11)}$$

where a_{ZB} is the cubic lattice constant and V_{ZB} is the volume of the zincblende unit cell. The factor $a_{ZB}\sqrt{3}/4$ is the separation between the cation and anion in zincblende, and multiplying this separation by the electron charge e gives the corresponding dipole moment. It is more convenient for us to work with the in-plane lattice constant of the wurtzite structure a_{WZ} (to avoid geometry optimization of the zincblende structure). The wurtzite equivalent of a_{ZB} is $\sqrt{2}a_{WZ}$ [60]. Given that the zincblende volume is $a_{ZB}^3/4$, we can rewrite Eq. (IV.11) as [26]:

$$P_{ZB} = \frac{\sqrt{3}e}{2a_{WZ}^2}. \qquad \text{(IV.12)}$$

The formal polarization of zincblende only depends on the lattice constant a_{WZ} and has nothing to do with chemical identification of the constituent atoms. We are not aware of the existence of a similar expression of the formal polarization of the trigonal (P_T) and wurtzite (P_{WZ}) phases, but because the ionic layers in both systems are, respectively, along the [001] and [0001] we expect their polarization to be parallel to these directions, as will be confirmed by explicit calculations shortly.

Table IV.4 Cartesian components P_x, P_y and P_z (given in C/m²) of the formal polarization associated with the zincblende, trigonal and wurtzite structures of AlN, GaN, InN, BeO and ZnO. The calculation of P_x and P_y for the trigonal and wurtzite polarizations give a value of 10^{-4} and 10^{-8} C/m², respectively, which we consider to be zero compared to P_z (0.5-1 C/m²).

Material	Zincblende			Trigonal			Wurtzite		
	P_x	P_y	P_z	P_x	P_y	P_z	P_x	P_y	P_z
AlN	0.817	0.817	0.817	0	0	−0.471	0	0	−0.558
GaN	0.767	0.767	0.767	0	0	−0.445	0	0	−0.480
InN	0.621	0.621	0.621	0	0	−0.360	0	0	−0.406
BeO	1.081	1.081	1.081	0	0	−1.255	0	0	−1.299
ZnO	0.739	0.739	0.739	0	0	−0.846	0	0	−0.893

Once the zincblende, trigonal and wurtzite structures are prepared, we perform a self-consistent field (SCF) calculation to determine the wavefunctions, from which the values of the formal polarizations P_{ZB}, P_T and P_{WZ} are evaluated with the software BerryPI [141]. The Cartesian components of the formal polarization vector P_x, P_y and P_z for the three phases and for the five materials studied are presented in Table IV.4. The in-plane x and y components of P_T and P_{WZ} vanish, which is consistent with the symmetry of the hexagonal and trigonal structures. For P_{ZB}, the three components are non-zero and equal, consistent again with the cubic symmetry.

B. Full formal polarization vector:

We turn our attention to the vector of the formal polarization. The trigonal and wurtzite formal polarizations simply equal the only non-vanishing component, which is P_z. In the case of zincblende, for which there are three non-zero components, we extract the value of the formal polarization via the norm $\sqrt{P_x^2 + P_y^2 + P_z^2}$, or simply $\sqrt{3}P_z$. The results are summarized in Table IV.5. The zincblende values are almost identical to those predicted by Eq. (IV.12), which validates the accuracy of our implementation of the Berry-phase theory.

Table IV.5 Formal polarization of III-nitrides and II-oxides in the zincblende, trigonal and wurtzite structures. These values are extracted from the Cartesian components of Table IV.4. The values of the wurtzite polarization quantum $P_{q,WZ}$ calculated via Eq. (IV.13) are also shown.

Materials	P_{ZB}	P_T	P_{WZ}	$P_{q,WZ}$
AlN	1.414	−0.471	−0.558	1.886
GaN	1.328	−0.445	−0.480	1.771
InN	1.075	−0.360	−0.406	1.434
BeO	1.873	−1.255	−1.299	2.497
ZnO	1.280	−0.846	−0.893	1.707

C. Relation between the zincblende and trigonal polarizations:

We observe from Table IV.5 that the formal polarization of zincblende (P_{ZB}) is different from that of the trigonal (P_T) structure. Since both the zincblende and trigonal systems can be used

as a reference to access the spontaneous polarization of wurtzite compounds, it is interesting to establish a relation between their formal polarizations. To begin with, we compute the polarization difference $P_{ZB} - P_T$ for GaN, we find a value of 1.771 C/m². This figure happens to be the quantum of polarization $P_{q,WZ}$ for the unit cell of wurtzite GaN, which is given by ec_{WZ}/V_{WZ}, where c_{WZ} is the lattice constant in the direction of the polar c-axis and V_{WZ} is the volume of the wurtzite unit cell. Using the formula of V_{WZ} allows $P_{q,WZ}$ to be written as:

$$P_{q,WZ} = \frac{2e}{\sqrt{3}a_{WZ}^2}. \tag{IV.13}$$

We have already presented this formula in the beginning of Sec. III.6. The wurtzite polarization quanta of the nitrides and oxides are shown in the last column of Table IV.5. From the value of the difference $P_{ZB} - P_T$, we conclude that the zincblende formal polarization is equal to the sum of the trigonal formal polarization and the wurtzite polarization quantum:

$$P_{ZB} = P_T + P_{q,WZ}. \tag{IV.14}$$

We can interpret this equation in terms of the polarization lattice discussed in detail in the previous chapter. But first we demonstrate that the quantum of polarization of the wurtzite structure, $P_{q,WZ}$, is equal to the quantum of polarization of the trigonal structure, $P_{q,T}$. The expression of the latter is ec_T/V_T, where c_T and V_T are the trigonal lattice constant and cell volume. Knowing that the volume of the trigonal unit cell is $V_T = \sqrt{3}a_T^2 c_T/2$ and the lattice constant in the basal plane $a_T = a_{WZ}$ we have:

$$P_{q,T} = \frac{ec_T}{V_T} = \frac{ec_T}{\sqrt{3}a_T^2 c_T} = \frac{2e}{\sqrt{3}a_{WZ}^2} = P_{q,WZ}. \tag{IV.15}$$

Eq. (IV.14) can be rearranged as (with replacing $P_{q,WZ}$ by $P_{q,T}$):

$$P_T = P_{ZB} - P_{q,T}. \tag{IV.16}$$

This formula is similar to Eq. (III.25), and can be interpreted as follows: the trigonal and zincblende formal polarizations are separated by the trigonal polarization quantum, meaning both polarizations P_{ZB} and P_T belong to the same polarization lattice. Equation (IV.14) [or (IV.16)] is very accurate for the nitrides, but this is not quite the case for the oxides, in the sense that the discrepancy between the results of the wurtzite (or trigonal) polarization quantum obtained from Eqs. (IV.13) and (IV.14) is about 25% for both BeO and ZnO.

The zincblende structure has a formal polarization along the main diagonal [111], so one could think that there exists a spontaneous polarization, but this is not true. Zincblende has a cubic symmetry, which means there are four main diagonals with eight [111] equivalent directions (crystallographically speaking they form the <111> family of directions) and it is not possible to have a special direction for the spontaneous polarization, i.e. there is no single polar axis. Therefore zincblende has no inversion symmetry but it is also a non-polar structure. This symmetry argument also applies to the trigonal structure, since it is just zincblende rotated

around the [111] axis by the matrix of Eq. (IV.1). It is only the wurtzite phase which is truly spontaneously polarized along the preferred polar direction [0001] or the *c*-axis [63].

D. Formal polarization of ideal wurtzite:

For completeness, we also calculate the formal polarization of the ideal wurtzite structure. This structure is obtained by setting the internal parameter u and the lattice constant ratio c/a of the wurtzite structure to 3/8 and $\sqrt{8/3}$, respectively (see Sec. I.5.2). The results of this calculation, including the three Cartesian components of the formal polarization and its total value P_{IWZ}, are gathered in Table IV.6 for all our compounds. We notice that the ideal wurtzite formal polarization is always smaller than its wurtzite counterpart. We conclude that the non-ideality of the real wurtzite phase increases its polarization.

Table IV.6 Polarization values (in C/m²) of AlN, GaN, InN, BeO and ZnO crystallizing in the ideal wurtzite structure. Like the real wurtzite phase, the formal polarization equals the *z*-component.

Materials	P_x	P_y	P_z	P_{IWZ}
AlN	0	0	−0.503	−0.503
GaN	0	0	−0.462	−0.462
InN	0	0	−0.385	−0.385
BeO	0	0	−1.000	−1.000
ZnO	0	0	−0.862	−0.862

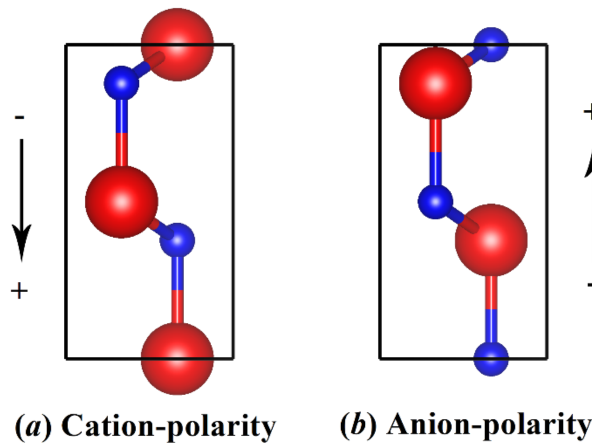

Figure IV.5 Two polarities of the wurtzite system: (*a*) cation and (*b*) anion polarities. The formal polarizations of both polarities are equal but point in opposite directions as indicated by the arrows. The anion-polarity unit cell is made by switching the positions of the cation (in red) and anion (blue) of the cation-polarity unit cell.

E. Wurtzite polarity:

Finally, we discuss the polarity of the wurtzite crystal structure, which affects the orientation of polarization. For wurtzite materials, there are two types of polarities, namely cation polarity and anion polarity. The polarization vector points to the $[000\bar{1}]$ direction (negative *z*-component)

for the cation polarity and to [0001] (positive z-component) for the anion polarity [63,158]. For both polarities, the polarizations have the same absolute value but opposite signs. In this work we always adopt the conventional choice of the cation polarity, as evidenced by the negative value of the wurtzite formal polarization in Table IV.5. Figure IV.5 shows a two-dimensional schematic of a wurtzite unit cell with the two reversed polarities. We calculate for wurtzite GaN the formal polarization P_{WZ} of the anion-polarity structure shown in Fig. IV.5 (*b*) and find it equal to 0.480 C/m², which has the opposite sign of the reported value in Table IV.5 for the cation polarity.

IV.3.4 Spontaneous polarization

In the present study, the calculation of the spontaneous polarization is done by computing the difference between the formal polarization of the wurtzite and trigonal structures:

$$P_{sp,T} = P_{WZ} - P_T, \tag{IV.17}$$

where WZ and T denote the wurtzite and trigonal polarizations, respectively. The index T in $P_{sp,T}$ means that the spontaneous polarization is referenced to the trigonal structure. We use in this chapter the wurtzite and trigonal unit cells to run the simulation. For this reason, Eq. (IV.17) should be expressed as:

$$P_{sp,T} = P_{WZ,1} - P_{T,1}, \tag{IV.18}$$

where the subscript 1 indicates that the wurtzite and trigonal formal polarizations are calculated for the respective unit cells, which corresponds to the polarization branch n= 1. If supercells of dimension n along the a- and b-directions are employed (branch n), Eq. (IV.18) becomes:

$$P_{sp,T} = P_{WZ,n} - P_{T,n}. \tag{IV.19}$$

Of course, the wurtzite and trigonal supercells must have the same dimensionality n to insure that we are on the same polarization branch, otherwise the calculation is wrong. Notice that since the two unit cells have different number of atoms (4 and 6 atoms for the wurtzite and trigonal systems respectively), supercells of the same dimensionality do not contain the same number of atoms. For example, a 2×2×2 wurtzite supercell has 32 atoms, while 48 atoms are contained within a 2×2×2 trigonal supercell. From Eqs. (II.25) and (III.27), we can write Eq. (IV.19) in the following way:

$$P_{sp,T} = P_{WZ,1} - P_{T,1} + \left(P_{q,n,WZ} - P_{q,n,T}\right), \tag{IV.20}$$

where $P_{q,n,WZ}$ and $P_{q,n,T}$ are the quantum of polarization of the wurtzite and trigonal supercells, respectively. It is important to recall that this expression is only valid for $n \geq 2$. We have shown in Section IV.3.3C that $P_{q,WZ} = P_{q,T}$. Because of this, Eq.(IV.20) reduces to Eq.(IV.18). This has the implication that the spontaneous polarization is independent of the polarization branch (the integer n), which is fully consistent with the experimental fact that the spontaneous polarization is an intrinsic property of solids, i.e. it has a single unique value. If the above

discussion is unclear, it is highly recommended to revise Sec. III.6 of Chap. III, particularly the discussion of the polarization lattice and branch in the first two examples.

In Table IV.7 we list the values of the formal polarization as well as the effective spontaneous polarization $P_{sp,T}$ for both the nitrides and oxides obtained with respect to the trigonal reference, together with the results of previous calculations that are based on cubic zincblende $P_{sp,ZB}$ for the sake of comparison.

Table IV.7 Berry-phase results of electric polarization (in C/m²) for AlN, GaN, InN, BeO, and ZnO in the wurtzite phase. The spontaneous polarization $P_{sp,T}$ is the difference between the formal polarizations P_{WZ} and P_T as described by Eq. (IV.17). Results from previous calculations that used the zincblende structure as a reference are listed for comparison.

Material	P_T	P_{WZ}	$P_{sp,T}$	Other calc. of $P_{sp,ZB}$
AlN	−0.471	−0.558	−0.087	−0.090 [a]
GaN	−0.445	−0.480	−0.035	−0.034 [a]
InN	−0.360	−0.406	−0.046	−0.042 [a]
BeO	−1.255	−1.299	−0.044	−0.036 [b], −0.045 [c]
ZnO	−0.846	−0.893	−0.047	−0.057 [b], −0.032 [d]

[a] Ref. [160], [b] Ref. [144], [c] Ref. [148], [d] Ref. [161]

We observe that wurtzite III-nitrides and II-oxides are highly polarized: their spontaneous polarization is quite large, only one order of magnitude smaller than that of typical ferroelectrics [53]. The spontaneous polarization referenced to the trigonal structure has a negative sign and is non-zero only along the c-axis, which corresponds to the $[000\bar{1}]$ direction. That is to say, the spontaneous polarization is directed from the anion to the cation (cation polarity). This is expected since the intrinsic asymmetry of the bonding is parallel to this specific direction. The magnitude of the spontaneous polarization of the nitrides increases with the non-ideality of the wurtzite phase, or with the size of the difference $u-3/8$ [162], where 3/8 is the value of the internal parameter for the ideal wurtzite structure. As such, the increase of $P_{sp,T}$ is from GaN to InN and AlN. Indeed, AlN has the most distorted structure with respect to the ideal tetrahedral configuration (with the highest u and the smallest c/a), and hence its spontaneous polarization is the largest among the tetrahedrally bonded compounds considered in this work. The same behaviour is observed for the oxides, with ZnO being more polarized than BeO.

It is worth emphasizing that when AlN and InN are constrained to have the lattice parameters (a, c, u) of GaN, the spontaneous polarization of the three materials is rather similar: we obtained a spontaneous polarization equal to −0.0349 C/m² for AlN and −0.0359 C/m² for InN, to be compared with the GaN value of −0.0350 C/m². The same trend is also observed for BeO, for which $P_{sp,T}$ is calculated at the lattice constants and atomic positions of ZnO. This result suggests that electric polarization is a geometric property, and that differences in polarization in real materials result primarily from the relaxation of the lattice parameters (especially the internal parameters) [149].

A. Comparison between the trigonal and zincblende references:

As can be readily seen from the data in Table IV.7, our values derived using the trigonal structure are in very good agreement with the values reported in the literature obtained with zincblende, i.e. $P_{sp,T} \approx P_{sp,ZB}$. This agreement holds extremely well for the nitrides. On the other hand, there is a moderate scatter in the theoretically determined spontaneous polarizations for the oxides. However, our results are within the range of the values reported in the literature. We have therefore verified that the trigonal and zincblende reference structures provide almost similar values when the spontaneous polarization of wurtzite crystals is concerned.

B. Spontaneous polarization of ideal wurtzite:

We have discussed the spontaneous polarization of the wurtzite structure, but what can we say about this quantity for the ideal wurtzite structure? It is often stated (e.g. in Ref. [163]) that the nitrides and oxides in the ideal wurtzite phase have a vanishing spontaneous polarization. This statement is a direct result of Eq. (I.14): when the internal parameter u equals its ideal value 3/8, the model equation gives a zero polarization. In order to check the validity of this claim, we compute the spontaneous polarization of the materials studied crystalizing in the ideal wurtzite phase following the same procedure, namely (the bar symbol indicates ideal wurtzite geometry):

$$\bar{P}_{sp,T} = P_{IWZ} - P_T. \tag{IV.21}$$

The values of P_{IWZ} and P_T are taken from Tables (IV.5) and (IV.6), respectively. The ideal wurtzite and trigonal formal polarizations in Eq. (IV.21) are not equal, which yields a non-zero $\bar{P}_{sp,T}$. Thus, the statement of a vanishing spontaneous polarization for the ideal wurtzite structure is actually incorrect. This point has been highlighted for the first time by Zoroddu et *al* [164]. The Berry-phase results of the spontaneous polarization in the ideal structure are −0.032 C/m² for AlN, −0.017 C/m² for GaN, −0.025 C/m² for InN, −0.021 C/m² for BeO and −0.016 C/m² for ZnO. These values are lesser than those for the real (non-ideal) wurtzite structure by a factor of 2 to 3. Quoting Zoroddu et *al.* [164]: “This confirms the intuitive idea that non-ideality, and especially changes in u, can increase polarization substantially, and indicates that an accurate determination of the structure is mandatory to obtain reliable polarization values”.

C. Failure of WIEN2k when using the zincblende reference:

At this stage there is an important point to elaborate. The cubic lattice constant a_{ZB} used to obtain the reported values of $P_{sp,ZB}$ is always fixed to the in-plane lattice constant a_{WZ} of the wurtzite structure for the same material [26]. We, however, could not calculate the structure of zincblende for which $a_{ZB} = a_{WZ}$. This deserves a special comment. We think that this impossibility is related to how WIEN2k works. We present in Figure IV.6 a cubic zincblende unit cell where $a_{ZB} = a_{WZ}$. For clarity, we refrain from showing the other atoms. By inspecting this figure, we see that the anion and cation are overlapping and penetrate each other. The code we use (WIEN2k) is based on the augmented plane wave (APW) method, which is not tolerate against such overlapping [118]. Indeed, when initiating the calculation for this structure the

code shows an error message and the simulation cannot be done (see the figure caption for some technical details).

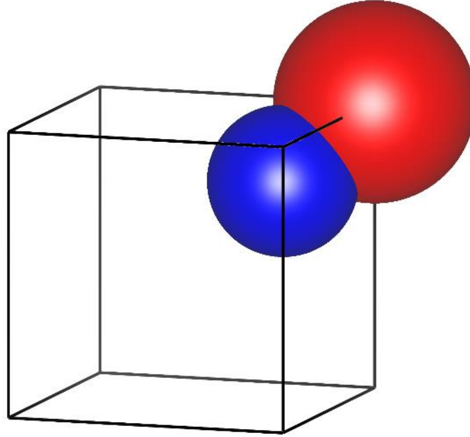

Figure IV.6 Cubic zincblende unit cell contains only two atoms instead of eight. This example is for GaN, where a_{WZ}= 6.10 Bohr. The atomic (muffin-tin) radius is 2 and 1.5 Bohr for Ga and N, respectively. The sum of these radii is 3.5 Bohr, and the separation between the two atoms is $a_{WZ}\sqrt{3}/4$= 2.64 Bohr. Because the radii of Ga and N sum up to a value greater than their separation, the cation and anion penetrate each other, preventing the energy and polarization calculation of the system. Reducing the atomic radii would not solve this problem: the overlapping vanishes for unphysically small radii.

IV.3.5 Electronic and ionic polarizations

In the Born-Oppenheimer approximation, electric polarization can be decomposed into two distinct terms [135,136]:

$$P_{sp,T} = P_{sp,T}^{ele} + P_{sp,T}^{ion}, \tag{IV.22}$$

where $P_{sp,T}^{ele}$ and $P_{sp,T}^{ion}$ are the electronic and ionic contributions to the spontaneous polarization, respectively. As we have explained in Chap. III, the Berry-Phase method is only used to evaluate the electronic part of polarization, and has nothing to do with the determination of the ionic part. This is because electrons are described by quantum wavefunctions, while ionic cores are treated as classical point charges [30]. To provide further insight into understanding the origin of the strong polarization in wurtzite crystals, we compute each term separately as the difference between the electronic and ionic formal polarizations of the wurtzite and trigonal structures:

$$\begin{aligned} P_{sp,T}^{ele} &= P_{WZ}^{ele} - P_{T}^{ele}, \\ P_{sp,T}^{ion} &= P_{WZ}^{ion} - P_{T}^{ion}. \end{aligned} \tag{IV.23}$$

The calculated contributions using the trigonal phase as a reference are given in Table IV.8.

Table IV.8 Calculated electronic (*ele*) and ionic (*ion*) formal and spontaneous polarizations (in C/m²) for each crystal studied. P_T^{ele} is of the order of 10^{-4} C/m², smaller than P_{WZ}^{ele} by a factor of 1000, so it is set to zero.

Material	P_T^{ele}	P_{WZ}^{ele}	$P_{sp,T}^{ele}$	P_T^{ion}	P_{WZ}^{ion}	$P_{sp,T}^{ion}$
AlN	0	−0.211	−0.211	−0.471	−0.347	0.124
GaN	0	−0.066	−0.066	−0.444	−0.413	0.031
InN	0	−0.102	−0.102	−0.360	−0.304	0.056
BeO	0	−0.143	−0.143	−1.256	−1.157	0.099
ZnO	0	−0.166	−0.166	−0.851	−0.652	0.119

The trigonal electronic polarization is zero for all materials. It has been stated elsewhere that the contribution of electrons vanishes for zincblende [26], and we have shown that this is also the case for the trigonal structure. We note that the electronic and ionic terms are of opposite sign. Specifically, the electronic part is negative while the ionic one is positive. This sign alternation seems typical for all tetrahedrally bonded materials. In addition, they have different magnitudes, with the electronic term being the largest, resulting in a negative value of the total polarization. One can safely anticipate, as remarked by Ahmed et *al.* [141], that in non-polar crystals the absolute value of each of the terms is roughly the same, so that they tend to cancel each other, yielding zero net polarization. In contrast, this cancellation is much less effective in wurtzite compounds, which is the reason of their large polarization. Notice that the $P_{sp,T}$ values shown in the fourth column of Table IV.7 can also be obtained as the sum of $P_{sp,T}^{ele}$ and $P_{sp,T}^{ion}$.

IV.3.6 Dependence of polarization on the internal parameter

We now investigate the linearity of the spontaneous polarization as a function of the internal parameter u. For this purpose, the spontaneous polarization is evaluated for internal strains ε_u ranging from 0 to 5%. The internal strain is introduced by displacing the anion (N and O) away from the cation (Al, Ga, In, Be and Zn) in the same manner used in Sec III.6.1. It is given by the variation:

$$\varepsilon_u = \frac{u - u_0}{u_0}, \qquad \text{(IV.24)}$$

where u_0 is the equilibrium internal parameter and $u > u_0$. The hexagonality of the structure is held constant throughout the calculation, since u can take on different values without altering the symmetry of the unit cell.

The results of this investigation are depicted in Figure IV.7. The polarization is generally largest in AlN, smallest in ZnO, and intermediate in BeO, GaN and InN. The spontaneous polarization is observed to vary linearly and remains linear over the entire range of internal strains. The same result was previously obtained in the case of ferroelectric perovskites [165,166], which makes this kind of linearity a general feature of systems exhibiting a spontaneous polarization.

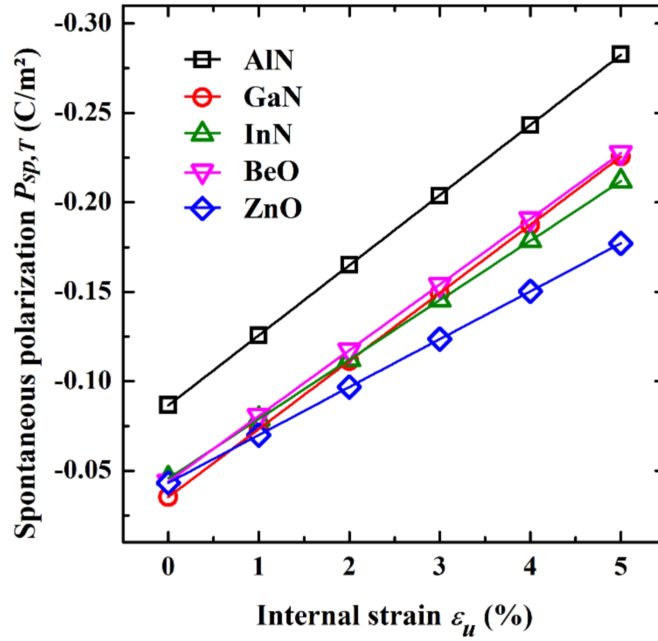

Figure IV.7 Internal-strain dependence of the spontaneous polarization for wurtzite nitrides and oxides. The lattice constants a and c are fixed to the equilibrium values and the internal parameter u is changed gradually up to 5%. The $P_{sp,T}$ values at zero strain correspond to those listed in Table IV.7. The curves result from a linear regression of the calculated data.

IV.4 Conclusion

In this chapter, we built a complete description of the spontaneous polarization for binary wurtzite III-nitrides (AlN, GaN and InN) and II-oxides (BeO and ZnO). The spontaneous polarization was computed as the difference between the polarization of the wurtzite and trigonal structures. The latter structure is a rotated version of cubic zincblende. Before presenting the polarization results, we undertook an energy-based structural optimization for the wurtzite phase of the materials studied. This was done by determining the lattice constants, the internal parameter, the bond lengths and the interbond angles.

Next, we calculated the formal polarization of the wurtzite, trigonal, zincblende and ideal wurtzite structures for both the nitrides and oxides, we also discussed the two wurtzite polarities. The main finding of this chapter is the values of the spontaneous polarization of wurtzite AlN, GaN, InN, BeO and ZnO referenced to the trigonal structure. We uncovered many results concerning this property. Our values obtained with the trigonal reference are practically equal to those referenced to zincblende, implying that both references can be used to access the spontaneous polarization of wurtzite compounds. We argued that since the functionality of our code WIEN2k is based on the APW approach, the trigonal structure is the one should be used as a reference, not zincblende. This is because the atomic muffin-tin spheres overlap in zincblende, which renders the calculation unfeasible.

We found that the magnitude of the spontaneous polarization increases with the tetrahedral distortion; that is, with the difference between the real-wurtzite internal parameter and its ideal

value 3/8. In order to understand the microscopic origin of the spontaneous polarization of wurtzite crystals, we computed the electronic and ionic contributions to polarization. Both terms have opposite signs with the electronic term being the largest in absolute value. This finding confirms the fact that the spontaneous polarization in this type of materials result from the partial cancelation of the electronic and ionic polarizations. Another finding is the linear dependence of the spontaneous polarization with the anion-cation displacement, also known as the internal strain.

Chapter V
Polarization properties of wurtzite III-nitride alloys

V.1 Introduction

The experimental determination of polarization properties is hindered by several factors, in particular the screening by surface charges and low crystal quality of the samples [66,167]. A fruitful alternative is to rely on calculations that provide polarization values which can be used in device design and analysis. The theoretical framework to carry out this kind of calculation is the Berry-phase approach [12,13]. In order to calculate the spontaneous polarization of a crystalline solid a reference structure is needed [135,136]. For wurtzite materials, such a reference has been invariably chosen to be the cubic zincblende structure [15,144,147,148] (or, as we have demonstrated in the previous chapter, the trigonal structure).

In an important paper [26], Dreyer et *al.* have demonstrated that zincblende is not an appropriate reference to compute spontaneous polarization differences that give rise to bound charges and electric fields in heterostructure layers. Contrary to the widespread belief, zincblende is not centrosymmetric, in the sense that it has a non-vanishing formal polarization along the [111] direction [26,38]. A consistent determination of polarization differences requires a centrosymmetric reference structure with zero polarization, which in the case of wurtzite systems turns out to be the layered-hexagonal structure, whose space group is P_3/mmc or 194, also known as hBN structure-type. [26]. The latter structure can be obtained by an increase of the internal structural parameter from u= 0.37-0.39 of the wurtzite structure to u= 0.5 [26]. Thus, whenever polarization differences between two wurtzite layers are considered, the computation of the spontaneous polarization of each layer should be performed using the layered-hexagonal structure, not zincblende. The same reasoning does not apply to the strain-induced piezoelectric polarization, because (as will be discussed later on) the piezoelectric response of wurtzite materials has nothing to do with the nature of the reference structure.

The hexagonal structure has been used to study the spontaneous polarization of wurtzite nitride binaries AlN, GaN, InN [26] and BN [168]. More recently, studies have relied on this reference to calculate the same quantity of wurtzite nitride alloys, namely ScAlN [169], BAlN and BGaN [170]. The work of Bernardini and Fiorentini [171] was the first one where the spontaneous polarization of the technologically important III-nitride alloys AlGaN, InGaN and InAlN could be theoretically accessed with zincblende being the reference. To our knowledge, however, there have not been any previous calculations of the spontaneous polarization of these alloys with respect to the layered-hexagonal structure.

Motivated by this gap, we report in this chapter a consistent set of composition-dependent values of electric polarization properties for the wurtzite ternary alloys $Al_xGa_{1-x}N$, $In_xGa_{1-x}N$ and $In_xAl_{1-x}N$ as well as the quaternary alloy $Al_xIn_yGa_{1-x-y}N$. Both spontaneous $P_{sp}(x)$ and piezoelectric $P_{pz}(x)$ polarizations are addressed over the entire range of alloy composition x, where the spontaneous polarization is referenced to the hexagonal structure. In order to access

the piezoelectric term of polarization, we apply a biaxial strain on the alloys studied by perfectly lattice-matching them to an underlying GaN substrate, which corresponds to the common situation in epitaxial growth experiments [171,172]. We compare the hexagonal-referenced values of the spontaneous polarization to those obtained by the trigonal structure and show that the two sets of results are very different in terms of magnitude, sign and the degree of composition non-linearity. In addition to this, we provide the polarization charge density $\sigma(x,y)$ for the $Al_xIn_yGa_{1-x-y}N$/GaN heterostructure. We demonstrate that a suitable choice of alloy concentrations x and y can lead to an effective reduction of the strong polarization fields across this system, thereby improving the efficiency of optoelectronic AlInGaN-based devices. We also provide the interface polarization charge $\sigma(x)$ of $Al_xGa_{1-x}N$/GaN, $In_xGa_{1-x}N$/GaN and $In_xAl_{1-x}N$/GaN fully consistent with the procedure for $Al_xIn_yGa_{1-x-y}N$/GaN. We thoroughly compare these values to previous simulations and experiments and find a good agreement, validating both our results and methodology.

After this introduction, an overview of the theoretical approach, including the choice of supercells and numerical details of the simulation, is presented (Section V.2). Next, we present the results of the structural and polarization properties and a detailed description of the approach required to calculate them. First we report the values of the spontaneous and piezoelectric polarizations of the ternary nitride alloys AlGaN, InGaN and InAlN (Section V.3 and V.4). Then we present the results of the interface polarization charge of the quaternary nitride alloy AlInGaN/GaN (Section V.5). We establish the accuracy of our calculations via comparing the interface polarization charge of the ternary alloys to results from the literature (section V.6). Finally, the conclusions of the chapter are summarized at the end (section V.7). The content of this chapter has appeared previously in the main text and supplementary material of our paper: Benbedra et *al*., ECS J. Solid State Sci. Technol. 12, 103008 (2023).

V.2 Theoretical approach

V.2.1 Supercells structure

In order to model the alloys of interest, we proceed in the following way. Starting with a wurtzite unit cell, we extend the periodicity along the c-axis while retaining it along the a- and b-directions, turning the 4-atom unit cell into a 16-atom supercell (i.e. 1×1×4 supercell). Then, the different compositions are realized by substituting different atoms in the cation sites. For $Al_xGa_{1-x}N$ and $In_xGa_{1-x}N$, we substitute a corresponding number of Ga atoms with Al and In atoms, respectively. As for $In_xAl_{1-x}N$, Al is substituted by In. 16-atom supercells are found to be adequate to compute polarization properties in wurtzite alloys [161,170].

The Al and In contents x (or the alloy concentration) are defined as the ratio N_i/N, where N_i is the number of the incorporated atoms and N is the total number of the original substituted atoms. N= 8 for our 16-atom supercells, and we choose N_i= 0, 2, 4, 6 and 8, which results in concentrations x= 0, 0.25, 0.5, 0.75 and 1, respectively. The values of Al content x and In content y in the quaternary alloy $Al_xIn_yGa_{1-x-y}N$ are limited by the constraint $0 \leq 1 - x - y \leq 1$, any combination of x and y that violates this constraint cannot be considered. In this way we obtain five values of x and y ranging from 0 to 0.5, corresponding to 25 combinations of x and y. The

layered-hexagonal supercells are constructed from the wurtzite ones by moving the anions into the plane of the cations (so that the internal parameter u= 0.5) [26,173], resulting in a centrosymmetric structure with zero formal polarization, as will indeed be confirmed by explicit calculations. The adopted supercells of some of the alloys are shown in two-dimensional representation in Figure V.1.

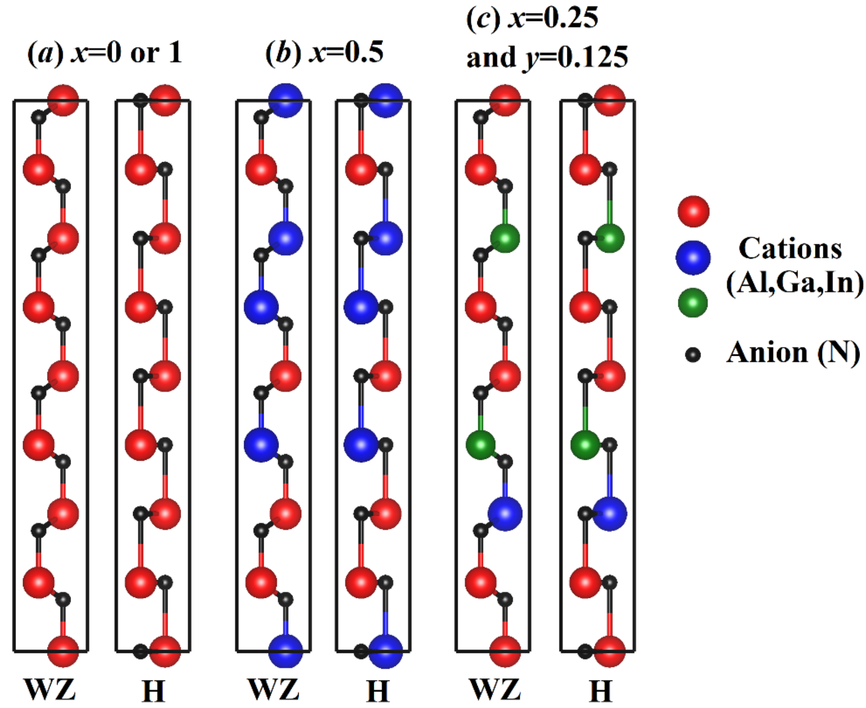

Figure V.1 16-atom supercells in the wurtzite (WZ) and hexagonal (H) structures used in this work to model the III-nitride alloys. (a) Pure binaries, i.e. the composition x= 0 or 1, (b) ternary alloy with x= 0.5 and (c) quaternary alloy having x= 0.25 and y= 0.125. The different coloured spheres represent the cations Ga, In and Al (red, blue and green) and the anion N (black). These supercells are constructed by extending the unit cell four times in the c-direction without changing it in the a- and b- directions.

V.2.2 Calculation details

Density-functional theory [100,116] calculations are performed using a linear augmented plane wave (LAPW) basis set [119,150] implemented in the WIEN2k code [125]. The generalized gradient approximation (GGA) of Perdew, Burke and Ernzerholf is used for the exchange-correlation potential [110]. The GGA functional predicts In-containing alloys to be metals for high In contents [174], preventing the calculation of their polarization. To surmount this difficulty we treat the exchange-correlation potential using the Tran and Blaha modified Becke-Johnson (mBJ) approximation [113], which provides more accurate and reliable results for the band gap. The cutoff parameters for the Kohn-Sham wavefunctions l_{max} and $R_{MT}^{min}K_{max}$ are set to 10 and 7, respectively, where l_{max}, R_{MT}^{min} and K_{max} are defined in Ref. [125]. A 7×7×7 Monkhorst-Pack k-mesh is adopted to sample the Brillouin zone. Total-energy calculations are considered to be converged when the energy difference between two successive iterations is less than 10^{-4} Ry and the residual forces on atoms are below 10^{-4} Ry/Bohr. We resort to an energy-strain method implemented in the IRelast software to obtain the elastic constants needed

to calculate the Poisson's ratio (see Secs. V.4.2 and V.4.3). Polarization properties are calculated with the Berry-phase approach [135,136], using the BerryPI implementation [141] of this method as available in WIEN2k.

In order to describe the variation with alloy composition of the investigated properties, one can use the so-called Vegard's law. The latter is an empirical rule which states that the values of alloy properties interpolates linearly between the limiting values determined by the parent compounds [175]. For a generic property *P* and a ternary alloy $A_xB_{1-x}C$, where BC and AC are the parent compounds, Vegard's law is written as:

$$P_{A_xB_{1-x}C}(x) = xP_{AC} + (1-x)P_{BC}. \tag{V.1}$$

However, most properties are found to deviate from this linear behaviour, making the predictions of Vegard's law not accurate enough [175]. To a fairly good approximation, the compositional non-linearities are described by a quadratic model via the introduction of the bowing parameter b [171]:

$$P_{A_xB_{1-x}C}(x) = xP_{AC} + (1-x)P_{BC} - bx(1-x). \tag{V.2}$$

Once the bowing parameter is known, the value of *P* can be predicted for any concentration *x*.

V.3 Results for the strain-free ternary alloys

In this section, the III-nitride ternary alloys are grown freely without being subjected to the dimensions of a substrate, which means that the lattice parameters of the alloys are not affected by those of the underlying substrate. In this case there is no strain, and the only contribution to polarization is the spontaneous term. The effect of the substrate will be considered in the next section.

V.3.1 Lattice constants

Since we are interested in the electric polarization of alloys, a careful identification of their crystalline structure is needed [148]. We begin by determining the equilibrium wurtzite structure of the ternary alloys AlGaN, InGaN and InAlN. This is done by conducting an energy minimization process [23,151], where the lattice parameters are relaxed as we incorporate Al and In atoms into the corresponding supercells. Since the crystalline structure is hexagonal, the volume depends on two parameters: the basal lattice constant a and the axial lattice constant c [148]. Hence, the energy of the system is evaluated as a function of the cell volume and lattice-constant ratio over the whole range of alloy concentrations ($0 \leq x \leq 1$). We take the InGaN alloy as a representative and show its energy-calculation results in Figure V.2. The equilibrium lattice constants are obtained from fitting the data in this figure using the Murnaghan equation [Fig. V.2 (*a*)] and a fourth degree polynomial [Fig. V.2 (*b*)] as discussed in the previous chapter.

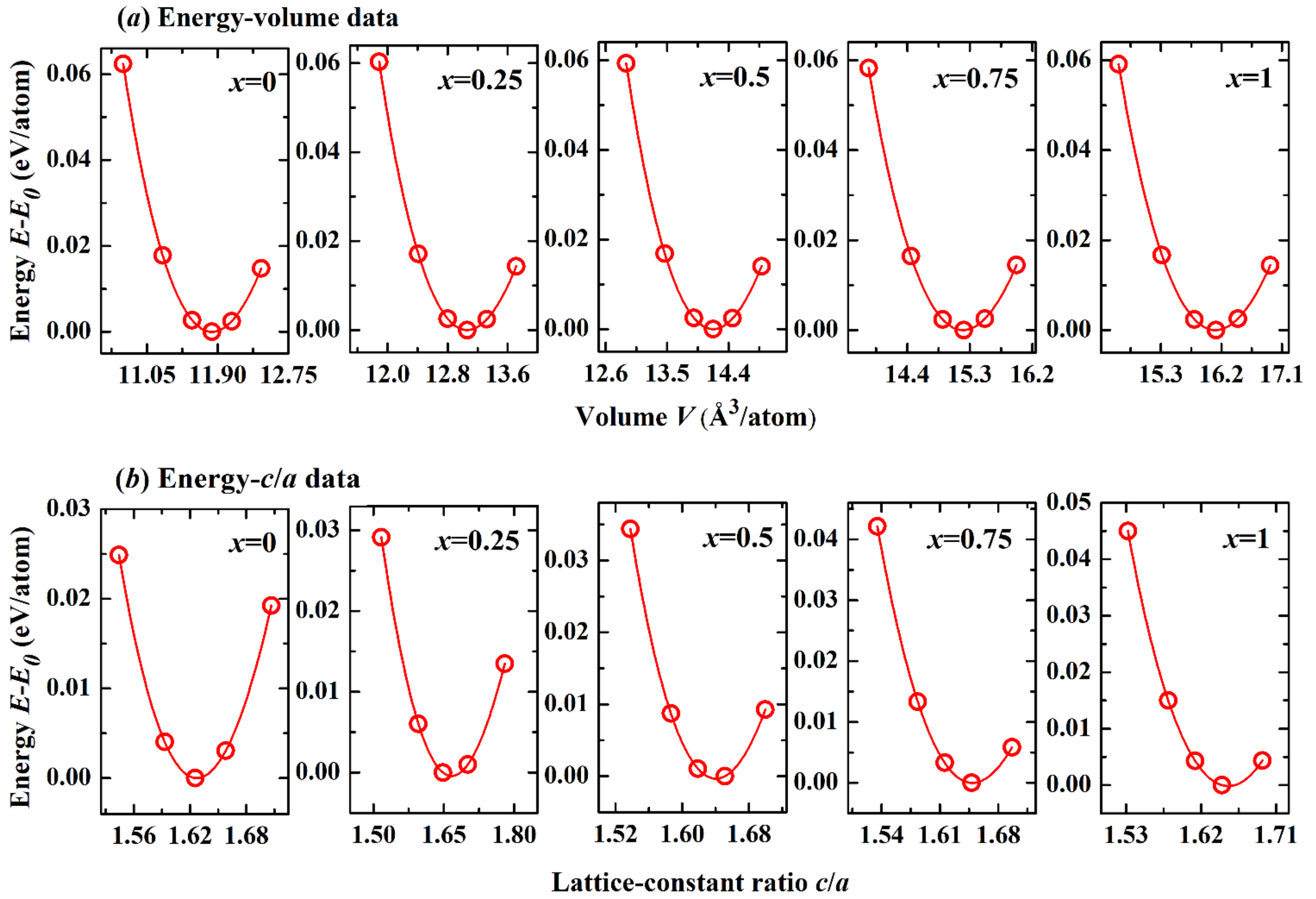

Figure V.2 Total energy versus (*a*) cell volume and (*b*) lattice-constant ratio *c*/*a* for the five compositions *x*. The origin of energy is taken to be the minimum value E_0 for each alloy concentration. The curves in (*a*) are a fit to the Murnaghan equation of state and those in (*b*) are a fit to a 4th degree polynomial. The calculation shown here is done for wurtzite InGaN.

Figure V.3 presents the variations of the lattice constants *a* and *c* of the ternary III-nitride alloys as a function of alloy composition, together with the results of previous DFT calculations [158] and X ray diffraction measurements [176–178]. Following Eq. (V.2), we use a quadratic interpolation to determine the dependence of the lattice parameters *a* and *c* (in Å) on the alloy concentration *x*. The resulting expressions are:

$$\begin{aligned} a_{Al_xGa_{1-x}N}(x) &= 3.12x + 3.23(1-x) + 0.01x(1-x), \\ c_{Al_xGa_{1-x}N}(x) &= 5.05x + 5.25(1-x) + 0.03x(1-x), \\ a_{In_xGa_{1-x}N}(x) &= 3.58x + 3.23(1-x) + 0.10x(1-x), \\ c_{In_xGa_{1-x}N}(x) &= 5.79x + 5.25(1-x) + 0.17x(1-x), \\ a_{In_xAl_{1-x}N}(x) &= 3.58x + 3.12(1-x) + 0.19x(1-x), \\ c_{In_xAl_{1-x}N}(x) &= 5.79x + 5.05(1-x) + 0.17x(1-x). \end{aligned} \quad \text{(V.3)}$$

Our results show the usual overestimation of the lattice constants calculated using the GGA functional [164], as their values are bigger than the ones determined through experiment. A weak non-linear behaviour with composition can be observed for all alloys. We note for InGaN

and InAlN that the lattice constants increase monotonically as the concentration increases from 0 to 1. This is explained by the addition of the large In atoms and their substitution with the small Ga ones, which induces an extension of the crystal. In contrast, the lattice constants of AlGaN decreases with composition because of the smaller size of Al compared to Ga (we have a contraction of the sample in this case). The transformation that leads from the wurtzite to the layered-hexagonal phase is cell-preserving, meaning the hexagonal lattice constants a and c are exactly equal to their wurtzite counterparts. In other words, no structural optimization is needed for the layered-hexagonal structure.

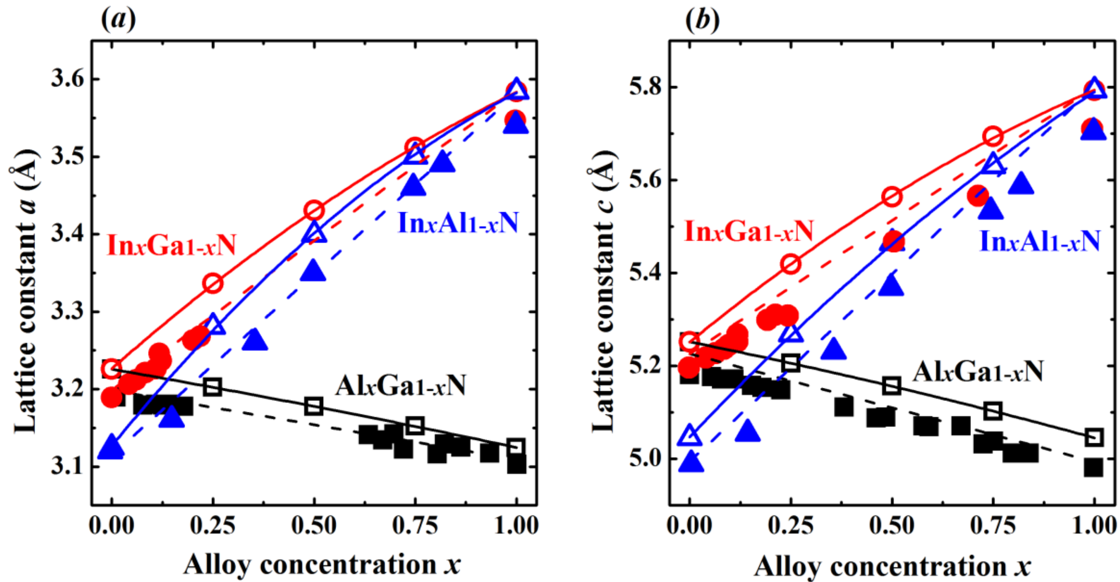

Figure V.3 Lattice constant (a) a and (b) c as a function of concentration x for strain-free wurtzite alloys AlGaN, InGaN and InAlN (without substrate). Open symbols are our data (solid curves are obtained by a quadratic fit). Dashed curves are the theoretical results of a prior work [158], whereas filled symbols denote measured values [176–178].

V.3.2 Average internal parameter

There is another structural degree of freedom that characterizes the wurtzite structure, namely the internal parameter u, defined as the cation-anion bond length parallel to the c-axis divided by the lattice constant c [148]. The different sizes of the incorporated and substituted cations [e.g. In and Ga in InGaN] results in deviations of bond lengths [179]. It is therefore necessary to fully relax the internal parameters to find their new equilibrium values. This is done by minimizing the applied atomic forces following the procedure of the Hellman-Feynman technique [153,180].

For alloyed compounds, what we really need to calculate is “the average” internal parameter u_{avg}. In wurtzite supercells, each cation is separated by one internal parameter (the double arrows in Figure V.4) from the anion. In this sense, the internal parameters are actually the cation-anion bond lengths (in units of c) along the c-axis. As shown in Fig. V.4, the size mismatch among the different cations is responsible for the presence of longer and shorter ionic bonds within the same supercell [181], making it necessary to compute the average bond length

and thus the average internal parameter. Note that relying on one value of the internal parameter (for example the dotted double arrow) would not allow to obtain the correct evolution of u with composition.

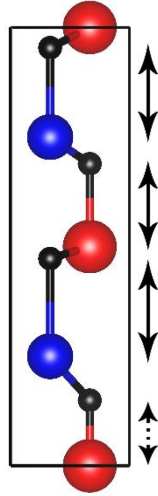

Figure V.4 8-atom wurtzite supercell modelling a ternary alloy for the composition *x*=0.5. The black spheres are anions while the red and blue spheres are cations. The vertical double arrows indicate the ionic bond lengths or the internal parameters u. The actual variation of bond lengths is minuscule, nothing like the variation shown in this figure.

The average internal parameter is calculated and plotted in Figure V.5. As we did with the lattice constants, we provide the quadratic composition formulae of u_{avg}:

$$\begin{aligned} u_{avg}^{Al_xGa_{1-x}N}(x) &= 0.380x + 0.376(1-x) - 0.001x(1-x), \\ u_{avg}^{In_xGa_{1-x}N}(x) &= 0.379x + 0.376(1-x) - 0.013x(1-x), \\ u_{avg}^{In_xAl_{1-x}N}(x) &= 0.379x + 0.380(1-x) - 0.009x(1-x). \end{aligned} \tag{V.4}$$

The internal parameter exhibits a significant bowing (no-linearity) for In-containing alloys [i.e. InGaN and InAlN]. In the case of AlGaN, the internal parameter varies almost linearly. The huge difference between our values (continuous curves) and those of Ambacher et *al.* [158] (discontinuous curves) may be attributed to the fact that in Ref. [158] the authors used the special quasirandom structure (SQS) method [182] to construct the supercells. This method consists in placing the different atoms in optimal lattice sites such that the periodic system mimics the real random alloy as closely as possible. We have not taken the effect of randomness into account and have used ordinary periodic supercells. By definition, the value of the internal parameter of the hexagonal structure is fixed to u_{avg}= u= 0.5 for all alloy compositions.

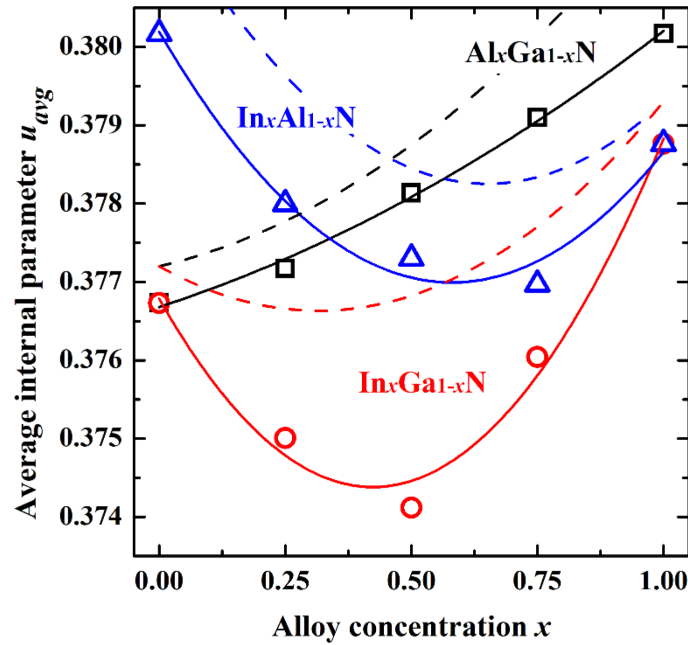

Figure V.5 Average internal parameter for the equilibrium structure of wurtzite alloys AlGaN, InGaN and InAlN calculated in this work (open symbols + continuous curves) and in Ref. [158] (discontinuous curves).

V.3.3 Polarization discontinuity

The Berry-phase treatment of the spontaneous polarization defines this quantity as the polarization difference between a non-centrosymmetric structure (wurtzite here) and a reference high-symmetry structure [135,136]. The zincblende phase has been used in the literature as a reference to access P_{sp} of wurtzite crystals. However, we choose in this study the layered-hexagonal structure as a reference, for which the internal parameter u= 0.5 [173,183]. Before presenting the results of the spontaneous polarization for the ternary nitride alloys, we investigate the evolution of the formal polarization vector as the supercell is transformed from the wurtzite to the hexagonal structure. For this purpose, we generate a set of structures that map the internal parameter from the relaxed wurtzite value to 0.5, and compute their formal polarization with the Berry-phase technique.

In Figure V.6 we show the results of this calculation for the intermediate concentration x= 0.5. The in-plane components of polarization P_x and P_y result to be numerically zero (due to symmetry), so that the values reported in Fig. V.6 are the z-components. We distinguish two sets of data: the first set (represented by solid symbols) is the original calculated values P_{WZ}, which presents a discontinuity at u= 0.5. Similar discontinuities have been reported for the wurtzite alloy $Sc_xAl_{1-x}N$ [9]. These linear curves are the branch of polarization n= 1 corresponding the 1×1×4 supercells. The polarization branches should be smooth curves without discontinuities at any point. To correct for the discontinuity present in Fig. V.6 at u= 0.5, one needs to change the polarization branch by shifting the original data using the wurtzite quantum of polarization $P_{q,WZ}$ of the 1×1×4 supercell [26,136]:

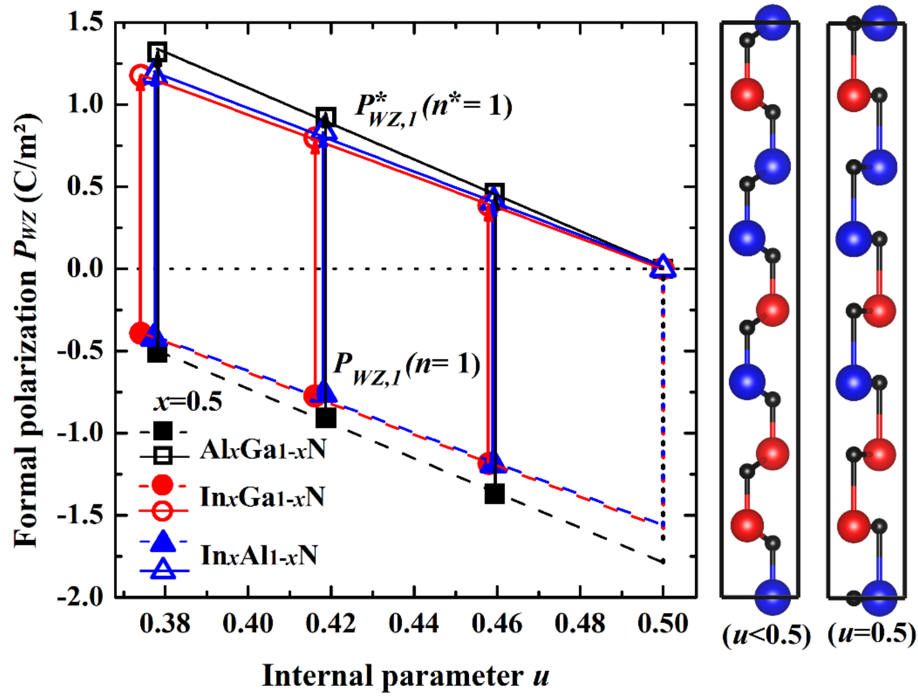

Figure V.6 Evolution of the formal polarization of AlGaN, InGaN and InAlN (for x= 0.5) as the supercells smoothly transform from the wurtzite (u< 0.5) to the hexagonal (u= 0.5) structure. The lattice constants a and c are held to the fully-relaxed wurtzite values. The dotted vertical line at u= 0.5 denotes the discontinuity of polarization. Solid symbols (discontinuous curves) refer to the original polarization results $P_{WZ,1}$ (branch n= 1), while open symbols (continuous curves) are the corrected values $P^*_{WZ,1}$ (branch n*= 1) obtained as explained in the text [via Eq. (V.6)]. Vertical arrows denote a shift by one polarization quantum. The zero polarization (represented by a horizontal dotted line) is not shifted. The fitting curves result from a linear regression of the calculated data. The supercell structures are illustrated to the right with the substituted atoms in red, the incorporated atoms in blue, and the N atoms in black.

$$P_{q,WZ}(x) = \frac{2e}{\sqrt{3}a^2(x)}, \tag{V.5}$$

where e is the (positive) electron charge. In the specific case of x=0.5, the polarization quantum is calculated to be 1.83 C/m² for AlGaN, 1.57 C/m² for InGaN, and 1.60 C/m² for InAlN.

We introduce the shifted formal polarization of wurtzite, labeled P^*_{WZ}, to be defined as:

$$\begin{aligned} P^*_{WZ}(x) &= P_{WZ}(x) + P_{q,WZ}(x) \\ &= P_{WZ}(x) + \frac{2e}{\sqrt{3}a^2(x)}. \end{aligned} \tag{V.6}$$

By shifting the original data P_{WZ} by $P_{q,WZ}$, it is as we have created a new branch without a polarization discontinuity, whose polarization values are P^*_{WZ} and integer is n*= 1. In this way we obtain the correct polarization values and reconstruct the true evolution, as shown by the second set of data (open symbols). It is indispensable to note that the zero polarization is left out of the shifting, i.e. Eq. (V.6) is not valid for u= 0.5 (otherwise the discontinuity remains). In addition, correcting for the polarization discontinuity guarantees that the polarization of AlGaN,

InGaN and InAlN belong to the same branch n^*= 1 [134]. For both sets of data, the formal polarization of wurtzite III-nitride alloys is seen to be approximately linear over the entire u interval and vanishes at u=0.5.

V.3.4 Spontaneous polarization

The spontaneous polarization $P_{sp,H}$ can be calculated, once the polarization quanta are known and added, as the difference between the shifted formal polarization of relaxed wurtzite P_{WZ}^* and that of the reference hexagonal structure P_H (which is zero) [26]:

$$P_{sp,H}(x) = P_{WZ}^*(x) - P_H(x), \tag{V.7}$$

where the index H in $P_{sp,H}$ indicates that the spontaneous polarization is referenced to the layered-hexagonal structure, and P_{WZ}^* is given by Eq. (V.6). Since we are using supercells of dimensions 1×1×4, the integer characterizing the polarization branch is n= 1 (actually n^*= 1), and the polarization difference in Eq. (V.7) can be rewritten as: $P_{WZ,1}^*(x) - P_{H,1}(x)$. Here, the subscript 1 does not mean that we use 4-atom unit cells as in chapter IV [Eq. (IV.18)], it rather reflects the fact that we are using 16-atom 1×1×4 supercells (in both cases the polarization branch is n= 1).

The evolution with composition of the spontaneous polarization for different alloys is plotted in Figure V.7. We see that the sign of $P_{sp,H}$ is positive over the whole composition regime. With reference of the wurtzite supercells in Fig. V.1, the polarization vector is vertical and directed from bottom to top. The composition-dependent expressions from a quadratic fit to the calculated data, given in C/m², are:

$$\begin{aligned}
P_{sp,H}^{Al_xGa_{1-x}N}(x) &= 1.339x + 1.299(1-x) + 0.005x(1-x),\\
P_{sp,H}^{In_xGa_{1-x}N}(x) &= 1.032x + 1.299(1-x) + 0.020x(1-x),\\
P_{sp,H}^{In_xAl_{1-x}N}(x) &= 1.032x + 1.339(1-x) - 0.031x(1-x).
\end{aligned} \tag{V.8}$$

The third numerical factor of the right-hand side of Eq. (V.8) is “minus” the bowing parameter b. There is no other data to compare our hexagonal-based values of b with, since this work seems to be the first one to report values. One can extract from the above expressions the spontaneous polarizations of the pure binaries, which are as follows: 1.339 C/m² for AlN, 1.299 C/m² for GaN and 1.032 C/m² for InN, in excellent agreement with the literature values [26] (AlN: 1.351 C/m², GaN: 1.312 C/m² and InN: 1.026 C/m²).

In the case of the ternary III-nitride alloys, a linearity with composition x of the spontaneous polarization can be observed, as evidenced by the very small values of the bowing parameters. In order to obtain a measure of how strongly the spontaneous polarization and alloy concentration are lineally associated, we provide the correlation coefficient R^2. We find that R^2 is around 0.98 for the three alloys studied. This implies a strong linear association, which indicates that the spontaneous polarization referenced to the hexagonal structure follows the linear behaviour predicted by Vegard’s law to an excellent degree of accuracy.

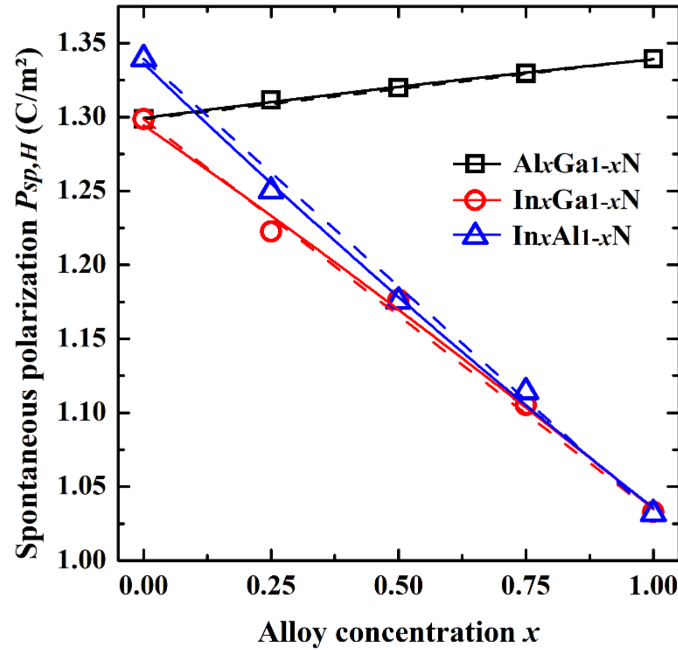

Figure V.7 Composition dependence of the spontaneous polarization for wurtzite alloys AlGaN, InGaN and InAlN as determined using Eq. (V.7) (using the hexagonal reference). The calculation is done with the equilibrium lattice parameters [lattice constants and atomic positions of Eqs. (V.3) and (V.4)]. The concentrations x=0 and 1 correspond to the relevant parent binaries GaN, AlN and InN. The quadratic curves are fits of equation (V.2) and dashed straight lines are fits of equation (V.1) (Vegard's law).

V.3.5 Effect of the exchange-correlation functional on polarization

To calculate the polarization of a crystalline solid (especially In-rich systems), one has to monitor the band gap. As mentioned in Sec V.2.2, we resort to the mBJ approach [113] to counterreact the band gap underestimation: whenever GGA incorrectly predicts a conducting state we perform a mBJ-based calculation to open the gap, otherwise the polarization cannot be accessed. The question remains whether the mBJ functional affects polarization values compared to GGA. To address this issue we select a case study where the GGA gap is close to zero, but not zero yet, and compute the polarization at the GGA and mBJ levels. We perform this calculation for $In_{0.75}Al_{0.25}N$ (x=0.75) for which the GGA-predicted gap is 0.044 eV. We find a spontaneous polarization of 1.114 C/m² and 1.111 C/m² without and with mBJ, respectively. This finding indicates that the mBJ exchange-correlation potential has practically no effect on the polarization values.

V.3.6 Effect of the supercell dimension on polarization

We have shown in Chapter III that the value of the formal polarization, in contrast to almost all material properties, depends on the choice of the crystal cell. In other words, the results of the unit cell are different from the ones of larger supercells for the same physical system. Most notably, two different $n\times n\times m$ supercells give different polarization values, depending on the dimensionality n along the basal plane. However, since the spontaneous polarization is a measurable quantity it must be cell-invariant: all possible choices of the crystal cell are expected

to yield the same value of P_{sp}. In the following, we discuss this issue by considering extended supercells along the a- and b-directions. In particular, we carry out a test calculation using a 2×2×2 (32-atom) wurtzite supercell such as the one illustrated in Figure V.8. The lattice parameters (a, c and u) of AlGaN are allowed to relax for this supercell for the alloy concentration x=0.5. Then, as we did in Sec. V.3.3, the formal polarization is computed as a function of the internal parameter u, varying between the relaxed (real) wurtzite value and the hexagonal value of 0.5.

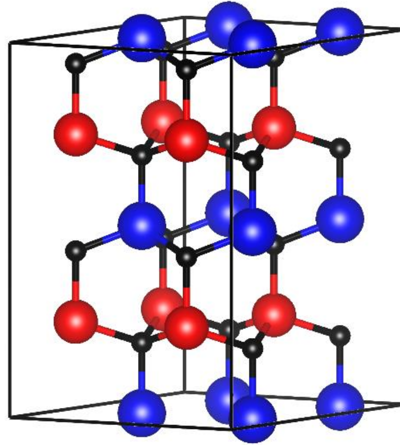

Figure V.8 Wurtzite supercell of dimension 2×2×2, which means that the lattice constants a and c of the underlying unit cell are both multiplied by 2. This has the effect of doubling the number of atoms in the unit cell along the a-, b- and c-directions. Since there are 4 atoms in the unit cell, the corresponding 2×2×2 supercell contains 32 atoms (i.e. 4×2×2×2= 32). The supercell is used to model $Al_xGa_{1-x}N$, where Al, Ga and N are the red, blue and black spheres, respectively. The alloy concentration is x= 8/16= 0.5, i.e. out of the 16 Ga atoms, 8 are replaced by Al atoms. The results plotted in Figure V.9 are obtained using this supercell.

We present in Figure V.9 the variation of the formal polarization of $Al_{0.5}Ga_{0.5}N$ modelled by a 2×2×2 wurtzite supercell with respect to the internal parameter. Before discussing this plot, it is important to introduce some useful notations. The formal polarization, the polarization quantum and the spontaneous polarization of our 1×1×4 (16-atom) wurtzite supercell (i.e. polarization branch n= 1) are labeled $P_{WZ,1}$, $P_{q,WZ,1}$and $P_{sp,H,1}$, respectively. These same quantities are labeled $P_{WZ,2}$, $P_{q,WZ,2}$ and $P_{sp,H,2}$ for the 2×2×2 (32-atom) supercell (i.e. branch n= 2). As in Fig. V.6, there are two sets of data regarding the results of the 32-atom supercell. In addition, we replot for reference the data of the original results (before the shifting) of the 16-atom supercell.

We consider the first data set represented by the dashed curve (n= 2). We find that at the equilibrium value of u, the calculated Berry-phase formal polarization is $P_{WZ,2}$= −0.0511 C/m². This value is different from the one obtained with the 1×1×4 supercell, which is $P_{WZ,1}$= −0.510 C/m² (this polarization corresponds to the first data point of AlGaN in Fig. V.6). The formal polarizations $P_{WZ,2}$ and $P_{WZ,1}$ are linked by Eq. (III.25) (see Sec. III.6.1), which we rewrite here as:

$$P_{WZ,2} = P_{WZ,1} + P_{q,WZ,2} = P_{WZ,1} + \frac{P_{q,WZ,1}}{2^2}, \quad \text{(V.9)}$$

where $P_{q,WZ,1}$= 1.83 C/m² is calculated via Eq. (V.5). For *u*= 0.5, both supercells yield zero polarization, i.e. $P_{H,1} = P_{H,2} = 0$ (our calculation yields a value of 10^{-15} C/m², which we consider to be zero compared to the wurtzite value). We observe in Fig. V.9 the same discontinuity at *u*= 0.5. In order to eliminate it, we follow the procedure outlined previously and shift the original data by one quantum of polarization $P_{q,WZ,1}$ (the red arrows). Notice that the quantum used in the shifting is the one corresponding to the 16-atom supercell, not the 32-atom supercell. Hence the second data set, the one represented by the continuous curve (n^*= 2), is obtained via:

$$P^*_{WZ,2} = P_{WZ,2} + P_{q,WZ,1}. \quad \text{(V.10)}$$

Despite the introduction of the above shift, we observe that the new polarization branch still has the discontinuity at *u*= 0.5, indicating another shift might be required.

To calculate the spontaneous polarization referenced to the hexagonal structure of the 2×2×2 supercell, we use an expression similar to Eq. (V.7):

$$P_{sp,H,2} = P^*_{WZ,2} - P_{H,2}. \quad \text{(V.11)}$$

The resulting value is $P_{sp,H,2}$= 1.799 C/m². We can see from Fig. V.7 or Eq. (V.8) that the spontaneous polarization of $Al_{0.5}Ga_{0.5}N$ in the 1×1×4 supercell is $P_{sp,H,1}$= 1.320 C/m². So the two supercells yield different results of $P_{sp,H}$, in opposition to the fact that this property has a unique value. This problem and the discontinuity issue can be solved by revisiting previous polarization formulae. We start by putting the branch index 1 in Eq. (V.6):

$$P^*_{WZ,1} = P_{WZ,1} + P_{q,WZ,1}, \quad \text{(V.12)}$$

and Eq. (V.7):

$$P_{sp,H,1} = P^*_{WZ,1} - P_{H,1}. \quad \text{(V.13)}$$

For simplicity, we have omitted the composition argument *x* in the polarization functions. If we merge Eqs. (V.12) and (V.13) we get:

$$P_{sp,H,1} = P_{WZ,1} + P_{q,WZ,1} - P_{H,1}. \quad \text{(V.14)}$$

Next, merging Eqs. (V.9), (V.10) and (V.11) gives:

$$P_{sp,H,2} = P_{WZ,1} + P_{q,WZ,2} + P_{q,WZ,1} - P_{H,2}, \quad \text{(V.15)}$$

By comparing the last two equations, we see clearly that for $P_{sp,H,2}$ to be equal to $P_{sp,H,1}$ we should subtract $P_{q,WZ,2}$ in the right-hand side of Eq. (15) (because $P_{H,1} = P_{H,2} = 0$). That is:

$$P_{sp,H,2} = P_{WZ,1} + P_{q,WZ,2} + P_{q,WZ,1} - [P_{H,2} + P_{q,WZ,2}]. \quad \text{(V.16)}$$

Graphically, this means that the layered-hexagonal formal polarization $P_{H,2}$ of the 2×2×2 supercell is shifted by the quantum of polarization $P_{q,WZ,2}$ of the same supercell (the blue arrow in Fig. VI.9]. The shifted $P_{H,2}$, which we label $P^{*}_{H,2}$, is then:

$$P^{*}_{H,2} = P_{H,2} + P_{q,WZ,2}. \quad \text{(V.17)}$$

Because the layered-hexagonal supercell is just a wurtzite supercell with u= 0.5, the polarization quanta of both supercells are equal, i.e. $P_{q,WZ} = P_{q,H}$ (for the same branch n). Substituting Eq. (V.17) in Eq. (V.11) gives us:

$$P_{sp,H,2} = P^{*}_{WZ,2} - P^{*}_{H,2}. \quad \text{(V.18)}$$

To summarize, when calculating the spontaneous polarization of a wurtzite crystal using the hexagonal structure as a reference, the calculation procedure depends on the dimension of the supercell used to model the crystal studied. Employing a 1×1×m supercell, where $m \geq 2$, requires the use of equation (V.13), where $P^{*}_{WZ,1}$ is determined Eq. (V.12), i.e. by shifting $P_{WZ,1}$ at the relaxed wurtzite values of u with $P_{q,WZ,1}$, but $P_{WZ,1}$ at u= 0.5 is not shifted. The formal-polarization values belong to the branch n^{*}= 1. When the simulation is done by an n×n×m supercell ($n \geq 2$ and $m \geq 2$), two polarization shifts must be performed. The first one is the same as the previous case, shifting $P_{WZ,n}$ by $P_{q,WZ,1}$. Again, the shift concerns only the relaxed values of the parameter u and not for u= 0.5. As for the second shift, it is done for $P_{H,n}$; specifically, $P_{H,n}$ is shifted by $P_{q,WZ,n}$ (and not by $P_{q,WZ,1}$ as before) to obtain $P^{*}_{H,n}$. The polarization branch in this case corresponds to n^{*}= 2 (in both cases the branch is the dimension of the supercell along the a- and b- axes). In terms of equations, we have for an n×n×m supercell:

$$P_{sp,H,n} = P^{*}_{WZ,n} - P^{*}_{H,n}, \quad \text{(V.19)}$$

where:

$$P^{*}_{WZ,n} = P_{WZ,n} + P_{q,WZ,1}, \quad \text{(V.20)}$$

and:

$$P^{*}_{H,n} = P_{H,n} + P_{q,WZ,n}. \quad \text{(V.21)}$$

It is imperative to note that Eqs. (V.13) and (V.19) are completely equivalent, in the sense that $P_{sp,H,1} = P_{sp,H,n} = P_{sp,H}$.

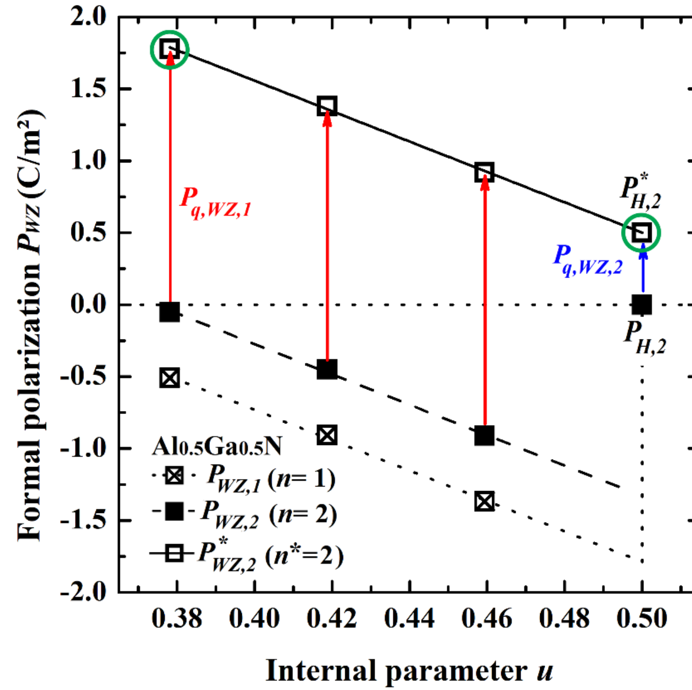

Figure V.9 Formal polarization of wurtzite $Al_{0.5}Ga_{0.5}N$ with respect to the average internal parameter. This is similar to the results shown in Fig. V.6, but the calculation here is done for a 2×2×2 supercell instead of a supercell of dimension 1×1×4. The values $P_{WZ,1}$ of the latter correspond to the branch n= 1 and are shown in this figure just for reference (represented by crossed symbols and a dotted curve). The values $P_{WZ,2}$ of the 2×2×2 supercell, shown as solid symbols and a dashed curve, correspond to the branch n= 2. Note that $P_{WZ,1}$ and $P_{WZ,2}$ are linked by Eq. (V.9). Like the values of the branch n= 1, those of the branch n= 2 have a discontinuity at u= 0.5. In order to eliminate this discontinuity we do as before and shift the polarization values (except the value at u= 0.5 which is $P_{H,2}$) by the quantum of polarization $P_{q,WZ,1}$ of the 1×1×4 supercell (red arrows). This gives us the branch n^*= 2 (open symbols and a solid curve). In addition, the hexagonal value $P_{H,2}$ is shifted by the polarization quantum $P_{q,WZ,2}$ of the 2×2×2 supercell (blue arrow), and the shifted value is denoted $P^*_{H,2}$. The role of the second shift [Eq. (V.17)] is to obtain the same spontaneous polarization for both supercells. Indeed, if we subtract the two circled data points in the branch n^*= 2 [i.e. we apply Eq. (V.18)] we find a $P_{sp,H}$ value that exactly matches the one based on the 1×1×4 supercell [Eq. (V.13)].

According to the lengthy (and important) discussion in this section, and based on our experience, we recommend the use of supercells of dimensions 1×1×m to model wurtzite alloys when studying electric polarization. This recommendation is justified by the fact that using such supercells is much simpler, as only one polarization shift is needed to find the correct value of the spontaneous polarization, while n×n×m supercells demand two different shifts. Finally, there is an important point to recognize when simulating alloyed compounds: the values of material properties at the end points x= 0 and 1 need to coincide with the known values of the constituent (parent) compounds. For example, one expects the spontaneous polarization of $Al_xGa_{1-x}N$ for x= 0 (x= 1) to be equal to that of GaN (AlN). This must be true for any choice of supercell dimension.

V.3.7 Comparison between the hexagonal and trigonal references

For the sake of comparison, we repeat the spontaneous polarization calculation using the trigonal structure as a reference. This computation is done by using many 1×1×m trigonal supercells (e.g. the one shown in Fig. V.10) whose in-plane lattice constant a is fixed to the in-plane lattice constant of the wurtzite phase for the corresponding alloy. The spontaneous polarization referenced to the trigonal structure $P_{sp,T}$ is computed as:

$$P_{sp,T}(x) = P_{WZ,1}(x) - P_{T,1}(x), \qquad \text{(V.22)}$$

were $P_{WZ,1}$ and $P_{T,1}$ are the formal polarization of the 1×1×4 wurtzite and the 1×1×m trigonal supercells, respectively. Even though the wurtzite and trigonal supercells have different number of atoms, they all correspond to the same polarization branch n= 1 (because their dimension in the basal plane is 1×1). As we have already proved in Chapter IV, the zincblende and trigonal structures yield the same results of the spontaneous polarization for wurtzite binaries. In the following we show that they give similar values for the wurtzite ternary alloys as well.

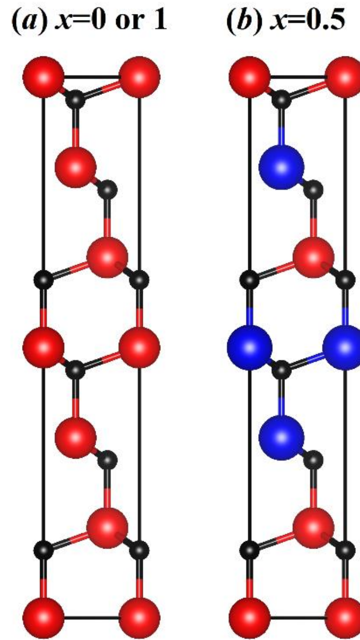

Figure V.10 Trigonal supercells used to calculate the spontaneous polarization $P_{sp,T}$ referenced to the trigonal structure for (a) parent binaries (x=0 or 1) and for (b) a ternary alloy (x=0.5). The supercell shown in (b) has 12 atoms (with dimension 1×1×2), which is the smallest trigonal supercell needed to achieve x=0.5. For other compositions x, one should use different supercells, e.g. x=0.25 and 0.75 demand at least a 24-atom (1×1×4) trigonal supercell.

The calculated values for wurtzite AlGaN, InGaN and InAlN using either the hexagonal or trigonal structures are shown in Figure V.11. The values of the corresponding bowing parameters are also included. It can be seen clearly that the choice of the reference structure does have a huge effect on the results. Both the magnitude and sign of P_{sp} are different for the two references, which results in different relative polarization differences between layers and materials. In addition, and

at variance with the prediction of the hexagonal structure, the spontaneous polarization obtained using the trigonal structure $P_{sp,T}$ is an appreciably non-linear function of composition x. Figure V.11 shows that the values of the bowing parameters calculated with the trigonal structure are around one order of magnitude greater than those calculated with the hexagonal structure. The trigonal reference structure succeeds in reproducing the zincblende-based values and the upward bowing of the spontaneous polarization reported in Ref. [181] [the discontinuous curves in Fig. V.11 (*b*)], which implies that the trigonal and zincblende references are equivalent for both the wurtzite binaries and their ternary alloys. Note that in Ref. [181], it should be the ordered chalcopyrite or CuPt-like ('CP' in Fig. 3 of that paper) results to be compared to our values, because the CuPt-like structure for nitride alloys is somehow similar to the wurtzite structure used here [170,171].

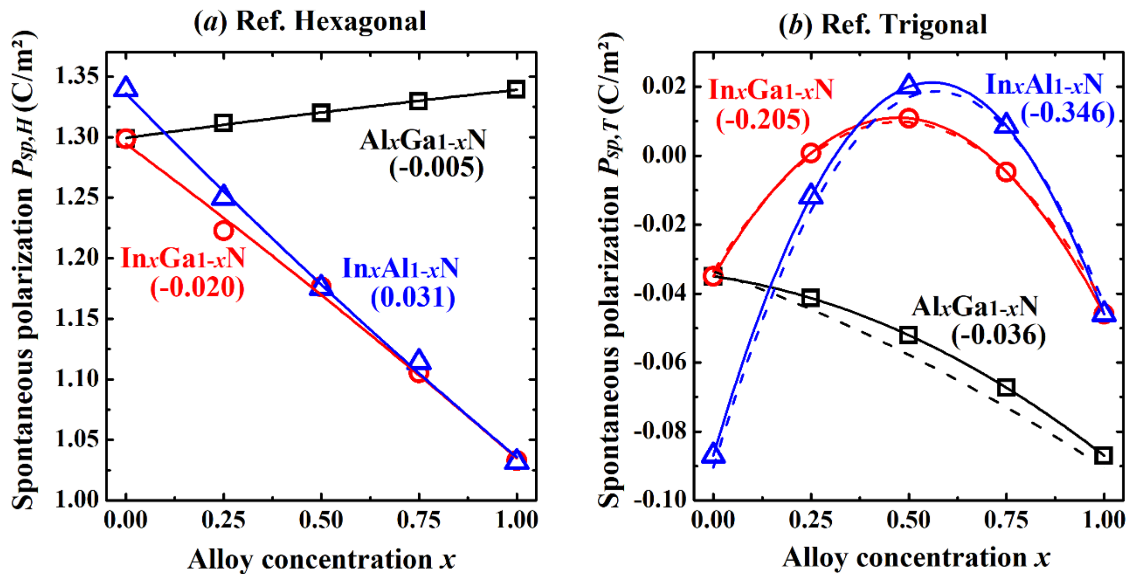

Figure V.11 Comparison between the (*a*) hexagonal and (*b*) trigonal results for the spontaneous polarization of the ternary III-nitride alloys. The curves are obtained using a quadratic fit. Numbers in parenthesizes are the respective bowing parameters b in units of C/m². Discontinuous curves in (*b*) present the spontaneous polarization referenced to zincblende from Ref. [181].

Bernardini and Fiorentini demonstrated that the composition non-linearity of the spontaneous polarization in III-nitride alloys is attributed to two main factors [171,181], which are the macroscopic deformation due to the binaries having different volumes, and the microscopic strain due to the different sizes of the constituent atoms. Our results indicate, however, that the non-linearity also depends on the choice of reference. This is because the hexagonal structure has a zero formal polarization whereas the trigonal/zincblende structure has a non-vanishing formal polarization.

V.3.8 Refined understanding of the wurtzite spontaneous polarization

In the previous section, we showed that the trigonal (or zincblende) and layered-hexagonal reference structures give different spontaneous polarizations of wurtzite ternary nitride alloys, both in terms of magnitude and orientation. This dependence on the choice of the reference structure is problematic, since the spontaneous polarization of III-nitride materials is an intrinsic property that should have a single value (like the band gap for instance). In other words, the trigonal- and hexagonal-based results cannot be *both* true. We are therefore left dealing with the following question: what reference structure yields the true or real values of the spontaneous polarization of wurtzite systems?

In order to answer this important question we resort to experimental measurements. Unfortunately, the spontaneous polarization of traditional nitride ternaries AlGaN, InGaN and InAlN has not been accessed experimentally. On the contrary, structural measurements of polarization were conducted on the nitride parent binaries AlN, GaN and InN by using atomically resolved scanning transmission electron microscope (STEM). The spontaneous polarization was quantified via Eq. (I.15), where the Born effective charge Z^* was derived from phonon spectra or DFT and the ionic relative displacement Δr was accurately determined using a two-dimensional Gaussian fitting process [184,185] on STEM images of the binary nitrides. Just recently Ye et *al*. [68] used this empirical technique for determining the spontaneous polarization. The measured values are 1.37 C/m² for AlN, 1.29 C/m² for GaN and 1.04 C/m² for InN, all exhibiting an upward polarity. In addition, Hasegawa et *al*. [186] employed an electrical measurement called positive-up/negative-down (PUND) to access the spontaneous polarization of AlN, they obtained a value of 1.5 C/m², which aligns well with the value obtained from STEM (1.37 C/m²).

Table V.1 Comparison of our theoretical and other experimental spontaneous polarization values (in C/m²) for the wurtzite III-nitride binaries AlN, GaN and InN.

Materials	Our DFT calculated P_{sp}		Measured P_{sp}
	Trigonal Ref.	Hexagonal Ref.	
AlN	-0.087	1.34	1.37 [a], 1.5 [b]
GaN	-0.035	1.30	1.29 [a]
InN	-0.360	1.03	1.04 [a]

[a] Ref. [68], [b] Ref. [186]

Table V.I lists our results alongside previously reported experimental measurements of the spontaneous polarization in III-nitride semiconductors AlN, GaN and InN. We report our theoretically predicted spontaneous polarisations using the trigonal (from the previous chapter) and the layered-hexagonal (the present chapter) structures. Notably, while the experimentally determined structural (STEM) and electrical (PUND) polarizations are well consistent with our hexagonal-based data, they show significant discrepancies when compared to our values referenced to the trigonal structure, in terms of both magnitude and orientation (or sign). Based on this comparison, we conclude that the layered-hexagonal reference structure is more suited for calculating the spontaneous polarization of wurtzite materials than the trigonal and

zincblende structures, predicting values very close to the ones determined experimentally. Different research groups came independently to the same conclusion [68,187,188].

Furthermore, recent studies have unambiguously demonstrated ferroelectric polarization reversal in some wurtzite alloyed and doped compounds, such as $Sc_xAl_{1-x}N$ [189] and $Y_xAl_{1-x}N$ [190]. As mentioned previously in Sec. I.4.3, understanding ferroelectricity requires a paraelectric structure which has two key properties: (i) it must be centrosymmetric with zero formal polarization, and (ii) it is linked to the ferroelectric polar and anti-polar structures by a simple structural transformation. The layered-hexagonal phase clearly satisfies both requirements, as it is non-polar and adiabatically linked to wurtzite through changing the internal parameter (which is not the case for the trigonal and zincblende structures). For ferroelectric wurtzite crystals, therefore, the structure that serves as a paraelectric state is the layered-hexagonal one [191,192], which further affirms our conclusion that the hexagonal reference is more appropriate than the trigonal and zincblende references for studying polarization phenomena in wurtzite crystals. A detailed account of ferroelectricity in wurtzite crystals can be found in the thesis perspectives.

V.4 Results for the ternary alloys lattice-matched to GaN

In the previous section, we presented the results of the structural optimization and electric polarization of the ternary nitride alloys in the absence of mechanical strain (at equilibrium), where the polarization state of the system is described in terms of the spontaneous polarization alone. In this section, we consider the interesting case where the strain is imposed by a GaN substrate upon which the alloys are grown. We open the section by explaining in detail how to optimize the structure of biaxially strained crystals. Then we move on to polarization results and show how to evaluate the piezoelectric polarization.

V.4.1 Mismatch-induced strain

In practice, wurtzite nitride alloys are grown as thin layers on a substrate with a different lattice constant, typically GaN or AlN buffer layer [172,193]. The direction of growth is commonly chosen to be the polar c-axis ([0001] direction), and the alloy layer is coherently lattice-matched to the underlying substrate [58]. This generates a biaxial strain perpendicular to the growth direction. The origin of this biaxial (or basal) strain is the difference between the in-plane lattice constant a of the alloy layer and the underlying substrate [58,75]. In this study, we consider the nitride alloys to be grown on top of a GaN substrate in the c-direction. The biaxial strain ε_1 is given, for example in the case of InGaN grown on GaN (which we denote as InGaN/GaN), by the following formula [194]:

$$\varepsilon_1(x) = \frac{a_{GaN} - a_{In_xGa_{1-x}N}(x)}{a_{GaN}}, \tag{V.23}$$

where $a_{In_xGa_{1-x}N}$ and a_{GaN} refer to the in-plane lattice constant of the alloy layer and the substrate, respectively. We use the Voigt notation where $\varepsilon_1 = \varepsilon_{xx} = \varepsilon_{yy}$, meaning the strain is applied to the xy-plane (or c-plane). The calculation of the strain as given by equation (V.23)

requires the knowledge of the in-plane lattice constants of the free-strain alloys [Eq. (V.3)]. In order for the biaxial strain to exist, the equality of the in-plane lattice constants of both layers must be enforced (i.e. $a_{In_xGa_{1-x}N} = a_{GaN}$) [171], a process called epitaxial matching (see Fig. V.12).

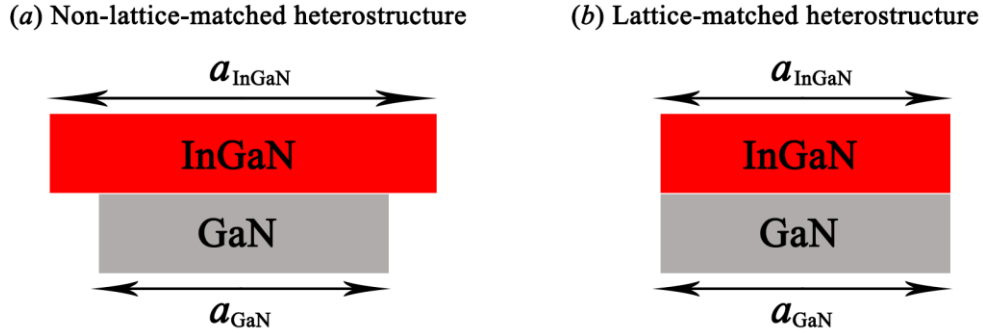

Figure V.12 Schematic of (*a*) free-strain ($a_{In_xGa_{1-x}N} > a_{GaN}$) and (*b*) strained ($a_{In_xGa_{1-x}N} = a_{GaN}$) heterostructures of InGaN/GaN. While the former structure is used to calculate only the spontaneous polarization, the latter is used to access both spontaneous and piezoelectric polarizations (i.e. total polarization).

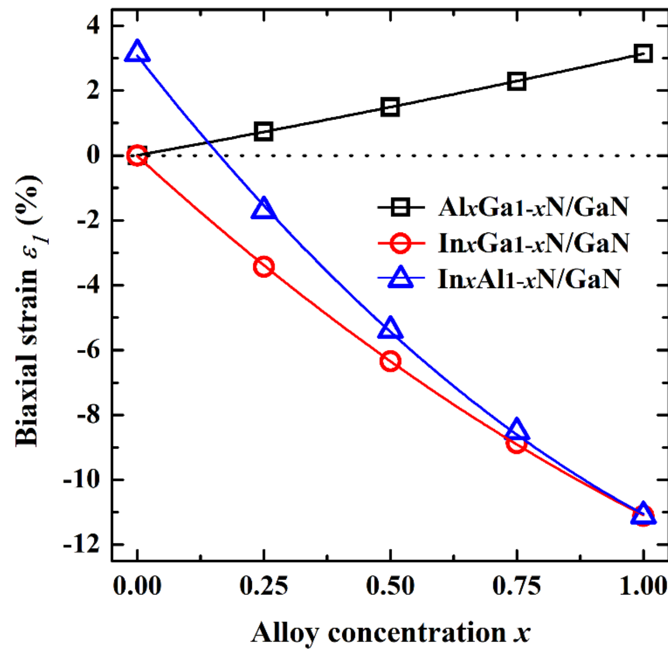

Figure V.13 Variation of biaxial-mismatch strain with alloy composition for wurtzite AlGaN/GaN, InGaN/GaN and InAlN/GaN heterostructures. The calculation of ε_1 is done via Eq. (V.23). The strain is zero at the horizontal dotted line.

We present in Figure V.13 the variation with alloy composition of the mismatch-induced biaxial strain. For AlGaN/GaN, the strain is positive and increases with Al content, where the mismatch between GaN and AlN is around 3% (at *x*= 1). The positive sign indicates that the alloy layer undergoes a tensile strain (i.e. extension). As for InGaN/GaN and InAlN/GaN, it can

be seen that the strain significantly increases (in magnitude) as the In molar fraction increases. The in-plane lattice mismatch is as high as -11% between GaN and InN. The strain is negative for all alloy concentrations for InGaN/GaN. For InAlN/GaN, however, the strain changes its sign from positive to negative at around $x = 0.16$. The minus sign means that the strain is compressive in nature (i.e. contraction). The mismatch strain leads to the formation of structural defects at the heterointerface [195], for instance dislocations.

V.4.2 Elastic constants

The elastic constants of the different alloys are needed for the structural optimization, so we have to compute them too via total-energy calculation. The amount of energy required to deform a solid (called elastic energy) is given, using Voigt notation, by [29]:

$$E(\varepsilon) = \frac{V_0}{2} \sum_{i,j} C_{ij} \varepsilon_i \varepsilon_j, \tag{V.24}$$

where V_0 is the equilibrium volume of the cell, C_{ij} are the elastic constants and ε_i are the components of the strain tensor. Equation (V.24) shows that the elastic energy is approximated by a quadratic function of the mechanical deformation. This quadratic approximation is known as harmonic elasticity [29], and it is only valid for sufficiently small strains.

Having hexagonal symmetry, our alloys are characterized by five independent elastic constants: C_{11}, C_{12}, C_{13}, C_{33}, and C_{44} [196], the determination of which relies on calculating the energy at appropriate mechanical deformations [197]. In this case, since we have five components of the elastic tensor, Eq. (V.24) reduces to five equations, which are as follows [198]:

$$\begin{aligned} E(\varepsilon) &= E_0 + V_0(C_{11} + C_{12})\varepsilon^2, \\ E(\varepsilon) &= E_0 + V_0(C_{11} - C_{12})\varepsilon^2, \\ E(\varepsilon) &= E_0 + \frac{1}{2} V_0 C_{33} \varepsilon^2, \\ E(\varepsilon) &= E_0 + 2V_0 C_{44} \varepsilon^2, \\ E(\varepsilon) &= E_0 + \frac{1}{2} V_0 (2C_{11} + 2C_{12} + 4C_{13} + C_{33})\varepsilon^2. \end{aligned} \tag{V.25}$$

In all these expressions, E_0 is the ground-state energy (i.e. without deformation) and ε is the applied strain. For more details, in particular the nature of the deformations that lead to Eq. (V.25), the reader is referred to the paper by Shein et *al.* [198]. Once the energies in Eq. (V.25) are calculated for the appropriate strains, the elastic constants can be found by evaluating the second derivative of E with respect to strain [196]:

$$C_{ij} = \frac{1}{V_0} \frac{\partial^2 E}{\partial \varepsilon^2}. \tag{V.26}$$

The simulation should be done for the alloys InGaN, InAlN and InAlN, but conducting a calculation of the elastic constants for 16-atom supercells is somehow unfordable. We follow instead some previous studies and perform the calculation for the parent binary compounds

AlN, GaN and InN, then we use the linear interpolation of Vegard's law [175] to obtain C_{ij} of the ternary alloys.

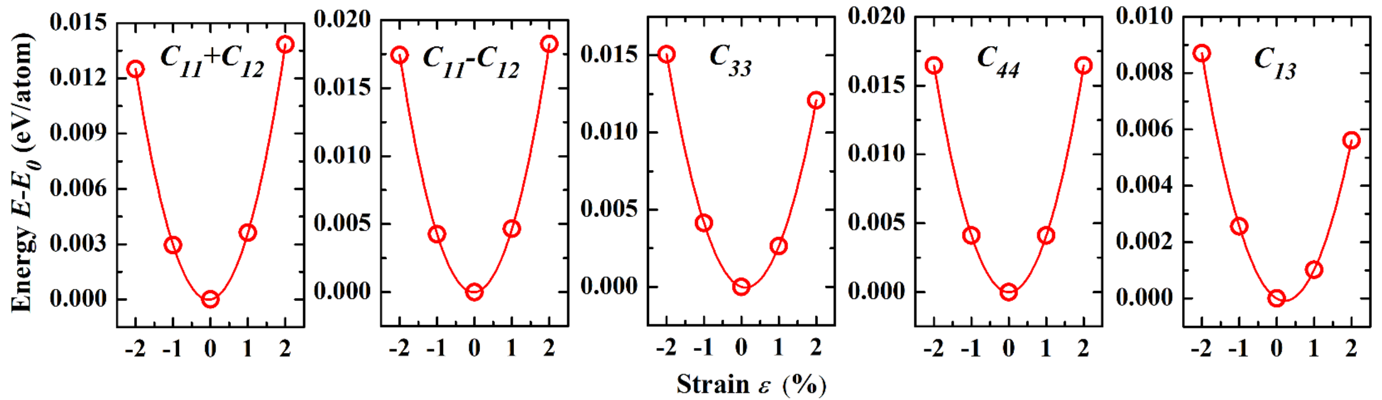

Figure V.14 Total energy per atom of deformed GaN as a function of different types of strains (biaxial, uniaxial and shear deformations). Each curve corresponds to one the five expressions listed in Eq. (V.25). Fitting these curves to a quadratic polynomials allows to find the five elastic constants C_{ij} as explained in the text. The scale of energy E is referenced to the equilibrium (ε= 0) value E_0, which equals -27185.27 eV/atom.

We prepare the deformed crystalline structures using IRelast [199], which is a program developed by Jamal et *al*. to extend the utility of WIEN2k to the calculation of elastic and mechanical properties. We show in Figure V.14 the results of the energy-stain calculation of wurtzite GaN. The elastic constants are derived by fitting the energy-strain data to a second order polynomial, so that the second partial derivative in Eq. (V.26) is proportional to the numerical coefficient multiplied by ε^2 in the fitting polynomial. We emphasize two important points: (i) we observe that E is indeed a quadratic function of ε as required by the theory of harmonic elasticity (which is the basis of the IRelast code), and (ii) the strains in the x-axis of Fig. V.14 are not of the same nature, for instance the strain needed to compute $C_{11}+C_{12}$ is a combination of tensile and compressive biaxial deformation applied to the xy-plane, whereas the strain needed to find C_{33} is a uniaxial deformation applied to the z-axis (see Ref. [198] for further details).

Table V.2 Elastic constants of wurtzite AlN, GaN and InN. They are extracted from curves similar to those shown in Fig. V.14. See Table 1 of Ref. [69] for a comparison.

Material	C_{11} (GPa)	C_{12} (GPa)	C_{33} (GPa)	C_{44} (GPa)	C_{13} (GPa)
AlN	372.27	128.31	418.58	110.36	103.39
GaN	327.71	113.44	380.05	91.98	83.16
InN	205.83	91.98	213.79	50.94	60.93

The calculated elastic constants of wurtzite AlN, GaN and InN are summarized in Table V.2. Our results show a good agreement with the theoretical and experimental literature results gathered in Ref. [69]. The corresponding parameters of InGaN, InAlN and InAlN are obtained simply via Vegard's law. The elastic constants are doubly interesting. On the one hand,

they provide access to several elastic properties that describe the mechanical behaviour of materials, such as the bulk and shear moduli. On the other hand, they make it possible to verify the mechanical stability of the system via the Born stability criteria. For a hexagonal crystal, these criteria are [196]:

$$C_{11} > |C_{12}|, 2C_{13}^2 < C_{33}(C_{11} + C_{12}), C_{44} > 0. \tag{V.27}$$

According to our numerical data, the elastic constants satisfy the stability conditions, which implies that the parent binaries, and hence the alloys, are mechanically stable.

V.4.3 Poisson effect

As mentioned before, the studied alloys are characterized by residual biaxial strains at the interface with the GaN substrate [58]. A biaxial strain ε_1 applied on the *xy*-plane is usually accompanied by a uniaxial strain ε_3 along the perpendicular direction to that plane, namely the *z*-axis. Such a phenomenon is known as the *Poisson effect* [200,201]. In order to take the Poisson effect into account, we calculate the resulting uniaxial strain by taking advantage of the Poisson's ratio ν. The latter is obtained from the aforementioned elastic coefficients C_{13} and C_{33} by the following formula [201]:

$$\nu = \frac{C_{13}}{C_{33}}, \tag{V.28}$$

The Poisson's ratio is found to be equal to 0.247, 0.219 and 0.285 for AlN, GaN and InN, respectively. Applying Vegard's law to these values yields these expressions of ν for the alloys:

$$\begin{aligned} \nu_{Al_xGa_{1-x}N}(x) &= 0.247x + 0.219(1-x), \\ \nu_{In_xGa_{1-x}N}(x) &= 0.285x + 0.219(1-x), \\ \nu_{In_xAl_{1-x}N}(x) &= 0.285x + 0.247(1-x). \end{aligned} \tag{V.29}$$

To find ν at a specific composition, simply use the corresponding value of x.

The Poisson's ratio is also defined in terms of the applied biaxial strain ε_1 and the ensuing uniaxial strain ε_3 [201]:

$$\nu(x) = -\frac{\varepsilon_3(x)}{\varepsilon_1(x)}, \tag{V.30}$$

with $\varepsilon_3 = \varepsilon_z$. So one calculates ν from Eq. (V.28) and extracts the values of ε_1 from Fig. V.13, then uses Eq. (V.30) to evaluate ε_3. Assuming ν to be positive (which is mostly the case), the minus sign in Eq. (V.30) indicates that the strains ε_1 and ε_3 have opposite signs and thus opposite natures, i.e. if ε_1 induces a contraction of the sample ε_3 would induce an elongation, and vice versa. This fact is illustrated schematically in Figure V.15.

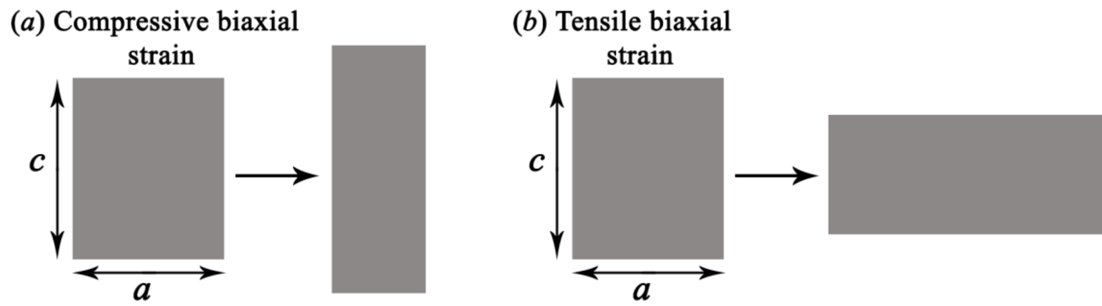

Figure V.15 Side-view of a hexagonal sample that demonstrates the Poisson effect. When a compressive biaxial strain is applied, as in (*a*), the sample compresses in the *xy*-plane (*a* decreases) and extends along the *z*-direction (*c* increases). The situation is reversed for the application of a tensile biaxial stain as shown in (*b*) (a similar figure can be found in [200]).

The variations of the uniaxial strain ε_3 along the *c*-axis with composition are depicted in Figure V.16 for the three alloys. From this figure, we notice that ε_3 is negative and decreases for AlGaN/GaN, positive and increases for InGaN/GaN, and changes its sign from negative to positive for InAlN/GaN. As expected, this behaviour of ε_3 is opposite of that of ε_1 shown in Fig. V.13, which corresponds to the common situation where the Poisson's ratio is positive [201]. Based on these results, restraining AlGaN (InGaN) to a GaN substrate extends (compresses) the alloy layer in the *x*- and *y*- directions and compresses (extends) it in the *z*-direction. InAlN/GaN is subjected to compression (for $x < 0.16$) and extension (for $x > 0.16$) in the *xy*-plane.

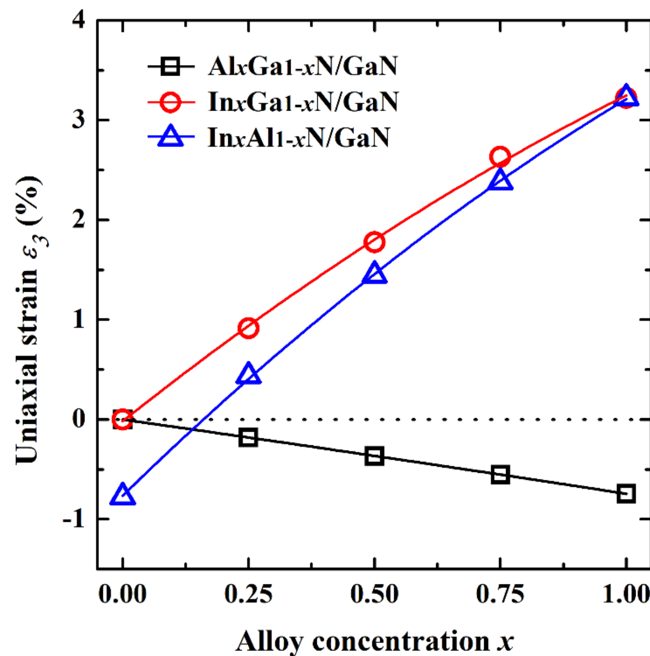

Figure V.16 Uniaxial strain produced by the applied biaxial strain versus concentration *x* for AlGaN/GaN, InGaN/GaN and InAlN/GaN. Zero strain is represented by the horizontal dotted line.

V.4.4 Lattice parameters

The biaxially-strained structures simulate the case of a wurtzite alloy epitaxially grown on an unstrained substrate (GaN here) along the polar direction [0001]. Recall that the lattice constant a is identical by construction for all alloys and concentrations x, i.e. $a_{alloy}(x) = a_{GaN}$ [78].The other two lattice parameters (lattice constant c and internal parameter u_{avg}) are expected to change due to the constraint of epitaxial matching, and thus they need to be optimized again. The relaxation of the lattice parameter c accounts for the Poisson effect and can be achieved by calculating the energy as a function of c. The strained lattice constant c is directly related to the uniaxial strain ε_3 that results from the biaxial strain ε_1:

$$\tilde{c}(x) = c(x)[1 + \varepsilon_3(x)], \qquad \text{(V.31)}$$

where the tilde symbol (~) denotes the strained structures and c is the zero-strain axial lattice constant. Instead of running an energy calculation, we compute c using Eq. (V.31), with the values of ε_3 being taken from Fig. V.16. The strained average internal parameter is obtained by an energy calculation based on the Hellman-Feynman method [153].

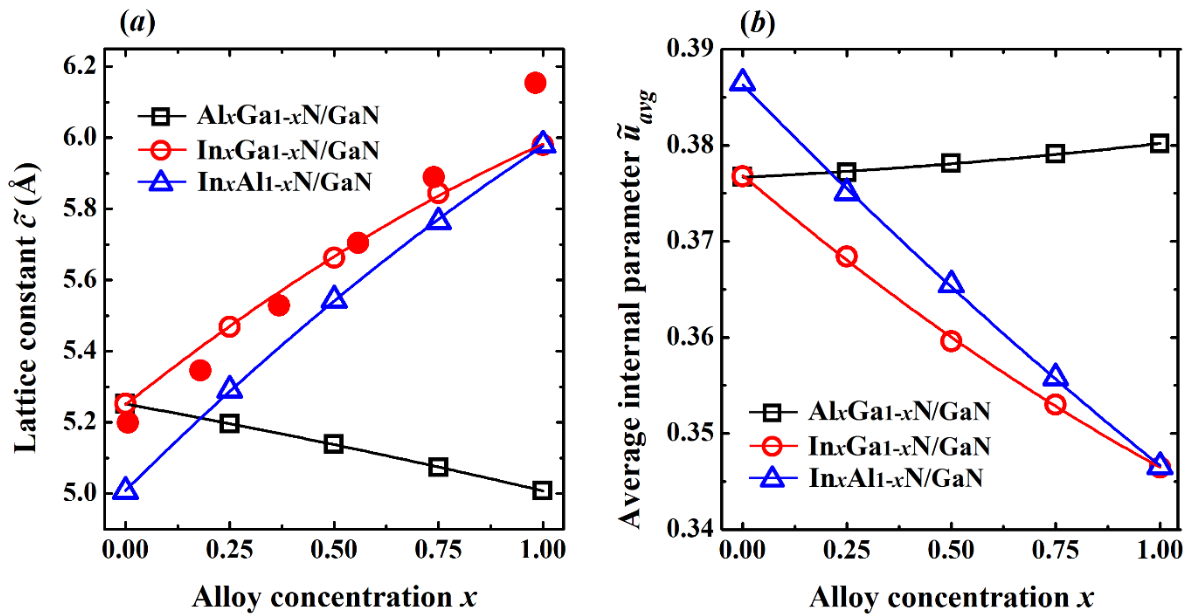

Figure V.17 Composition dependence of (a) the lattice constant $\tilde{c}$ and (b) average internal parameter $\tilde{u}_{avg}$ of biaxially-strained wurtzite AlGaN/GaN, InGaN/GaN and InAlN/GaN. The lattice constant a of these systems is equal to that of GaN. The data points represented by filled red symbols in panel (a) are experimental values for InGaN/GaN taken from Ref. [177].

The results for the lattice parameters $\tilde{c}$ and $\tilde{u}_{avg}$ of the strained ternary alloys are shown in Figure V.17. The fitting composition expressions of these lattice parameters in the epitaxially-strained case are as follows:

$$
\begin{aligned}
\tilde{c}_{Al_xGa_{1-x}N/GaN}(x) &= 5.01x + 5.25(1-x) + 0.03x(1-x),\\
\tilde{u}_{avg}^{Al_xGa_{1-x}N/GaN}(x) &= 0.380x + 0.376(1-x) - 0.001x(1-x),\\
\tilde{c}_{In_xGa_{1-x}N/GaN}(x) &= 5.98x + 5.25(1-x) + 0.20x(1-x),\\
\tilde{u}_{avg}^{In_xGa_{1-x}N/GaN}(x) &= 0.346x + 0.376(1-x) - 0.007x(1-x),\\
\tilde{c}_{In_xAl_{1-x}N/GaN}(x) &= 5.98x + 5.01(1-x) + 0.20x(1-x),\\
\tilde{u}_{avg}^{In_xAl_{1-x}N/GaN}(x) &= 0.347x + 0.387(1-x) - 0.005x(1-x).
\end{aligned}
\tag{V.32}
$$

With increasing Al content of AlGaN/GaN, the internal parameter increases (very slowly) while the lattice constant $\tilde{c}$ decreases. The reversed trend is observed in the case of In-containing alloys InGaN/GaN and InAlN/GaN, for which $\tilde{u}_{avg}$ decreases and $\tilde{c}$ increases with In content. These reversed variations are attributed to the different behaviour of the biaxial and uniaxial strains (see Figs. V.13 and V.16). Note that in every case discussed above, the variation of the lattice constant $\tilde{c}$ is consistent with the positive value of the Poisson ratio; that is, $\tilde{c}$ decreases (increases) in going from lower to higher tensile (compressive) strains, which is the case of AlGaN/GaN (InGaN/GaN and InAlN/GaN).

V.4.5 Piezoelectric polarization

The mismatch-biaxial and the corresponding uniaxial strains studied here contribute in a piezoelectric polarization P_{pz} [58,171]. The combination of spontaneous and piezoelectric components in heterostructures is known as the total polarization P_{tot}, which is given by [171]:

$$P_{tot}(x) = P_{sp}(x) + P_{pz}(x). \tag{V.33}$$

To access the piezoelectric polarization we need to calculate the formal polarization $\tilde{P}_{WZ}$ of the strained wurtzite structure. Then the piezoelectric polarization is computed as the difference between $\tilde{P}_{WZ}$ obtained in this calculation and the formal polarization P_{WZ} of the equilibrium (unstrained) wurtzite structure calculated previously in Sec. V.3:

$$P_{pz}(x) = \tilde{P}_{WZ}(x) - P_{WZ}(x), \tag{V.34}$$

where $\sim$ means that the formal polarizations are those of the biaxially-strained structures (i.e. lattice-matched to GaN). Note that there is no H index in P_{pz} as in $P_{sp,H}$. This is because the piezoelectric behaviour is determined by the polarization of the wurtzite structure after and before applying the strain, without any role of an external reference (neither the hexagonal nor the trigonal structures). At equilibrium or zero-strain, the total polarization coincides with the spontaneous one, yielding a vanishing piezoelectric polarization.

The results obtained of the piezoelectric polarization are depicted in Figure V.18, where a non-linearity is observed as opposed to the spontaneous polarization results. Except for AlGaN/GaN, the piezoelectric polarization changes non-linearly with respect to alloy composition. Regarding the sign of the piezoelectric polarization, it is negative (positive) over the entire concentration range for AlGaN/GaN (InGaN/GaN). It is established that for wurtzite systems, the piezoelectric polarization is always negative for layers under tensile biaxial strain (the case of AlGaN/GaN) and positive for layers under compressive biaxial strain (the case of

InGaN/GaN) [158]. Such a claim deserves a demonstration. To do so we consider the following formula of the piezoelectric polarization [26,158]:

$$P_{pz} = 2\varepsilon_1 \left(e_{31} - e_{33}\frac{C_{13}}{C_{33}}\right), \tag{V.35}$$

where e_{ij} are the piezoelectric coefficients and ε_1 and C_{ij} have the same meaning as before. This equation is only applied to biaxially-strained wurtzite crystals. For such systems, e_{31} is negative whereas $e_{33}\, C_{13}/C_{33}$ is positive. However, the absolute value of the first term is about one order of magnitude greater than that of the second one, which means that $e_{31} - e_{33}\, C_{13}/C_{33}$ is always negative [55]. The sign of the piezoelectric polarization then only depends on the sign of the applied strain: P_{pz} would be negative for tensile biaxial strains ($\varepsilon_1 > 0$) and positive for compressive strains ($\varepsilon_1 < 0$). The results of our simulation are fully consistent with this reasoning (see Fig. V.18). For InAlN/GaN a sign reversal is observed: the piezoelectric polarization vanishes at the composition $x = 0.33$, meaning $In_{0.33}Al_{0.67}N$ is naturally lattice-matched to GaN. However, we can see from Figs. V.13 and V.16 that there is no strain for $x = 0.16$, so P_{pz} should disappear at $x = 0.16$, not at $x = 0.33$ as Fig. V.18 indicates. We will address this apparent contradiction in more detail in the next section.

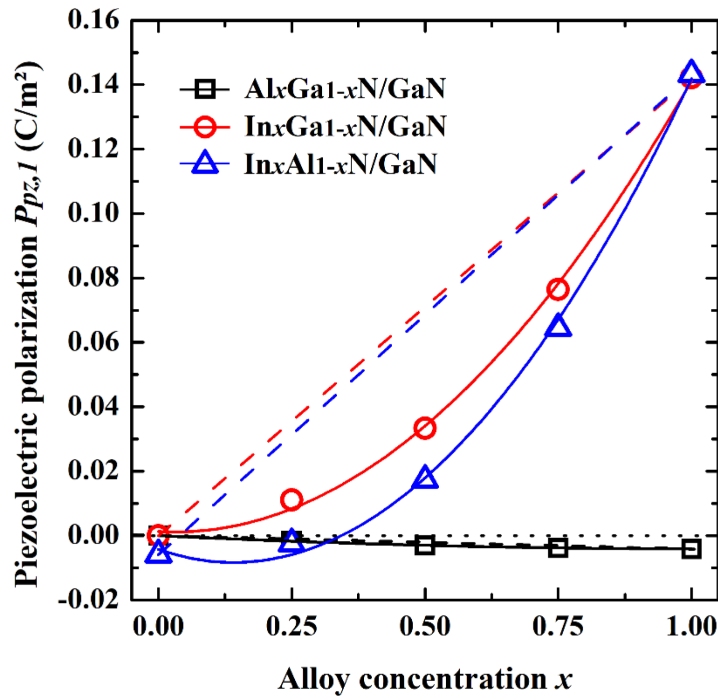

Figure V.18 Variation with composition of the piezoelectric polarization of the wurtzite III-nitride alloys AlGaN, InGaN and InAlN grown on a relaxed GaN substrate. The lattice constant a is fixed to the calculated value of GaN (3.23 Å), and the lattice parameters c and u are fully reoptimized. The quadratic and linear curves are as in Fig. V.7. The dotted horizontal line indicates zero polarization.

Fitting the calculated data to a second-order polynomial in x yields the following expressions for P_{pz} (in C/m²):

$$\begin{aligned} P_{pz}^{Al_xGa_{1-x}N/GaN}(x) &= -0.00414x + 0(1-x) - 0.00375x(1-x), \\ P_{pz}^{In_xGa_{1-x}N/GaN}(x) &= 0.142x + 0(1-x) - 0.149x(1-x), \\ P_{pz}^{In_xAl_{1-x}N/GaN}(x) &= 0.142x - 0.0059(1-x) - 0.204x(1-x). \end{aligned} \quad \text{(V.36)}$$

The bowing parameter b is 0.00375 C/m² for AlGaN/GaN, 0.149 C/m² for InGaN/GaN and 0.204 C/m² for InAlN/GaN. Since b is positive, all the investigated systems exhibit an upward bowing.

V.4.6 Effect of the supercell dimension on polarization

Unlike the spontaneous polarization, the value of the piezoelectric polarization depends on the dimension of the supercell used in the simulation, or in the language of the Berry-phase theory (see Sec. III.6.2) it depends on the polarization branch n. The supercells used to obtain the results of Fig. V.18 and Eq. (V.36) are 1×1×4 wurtzite supercells, so we alternatively express Eq. (V.34) as:

$$P_{pz,1} = \tilde{P}_{WZ,1} - P_{WZ,1}, \quad \text{(V.37)}$$

where the subscript 1 indicates that the formal polarizations $\tilde{P}_{WZ,1}$ and $P_{WZ,1}$ and the effective polarization $P_{pz,1}$ belong to the branch n= 1. Eq. (V.37) can be applied to any supercell of dimension $1\times1\times m$. For $n\times n\times m$ wurtzite supercells, where the branch $n \geq 2$, the piezoelectric polarization is:

$$P_{pz,n} = \tilde{P}_{WZ,n} - P_{WZ,n}, \quad \text{(V.38)}$$

where $\tilde{P}_{WZ,n}$ is related to $\tilde{P}_{WZ,1}$ by:

$$\begin{aligned} \tilde{P}_{WZ,n} &= \tilde{P}_{WZ,1} + \tilde{P}_{q,WZ,n} \\ &= \tilde{P}_{WZ,1} + \frac{\tilde{P}_{q,WZ,1}}{n^2}, \end{aligned} \quad \text{(V.39)}$$

and $P_{WZ,n}$ is related to $P_{WZ,1}$ by:

$$\begin{aligned} P_{WZ,n} &= P_{WZ,1} + P_{q,WZ,n} \\ &= P_{WZ,1} + \frac{P_{q,WZ,1}}{n^2}. \end{aligned} \quad \text{(V.40)}$$

The polarization quanta of the branch n= 1 are:

$$\tilde{P}_{q,WZ,1} = \frac{2e}{\sqrt{3}a_{GaN}^2}, \quad \text{(V.41)}$$

for alloys coherently strained to GaN (i.e. their lattice constant is a_{GaN}), and:

$$P_{q,WZ,1} = \frac{2e}{\sqrt{3}a^2}, \quad \text{(V.42)}$$

for unstrained alloys whose equilibrium lattice constant a is given by Eq. (V.3). Putting Eqs. (V.39-V.42) into Eq. (V.38) allows us to obtain:

$$P_{pz,n} = \tilde{P}_{WZ,1} - P_{WZ,1} + \frac{2e}{\sqrt{3}n^2}\left(\frac{1}{a_{GaN}^2} - \frac{1}{a^2}\right). \quad \text{(V.43)}$$

This is basically identical to equation (III.34) of Sec. III.6.2, which describes the piezoelectric polarization induced by a uniaxial strain applied along the c-axis. Eq. (V.43), on the other hand, evaluates the same quantity for a biaxial strain applied to the a- and b-axes. The important point here is that P_{pz} is branch dependent as its value varies with the integer n.

Figure V.19 displays the composition dependence of the piezoelectric polarization of InAlN/GaN predicted using 1×1×4 (16-atom) and 2×2×2 (32-atom) wurtzite supercells. The two types of supercell provide different results in terms of values and curvature, which confirms the opening statement of the present section. The data points of the 1×1×4 supercell correspond to the branch n= 1 and are found by using Eq. (V.37). The fitted expression is taken from the last line of Eq. (V.36), which is:

$$P_{pz,1}^{In_xAl_{1-x}N/GaN}(x) = 0.142x - 0.0059(1-x) - 0.204x(1-x). \quad \text{(V.44)}$$

The P_{pz} values of the 2×2×2 supercell, whose branch n= 2, can be obtained by two methods: either by simulating the 2×2×2 supercells directly and using Eq. (V.38) (with n= 2), or from the data of the 1×1×4 supercell with the help of Eq. (V.43) (i.e. without constructing 2×2×2 supercells). The results are expressed by:

$$P_{pz,2}^{In_xAl_{1-x}N/GaN}(x) = 0.228x - 0.035(1-x) - 0.136x(11-x). \quad \text{(V.45)}$$

As stated at the end of the previous section, the piezoelectric polarization of InAlN/GaN calculated using a 1×1×4 supercell vanishes at the composition x= 0.33 [i.e. Eq. (V.44) equals zero for x= 0.33]. This is in contrast with the strain analysis (Figs. V.13 and V.16), which show that P_{pz} should vanish at the lower alloy concentration of x= 0.16. From the continuous curve of Fig. V.19 or Eq. (V.45) we can see that P_{pz} is zero at x= 0.21 for 2×2×2 supercells, which is much closer to the composition where the strain disappears x= 0.16. So it seems that the 2×2×2 supercells are more adequate to study the piezoelectric polarization of wurtzite InAlN/GaN and perhaps the other III-nitride alloys (the use of 3×3×3 supercells, or branch n= 3, makes P_{pz} vanishes at x= 0.25).

The discussion in this section and section III.6.2 indicates that the dependence of the piezoelectric polarization on the choice of supercell (or the polarization branch n) questions the fact that this quantity is a measurable observable, even though it is defined as a polarization difference. To access the measured piezoelectric response of the wurtzite alloys (which is independent of the polarization branch), one should calculate the proper piezoelectric coefficients $e_{15}(x)$, $e_{31}(x)$ and $e_{33}(x)$ [9,26,140].

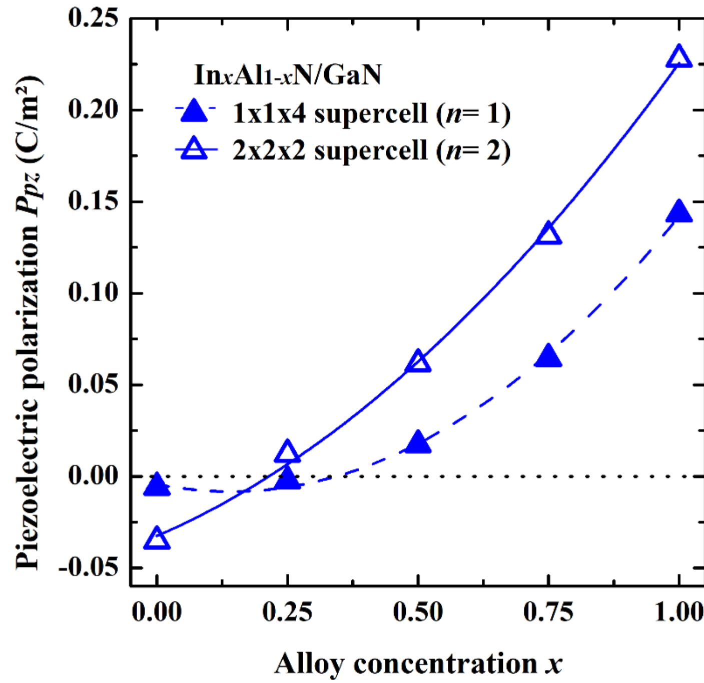

Figure V.19 Piezoelectric polarization of the biaxially-strained ternary alloy InAlN/GaN predicted by 1×1×4 wurtzite supercell (filled symbols and discontinuous curves) and 2×2×2 supercell (open symbols and continuous curves). The two supercells give different values for the same system because P_{pz} varies with basal dimensionality n of the supercell [see Eq.(V.43)]. Most notably, the piezoelectric polarization is zero at x= 0.33 for n=1 and at x= 0.21 for n= 2.

V.5 Results for the quaternary alloy AlInGaN/GaN

V.5.1 Structural optimization

We now address the case of the quaternary alloy AlInGaN grown on a GaN buffer layer. Using the theoretical approach described earlier, we determine the strained crystal structure of AlInGaN/GaN. We will not present the numerical results; we will give instead a sketch of the approach with the different formulae used during the structural optimization. The supercells used to model this alloy are as usual 1×1×4 supercells [e.g. the supercell shown in Fig. V.1 (c)]. First of all the basal lattice constant a is fixed to that of GaN: $a_{Al_xIn_yGa_{1-x-y}N}(x,y) = a_{GaN}$. The strained axial lattice constant $\tilde{c}$ is calculated from an equation similar to Eq. (V.31), namely:

$$\tilde{c}(x,y) = c(x,y)[1 + \varepsilon_3(x,y)]. \qquad \text{(V.46)}$$

The zero-strain lattice constants a and c are obtained by the linear interpolation of Vegard's law rather than by energy minimization. This is justified by the fact that the lattice constants of the ternary alloys are roughly linear functions of compositions (*c.f.* Fig. V.3). For the equilibrium lattice constants a and c of the quaternary alloys AlInGaN, Vegard's law is expressed as:

$$\begin{aligned} a_{Al_xIn_yGa_{1-x-y}N}(x,y) &= xa_{AlN} + ya_{InN} + (1-x-y)a_{GaN}, \\ c_{Al_xIn_yGa_{1-x-y}N}(x,y) &= xc_{AlN} + yc_{InN} + (1-x-y)c_{GaN}. \end{aligned} \qquad \text{(V.47)}$$

Next we compute the uniaxial strain ε_3 generated by the epitaxial growth. To do so the applied biaxial strain ε_1 is derived using:

$$\varepsilon_1(x,y) = \frac{a_{GaN} - a_{Al_xIn_yGa_{1-x-y}N}(x,y)}{a_{GaN}}. \tag{V.48}$$

This expression is analogous to equation (V.23) for the ternary alloys. We also provide Poisson's ratio ν by employing Vegard's law:

$$\nu_{Al_xIn_yGa_{1-x-y}N}(x,y) = x\nu_{AlN} + y\nu_{InN} + (1-x-y)\nu_{GaN}. \tag{V.49}$$

Since we have both ε_1 and ν, ε_3 can be calculated by:

$$\nu(x,y) = -\frac{\varepsilon_3(x,y)}{\varepsilon_1(x,y)}. \tag{V.50}$$

At variance with the strained lattice constant $\tilde{c}$, the strained (average) internal parameter $\tilde{u}_{avg}$ is computed through an energy-minimization process as we did with ternary alloys in the previous sections.

V.5.2 Interface polarization charge

The heterostructure AlInGaN/GaN can be viewed a quantum well. The formal polarization differs for each side of the interface, and this abrupt change in polarization induces a two-dimensional polarization charge density $\sigma(x,y)$ [34–36], which in the case of AlInGaN/GaN is expressed as:

$$\sigma(x,y) = P_{WZ,1}^{GaN} - \tilde{P}_{WZ,1}^{Al_xIn_yGa_{1-x-y}N/GaN}(x,y). \tag{V.51}$$

Here, $P_{WZ,1}^{GaN}$ is the formal polarization of the bottom layer and $\tilde{P}_{WZ,1}^{Al_xIn_yGa_{1-x-y}N/GaN}$ is that of the top layer. Both layers are modelled by a 1×1×4 supercell (hence the index 1 in the polarizations). Note that since the GaN substrate is unstrained, the polarization of this layer is determined by the formal polarization of wurtzite GaN at equilibrium. As in the case of the piezoelectric polarization, the hexagonal reference structure is not employed for the determination of the polarization interface charge. Indeed, the reference structure (hexagonal or trigonal or other structures) is only needed to study the spontaneous polarization. As we saw previously in Sec. I.4.2, the formula given by Eq. (V.51) is referred to as the interface theorem [38]. We have verified that AlInGaN/GaN preserves its band gap for all compositions studied, so our use of the interface theorem is justified. Before moving on, we mention that for $n \times n \times m$ supercells, where $n \geq 2$ (e.g. a 2×2×2 supercell), Eq. (V.51) becomes:

$$\sigma(x,y) = P_{WZ,n}^{GaN} - \tilde{P}_{WZ,n}^{Al_xIn_yGa_{1-x-y}N/GaN}(x,y). \tag{V.52}$$

Following the procedure of Sec. V.4.6, σ is computed by a formula similar to Eq. (V.43), which is:

$$\sigma(x,y) = P_{WZ,1}^{GaN} - \tilde{P}_{WZ,1}^{Al_xIn_yGa_{1-x-y}N/GaN}(x,y) + \frac{2e}{\sqrt{3}n^2}\left(\frac{1}{a_{GaN}^2} - \frac{1}{a_{GaN}^2}\right). \quad \text{(V.53)}$$

Notice that the quantum of polarization of the GaN and AlInGaN layers has the same value for all compositions ($P_{q,\mathrm{WZ},1}^{GaN} = \tilde{P}_{q,WZ,1}^{Al_xIn_yGa_{1-x-y}N/GaN}$) due to the condition $a_{Al_xIn_yGa_{1-x-y}N} = a_{GaN}$. This leads to the conclusion that Eq. (V.52) for branch $n \geq 2$ always reduces to Eq. (V.51) for the branch n= 1. Thus, one similarity between the polarization charge of biaxially-strained wurtzite systems and the spontaneous polarization is that both quantities are independent of the branch (we have discussed this point in Sec. III.6.3).

Using the Berry-phase method as implemented in BerryPI, we compute the formal polarization of AlInGaN/GaN for each possible combination of x and y allowed by our choice of supercell. The polarization charge that bounds at the interface can then be calculated in straightforward manner using equation (V.51). In Figure V.20 we display, as a function of alloy concentrations x and y, the values of the interface polarization charge of wurtzite AlInGaN/GaN. The first observation that can be made is with regards to the sign of σ: the AlInGaN/GaN interface has a negative polarization charge over the majority of the compositional space, meaning this interface when p-doped will attract holes, which results in the formation of a two-dimensional hole gas (2DHG) [202] desirable in power electronics. There is also a relatively narrow region where the charge is positive. The latter should tend to form a 2D electron gas (2DEG) [203] which can be exploited in high electron mobility transistors (HEMT). Additionally, large charges of the order of 10^{13} cm^{-2} can be found, which is the same order of magnitude for ternary nitride heterostructures (see Sec. V.6).

Heterostructures based on III-nitride alloys are the main building blocks of various optoelectronic applications. AlInGaN systems have been already exploited in the fabrication of green, white and ultraviolet light-emitting diodes [204–206]. However, there are still some polarization-related obstacles to achieving high-efficiency devices. In the lighting industry, one bottleneck limiting device performance arises from the existence of strong electric fields that originate from polarization charges at the interface of heterostructures [4,207]. The fabrication of light emitters with high optical efficiency requires the minimization of these polarization fields. As already proposed by many authors [78,208,209], a promising method to effectively reduce polarization effects is by tuning the composition of the alloyed compounds. Looking again at Figure V.20, it is worth emphasizing that the polarization charge vanishes at certain compositions. The black curve in Fig. V.20 indicates zero polarization charges: every point on this curve gives the Al and In contents for which σ is null (e.g. x= 0.438 and y= 0.115). The resulting heterostructures are free of internal electrostatic fields and hence are advantageous for high-efficiency optical devices, including lasers, light-emitting diodes, and photovoltaic solar cells.

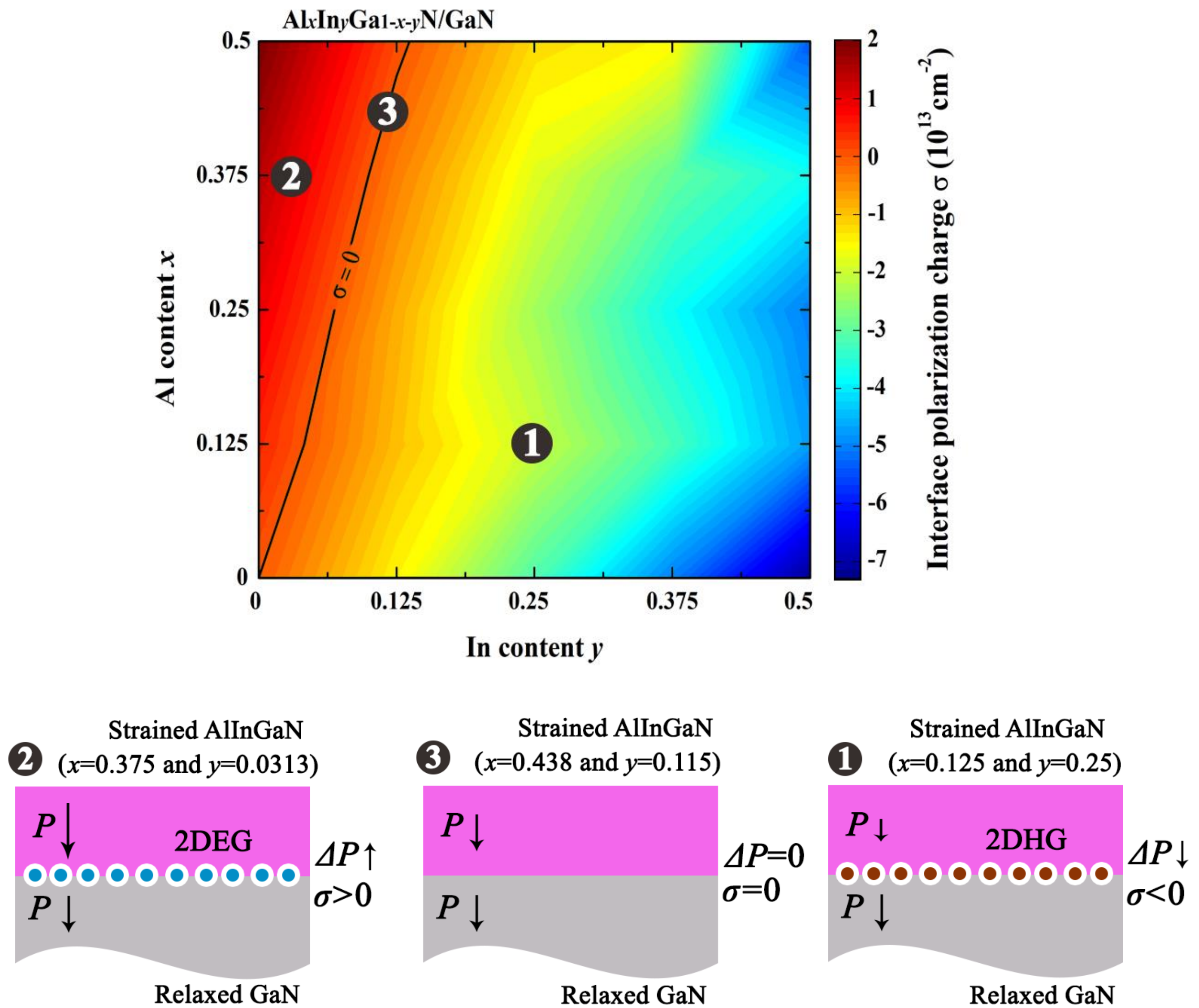

Figure V.20 Contour plot of the electric charge density induced by polarization discontinuities at the interface of wurtzite AlInGaN/GaN heterostructure. This charge has the same unit as polarization, i.e. C/m², but is expressed here in electrons per cm² (or simply cm^{-2}). The conversion from C/m² to cm^{-2} is done by dividing σ by the charge of one electron (1.6×10^{-19} C) to get rid of the Coulomb (C) and then by dividing by 10^4 to convert m² to cm², which gives a conversion factor of 6.25×10^{14}. The black curve corresponds to the Al and In molar fractions for which the polarization charge vanishes. Heterostructure (1) exhibits a negative polarization charge which will be screened by holes in p-type samples, leading to the formation of a two-dimensional hole gas (2DHG) at the interface between AlInGaN and GaN. The situation is reversed in heterostructure (2), where the positive polarization charge attracts electrons, generating a two-dimensional electron gas (2DEG). No charge accumulation takes place in heterostructure (3) due to the polarization charge being zero.

V.6 Comparison to other theoretical and experimental data

V.6.1 Evaluation of polarization charge in wurtzite ternary alloys

We present in the following an example of calculating the interface polarization charge of an alloy-based heterostructure crystallizing in the wurtzite phase. Table V.3 reports the results of such a calculation for the specific case of InGaN/GaN. After the 1×1×4 wurtzite supercells of biaxially-strained InGaN are optimized for each alloy concentration x, one starts by computing the formal polarizations $\tilde{P}_{WZ,1}^{In_xGa_{1-x}N/GaN}$. This has already been done in Sec. V.4. The polarization charge σ (expressed in C/m² or cm^{-2}) is accessed via the interface theorem as described in detail in Sec. V.5.2. For InGaN/GaN, equation (V.51) take the following form:

$$\sigma(x) = P_{WZ,1}^{GaN} - \tilde{P}_{WZ,1}^{In_xGa_{1-x}N/GaN}(x). \qquad \text{(V.54)}$$

These steps can be followed to obtain the interface polarization charge for AlGaN/GaN and InAlN/GaN and any other wurtzite ternary alloy.

Table V.3 Parameters needed in the evaluation of the polarization charge σ for different compositions x of $In_xGa_{1-x}N$/GaN heterostructure (see text).

x	$P_{WZ,1}^{GaN}$ (C/m²)	$\tilde{P}_{WZ,1}^{In_xGa_{1-x}N/GaN}$ (C/m²)	σ (C/m²)	σ (10^{13} cm^{-2})
0	−0.477	−0.477	0	0
0.25	−0.477	−0.426	−0.051	−3.196
0.5	−0.477	−0.360	−0.116	−7.280
0.75	−0.477	−0.316	−0.160	−10.02
1	−0.477	−0.263	−0.214	−13.34

V.6.2 Accuracy of the theoretical calculations

In order to gauge the accuracy of our calculated results, an extensive comparison with the literature is performed. The available experimental data is for polarization-induced charges and fields, rather than polarizations themselves. So to be able to compare to experiment we calculate the polarization charge at the interface of the ternary-alloy heterostructures AlGaN/GaN, InGaN/GaN and InAlN/GaN. Some experimental studies report the polarization field E that builds up at the heterointerface of quantum wells. For our purposes, we perform a field-charge (E-σ) conversion using a simple parallel-plate capacitor model, namely $E = \sigma/\varepsilon_0\varepsilon$ [26,210], where ε_0 is the permittivity of free space and ε is the relative dielectric constant. The latter is taken to be 9.2 for AlN [211], 10 for GaN [212], 15 for InN [213] and a linear interpolation of these values is used for the alloys. We also compare our charge values to previous theoretical studies. The comparison is summarized in Figure V.21.

A. AlGaN/GaN:

Reported values for the AlGaN/GaN system [Fig. V.21 (*a*)] are more abundant. For low and moderate Al content, the agreement between the present work is not too bad with Ambacher's results [158] but is less good with Dreyer's values [26]. For higher Al content the deviation between the three sets of results increases. To achieve consistency with our calculations, we consider comparisons only with measurements that report polarization charges over a composition range, rather than at singular composition values. There is a very good agreement between our calculations and the data reported by Arulkumaran et *al.* [214] obtained using Hall-effect measurements. The values from Susilo et *al.* [215] and Smorchkova et *al.* [216], extracted from capacitance-voltage measurements, also show reasonable agreement with our simulation. Our predicted charges seem to slightly underestimate (overestimate) the results of Davidsson et *al.* [217] (Ng et *al.* [218]).

B. InGaN/GaN:

For the case of InGaN/GaN [Fig. V.21 (*b*) or Table V.3], our results seem to be in accordance with those reported by Dreyer et *al.* [26] and Ambacher et *al.* [158] over more or less the full compositional range. With regards to comparison with experiment, the available experimental sources only report one value of polarization charge at a particular alloy concentration [219–223]. Our predicted values are in line with experimental observations, appearing to be to a lower bound to the data.

C. InAlN/GaN:

There is lack of published results regarding the polarization-induced charge of InAlN/GaN [Fig. V.21 (*c*)]. No experimental reports are available for this heterostructure. Our polarization charge agrees well with the one previously calculated by Ambacher et *al.* [158]. This agreement extends over the whole interval of alloy composition. The only other theoretical result seems to be that obtained by Caro et *al.* [208], which our simulation slightly underestimates. We point out that Caro et *al.* have calculated the built-in electric field from the polarization potential of the quantum well. Both Ambacher et *al.* and Caro et *al.* provided results for $Al_xIn_{1-x}N$/GaN. The values of $In_xAl_{1-x}N$/GaN can be found by simply reversing the molar fraction of Al and In, e.g. $Al_{0.25}In_{0.75}N$ is the same as $In_{0.75}Al_{0.25}N$.

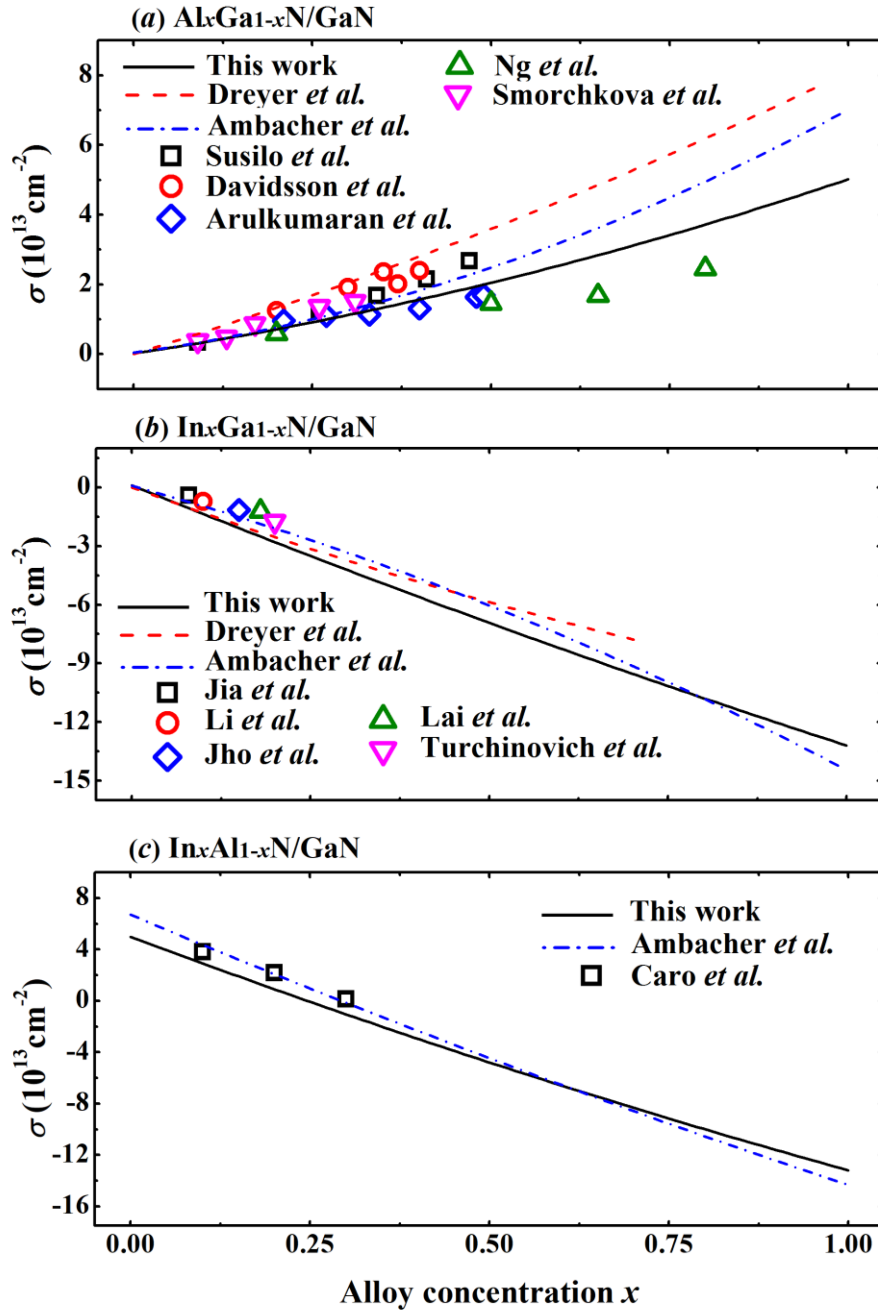

Figure V.21 Interface polarization charge σ of wurtzite (*a*) AlGaN/GaN, (*b*) InGaN/GaN and (*c*) InAlN/GaN. We compare the present results (black curves) to available literature data. Red dashed and blue dashed-dotted curves correspond to the simulation results of Dreyer et *al.* [26] and Ambacher et *al.* [158], respectively. Data points in (*a*) and (*b*) are experimental values taken from: Susilo et *al.* [215], Davidsson et *al.* [217], Arulkumaran et *al.* [214], Ng et *al.* [218], Smorchkova et *al.* [216], Jia et *al.* [219], Li et *al.* [220], Jho et *al.* [221], Lai et *al.* [222] and Turchinovich et *al.* [223]. Some of these values are modified from field to charge for comparison. Data points in (*c*) are theoretical values obtained by Caro et *al.* [208]. See text for a thorough discussion.

D. Summary:

To the best of our knowledge there are no other works on the polarization properties of AlInGaN/GaN. Future calculations and measurements are needed to compare our results with. Overall, the theoretical predictions of the present work are in reasonably good agreement with experimental investigations. There are however deviations due to some uncertainties. Several factors can contribute to discrepancies observed between theory and experiment. DFT provides a zero-temperature and zero-pressure description of materials, whereas most experiments are done at higher temperatures and pressures [224,225]. These can have a significant effect on the measured piezoelectric response of materials. In addition to temperature and pressure effects, theoretical investigations deal with ideal systems, i.e. perfectly ordered crystals, whereas experiments are influenced by the quality of the material samples under study, given by the possible existence of crystalline defects [195], such as dislocations and stacking faults. The influence of different types of defects on the polarization properties could be an interesting topic to be explored in future studies (in fact we have addressed a part of this issue in Chapter VII). Other factors that might contribute to discrepancies are the complexity of the measurement procedure and unrealistic theoretical models used to interpret the experimental results [226,227].

V.7 Conclusion

We dealt in this chapter with the polarization of the wurtzite III-nitride alloys. We considered both the equilibrium and biaxially-strained configurations. The equilibrium structure of the 16-atom (1×1×4) supercells was used to study the spontaneous polarization of the ternary alloys AlGaN, InGaN and InAlN. But contrary to what we did in chapter IV, the structure functioning as a reference was not the trigonal structure, it was instead the layered-hexagonal phase. Hence, the spontaneous polarization in this chapter was defined as the formal polarization difference between the wurtzite and hexagonal structures.

We showed that when using the hexagonal structure as a reference, the wurtzite formal polarization presents a discontinuity when the internal parameter u equals 0.5, which is the value of the hexagonal internal parameter. Removing this discontinuity requires shifting the polarization branch by one quantum of polarization for the branch n= 1. The spontaneous polarization referenced to the hexagonal structure was found to be almost a linear function of alloy composition. We also made a comparison between the predictions of the hexagonal and trigonal (or equivalently zincblende) structures. The two references give different results regarding the value, sign and bowing of the spontaneous polarization of the investigated alloys. Based on our experience, we recommended the use of wurtzite supercells with dimension $1\times1\times m$. Using $n\times n\times m$ (m and n are integers) supercells needs a special treatment that might not be obvious to the beginner. We also emphasized the important fact that both $1\times1\times m$ and $n\times n\times m$ supercells must predict the same spontaneous polarization value for the same system.

We used the strained structures of the ternary alloys to investigate their piezoelectric polarization. The applied biaxial stain was provided by a GaN substrate, and the ensuing uniaxial strain was obtained via the Poisson's ratio (calculated using the elastic constants).

There was no need for a reference structure to calculate the strain-induced piezoelectric polarization. We computed the piezoelectric polarization as the difference between the formal polarization of the equilibrium and strained wurtzite geometries, and found it to vary non-linearly with alloy concentration x for InGaN/GaN and InAlN/GaN (the variation is linear for AlGaN/GaN). Unlike the spontaneous component of the total polarization, which is independent of the polarization branch, we found the piezoelectric component to be branch dependent, i.e. different supercells result in different values of P_{pz}. As explained in Chapter III, this is because the in-plane lattice constant a (and consequently the polarization quantum) of strained crystal cells varies with the applied strain.

After studying the nitride ternary alloys, we investigated the structure and polarization of the quaternary alloy AlInGaN lattice-matched to GaN. We did not calculate the variation with composition of the spontaneous and piezoelectric polarizations of this alloy. Rather, we studied another polarization property, namely the polarization charge that develops at the interface between AlInGaN and GaN. We calculated the charge σ as the difference between the formal polarization of strained AlInGaN and unstrained GaN. The contour plot of the polarization charge revealed the existence of many Al and In contents (x and y respectively) for which the charge is zero. This observation is relevant to the optoelectronic industry, since the performance and lifetime of many instruments, such as LEDs, is plagued by the electric fields produced by the interface polarization charge. As such, we showed that composition engineering offers the possibility to solve this problem by reducing the interface polarization charge. The same quantity of the ternary alloys AlGaN/GaN, InGaN/GaN and InAlN/GaN was also investigated. The goal was to assess the validity of our calculations by comparing them to simulations and experiments from the literature. A reasonably good agreement was found, which validates our numerical results and the theoretical approach followed to determine them.

Chapter VI

Influence of compressive uniaxial strain on the piezoelectric response of wurtzite III-nitrides and II-oxides

VI.1 Introduction

Piezoelectric materials are now exploited in numerous technological applications, including transducers [228], pressure sensors [229] and surface acoustic wave resonators [230] to name a few. The device concept of these systems is based on the conversion of electric polarization (or equivalently electric voltage) into mechanical strain or vice versa [131]. It is therefore desirable to establish an understanding of the factors that enhance this electromechanical conversion in order to improve device performance. As will be shown later on, one promising avenue to do this is by tuning the uniaxial strain applied to the piezoelectric materials.

Carefully controlled uniaxial compression has long been used to study semiconductors and to reveal new information regarding their properties [231,232]. Many high-pressure experiments have been designed to highlight the effects of uniaxial strain along different crystallographic directions. For instance, combined uniaxial and hydrostatic pressures have been used to improve the quantum efficiency of commercial semiconductor lasers [233]. The transport properties of uniaxially-strained lanthanum-strontium thin films have been also measured using standard isosceles cantilever [234]. In the piezoelectric industry, transducers based on ferroelectric ceramics usually operate under pressure conditions, and an experimental study was carried out to quantify the effect of applied uniaxial strain on the piezoelectric, dielectric and mechanical responses of the samples [235]. In addition to this, application of uniaxial strain was observed to change the symmetry of the crystalline structure, e.g. a [100] strain is expected to lower the cubic symmetry to the tetragonal one [231].

Group III-nitrides and II-oxides crystallizing in the wurtzite structure have emerged as attractive candidates for the piezoelectric applications mentioned above [236–238]. Indeed, these compounds were found to exhibit large polarizations, which accounts for a much stronger piezoelectric effect compared to other conventional III-V and II-VI materials [144,148]. The impact of strain on the piezoresponse of wurtzite nitrides and oxides has been theoretically studied via first-principles methods. Most of these investigations have focused on the technologically relevant case of pseudomorphically grown structures, in which the strain is biaxial and is due to an underlying substrate [158,208,239,240]. However, the effect of uniaxial strain on piezoelectricity for these material system is somewhat lacking from the literature.

In the present chapter we investigate the effect that imposing a uniaxial strain has on the structural and piezoelectric properties of wurtzite crystals, taking III-nitrides XN (X=Al, Ga and In) and II-oxides YO (Y=Zn and Be) as case studies. In particular, we report the dependence of the lattice parameters, piezoelectric polarization and piezoelectric coefficient as a function of compressive uniaxial strain applied along the *c*-axis. Our main findings are fourfold: (i) we

identify a strain-induced phase transition from the wurtzite to the layered-hexagonal structure, (ii) the rapid non-linear increase with biaxial strain of piezoelectric polarization reported in previous studies is confirmed here for uniaxial strain, (iii) the piezoelectric coefficient is found to increase under compressive uniaxial strain in a linear-like fashion, and (iv) the key factor leading to the enhanced piezoelectric effect is the strain sensitivity of the wurtzite internal parameter. The theoretical methodology employed is fully presented, and can be used as a recipe to calculate the uniaxial-strain dependence of the piezoelectric properties of other wurtzite compounds as well. Most of the material presented here can be found in our research article: Benbedra et *al.*, J. Phys. D: Appl. Phys. 56, 385304 (2023).

VI.2 Computational details

Physical properties of the materials under study are obtained within the framework of density functional theory (DFT) [105] as implemented in the WIEN2k software package [125] in the context of the full-potential linearized augmented plane wave (FP-LAPW) method [119]. The exchange-correlation interactions are parameterized using the Perdew, Burke and Ernzerhof generalized gradient approximation (PBE-GGA) [110]. For a reason described below, we also use the modified Becke-Johnson (mBJ) approximation [113]. Following the FP-LAPW method, the Kohn-Sham wavefunctions are expanded on two different basis sets: these are atomic-like orbitals and plane waves. The cutoff of the former expansion is set to l_{max}= 10, while the cutoff of the latter is the product $R_{MT}^{min}K_{max}$= 8.5, where l_{max} is the angular quantum number associated with the maximum angular momentum, R_{MT}^{min} is the smallest muffin-tin radius, and K_{max} is the norm of the highest wave vector in the plane-wave expansion. The first Brillouin zone is sampled uniformly using a 10×10×10 mesh, which corresponds to 1000 k-points. We set the energy that separates core and valence electrons to be equal to −6 Ry. The radii R_{MT} of muffin-tin spheres centered at individual atoms are chosen as follows: 1.80, 2.00, 2.10, 1.50, 1.40, 2.05 and 1.60 Bohr for Al, Ga, In, N, Be, Zn and O, respectively. Total-energy calculations are considered to be converged when the energy difference is less than 10^{-4} Ry and the residual forces on atoms are below 10^{-4} Ry/Bohr. Finally, polarization properties are computed as finite differences using the Berry-phase theory [12,13] as implemented in BerryPI [141].

VI.3 Results

VI.3.1 Lattice constants

Before studying the influence of uniaxial strain, a careful determination of the equilibrium structure is needed. The wurtzite phase is completely defined by three parameters: the basal lattice constant a, the axial lattice constant c and the internal parameter u such that the product uc is the length of the cation-anion bond parallel to the c-axis [148]. The equilibrium lattice parameters required for the calculations are gathered in Table VI.1 for each compound. We find that our calculated values agree well with the reported experimental data.

Table VI.1 Calculated equilibrium lattice constants *a* and *c*, the internal parameter *u* (in units of *c*) and the Poisson's ratio ν within the GGA approximation for wurtzite AlN, GaN, InN, BeO and ZnO.

Material	*a* (Å)		*c* (Å)		*u*		ν	
	Our work	Exp.	Our work	Exp.	Our work	Exp.	Our work	Exp.
AlN	3.13	3.11[a]	5.02	4.50[a]	0.381	0.382[a]	0.247	0.233[d]
GaN	3.23	3.19[a]	5.25	5.19[a]	0.376	0.377[a]	0.219	0.222[d]
InN	3.59	3.54[a]	5.79	5.70[a]	0.379	-	0.285	-
BeO	2.72	2.70[b]	4.41	4.38[b]	0.378	0.378[b]	0.176	0.249[e]
ZnO	3.29	3.25[c]	5.28	5.21[c]	0.381	0.383[c]	0.378	0.357[e]

[a] Ref. [154], [b] Ref. [155], [c] Ref. [156], [d] Ref. [241], [e] Ref. [198]

The strain state of the system is defined by reducing the lattice constant *c* via:

$$c(\varepsilon_3) = c_0(1 + \varepsilon_3), \qquad \text{(VI.1)}$$

where c_0 is the equilibrium (zero-strain) lattice constant and ε_3 is the applied uniaxial strain along the *c*-axis. In this study we impose five such strains, whose range goes for -1% to -5%. The minus sign of ε_3 indicates that the strain is compressive in nature. Compression along one direction always induces an elongation of the material in the perpendicular directions, which is nothing else but the Poisson effect [200,201] discussed in detail in Chapter V. In that chapter, you will recall, we have set a biaxial strain on the *ab*- or *c*-plane, which gave rise to a uniaxial strain in the *c*-direction. This situation is reversed in the present chapter: a uniaxial strain ε_3 is applied along the *c*-axis, which means the response would be a biaxial strain ε_1 on the *ab*-plane.

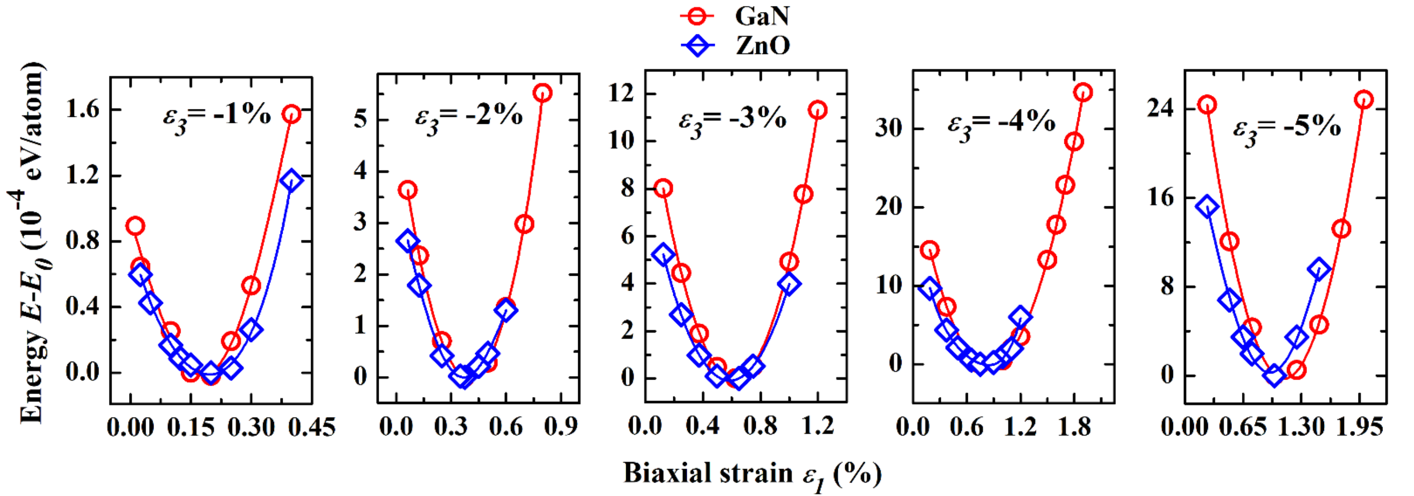

Figure VI.1 Total energy of the compressed wurtzite GaN and ZnO versus the ensuing biaxial strain for each applied uniaxial strain. In all cases, the energy scale is shifted by the corresponding minimum value E_0. The strain ε_1 required to calculate the relaxed lattice constant *a* (Poisson effect) corresponds to the minima of the curves.

Here, we deal with the Poisson effect by an optimisation process based on two different protocols: the Poisson's ratio (as we did in the previous chapter) and total-energy calculation. The latter method amounts to calculating for each value of ε_3 the total energy of the compressed structure over a grid of values of ε_1, with ε_1 being the ensuing biaxial strain. The internal parameter u is allowed to relax during the calculation because, as we will show in Sec. VI.3.2, the parameter u is found to vary under c-axis compression. Figure VI.1 shows the variation of the energy of GaN (representative for the nitrides) and ZnO (representative for the oxides) with respect to the biaxial strain that results from applying the uniaxial strain.

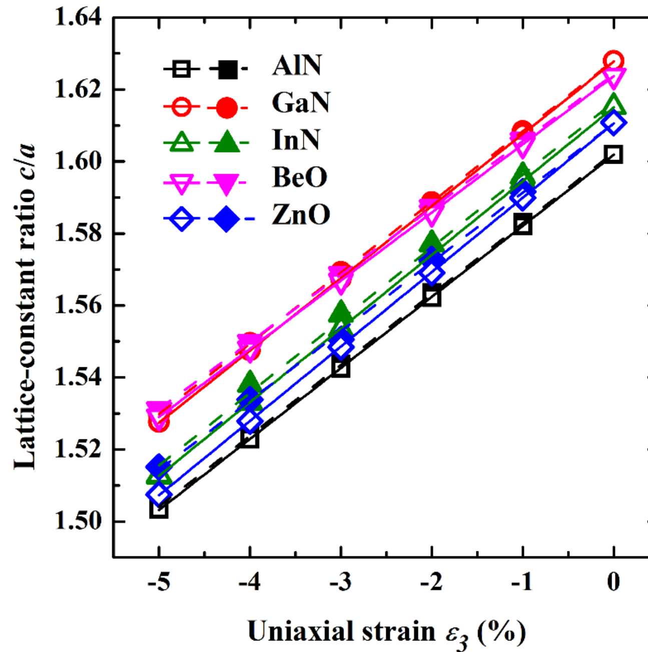

Figure VI.2 Lattice-constant ratio c/a as a function of compressive uniaxial strain. The value of the lattice constant c is fixed by the applied strain [Eq. (VI.1)], whereas the lattice constant a is obtained by relaxing the structure in the perpendicular directions to the c-axis. There are two sets of data: solid curves (open symbols) refer to the values of a obtained from total-energy calculation, and dashed curves (filled symbols) are the values based on the Poisson's ratio.

The values of the lattice constant a can be determined by an expression similar to that of the lattice constant c, namely $a(\varepsilon_1) = a_0(1 + \varepsilon_1)$, where a_0 is the equilibrium value. Notice that a depends implicitly on ε_3. We extract the values of ε_1 from either the curves of Fig. VI.1 (the minima of the curves) or from the calculated Poisson's ratio (via $\nu = -\varepsilon_1/\varepsilon_3$ [201]). The Poisson's ratio for each material is given in Table VI.1. We present in Figure VI.2 the computed values of the lattice-constant ratio c/a as a function of uniaxial strain for all the materials of interest, obtained from total-energy calculation and the Poisson's ratio. It can be seen that applying a compressive uniaxial strain causes the ratio c/a to decrease, fully consistent with the fact that ν is positive [201], i.e. the decrease of c generates an increase of a in going from lower to higher compressive uniaxial strains along the c-axis. We note that both sets of results (energy and Poisson's ratio calculations) compare extremely well.

VI.3.2 Internal parameter and phase transition

The internal parameter of the wurtzite structure can be viewed as the fractional coordinate of the anion on the c-axis. It is established that macroscopic strain is generally accompanied by a microscopic displacement of atoms out of their equilibrium sites [147]. This means that we have to relax the internal parameters as the strain is applied through minimizing the Hellman-Feynman forces acting on atomic positions [153]. The results are plotted in Figure VI.3, where the internal parameter is observed to increase with increasing uniaxial strain for all wurtzite crystals studied.

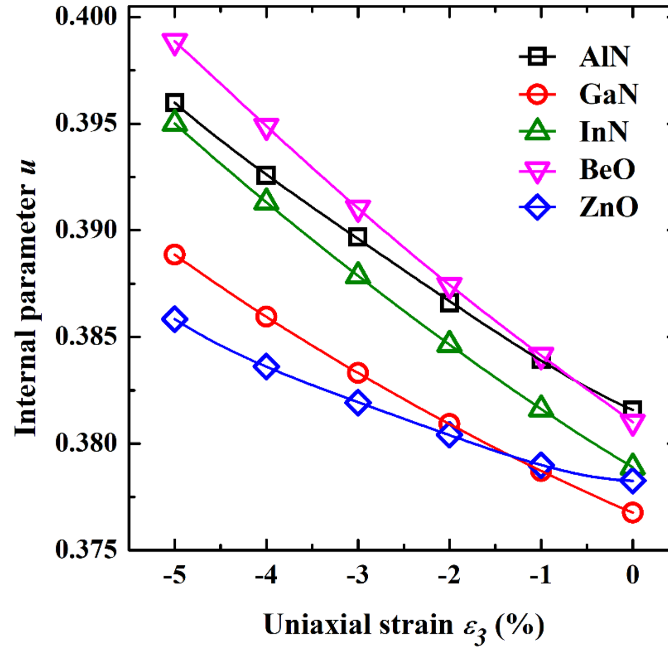

Figure VI.3 Evolution with uniaxial strain of the internal parameter for wurtzite nitrides and oxides. A quadratic interpolation is used to fit the data points.

For sufficiently high compressive strains (around −20% for all compounds), the internal parameter reaches the value 0.5. This value of u is a characteristic of the layered-hexagonal structure [183] used in Chapter V as a reference to access the spontaneous polarization of wurtzite crystals. The unit cell of a layered-hexagonal crystal is shown in Figure VI.4 alongside the wurtzite one. This implies the occurrence of a strain-induced phase transition: the wurtzite structure transforms into the layered-hexagonal structure. One can obtain an estimate of the corresponding transition pressure using the following formula [242]:

$$p = -\frac{1}{V}\frac{dE}{d\varepsilon_3}, \qquad \text{(VI.2)}$$

with V and E are the volume and energy of the strained unit cell, respectively. To evaluate the derivative in Eq. (VI.2) we interpolate the variation of E with ε_3 via a polynomial of degree four as presented in Figure VI.5 for GaN and ZnO.

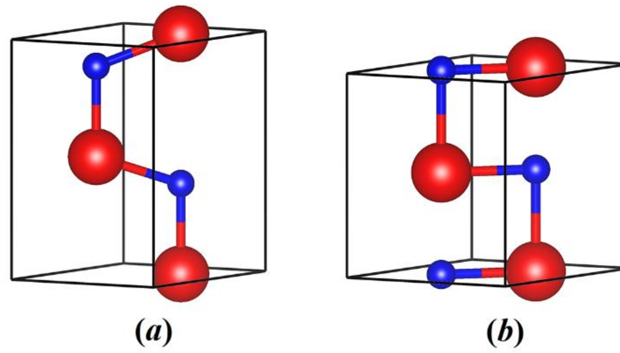

Figure VI.4 Wurtzite structure (space group $P6_3mc$ or 186) shown in (*a*) transforms into the layered-hexagonal structure ($P6_3/mmc$ or 194) shown in (*b*). The transformation occurs when the wurtzite internal parameter u reaches the value 0.5 upon applying compressive uniaxial strain. Red and blue spheres correspond to the cations and inions, respectively.

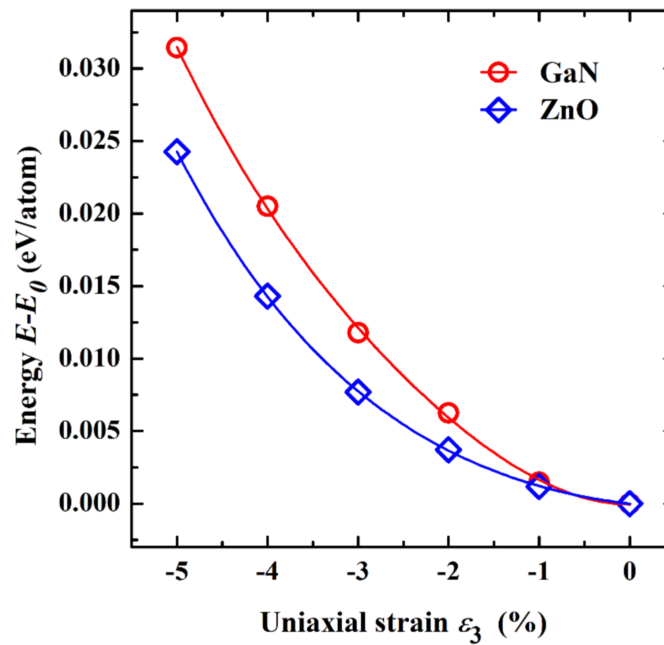

Figure VI.5 Energy as a function of compressive uniaxial strain up to −5% for wurtzite GaN and ZnO. The curves are obtained by fitting the calculated values of E to a fourth degree polynomial in ε_3, which allows to compute the derivative $dE/d\varepsilon_3$ and the uniaxial pressure p. The range of strain should be expanded beyond −5% in order to access the wurtzite-hexagonal transition pressure p_t.

Figure VI.6 shows the internal parameter as a function of uniaxial pressure p. Direct inspection of this figure permits to deduce the wurtzite-hexagonal transition pressure p_t, i.e. the pressure beyond which u= 0.5. The transition pressure is calculated to be 19.0 GPa for AlN, 43.2 GPa for GaN, 16.1 GPa for InN, 82.1 GPa for BeO, and 11.9 GPa for ZnO. Kobayashi [242] has investigated AlN and ZnO under various pressure conditions, including uniaxial c-axis pressure. He observed the same transformation with transition pressures of 20 and 10 GPa for AlN and ZnO, respectively. These values compare well with ours. As for the other not mentioned compounds, there is no data to compare our results with. Further increasing

the pressure above p_t does not result in any measurable increase in u, meaning 0.5 is the limiting value of the internal parameter in the hexagonal system. Also, the changes in the in-plane lattice constant a at the transition are found to be quite large and unusual, suggesting the Poisson effect is very important. We point out that the calculation of the pressure by equation (VI.2) is very sensitive to convergence parameters, namely the number of k-points, the expansion cutoff $R_{MT}^{min}K_{max}$ and the muffin-tin radii R_{MT}. In order to get consistent results, the simulation must be performed with the same computational setup for all strains.

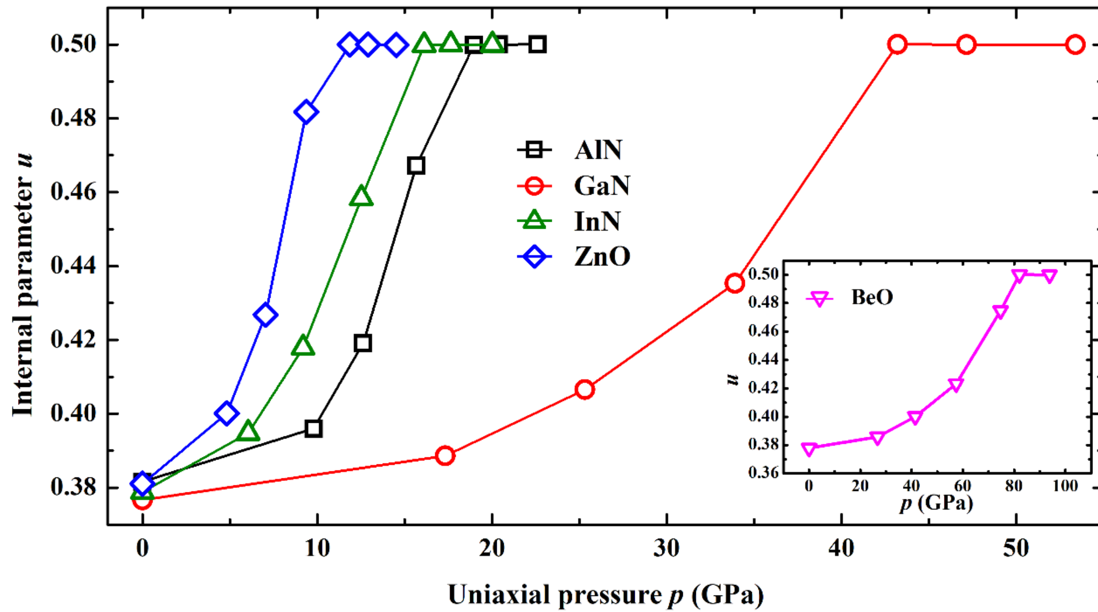

Figure VI.6 Variation of the internal parameter with uniaxial c-axis pressure for AlN, GaN, InN and ZnO. The results for BeO are presented in the inset. The pressure values are calculated using Eq. (VI.2) for different strains. Note that u= 0.5 for $p \geq p_t$.The lines connecting the data points are a guide to the eye.

VI.3.3 Piezoelectric polarization

Because of their relatively low symmetry, wurtzite crystals exhibit a non-zero polarization that exists even in equilibrium, which we refer to as the spontaneous polarization P_{sp}. When the uniaxial strain is applied the polarization will include an additional term, the so-called piezoelectric polarization P_{pz}. As a result, the total polarization P_{tot} of the strained solid is the sum of a spontaneous and piezoelectric parts [171]:

$$P_{tot}(\varepsilon_3) = P_{sp} + P_{pz}(\varepsilon_3), \qquad \text{(VI.3)}$$

Following the methodology described in Section V.4.5 of Chapter V, the piezoelectric polarization is given directly by the polarization difference between the uniaxially-strained wurtzite structure and its unstrained counterpart:

$$P_{pz,1}(\varepsilon_3) = \tilde{P}_{WZ,1}(\varepsilon_3) - P_{WZ,1}, \qquad \text{(VI.4)}$$

where $\tilde{P}_{WZ,1}$ and $P_{WZ,1}$ denote the wurtzite polarization under strain and without strain, respectively, and the subscript 1 means that the systems studied are modelled by wurtzite unit cells (the polarization branch n= 1).

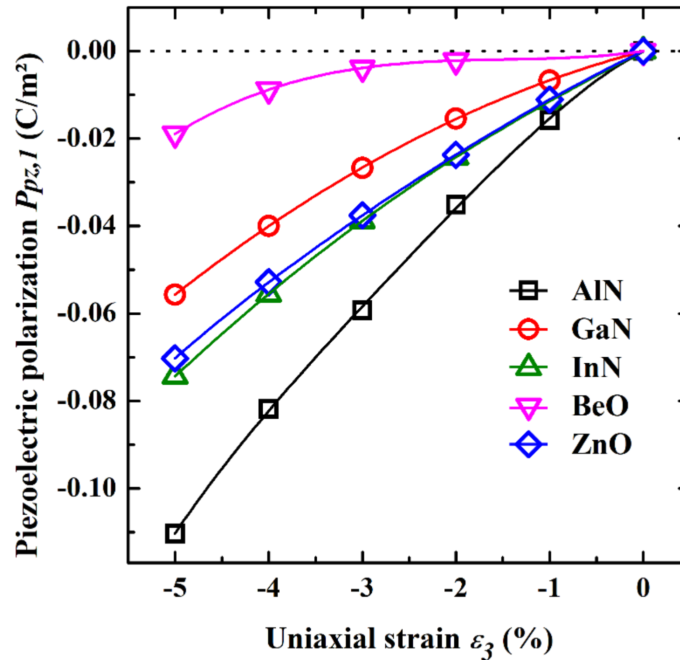

Figure VI.7 Uniaxial-strain dependence of the piezoelectric polarization for wurtzite nitrides and oxides. Note that P_{pz} is identically zero at equilibrium (the dotted horizontal line). The piezoelectric polarization values presented in this graph correspond to the branch n= 1.

The evolution with uniaxial strain of the piezoelectric polarization for different compounds is plotted in Figure VI.7. The piezoelectric term of the total polarization results to be negative and non-zero only along the hexagonal c-axis, corresponding to the $[000\bar{1}]$ direction. The polarization is generally largest in AlN, smallest in BeO, and intermediate in InN, ZnO and GaN. The magnitude of the piezoelectric polarization for wurtzite nitrides was found to increase as a non-linear function of biaxial strain [158,171]. Our results indicate that this is also the case for the application of uniaxial strain. The enhancement of polarization is attributed to the dependence of the internal parameter on the applied strain (see Fig. VI.3). Indeed, electric polarization is found to be most sensitive to the structural internal parameter [160], and any increase in its value leads to a corresponding increase in the value of polarization.

Finally, the standard GGA functional fails to obtain a band gap for wurtzite InN [174], which prevents access to its polarization. To overcome this problem we correct GGA by using the modified Becke-Johnson (mBJ) approximation [113]. This exchange-correlation potential gives a non-vanishing band gap for InN, in accordance with experiment [117]. Hence, whenever the polarization of InN is considered, the calculation is performed using the mBJ functional.

VI.3.4 Piezoelectric coefficient

The response of piezoelectric materials, or the coupling between electric polarization and mechanical strain, is usually quantified by a set of parameters called piezoelectric constants [131]. The wurtzite structure has three such constants [148]. Here we restrict ourselves to the axial piezoelectric coefficient e_{33} that describes the polarization induced by a strain applied along the c-axis [144]. The piezoelectric coefficient is given in terms of the polarization difference between two different states, corresponding to the strained and unstrained structures [243]. Specifically, the piezoelectric coefficient is expressed as:

$$e_{33}(\varepsilon_3) = \frac{\tilde{P}_{WZ}(\varepsilon_3) - P_{WZ}}{\varepsilon_3}, \qquad \text{(VI.5)}$$

where $\tilde{P}_{WZ}(\varepsilon_3) - P_{WZ}$ refers to the difference of polarization before and after the application of the macroscopic strain ε_3. In order to determine the piezoelectric constants, the wurtzite unit cells are strained along the c-axis, then the polarizations are calculated as Berry phases. Conveniently, the values of e_{33} of the ground-state structure are obtained by applying a strain $\varepsilon_3= -1\%$ (except BeO for which $\varepsilon_3= -2\%$). The values of e_{33} are equal to 1.58 C/m² for AlN, 0.684 C/m² for GaN, 1.14 C/m² for InN, 0.0105 C/m² for BeO and 1.11 C/m² for ZnO. There is a considerable scatter in the reported values, but our results are within the range of earlier computational and experimental data [144,244] (AlN: 1.29-1.80 C/m², GaN: 0.63-0.86 C/m², InN: 0.81-1.09 C/m², BeO: 0.04-0.1 C/m², and ZnO: 0.96-1.3 C/m²).

When studying the piezoelectric response of materials, it is imperative to make the distinction between the improper and proper piezoelectric constants. The improper coefficients are obtained from expressions similar to Eq. (VI.5) (variation of polarization with strain). It is the proper coefficients that should be compared to experimental measurements. To find the proper values, a set of transformations must be applied to the improper coefficients [9]. However, the issue of proper versus improper piezoelectric constants is only present for the components e_{15} and e_{31}. The axial coefficient e_{33} studied in this section (which is frequently of most interest) does not require this distinction, as its improper value equals the proper one. For more details see the discussion at the end of Section III.6.2 and the references cited there.

The variations of the piezoelectric coefficient versus uniaxial strain for all materials studied are shown in Figure VI.8. Under the loading of c-axis compressive strain, the nitrides and oxides share the same behaviour: the piezoelectric coefficients have a tendency to increase linearly and remain linear over the range of exploited strains, leading to the improvement of the piezoelectric effect in these compounds. The piezoelectric coefficient can be seen to be much larger for AlN than in InN, ZnO, GaN and BeO. This ordering is consistent with the variation of the piezoelectric polarization presented in Fig. VI.7. Wang et *al.* [245] have shown that the piezoelectric constant of AlN increases as a linear function under c-axis uniaxial strain, a result that is in accordance with our work.

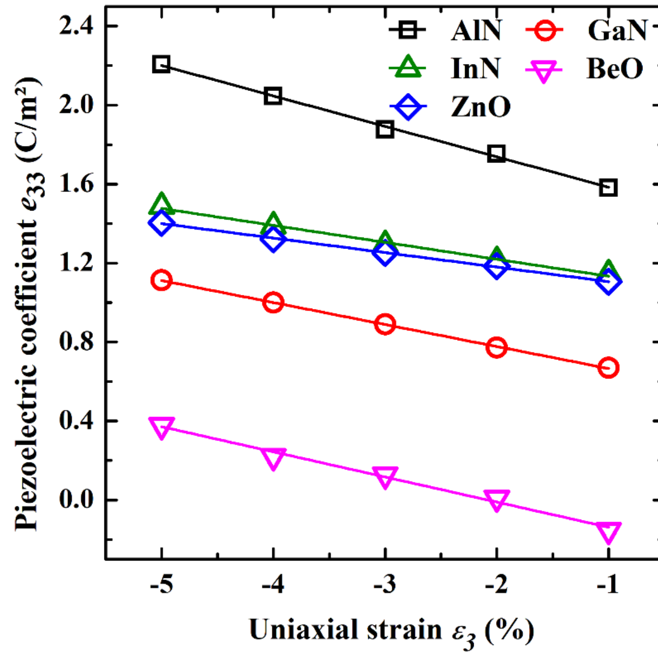

Figure VI.8 Variations of the piezoelectric coefficient with respect to compressive *c*-axis strain. The curves are obtained by a linear regression of the calculated data. These values of e_{33} correspond to the proper coefficients.

VI.4 Discussion

In this section we take a closer look at some of the results presented in Sec. V.3, seeking to explain the origin of the enhanced piezoelectric response. The piezoelectric coefficient of wurtzite crystals is found to depend on two terms [144,147,148]:

$$e_{33} = e_{33}^{c} + e_{33}^{nc}, \tag{VI.6}$$

where e_{33}^{c} is called the clamped-ion term which describes the electronic response to strain. The ionic response is given by the non-clamped-ion term e_{33}^{nc}. Previous studies have shown that e_{33}^{c} is always smaller than e_{33}^{nc}, sometimes by one order of magnitude, so the clamped-ion term is not expected to contribute to the strong increase of e_{33} [246]. For that reason we only consider the non-clamped-ion term, which can be written as [144,147,148]:

$$e_{33}^{nc} = kZ_{33}^{*}\frac{du}{d\varepsilon_3}. \tag{VI.7}$$

Here, Z_{33}^{*} stands for the Born effective charge along the *c*-axis and $du/d\varepsilon_3$ for the strain sensitivity of the internal parameter. The index 33 in Z_{33}^{*} means that the Born effective charge is a tensor quantity, and that Z_{33}^{*} describes the polarization induced along the *z*-axis by an ionic displacement along the *z*-axis. The factor k is just a constant of proportionality. We study the effect of uniaxial strain on both quantities (Z_{33}^{*} and $du/d\varepsilon_3$) separately in order to identify the main factor responsible for the increased piezoelectric coefficient observed in all investigated materials.

VI.4.1 Born effective charge

The displacement of a given ion from its equilibrium position induces an electric polarization, which is best described by the Born effective charge Z^* of the displaced ion [247]. As emphasized in the Berry-phase theory [135,136] and throughout this work, the Born effective charge is accessible via a finite difference of polarization between two states: the structure where the ions are slightly displaced from their equilibrium sites, and the structure where they are displaced by the same amount but in the opposite direction [248]. The quantity of interest is then obtained as the change in polarization divided by the amount that an ion is displaced [144,147,148]:

$$Z_{33}^*(\varepsilon_3) = \frac{V(\varepsilon_3)}{e} \frac{\Delta P(\varepsilon_3)}{\Delta r(\varepsilon_3)}, \tag{VI.8}$$

where V represents the cell volume, e is the electronic charge and ΔP is the polarization difference induced by the relative ionic displacement Δr. According to the acoustic sum rule, the sum of the effective charge of all ions in the unit cell must vanish [249]. This rule guarantees that the charge neutrality in the solid is fulfilled at the level of Z^*.

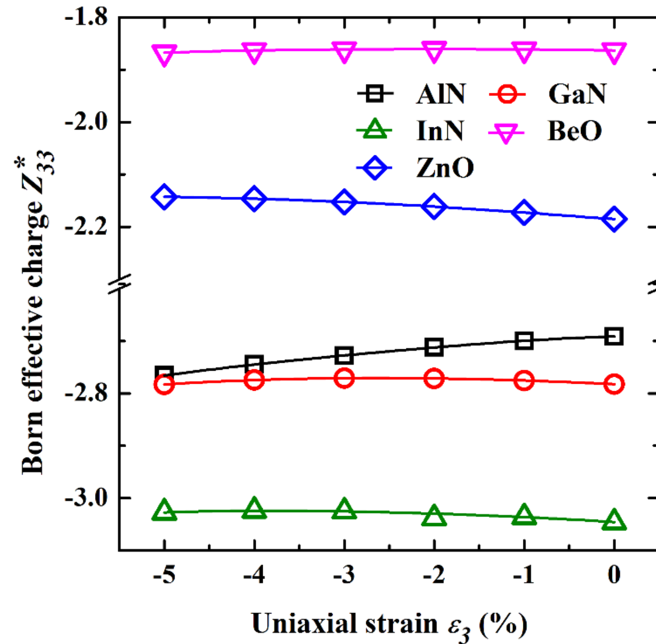

Figure VI.9 Born effective charge (in units of e) of the anions, i.e. N and O, as a function of applied uniaxial strain [determined using Eq. (VI.10)].

For the calculation of the axial effective charge Z_{33}^* of binary wurtzite compounds, and because of the sum rule just mentioned, it suffices to displace the anions along the c-axis (or z-axis) while keeping the positions of the cations unchanged, or vice versa. In this work we choose to displace the anions, whose equilibrium z-coordinates are $z_1 = uc$ and $z_2 = c(u + 0.5)$. The two anions are displaced in opposite directions by an amount δ, so that their final positions

on the c-axis are $z_{1,\pm\delta} = c(u \pm \delta)$ and $z_{2,\pm\delta} = c(u + 0.5 \pm \delta)$. Note that the internal parameter in both cases is a function of strain [$u = u(\varepsilon_{33})$]. This gives an ionic displacement of:

$$\begin{aligned} \Delta r = \Delta r_1 + \Delta r_2 &= (z_{1,+\delta} - z_{1,-\delta}) + (z_{2,+\delta} - z_{2,-\delta}) \\ &= [c(u+\delta) - c(u-\delta)] + [c(u+0.5+\delta) - c(u+0.5-\delta)] \\ &= 4\delta c. \end{aligned} \quad \text{(VI.9)}$$

Given that the hexagonal cell volume $V = \sqrt{3}a^2\, c/2$, Eq. (VI.8) becomes:

$$Z_{33}^*(\varepsilon_3) = \frac{\sqrt{3}a^2(\varepsilon_3)}{8e} \frac{[P_{WZ}^{+\delta}(\varepsilon_3) - P_{WZ}^{-\delta}(\varepsilon_3)]}{\delta}, \quad \text{(VI.10)}$$

where $P_{WZ}^{+\delta}$ and $P_{WZ}^{-\delta}$ are the formal polarizations of the wurtzite structure for a fractional ionic displacement $+\delta$ and $-\delta$, respectively. Using the above equation with a displacement of $\delta = 0.001$, the Z_{33}^* component of the Born effective charge is calculated as a function of uniaxial strain and plotted in Figure VI.9. We observe that the applied strain has a very little impact on the effective charges, as their values are practically constant over the whole strain interval. Our calculated equilibrium values of Z_{33}^*, extracted from Fig. VI.9, are grouped in Table VI.2. Also included are the static nominal charges Z of the corresponding ions. Comparison with previous measurements [250–252] shows a reasonable agreement. From an experimental standpoint, one has access to the effective charge via measurements of the phonon spectra. In particular, Z_{33}^* is directly related to the splitting of the longitudinal and transverse optic phonon modes at the center of the Brillouin zone [165].

Table VI.2 Equilibrium Born effective charges Z_{33}^* (in unit of e) of individual ions for each wurtzite crystal with their nominal values Z. The summation of Z_{33}^* is a verification of the acoustic sum rule. Our results are compared to those of other works. For details see text.

Material	Ion	Z	Z_{33}^*	$\Sigma\, Z_{33}^*$	Exp.
AlN	N	−3	−2.691	−0.001	2.57[a]
	Al	+3	+2.690		
GaN	N	−3	−2.763	0	2.82[b]
	Ga	+3	+2.763		
InN	N	−3	−3.013	−0.001	-
	In	+3	+3.012		
ZnO	O	−2	−2.156	0	2.10[c]
	Zn	+2	+2.156		
BeO	O	−2	−1.862	0	1.85[c]
	Be	+2	+1.862		

[a] Ref. [250], [b] Ref. [251], [c] Ref. [252]

The fifth column of Table VI.2 is a check of the acoustic sum rule: the results obey this rule with a negligible error and provides therefore an indication of the accuracy of our Berry-phase computation. We note that the effective charges are very close to the nominal values (± 3 for the nitrides and ± 2 for the oxides), suggesting a strongly ionic character of the anion-cation bonds in these materials [148,253]. Since the effective charges remain almost constant, the key

factor that leads to increasing piezoelectric effect is the response of the internal parameter to strain, to which we now turn.

VI.4.2 Strain sensitivity of the internal parameter

The strain sensitivity $du/d\varepsilon_3$ reflects the slope of the internal parameter versus strain (Fig. VI.3). Figure VI.10 presents the evolution of this quantity as a function of applied uniaxial strain. At very low strains, the value of $du/d\varepsilon_3$ coincides with that of the so-called internal strain parameter ζ_3, which describes the redistribution of atomic coordinates on the *c*-axis as a response of the macroscopic strain [59,174]. We obtain the following values of ζ_3: −0.226, −0.188, −0.261, −0.0683, and −0.295 for AlN, GaN, InN, BeO and ZnO, respectively. Our results for the III-nitrides (II-oxides) are in good agreement with those reported by Bernardini et *al.* [148]. (Noel et *al.* [144]).

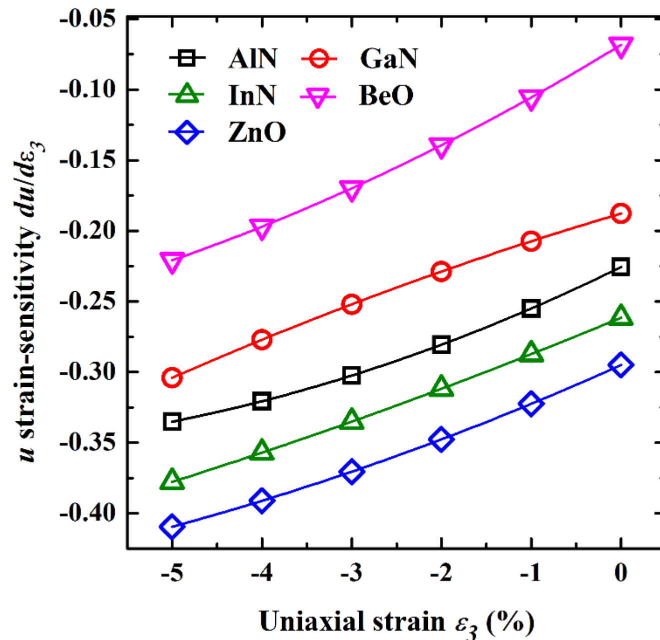

Figure VI.10 Response of the wurtzite internal parameter to *c*-axis strain. The calculated data are obtained directly from Fig. VI.3.

It can be seen that $du/d\varepsilon_3$ increases significantly (in absolute value) as the strain increases. The variation is as high as 220% for BeO. For other compounds the variation is much lower (between 40% and 60%). This unambiguously demonstrates that the change in polarization is mainly induced by structural distortions around the ionic sites. Consequently, the strong increased internal-parameter strain sensitivity is mostly responsible for the linear enhancement of the piezoelectric coefficient in uniaxially-strained wurtzite crystals. We stress that the increase in the rate of change of *u* with strain, not *u* itself, is the reason for the strain-induced enhancement. Finally, note that both Z^*_{33} and $du/d\varepsilon_3$ are negative, thus resulting in a positive value of e_{33} [see Eq. (VI.7)].

VI.5 Conclusion

In this Chapter, we went back to wurtzite binary III-nitrides (AlN, GaN and InN) and II-oxides (BeO and ZnO) and studied the crystal structure and polarization of these materials when they are subjected to a compressive uniaxial strain. The latter was applied along the hexagonal c-axis, which is different from the situation of Chapter V where the strain was biaxial and applied in the c-basal plane. The compressive uniaxial strain was realized by reducing the lattice constant c, and the resulting change of the lattice constant a, which quantifies the Poisson effect, was determined via the Poisson ratio and total-energy calculation. Both methods give similar results as expected. The internal parameter was found to increase with strain for all systems studied. When we increased the uniaxial strain up to around -20%, the internal parameter reached the value 0.5, which indicates the occurrence of a phase transition from the wurtzite to the layered-hexagonal structure. We were able to deduce the transition pressure of this structural transformation by converting the strain (in %) into pressure (in GPa). This was done by fitting the energy-strain variation to a polynomial function.

We then explored the piezoelectric polarization induced by the c-axis compressive strain as well as the proper piezoelectric constant e_{33}. As we did in Chapter IV, we employed 4-atom wurtzite unit cells in the simulation, meaning the branch of P_{pz} is n= 1 (e_{33} is independent of the branch). For the two groups of materials, both quantities increase as the applied uniaxial strain increases. The piezoelectric polarization was observed to evolve non-linearly with strain. On the contrary, the piezoelectric coefficient varies as a linear function.

In order to interpret the strain-induced piezoelectric enhancement, we determined the main factor that leads to the increase of the piezoelectric coefficient. We achieved this by decomposing the clamped-ion (ionic) term of e_{33} to its two contributions: the Born effective charge Z^*_{33} and the strain-sensitivity of the internal parameter $du/d\varepsilon_3$. We calculated both contributions as a function of compressive uniaxial strain. This calculation led us to the conclusion that the rapid increase of $du/d\varepsilon_3$ with strain is the cause of the improvement of the piezoelectric effect in uniaxially-strained wurtzite crystals. The effective charge is virtually constant with respect to uniaxial strain and thus has no effect on the piezoelectric enhancement. Lastly, we point out that the present study has some technological relevance, as it suggests that imposing a compressive uniaxial strain may improve the performance of piezoelectric devices in which wurtzite crystals are being used.

Chapter VII

Energetics, electronic structure and electric polarization of basal stacking faults in wurtzite GaN and ZnO

VII.1 Introduction

At present, there is a regain of interest in wide band gap semiconductors. Those with direct band gap like GaN and ZnO, are not only very interesting for optoelectronics, but also in power electronics [254–256]. Nanostructuration gives new functionalities and opens a huge field of fundamental and applied research [257–260]. For instance, nanowires are thought to be an essential ingredient of future nanoelectronics. Especially compelling in that respect are polar crystals with wurtzite structure since controlling the inherent electric field gives rise to an additional leverage for manipulating electric currents.

Both wurtzite GaN and ZnO are usually grown as thin films on mismatched substrates such as sapphire and SiC [261–264]. Such systems are characterized by residual strains at the interface, invariably chosen to be the (0001) plane (or *c*-plane) [58]. The origin of these strains is the difference in the in-plane lattice constant *a* of the film and substrate layers [208]. The mismatch-induced strains can be very high, thus resulting in the formation of a large density of extended structural defects. These include, but not limited to, dislocations [265,266], inversion domain boundaries [267,268] and *stacking faults* [269–272]. These defects can also be generated during growth on crystallographic planes without strain relaxation [273].

Stacking faults constitute a common type of extended two dimensional defects in GaN and ZnO, which are expected to have an impact on physical properties and hence on device performance. Typically, they can be generated either through the dissociation of a full dislocation into two partial dislocations (whose separation is related to the energy of the stacking fault), or the nucleation and propagation of isolated partial dislocations, or the condensation of isolated point defects (i.e. interstitial atoms or vacancies) leading to the insertion or the removing of an atomic bilayer within the crystalline stacking sequence [274]. High-resolution transmission electron microscopy (TEM) revealed the existence of such defects even in GaN (ZnO) films epitaxially grown on GaN (ZnO) substrates [210,275]. There are three types of stacking faults in hexagonal crystals, depending on the plane on which the defect occurs. These are prism-, pyramidal- and basal-plane stacking faults [276]. The latter are the subject of the present study.

Most theoretical investigations so far have focused on the energetics and electronic structure of basal stacking faults in wurtzite III-nitrides and II-oxides. However, there seems to be lack of published data regarding other properties of stacking faults, for instance electric polarization. Indeed, wurtzite materials are found to be highly polarized [147,148], and a study of the effect of stacking faults on the polarization-related quantities is of central importance. Such a study has until now been surprisingly overlooked by the condensed-matter community.

This lack motivates the present work, in which we study the structural, electronic and polarization properties of basal-plane stacking faults in wurtzite GaN and ZnO via first-principles methods applied to periodic hexagonal supercells. This amounts to calculating structural parameters, formation energies, band gaps, band offsets, effective masses, spontaneous polarizations, polarization charges and piezoelectric coefficients. The main goal is to investigate to what extent these quantities can be affected by the presence of different types of basal stacking faults. We compare our results to experimental and theoretical data available from the literature and explain the observed trends in terms of the properties of the wurtzite and zincblende polytypes of both materials. We also reproduce the reported experimental value of the spontaneous polarization of wurtzite GaN. Furthermore, we detect a simple rule of thumb which connects the formation energies, band gaps, and polarizations of different stacking faults simply with the number of the corresponding cubic bonds.

The chapter is structured as follows. Section VII.2 describes the theoretical approach: in section VII.2.1 we give an overview of the basal-plane stacking faults in hexagonal crystals. Section VII.2.2 deals with the supercell representation of all types of stacking faults studied here. Section VII.2.3 introduces the numerical details of the simulation. Section VII.3 contains the main results of the chapter: sections VII.3.1-VII.3.3 present the computational results and discussion of the structural optimization, electronic structure and electric polarization, respectively. Finally, we present our conclusions in section VII.4. This chapter mostly follows the lines of our published paper: Benbedra et *al*., Comput. Condens. Matter 43, e01033 (2025).

VII.2 Theoretical methodology

VII.2.1 Basal stacking faults in hexagonal crystals

The wurtzite structure in which GaN and ZnO crystallize is formed by the stacking of atoms in the sequence ..AaBbAaBb.. along the [0001] direction [55]. The zincblende structure, on the other hand, can be described by the stacking sequence ..AaBbCcAaBbCc.. along the [111] direction [55]. Here, upper-case and lower-case letters correspond to cations (Ga and Zn) and anions (N and O), respectively. The letters Aa, Bb and Cc indicate three different positions of basal or *c*-plane atomic bilayers. The *x*- and *y*- coordinates of atoms at the Aa, Bb and Cc layers are respectively (1/3,2/3), (2/3,1/3) and (0,0). In the wurtzite structure, every bilayer is surrounded by two identical bilayers (e.g. Aa<u>Bb</u>Aa). In this case Aa-Bb bonds are called hexagonal bonds. In the zincblende structure, the two bilayers surrounding a given bilayer are different (e.g. Aa<u>Bb</u>Cc), and the Aa-Bb bonds are called cubic bonds [277]. Stacking faults can then be viewed as local deviations of the perfect wurtzite stacking sequence. In other words, stacking faults are embedded cubic units surrounded by a hexagonal matrix [278].

There are three types of basal-plane stacking faults reported in the literature [273,277,279,280]: two intrinsic stacking faults of type-I and type-II, and one extrinsic stacking fault. The type-I stacking fault originates from one violation of the wurtzite stacking rule. Specifically, it changes an Aa or Bb layer into a Cc one, leading to a stacking sequence of ..AaBb**Cc**BbAa.. or ..AaBbAa**Cc**AaBb..This stacking fault introduces one cubic bond. The type-II stacking fault results from two violations of the normal stacking rule. This is

done by changing Aa (Bb) into Cc and the next Bb (Aa) into Aa (Bb). The resulting sequence is ..AaBb**CcAa**BbAa.. (..AaBbAa**CcBb**AaBb..). This stacking fault introduces two cubic bonds. Lastly, the extrinsic stacking fault contains an additional Cc layer inserted in the midst of the original stacking sequence: ..AaBb**Cc**AaBb... It introduces three cubic bonds at the faulted interface [273,277,279,280].

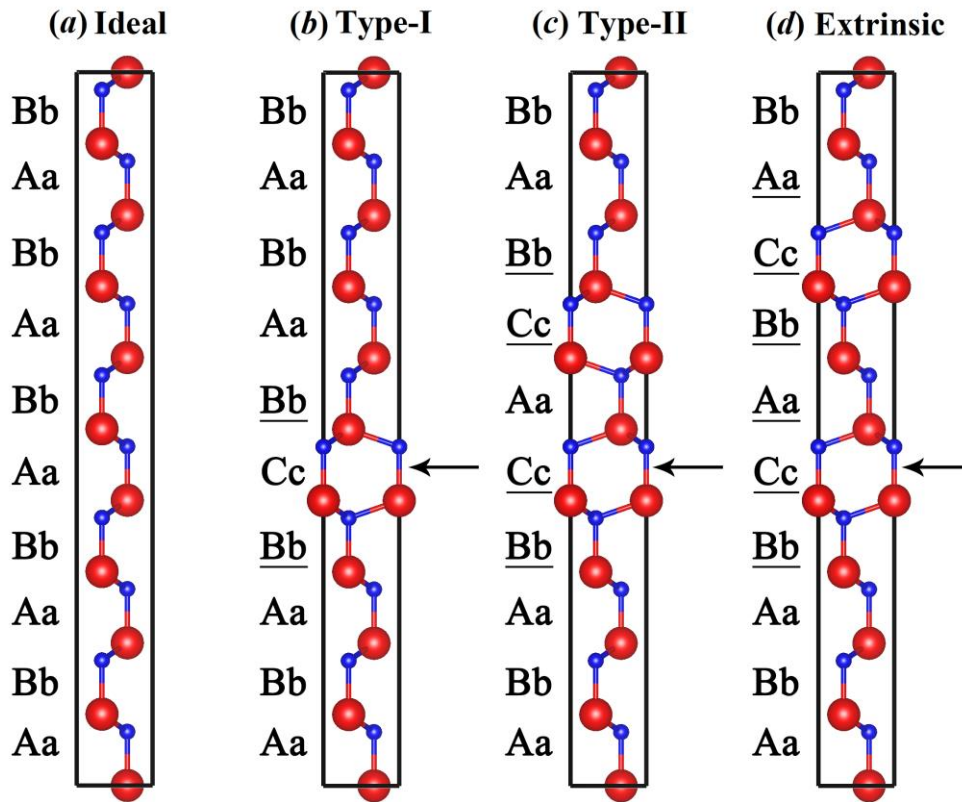

Figure VII.1 20-atom supercell models (in 2D) representing the studied structures for (*a*) ideal crystal, (*b*) type-I, (*c*) type-II and (*d*) extrinsic stacking faults. The position of the defects is indicated by an arrow, and the cubic bonds are indicated by underlined letters. Red and blue spheres correspond to Ga/Zn and N/O atoms, respectively.

VII.2.2 Supercells choice

In order to model the stacking faults, we use periodic supercells containing 20 atoms (10 double-layers), in a construction of 1×1×5 wurtzite supercells. The different types of stacking faults are achieved by a proper manipulation of specific atomic positions applied to the original wurtzite stacking sequence. As an example, the x- and y-coordinates of the atoms in a Bb layer are changed from (2/3,1/3) to (0,0) to form a Cc layer. Note that we did not highlight the z-coordinates because they are irrelevant, since they are kept fixed during the creation of the new Cc layer. In this way we obtain a type-I stacking fault. The constructed supercells of the stacking faults in both GaN and ZnO are represented in Figure VII.1. Due to imposing periodic boundary conditions, the beginning and the end of the supercells along the c-axis have to match. This has the effect of doubling the number of cubic bonds for each type of stacking faults. Indeed, the type-I stacking-fault supercell shown in Fig. VII.1(*b*) contains two cubic bonds

instead of one. The same remark can be deduced for type-II and extrinsic stacking-fault supercells [Figs. VII.1(c) and (d)], for which there are four and six cubic bonds respectively (instead of two and three). This effect must be taken into account when calculating the formation energy of stacking faults [see Eq. (VII.1) below].

VII.2.3 Simulation settings

The properties of basal-plane stacking faults (henceforth called stacking faults for brevity) in wurtzite GaN and ZnO are calculated within density functional theory [100,105]. We use the WIEN2k package [125] with the generalized gradient approximation (GGA) [110] to treat the exchange-correlation interactions. The modified Becke-Johnson (mBJ) approach [113,114] is chosen for dealing with electronic properties, since it was successfully applied for studying such properties in many materials. The Kohn-Sham equations [106] are solved self-consistently employing the full-potential linearized augmented plane wave (FP-LAPW) algorithm [119,150]. The wavefunctions cutoff parameters l_{max} and $R_{MT}^{min}K_{max}$ are set to 10 and 7, respectively, where l_{max}, R_{MT}^{min} and K_{max} are defined in Ref. [125]. The first Brillouin zone is sampled non-uniformly using a 4×4×8 mesh. The energy that separates core and valence states is chosen such that the following orbitals are treated as valence electrons: Ga ($3d$ $4s$ $4p$), N ($2s$ $2p$), Zn ($3d$ $4s$) and O ($2s$ $2p$).

The structural equilibrium parameters and electronic properties for each stacking fault are studied by means of standard total-energy calculations. Because energy differences associated with stacking faults are quite small (in meV), a special care should be taken to obtain accurate values of energy. This is why in our calculation the energy convergence criterion is reduced down to 10^{-6} Ry, which is less than the default value by a factor of 100. To determine the internal parameter of the wurtzite structure (i.e. the z-coordinate of the anion), we carry out a relaxation process by minimizing the Hellman-Feynman forces [153,180] acting on atomic sites, such that the convergence condition of the forces is 10^{-6} Ry/Bohr. Finally, the code BerryPI [141] is used to evaluate polarization properties as finite differences following the guidance of the Berry-phase theory [12,13].

VII.3 Results and discussion

VII.3.1 Energetics and structural optimization

A. Structural parameters:

We begin our study by determining the equilibrium structure of each stacking fault. In doing so, we calculate the energy of the system on a grid of values of supercell volume and lattice-constant ratio c/a [23]. Also, the atomic positions along the hexagonal axis (c-axis) are allowed to relax. The equilibrium lattice parameters are those who minimize the total energy. The results of this calculation, namely the lattice constants a and c as well as the internal parameter u, are gathered in Table VII.1 for the ideal defect-free structure and stacking-fault structures of wurtzite GaN and ZnO. Our calculated lattice parameters show good agreement with the ones determined from X ray diffraction measurements [154,156]. It can be seen that the structural

relaxation has a negligible effect on the lattice parameters, as their values are practically the same for all the structures studied. In particular, stacking faults lying on the basal plane do not seem to perturb the value of the internal parameter. This is in accordance with the previous studies of stacking faults in GaN and ZnO [277,280].

Table VII.1 Equilibrium lattice constants a and c, internal parameter u (in units of c), and stacking-fault thickness ℓ for the ideal and stacking-fault structures of wurtzite GaN and ZnO. Experimental and theoretical values from the literature (when available) are in parenthesizes.

	Ideal	Type-I	Type-II	Extrinsic
GaN				
a (Å)	3.23 (3.20[a])	3.23	3.23	3.23
c (Å)	5.25 (5.22[a])	5.25	5.25	5.25
u	0.377 (0.376[a])	0.377	0.377	0.377
ℓ (Å)	0	2.63 (4.41[b])	5.25 (7.10[b])	7.88 (9.6[b])
ZnO				
a (Å)	3.29 (3.250[c])	3.29	3.29	3.29
c (Å)	5.29 (5.204[c])	5.30	5.30	5.30
u	0.381 (0.383[c])	0.380	0.380	0.380
ℓ (Å)	0	2.65	5.29	7.94

[a] Ref. [154], [b] Ref. [210], [c] Ref. [156]

Another structural parameter characterizing stacking faults, also presented in Table VII.1, is their thickness ℓ. Intuitively, this is defined as the length of one cubic bond (which is $0.5c$) multiplied by the number of these bonds contained in the stacking fault. Hence, the thickness of type-I, -II, and extrinsic basal stacking faults would be $0.5c$, c and $1.5c$, respectively. Compared to the work of Lähnemann, et *al*. [210], who obtained the values of ℓ for GaN from the profile of the microscopic electrostatic potential, our results are lower by less than 2 Å.

B. Formation energy:

Stacking faults are not the ground state of the material, they cost energy, which we refer to as formation energy E_f. The latter is given by the following formula [277,280]:

$$E_f = E^{SF} - E^{Id}, \tag{VII.1}$$

with E^{SF} is the total energy of the supercell containing the stacking fault and E^{Id} is that of the ideal defectless supercell. As already mentioned, due to periodic boundary conditions the number of cubic bonds for each stacking fault is doubled. To account for this one should divide the result of Eq. (VII.1) by two. Table VII.2 gives the calculated stacking-fault formation energies. All stacking faults are found to have a very low formation energy, implying these defects may form very easily in GaN and ZnO grown on mismatched substrates.

Using smaller (12-atom) and larger (32-atom) supercells produces the same results as the 20-atom supercell. We have checked that the formation energy is not sensitive to the number of stacking faults within the supercell. To demonstrate this fact, we construct a supercell containing three type-I stacking faults as illustrated in Figure VII.2 (*b*), we then run an energy calculation using the same convergence parameters (i.e. the number of *k*-points and expansion

cutoffs) as for the supercell with one stacking fault shown in Figure IIV. 2 (*a*). Both supercells give the same value of stacking-fault formation energy. Also, the separation between stacking faults does not seem to affect E_f: the energy converges to the same value for the supercell in which the separation is one atomic layer [Fig VII.2 (*c*)] and for the supercell where the separation is six layers [Fig VII.2 (*d*)]. As a summary, the formation energy of stacking faults only depends on the number of cubic bonds: all the supercells of Figure VII.2 used in this calculation contain one cubic bond (or two if we consider periodicity), this is the reason why we obtain the same value of energy.

Table VII.2 Stacking-fault formation energies E_f of wurtzite GaN and ZnO. The energy is given in meV per unit cell area of the faulted basal plane (uca) and in mJ/m². The area of the basal plane is given by $a^2\sqrt{3}/2$, and the conversion factor between the two units is 0.56 for GaN and 0.59 for ZnO. In brackets are previous literature data taken from: Stampfl and Van de Walle [280] (simulation), Batyrev et *al*. [281] (simulation), Takeuchi and Suzuki [282] (experiment), Yan et *al*. [277] (simulation) and Nakamura et *al*. [283] (simulation and experiment). See text for discussion.

	Type-I	Type-II	Extrinsic
GaN			
E_f (meV/uca)	10.5 (10^a, 12.32^b, 11.2^c)	21.5 (24^a, 25.20^b)	32.9 (38^a)
E_f (mJ/m²)	18.8 (17.9^a, 22^b, 20^c)	38.4 (42.9^a, 45^b)	58.8 (67.9^a)
ZnO			
E_f (meV/uca)	16.0 (15^d)	31.9 (31^d, 43.07^e)	47.6 (47^d, 82.6^e)
E_f (mJ/m²)	27.1 (25.4^d)	54.01 (52.5^d, 73^e)	80.7 (79.7^d, 140^e)

^{a} Ref. [280], ^{b} Ref. [281], ^{c} Ref. [282], ^{d} Ref. [277], ^{e} Ref. [283]

We compare our theoretical results with previous simulations. For stacking faults in GaN, our calculation shows reasonable agreement with the results of Stampfl and Van de Walle [280] obtained from DFT using 16- and 18-atom supercells. The type-I and type-II stacking-fault energies from Batyrev et *al*. [281] agree well with our results. As for ZnO, there is an excellent agreement between the DFT results of Yan et *al*. [277] and the present work for all types of stacking faults. Nakamura et *al*. [283] computed the energy of type-II stacking fault associated with the dissociation of 60° dislocations into two Shockley partial dislocations, they found a formation energy 10 meV higher than our value for the same defect.

Regarding experimentally obtained values, the energy of type-I stacking fault of GaN reported by Takeuchi and Suzuki. [282] (deduced from dissociation width measurements by TEM) compares extremely well with our result. Nakamura et *al*. [283] also estimated the formation energy of ZnO using a model based on the measured separation of two partial dislocations, which resulted in a value of 0.14 J/m² or 82.6 meV/uca. The authors did, however, not specify the type of the studied fault. Assuming it is the extrinsic type this value is significantly larger than our calculated energy of 47.6 meV/uca. This discrepancy might be attributed to uncertainties related to the measurement of the separation between the two partial dislocations or to the validity of the theoretical model used to estimate E_f.

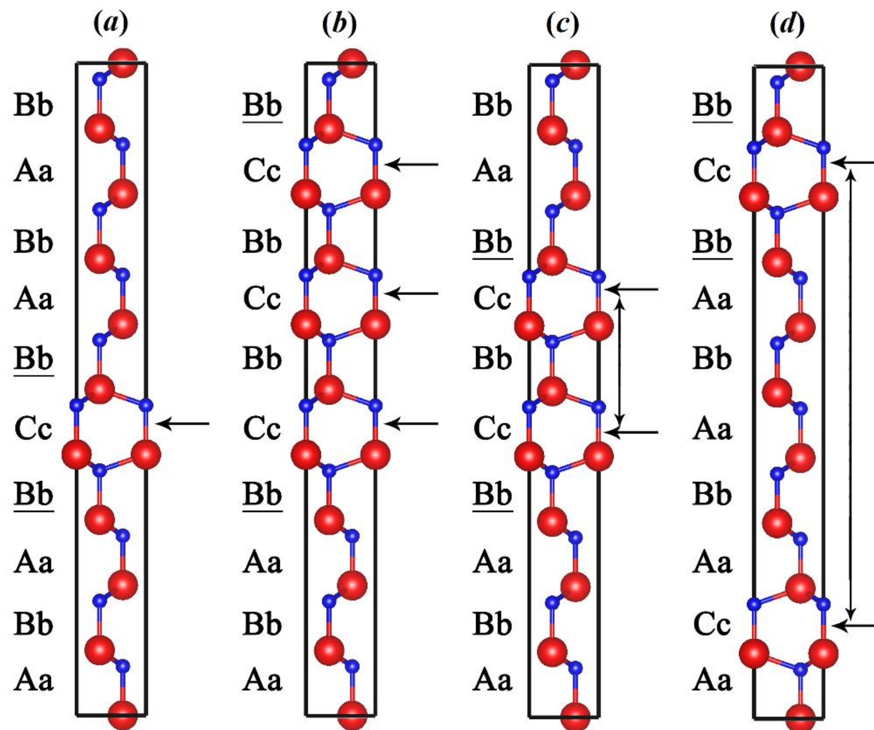

Figure VII.2 Supercells containing (*a*) one and (*b*) three stacking faults of type-I. The supercell in which the two type-I stacking faults are separated by one atomic layer is shown in (*c*) and the supercell where the separation is six atomic layers is shown in (*d*). Horizontal arrows point to the position of the stacking faults and vertical double arrows indicate the separation between two of them. Note that there are two cubic bonds in each configuration (underlined letters). These supercells are used to study the effect of the number of stacking faults and their separation on the formation energy.

As can be seen from Table VII.2, the formation energy for both compounds is the lowest for type-I, followed by type-II and then extrinsic stacking fault. Specifically, stacking fault of type-II is twice as high in energy compared to type-I, while extrinsic stacking fault is three times larger. To explain this trend we plot in Figure VII.3 the formation energy of different stacking faults versus the corresponding number of cubic bonds. We observe a linear behaviour of high precision, which means that the formation energy is proportional to the number of cubic bonds at the stacking fault [277]. As such, the energy needed to form one cubic bond is equal to that of type-I stacking fault (since this fault contains only one cubic bond). The same reasoning applies to the other types as well: the energy of the type-II (extrinsic) stacking fault is two (three) times the energy of one cubic bond.

In order to shed more light on E_f, we calculate the energy difference between the zincblende and wurtzite polytypes. This difference is calculated to be 11.87 meV for GaN and 19.01 meV for ZnO. We note that both values are very close to the formation energy of type-I stacking fault. This is to be expected since the wurtzite-zincblende transformation involves the changing of the stacking sequence from AaBb to AaBbCc (or equivalently the creation of one cubic bond), so the energy difference between the two competing phases is consistent with the trend observed for the stacking-fault formation energies [282].

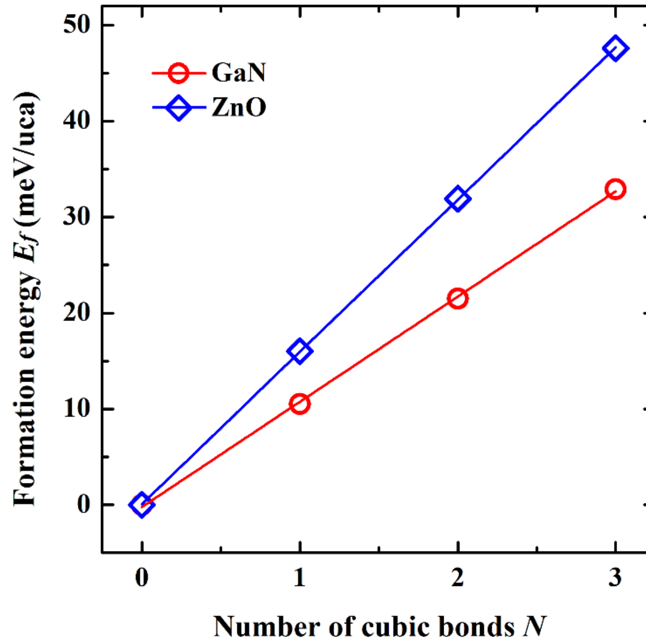

Figure VII.3 Variation of stacking-fault formation energy as a function of the number of cubic bonds (0, 1, 2 and 3 for ideal, type-I, type-II and extrinsic stacking fault, respectively) for wurtzite GaN (red curve) and ZnO (blue curve). Curves are linear fits to the calculated data.

VII.3.2 Electronic structure

A. Band gap:

Next, we investigate the electronic structure of stacking faults. The GGA and mBJ approximations are both employed to model the exchange-correlation part of the total-energy functional. The band structures calculated at the points of high symmetry of the Brillouin zone are illustrated in Figure VII.4. We only show the band structure obtained by the mBJ functional due to its more accurate prediction for the band gap as compared to GGA (more about this point below). By definition, the band gap E_g is given by the difference between the conduction-band minimum E_C and the valence-band maximum E_V [29]:

$$E_g = E_C - E_V. \qquad \text{(VII.2)}$$

A detailed analysis of the band structure reveals that stacking faults introduce a downward (upward) shift of E_C (E_V), resulting in a narrowing of the band gap. In addition, we find that all stacking faults show a direct gap at the point Γ. These findings are consistent with the previous works concerning stacking-fault electronic structure in GaN and ZnO [277,280].

The computed band gaps at the level of GGA and mBJ are listed in Table VII.3 for all GaN and ZnO stacking faults as well as the perfect structures. Our results show that the gap is generally largest for type-I, smallest for extrinsic, and intermediate for type-II stacking fault. Using the local density approximation, Stampfl and Van de Walle [280] have found that the band gap reduces by 0.02 eV for GaN type-I stacking fault. From our data in Table VII.3, we

obtain a decrease of 0.05 eV. To the best of our knowledge, there are only published data of the energy gap for wurtzite GaN and ZnO without stacking faults.

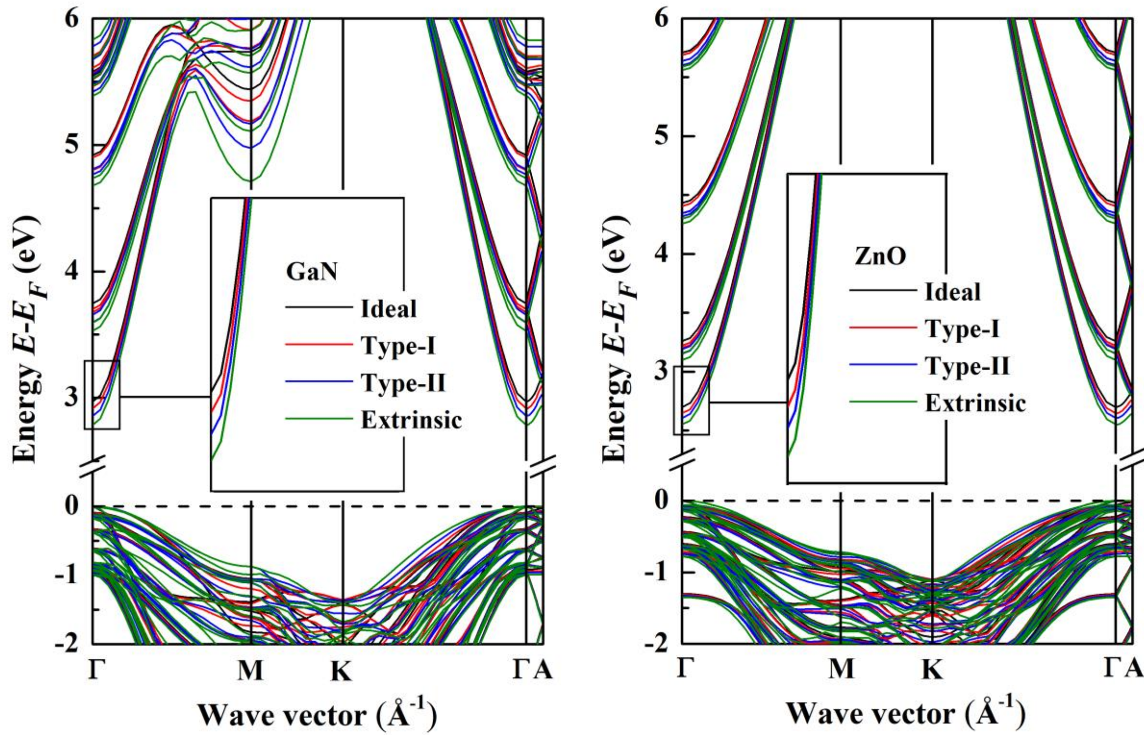

Figure VII.4 Band structures for the ideal and stacking-fault structures of wurtzite GaN and ZnO obtained using the mBJ approximation. The origin of energies is the Fermi level E_F (the dashed horizontal line). The values of the band gaps and band offsets are extracted from these curves. The insets give a closer look at the conduction-band minimum for all the structures studied.

Table VII.3 Band gap E_g within the GGA and mBJ approximations for the ideal and stacking-fault structures of wurtzite GaN and ZnO.

	Ideal	Type-I	Type-II	Extrinsic
GaN				
E_g GGA (eV)	1.68 (1.58 [a])	1.63	1.56	1.54
E_g mBJ (eV)	2.97 (2.88 [a])	2.92	2.86	2.78
ZnO				
E_g GGA (eV)	0.75 (0.70 [b])	0.72	0.69	0.67
E_g mBJ (eV)	2.67 (2.61 [b])	2.62	2.58	2.53

[a] Ref. [284], [b] Ref. [285]

The variation of the gap with the number of cubic bonds for each type of stacking faults is shown in Figure VII.5. The band gap, like the formation energy, also varies linearly with the number of cubic bonds. A by-product of the calculation of the zincblende/wurtzite energy difference reported above is the values of the mBJ band gap for each phase. In the case of zincblende, we obtain the following values: 2.74 and 2.51 eV for GaN and ZnO, respectively. The corresponding mBJ gaps for the wurtzite system are listed in the second column of Table VII.3. In going from type-I to type-II to extrinsic stacking faults, the crystalline structure

gets closer and closer to the zincblende phase. Therefore, the band gaps associated with the stacking faults lie between the limiting values of the wurtzite and zincblende polytypes.

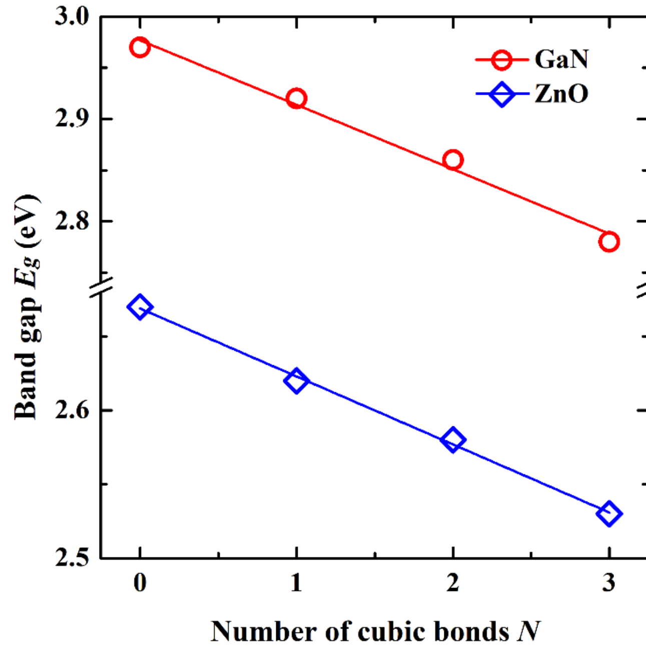

Figure VII.5 Band gap obtained at the level of mBJ versus the number of cubic bonds corresponding to each type of stacking fault for wurtzite GaN and ZnO. The curves are as in Fig. VII.3.

The experimental band gap of wurtzite GaN (ZnO) is around 3.5 eV [286] (3.4 eV [287]). It is evident that the gap values for the ideal crystals obtained by GGA are severely underestimated compared to those found experimentally. In particular, for the case of ZnO the discrepancy between theory and experiment is about 76%. It is well established that the GGA functional fails to reproduce the band structure of semiconductors by underestimating their band gap [111], often by several electronvolts. In order to overcome the inherent shortcoming of GGA in reproducing band gaps, we use the mBJ functional, which provides much more accurate and reliable results for the energy gap [113,114]. This fact is demonstrated by our results (see Table VII.3), where mBJ-corrected gaps are found to be in better agreement with experiment than GGA.

B. Band offsets:

In our implementation, the band structure is calculated with respect to the Fermi energy level E_F, with the origin of energy coincides with E_V and the gap coincides with E_C, so we can write:

$$\begin{aligned} E_V - E_F &= 0, \\ E_C - E_F &= E_g. \end{aligned} \qquad \text{(VII.3)}$$

Energy calculation provides the values of the gap and Fermi level, so that both E_V and E_C can be accessed from Eq. (VII.3). We report in Table VII.4 the mBJ-corrected values of the Fermi level E_F and band extrema E_V and E_C. We also report the conduction- and valence-band offsets (discontinuities) ΔE_C and ΔE_V. The conduction-band offset is calculated by the difference:

$$\Delta E_C = E_C^{Id} - E_C^{SF}, \qquad \text{(VII.4)}$$

where E_C^{Id} and E_C^{SF} are the conduction-band minimum of the ideal and defected crystals, respectively. A similar expression exists for ΔE_V, for which the valence-band maxima E_V^{Id} and E_V^{SF} are used. As will be shown later on, these quantities are of interest for the design of GaN- and ZnO-based optoelectronic devices, since band offsets affect the confinement energies of electrons and holes [174]. Both ΔE_C and ΔE_V are observed to be smaller for type-I stacking fault, but larger for the extrinsic one. We also note that the conduction- and valence-band offsets are of opposite sign, with the dominant offset being the conduction part. Most of the available data for the band offsets are for wurtzite/zincblende superlattice interfaces, rather than the stacking faults themselves. Yan et *al*. [277] have shown that ΔE_C for stacking faults in ZnO ranges from 0.02 to 0.04 eV, but have not reported explicit values. Compared to these calculations, our values are in rather good agreement.

Table VII.4 Results of the Fermi energy E_F, valence-band maximum E_V, conduction-band minimum E_C as well as valence-band offset ΔE_V and conduction-band offset ΔE_C, obtained in the framework of the mBJ potential for the ideal and stacking-fault structures of wurtzite GaN and ZnO. According to Eq. (VII.3), $E_V = E_F$ and $E_C = E_g + E_F$. ΔE_V and ΔE_C are given by Eq. (VII.4).

	Ideal	Type-I	Type-II	Extrinsic
GaN				
E_F (eV)	6.35	6.36	6.37	6.38
E_V (eV)	6.35	6.36	6.37	6.38
E_C (eV)	9.32	9.28	9.23	9.16
ΔE_V (eV)	0	−0.011	−0.019	−0.028
ΔE_C (eV)	0	0.045	0.096	0.160
ZnO				
E_F (eV)	4.74	4.75	4.76	4.79
E_V (eV)	4.74	4.75	4.76	4.79
E_C (eV)	7.41	7.36	7.34	7.32
ΔE_V (eV)	0	−0.002	−0.021	−0.046
ΔE_C (eV)	0	0.048	0.070	0.094

C. Stacking faults as quantum wells:

Stacking faults considered here can be pictured as thin zincblende layers surrounded by a wurtzite lattice, so that one speaks of zincblende/wurtzite interfaces [288]. Because of the band gap lowering discussed earlier, these stacking faults give rise to quantum-well-like regions as already discussed by many authors [278,289,290]. The band profile of such quantum wells is shown in Figure VII.6 for GaN and ZnO. Electrons in the conduction band with small energy gap will be trapped in this region [72]. The situation is similar for holes in the valence band. We point out that the confinement energy barrier, or the height of the quantum well, is equal to the band offsets. As a consequence, the quantum well associated with the extrinsic stacking fault has the highest barrier, as shown in Fig. VII.6.

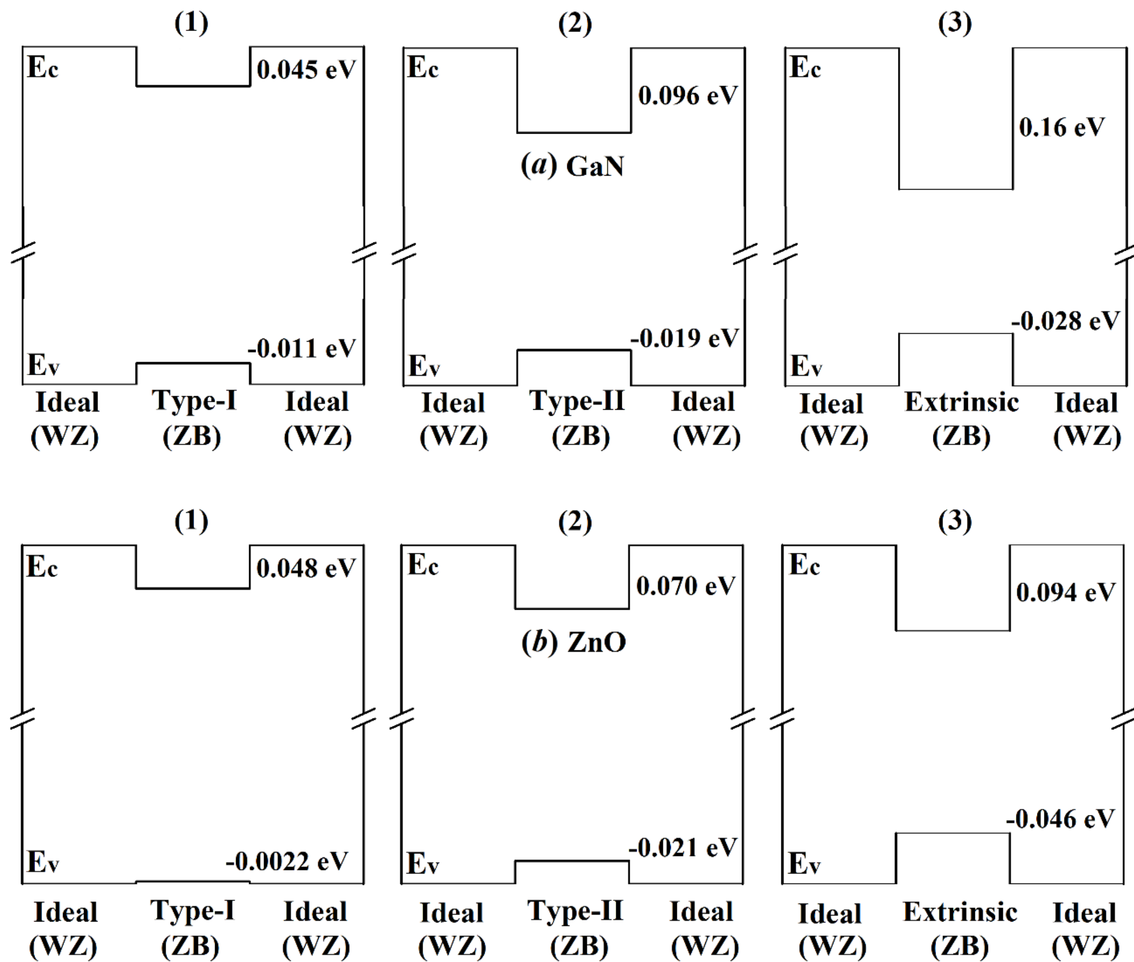

Figure VII.6 Schematic plot of the band profile of quantum wells associated with (1) type-I, (2) type-II and (3) extrinsic stacking faults in (*a*) GaN and (*b*) ZnO. "Ideal" refers to the wurtzite (WZ) side of the interface while the stacking faults refer to the zincblende (ZB) side. The values of the conduction- and valence-band offsets are also shown.

In what follows we discuss the practical implications of the defect-induced gap reduction for quantum-well devices. We consider a light emitting diode (LED) made from ZnO as an example. It is well known that most grown ZnO crystals are n-doped due to the presence of oxygen vacancies which is hard to avoid in real systems, which means that the majority charge carriers in ZnO are usually electrons. As it is visible in Fig. VII.6, each stacking fault in ZnO gives rise to a potential well. According to basic quantum mechanics, the doped electron in the conduction band with low energy will be trapped in a bound state of the quantum-well region (the zincblende or stacking-fault layer).

Because the band gap is reduced by the presence of the stacking faults, the electronic transition between the conduction and valence bands leads to light emission at lower energies (or equivalently longer wavelengths) than for the ideal bulk crystal. Such emissions are referred to as *photoluminescence* [159,291–293]. In the case of pure wurtzite ZnO, where our theoretical (mBJ) band gap is 2.67 eV (see Table VII.3), we calculate an emission wavelength of 466 nm. For the extrinsic stacking fault of ZnO, on the other hand, the gap of 2.53 eV yields a

photoluminescence line positioned at 491 nm, which is longer than the wavelength associated with the ideal crystal.

In this context we cite an experimental study performed by Schirra et *al*. [292], where a 3.31 eV emission in ZnO samples have been detected. Such an emission has a wavelength of 376 nm and belongs to the near ultraviolet region of the spectrum. Using complementary characterization techniques, namely cathodoluminescence and transmission electron microscopy, the authors identified the 3.31 eV emission to be a photoluminescence emission produced by stacking faults. While our simulation captures the mechanism of the photoluminescence phenomenon, it falls short in reproducing the measured wavelength of the corresponding emission line: the experimental emission is ultraviolet (376 nm) and our theoretical emission is blue (491 nm). This apparent discrepancy is due to the band-gap underestimation predicted by DFT. For a comprehensible picture of the luminescence properties related to stacking faults in GaN we refer to the review by Lähnemann et *al*. [159].

D. Effective mass:

One of the key material parameters in the band theory of solids is the effective mass m^* of the charge carriers [294]. A particle moving in a crystal lattice is not free as it interacts with the periodic potential generated by the ionic cores. The concept of the effective mass is that the particle can be considered free (i.e. it moves in vacuum) provided that its mass is m^* [29], which is different from the rest mass m_0 (for electrons m_0= 9.31×10^{-31} kg). It is possible to determine by cyclotron resonance experiments the effective mass of semiconductors [295–297], where the electrons and holes are accelerated along helical paths about a static magnetic field. The effective mass of the particles is related to the cyclotron frequency.

In the framework of first-principles calculations, the value of the effective mass is extracted from the band structure. At the maximum of the valence band E_V and the minimum of the conduction band E_C (collectively called band edges), the band structure can be locally approximated by the following quadratic formula [29]:

$$E(k) = E_0 + \frac{\hbar^2 k^2}{2m^*}, \tag{VII.5}$$

where $E(k)$ is the energy of an electron or hole at the wave vector k, $\hbar$ is the reduced Plank constant and E_0 is the band-edge energy E_C or E_V. Taking the second derivative of E with respect to k, we see that the effective mass is given by [29,298]:

$$m^* = \hbar^2 \left[\frac{d^2E(k)}{dk^2}\right]^{-1}. \tag{VII.6}$$

Graphically, m^* is inversely proportional to the curvature of the band structure. Since the lattice constants a and c are different, wurtzite crystals are anisotropic, which means that the values of many properties, including the effective mass, depend on the crystallographic direction. Figure VII.7 displays the Brillouin zone of the wurtzite structure. We distinguish two values of m^* [299]: the longitudinal effective mass along the high-symmetry direction ΓA (parallel to the

c^*-axis in reciprocal space), and the transverse effective mass along the ΓM or ΓK direction (perpendicular to the c^*-axis). In addition, there are two types of holes, namely heavy and light holes, each type has its own value of m^*.

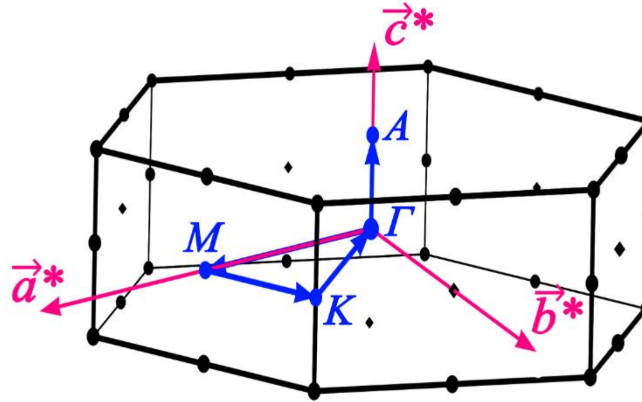

Figure VII.7 Brillouin zone of a hexagonal crystal, which is the unit cell in reciprocal space. The reciprocal lattice vectors **a***, **b*** and **c*** are related to the (real) lattice constants a and c via the following relations: $\mathbf{a}^* = \frac{2\pi\mathbf{i}}{a} + \frac{2\pi\mathbf{j}}{a\sqrt{3}}$, $\mathbf{b}^* = -\frac{2\pi\mathbf{i}}{a} + \frac{2\pi\mathbf{j}}{a\sqrt{3}}$ and $\mathbf{c}^* = \frac{2\pi\mathbf{k}}{c}$. The high-symmetry points are Γ (0,0,0), M (1/2,0,0), K (1/3, 1/3,0) and A (0,0,1/2) [300]. There are other points not shown here such as H (1/3,1/3,1/2) and L (1/2,0,1/2). The path in k-space Γ-M-K-Γ-A is shown by the blue arrows. The band structures in this work are obtained by following this exact path (e.g. see the x-axis of the graph of Fig. VII.4). The longitudinal (transversal) effective mass is calculated along the ΓA (*Γ*M) direction. This Brillouin zone is generated by the code XCrySDen [301].

In what follows, we evaluate the effective mass of wurtzite GaN and ZnO for the ideal and staking-fault structures using Eq. (VII.6). We only focus on the longitudinal effective mass of electrons. We stress that the formula given by Eq. (VII.6) is only valid near the band edge, which is in our case the conduction-band minimum at the Γ point. We start our analysis by extracting the conduction band from the band structure of Fig. VII.4 and zooming the band along the direction ΓA around the point Γ. The resulting graph shown in Figure VII.8 is almost a parabola as required by Eqs. (VII.5) and (VII.6). Fitting the E-k data to a quadratic polynomial allows to calculate the second derivative d^2E/dk^2 and hence m^*.

The results are summarized in Table VII.5. As anticipated, electrons have a positive effective mass as the curvature of the corresponding parabola points upward. Experimentally determined electron effective masses of defectless GaN scatter quite significantly, ranging from 0.18 to 0.29 [69]. Compared to experiment our value of m^* for GaN (0.24) is therefore within the reported range. For ZnO without stacking faults, our prediction (0.35) is greater than the measured value 0.30 by around 20% [21]. This discrepancy might arise from the band-gap problem of DFT discussed earlier in subsection A, even though the calculation of the effective mass is done using the mBJ-corrected band structure.

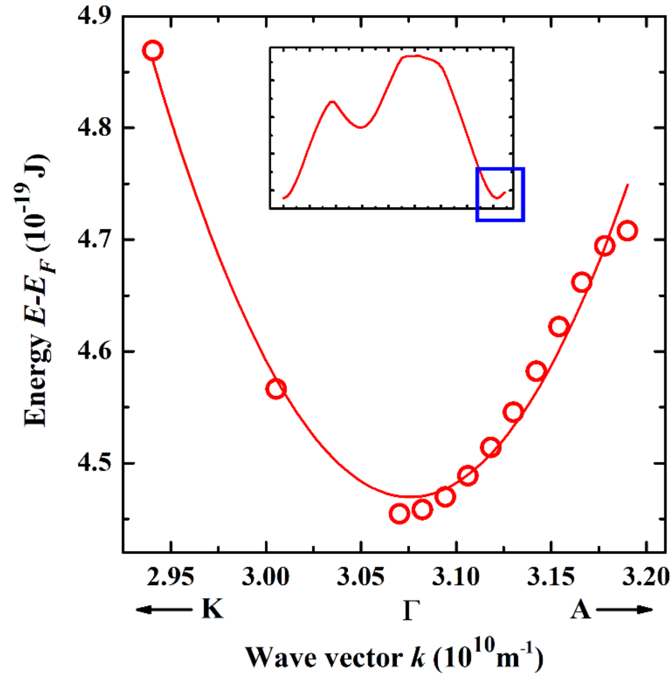

Figure VII.8 Conduction band near the point Γ utilized to compute the effective mass of electrons for the extrinsic stacking fault of GaN. We extract the value of the curvature d^2E/dk^2 from a quadratic fit of the energy-wave vector data: $E(k) = \alpha k^2 + \beta c + \gamma$, which means that the band curvature is simply 2α. The inset shows the entire conduction band, and the blue rectangle encloses the minimum of the band, i.e. the quadratic curve below the inset.

Table VII.5 Band curvature d^2E/dk^2 (near the high-symmetry point Γ) and longitudinal electron effective mass m^* for the ideal and stacking-fault structures of wurtzite GaN and ZnO. The value of m^* is written in units of the free electron mass m_0, e.g. for ideal GaN we have m^*/m_0= 0.24. Our results of m^* are compared to selected experimental literature values (put between parentheses).

	Ideal	Type-I	Type-II	Extrinsic
GaN				
d^2E/dk^2 (10^{-38} J m²)	5.01	4.59	4.45	4.27
m^*	0.24 (0.18-0.29) [a]	0.27	0.28	0.29
ZnO				
d^2E/dk^2 (10^{-38} J m²)	3.47	3.12	3.03	2.81
m^*	0.35 (0.30 [b])	0.39	0.40	0.44

[a] Ref. [69], [b] Ref. [21]

What interests us here is the effect of stacking faults on the effective mass. From the data listed in Table VII.5, the presence of the stacking faults causes m^* to increase. This observation holds for both GaN and ZnO. Among the physical parameters that can be altered by the electronic effective mass are the transport coefficients such as the carrier mobility μ [294]. The latter characterizes the drift velocity of electrons and is defined as the ratio of the relaxation time to the effective mass [29]:

$$\mu = \frac{e\tau}{m^*}, \qquad \text{(VII.7)}$$

where e is the usual electron charge. The relaxation time τ (also called the scattering time) is a statistical property defined as the average time between two successive collisions of particles (electrons here). Because the effective mass increases in the presence of basal stacking faults, equation (VII.7) indicates that the mobility of electrons decreases, which has the effect of impeding the flow of electronic current in semiconductor devices like transistors.

E. Unfolded band structure:

The different band structures presented in Fig. VII.4 are obtained by performing energy calculation on 20-atom 1×1×5 wurtzite supercells. The use of supercells in the calculation of the electronic band structure imposes a number of drawbacks. The most immediate consequence is that the electronic properties of a material (e.g. band gaps and effectives masses) may not be reproduced exactly. Put in other terms, the electronic properties extracted from the band structure of a supercell are generally different than those obtained from the band structure of the unit cell [302]. To understand the reason of this disagreement, note that the supercell, being larger than the unit cell, shrinks the Brillouin zone of the crystalline solid in reciprocal space, which necessarily leads to a modified energy-momentum (or wave vector) dispersion relation as compared to that of the unit cell.

Dealing with this issue necessitates the adoption of a band unfolding technique, in which the band structure of the supercell is transformed into a version similar to the band structure of the unit cell. As we will see, this allows to better visualize the band structure of the system via removing the ambiguities introduced by the supercell's geometry. The most successful approach for this task turns out to be the *Bloch spectral weight projection* [303] implemented in the package fold2Bloch [304]. Like BerryPI [141] and IRelast [199], fold2Bloch is a software integrated in WIEN2k. This unfolding scheme is explained in Ref. [304]. As wurtzite GaN and ZnO share very similar band structures (*c.f.* Fig. VII.4), we choose GaN in the rest of this section as the representative material to introduce the results of the unfolded band structure.

We first obtain the band structure of the 4-atom unit cell of ideal GaN and plot it along the high-symmetry directions in Figure VII.9 (*a*). The calculated band structure reproduces some experimental features such as the direct band gap. Next we repeat the band-structure calculation for the 20-atom 1×1×5 supercell, which model the ideal structure of GaN (i.e. without stacking faults). The results are presented in Fig. VII.9 (*b*), where we observe two main differences as compared to Fig. VII.9 (*a*). First, the separation in reciprocal space (given in $Å^{-1}$) between some high-symmetry points is not the same. This is most exemplified in the points Γ and A: whereas these two points are separated by 0.32 $Å^{-1}$ for the unit cell, the separation is only 0.063 $Å^{-1}$ for the supercell. The coordinates of A in reciprocal space are (0,0,1/2) [300], meaning the point A is situated on the c^*-axis as shown in the Brillouin zone of Fig. VII.7. The studied supercell is built by expanding the unit cell five times along the c- or z-axis, which corresponds to shrinking the Brillouin zone five times along the c^*-axis. Indeed, the ratio of the previously mentioned distances is 0.32/0.063= 5; in other words, the distance ΓA for the supercell is five times smaller

than that for the unit cell. As for the separations between other points, such as M and K, they are basically equal because the basal lattice constants *a* of the supercell and the unit cell are identical and these points exist on the (reciprocal) basal plane, their coordinates are of the form (na*,ba*,0) [300], with a* being the basal reciprocal lattice constant and *n* and *m* are integers.

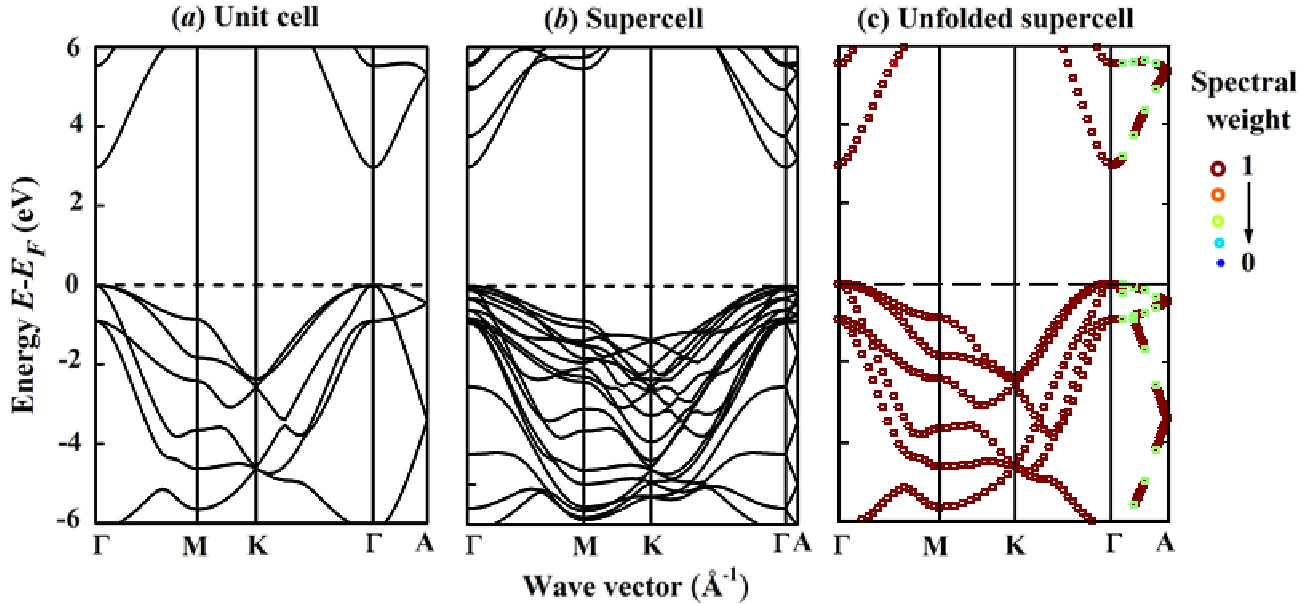

Figure VII.9 Electronic band structure of wurtzite ideal GaN for (*a*) the 4-atom unit cell and (*b*) 20-atom supercell. The unfolded band structure of the supercell is illustrated on panel (*c*), which is the output of the code fold2Bloch. The size and colour of the data points in (*c*) represent the value of the Bloch spectral weight (between 0 and 1). For the three band structures, the energy scale is kept fixed (from 6 to −6 eV) and the Fermi energy E_F is set to zero (dashed horizontal lines).

The second major difference between the band structures of Figs. VII.9 (*a*) and (*b*) is with regards the energy bands. Evidently there are more bands in the band structure of the supercell than of the unit cell. This is to be anticipated since the supercell has more atoms and correspondingly more electronic orbitals (each energy band is associated to an orbital). Additionally, we note that the bands of negative energy for the supercell are shifted upward. Here, the nature and value of the mBJ gap extracted from both band structures are the same, i.e. for both the unit cell and the supercell the gap is direct with a value of 2.97 eV. We have also verified that the curvature of the conduction band around the point Γ result in similar electronic effective masses for both types of cells. It is important to note that this is not always the case, especially for doped and alloyed compounds, in which impurities are introduced to the supercell. For such systems, the electronic properties of the supercell can be quite different from the properties of the unit cell, as discussed in detail in Ref. [304]. Our supercell has no impurities, perhaps this is the reason why the band structures of Figs. VII.9 (*a*) and (*b*) reproduce the same values of E_g and m*.

Now we apply the spectral weight projection method using fold2Bloch in the attempt to recover the GaN band structure in its conventional unit-cell representation from the 20-atom supercell. In this simulation, the band structure of the supercell is used as an input for the unfolding calculation. The output unfolded band structure is plotted in Fig. VII.9 (*c*), where we can see that it is extremely similar to the band structure of the 4-atom unit cell [Fig. VII.9 (*a*)]. The colour of most of the data points is brown and corresponds to a Bloch spectral weight of 1, indicating the energy eigenstates are Bloch wavefunctions.

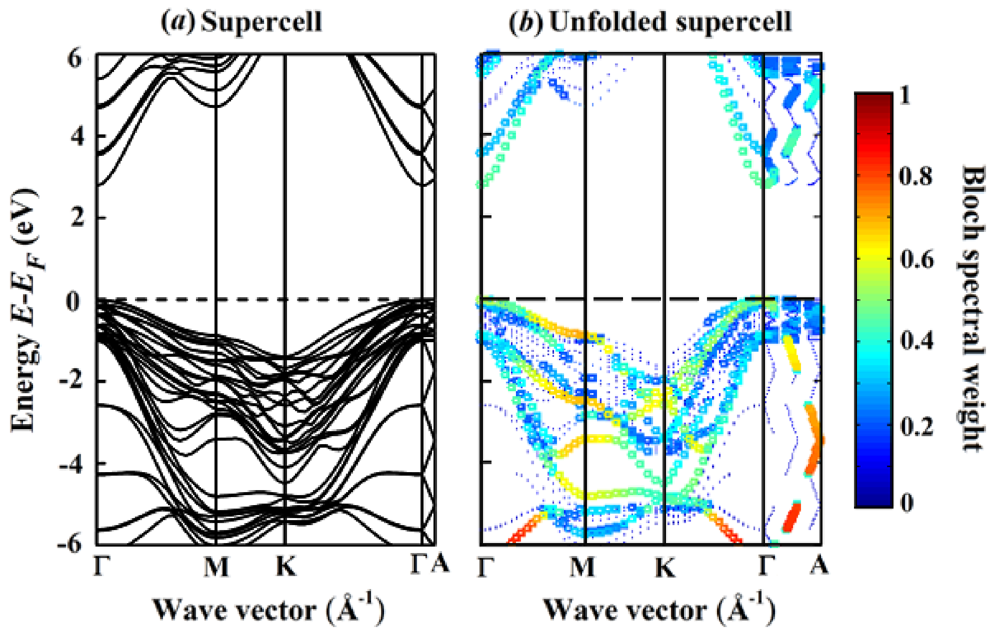

Figure VII.10 Band structure of (*a*) 20-atom supercell and (*b*) its unfolded version for the extrinsic stacking fault of GaN. The colour scale represents the Bloch spectral weight and goes from 0 to 1.

Finally, the unfolding calculation is performed for the band structure of the supercell representing the extrinsic stacking fault of GaN. Of course, there is no unit cell here, as it is not possible to realize a stacking fault in such a small cell. The band structure of the supercell shown in Fig. VII.10 (*a*) is transformed into the unfolded band structure of Fig. VII.10 (*b*) via the procedure outlined above. The unfolded bands are somehow similar to those of Figs. VII.9 (*a*) and (*b*), but there are some differences due to the perturbation induced by the presence of the extrinsic stacking fault. The values of the Bloch weight character in this case are 0.3, 0.55 and 0.65, which corresponds to the blue, green and orange symbols, respectively.

VII.3.3 Electric polarization

A. Spontaneous polarization:

The polarization of any wurtzite crystal is the sum of spontaneous and piezoelectric components. The first component is due to the intrinsic low symmetry of the wurtzite phase, whereas the latter results from the applied mechanical strain [305]. The origin of strain in the defected layers of thin films is usually the in-plane lattice mismatch. Since all types of stacking

faults are almost perfectly matched to the ideal structure (see Table VII.1), the piezoelectric polarization can be assumed to be negligible [210].

Within the Berry-phase method, the spontaneous polarization is defined as the polarization difference between two different structures of the same solid: a polar non-centrosymmetric structure and its non-polar high-symmetry counterpart called the reference structure [135,136]. In our case, the polar non-centrosymmetric structure is wurtzite and the structure that serves as a reference is either the trigonal (equivalently zincblende) and the layered-hexagonal structures:

$$P_{sp,T} = P_{WZ,1} - P_{T,1},$$
$$P_{sp,H} = P_{WZ,1} - P_{H,1} + \frac{2e}{\sqrt{3}a^2}, \qquad \text{(VII.8)}$$

where $P_{sp,T}$ ($P_{sp,H}$) is the spontaneous polarization with respect to the trigonal (hexagonal) reference. WZ, T and H denote the wurtzite, trigonal and hexagonal structures, respectively. The index 1 in the formal polarizations is an indication that we use supercells of dimension 1 along the a- and b- directions (1×1×4 supercells), which means that the polarization branch is n=1 for the trigonal reference and n^*= 1 for the hexagonal reference. We remind the reader that the third term in the right-hand side of $P_{sp,H}$ is the quantum of polarization $P_{q,1}$ of the 1×1×4 supercells needed to correct the polarization discontinuity (see Sec V.3.3). Using the Berry-phase technique implemented in BerryPI, the spontaneous polarization of each stacking fault for the two references is calculated and reported in Table VII.6 together with the available simulation data from the literature [26,36,144,160,210]. The spontaneous polarization is found to be non-zero only along the hexagonal c-axis, which corresponds to the ideal stacking direction.

Table VII.6 Berry-phase results of the spontaneous polarization with respect to the trigonal ($P_{sp,T}$) and to the hexagonal ($P_{sp,H}$) references for the ideal and stacking-fault structures of wurtzite GaN and ZnO. Previous theoretical values are given in parenthesizes.

	Ideal	Type-I	Type-II	Extrinsic
GaN				
$P_{sp,T}$ (C/m²)	−0.035 (−0.034[a])	−0.026	−0.021	−0.016 (−0.018[b])
$P_{sp,H}$ (C/m²)	1.293 (1.312[c])	1.302	1.307	1.312
ZnO				
$P_{sp,T}$ (C/m²)	−0.045 (−0.057[d])	−0.037	−0.031	−0.025
$P_{sp,H}$ (C/m²)	0.807 (0.835[e])	0.814	0.820	0.826

[a] Ref. [160], [b] Ref. [210], [c] Ref. [26], [d] Ref. [144], [e] Ref. [36]

It is important to observe the trend followed by the stacking faults: the spontaneous polarization calculated by the *trigonal* reference decreases in magnitude with the number of cubic bonds, i.e. from the ideal to type-I to type-II and, more significantly, to extrinsic stacking fault. The latter is the closest structure to the non-polar trigonal or zincblende lattices (with three cubic bonds); consequently, it has the smallest polarization among the stacking faults considered in this study. However, the spontaneous polarization referenced to the *hexagonal* structure decreases in the reversed order: from extrinsic to type-II to type-I stacking fault. We

do not fully understand the reason for this behaviour, and we remain with an open question regarding this issue.

Our values of $P_{sp,T}$ and $P_{sp,H}$ for the ideal structure (i.e. without any cubic bonds) agree well with the ones reported in the literature [26,36,144,160,210]. A self-consistent Poisson Schrödinger calculation in Ref. [210] results in a value of $P_{sp,T}$ equal to -0.018 C/m² for the extrinsic stacking fault of GaN, which is very close to our value of -0.016 C/m² (more details below). Figure VII.11 displays the variation of the spontaneous polarization of stacking faults with the number of cubic bonds for each fault. A linear dependence is observed for the trigonal- and hexagonal-referenced values.

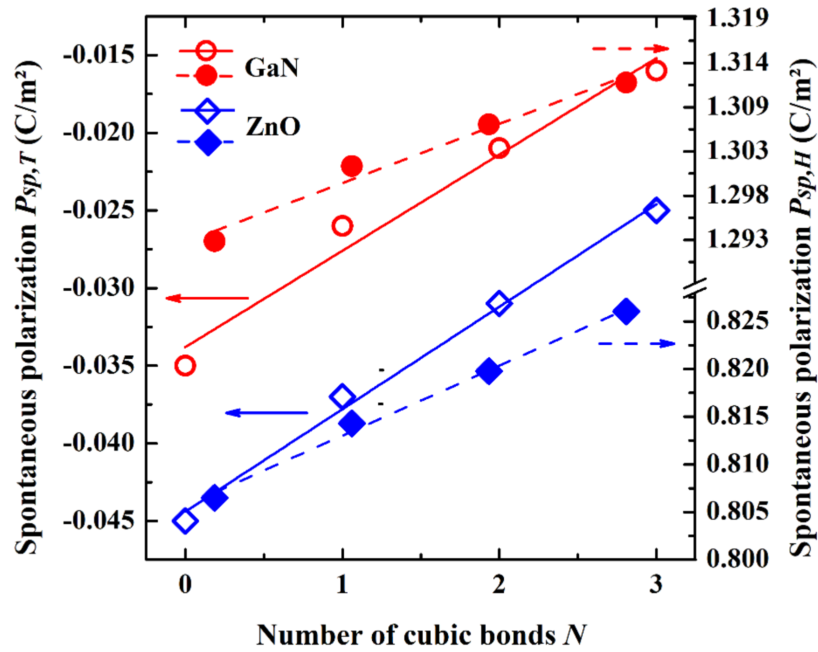

Figure VII.11 Spontaneous polarization of the ideal and stacking-fault structures as a function of the cubic-bond number for GaN and ZnO. The values referenced to the trigonal (hexagonal) structure $P_{sp,T}$ ($P_{sp,H}$) are marked on the *y*-axis on the left (right) and represented by open (solid) symbols and continuous (discontinuous) curves.

B. Interface polarization charge:

As pointed out in Sec. VII.3.2 C, stacking faults can be considered as quantum wells with zincblende/wurtzite interfaces. The formal polarization differs for each side of the interface, thus giving rise to the accumulation of interfacial electric charge [35,37,158]. According to the interface theorem [38], the interface charge σ is equal to the difference between the formal polarization of zincblende $P^{SF}_{WZ,1}$ [with stacking faults (SF)] and wurtzite $P^{Id}_{WZ,1}$ [without stacking faults (Id)]:

$$\sigma = P^{SF}_{WZ,1} - P^{Id}_{WZ,1}. \tag{VII.9}$$

We calculate the interface charge using the formal polarizations $P^{SF}_{WZ,1}$ and $P^{Id}_{WZ,1}$ used to obtain the spontaneous polarizations $P_{sp,T}$ and $P_{sp,H}$. We present the results of σ in Table VII.7 in the units of C/m² and cm^{-2}.

Table VII.7 Interface polarization charge for the ideal and stacking-fault structures of wurtzite GaN and ZnO. The results of σ are presented by two units: C/m² and cm^{-2}.

	Type-I	Type-II	Extrinsic
GaN			
σ (C/m²)	0.009	0.014	0.019 (0.018[a])
σ (10^{12} cm^{-2})	5.63	8.75	11.88 (11.25[a])
ZnO			
σ (C/m²)	0.0078	0.013	0.020
σ (10^{12} cm^{-2})	4.88	8.30	12.24

[a] Ref. [306]

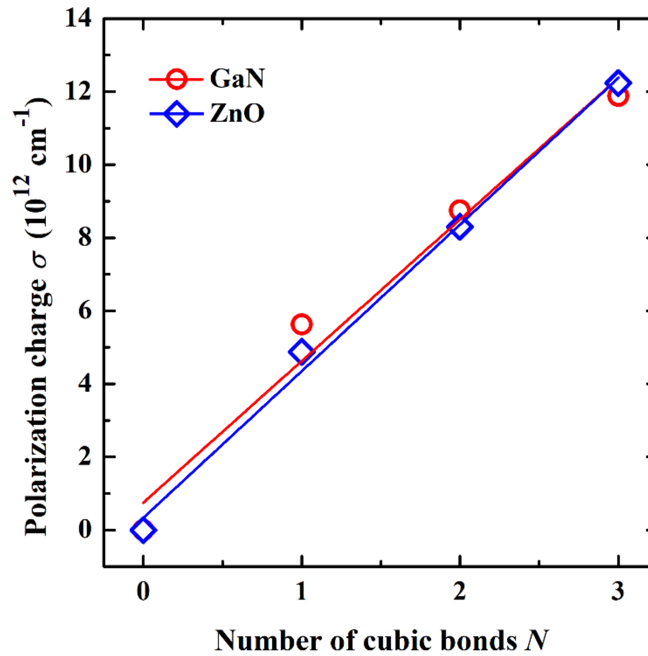

Figure VII.12 Values of the polarization charge as a function of the number of cubic bonds for intrinsic and extrinsic stacking faults in GaN and ZnO. The charge builds-up at the wurtzite (without stacking faults) and zincblende (with stacking faults) interface.

We find that the polarization charges for GaN stacking-faults are comparable to those for ZnO. The most charged interface is the one associated with the extrinsic stacking fault. The agreement between our Berry-phase value and the band-structure result of Ref. [306] for the extrinsic fault is very good, indicating the validity of both approaches in evaluating the polarization charge at interfaces. The proportionality with the number of cubic bonds seems to hold for the polarization charge as well, as indicated by Figure VII.12. The linear behaviour is less evident than for the formation energy and band gap but still valid, especially for ZnO.

The main consequence of the charged layer is the built-in electric fields present at the stacking faults [78,158]. Such fields are about 2.5 MV/cm for stacking faults in GaN [210]. The polarization-induced charges and the ensuing electric fields considerably affect the performance of GaN- and ZnO-based applications. For example, the presence of polarization fields tends to reduce the optical efficiency, thereby limiting the performance of light-emitting devices [3,4].

C. Piezoelectric coefficient:

Wurtzite GaN and ZnO are attractive piezoelectric materials for applications that require efficient electromechanical coupling [307,308]. As such, it is interesting to investigate the effect of stacking faults on the piezoelectric coefficients of both materials. Given that the hexagonal stacking direction coincides with the c-axis, we calculate only the axial piezoelectric constant e_{33} that describes the polarization induced by a strain applied to the c-axis [144]. As stated in the previous chapter, the piezoelectric coefficient is accessible via a finite difference of polarization between two states, corresponding to the strained and unstrained structures [243]:

$$e_{33} = \frac{\tilde{P}_{WZ,1} - P_{WZ,1}}{\varepsilon_3}, \qquad \text{(VII.10)}$$

with $\tilde{P}_{WZ,1}$ and $P_{WZ,1}$ being respectively the formal polarization of the strained and equilibrium wurtzite structures and ε_3 is applied strain along the c-axis. In order to evaluate the piezoelectric constants of the stacking faults, the corresponding wurtzite supercells are strained by $\varepsilon_3 = -1\%$ and relaxed with respect to the lattice constant a (the Poisson effect) and the internal parameter u. Then, the polarizations are computed with the Berry-phase formalism as usual. It is found that this value of the strain allows to reproduce the previously reported coefficients for ideal GaN and ZnO (without stacking faults). The results of the piezoelectric coefficient for each type of stacking faults are displayed in Table VII.8. Comparing our results for the perfect crystals with previous calculations [21,244] shows a reasonable agreement.

Table VII.8 Calculated piezoelectric coefficient e_{33} for the ideal and stacking-fault structures of wurtzite GaN and ZnO.

	Ideal	Type-I	Type-II	Extrinsic
GaN				
e_{33} (C/m²)	0.67 (0.63-0.83) [a]	0.62	0.56	0.51
ZnO				
e_{33} (C/m²)	1.10 (0.96-1.3) [b]	1.06	1.02	0.98

[a] Ref. [244], [b] Ref. [21]

We note that the piezoelectric coefficient follows the same trend identified earlier for the spontaneous polarization referenced to the trigonal structure: e_{33} decreases in going from type-I to type-II and to extrinsic stacking fault. This implies that the piezoelectric performance of GaN and ZnO decreases in the presence of these extended defects. It is therefore desirable to exploit materials with low concentration of stacking faults in the fabrication of electromechanical devices in order to improve their performance. Like other polarization

properties, the piezoelectric coefficient is a linear function of the number of cubic bonds contained in each type of stacking faults, as shown graphically in Figure VII.13.

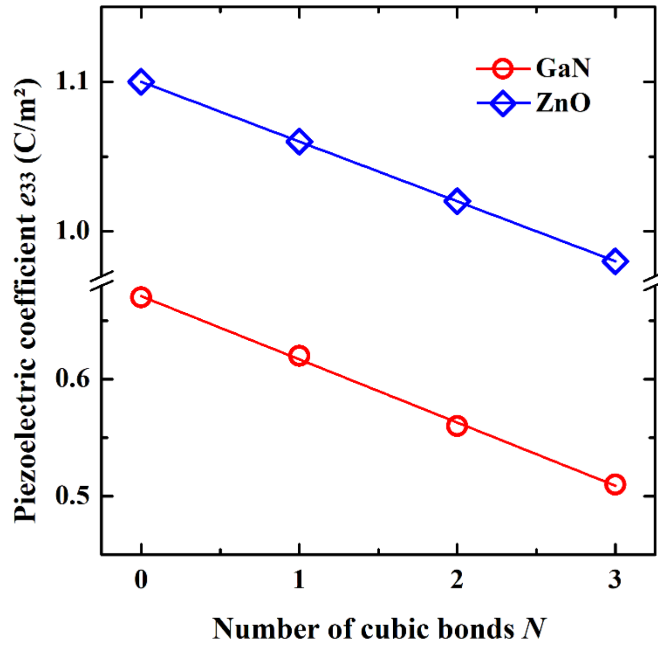

Figure VII.13 Variation of the piezoelectric coefficient with the cubic-bond number for wurtzite GaN and ZnO. As in the previous graphs, a linear fit to the calculated data is used to generate the curves.

D. Spontaneous polarization of stacking faults in GaN:

Lähnemann et *al*. [210] have succeeded for the first time in measuring the spontaneous polarization of wurtzite GaN referenced to zincblende, i.e. $P_{sp,T}$ in our context. They reported a value of -0.022 C/m² [210]. We conclude this chapter by reproducing this experimental value. However, we first present a brief overview of the experimental method used in Lähnemann's paper. This method is based on a model in which the basal stacking faults are treated as a plate capacitor. The output of the measurement is the sheet charge σ that builds up at the wurtzite/zincblende interface, which is directly related to the spontaneous polarization of the low-symmetry structure (i.e. wurtzite) [210]:

$$P_{sp,T} = \sigma = \varepsilon_0 \varepsilon \frac{\Delta V}{\Delta d}. \qquad \text{(VII.11)}$$

In the above expression, Δd is the difference in thickness between each of the stacking faults, ε is the dielectric constant of GaN and ε_0 is the permittivity of free space. The potential change ΔV in this case is equal to the difference in transition energy between the stacking faults. The latter is the key ingredient of this model: the use of equation (VII.11) for determining $P_{sp,T}$ requires at least a rough estimate of the transition energy for all types of stacking faults. This was done by two sets of spectroscopic measurements performed on samples of strain-free GaN microcrystal. Interested readers are referred to Refs. [159,210] for more details.

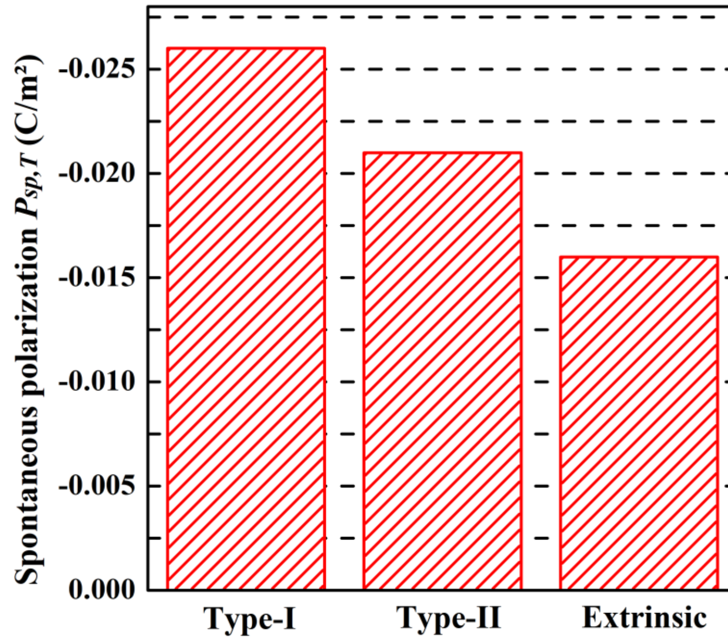

Figure VII.14 Spontaneous polarization of type-I, type-II and extrinsic stacking faults for wurtzite GaN. The values are referenced to the trigonal structure. The grid lines are guide to the eye.

It should be emphasized that the structure that serves as a reference in this measurement is zincblende, not the layered-hexagonal structure, so the value of polarization given in Eq. (VII.11) should be compared to our values referenced to the trigonal structure ($P_{sp,T}$ in Table VII.6). Our calculated values of $P_{sp,T}$ for the intrinsic and extrinsic stacking faults of GaN are shown once again in the histogram of Figure VII.14. To confirm the validity of the plate-capacitor model, equation (VII.11) was used in Ref. [210] to estimate the spontaneous polarization for the extrinsic stacking fault. In this case, ΔV and Δd are obtained from self-consistent Poisson Schrödinger calculations. This results in a value of −0.018 C/m² [210], which is very close to our value of −0.016 C/m² for the same stacking fault (see Figure VII.14 or Table VII.6).

The spectroscopically observed ΔV in Eq. (VII.11) is actually the *average value* of the transition-energy difference between the three types of stacking faults [210]. So in a sense, the recommended experimental value of −0.022 C/m² is the spontaneous polarization of type-I, type-II and extrinsic stacking faults combined. Motivated by this, we compute the average of the three spontaneous polarization values given in Figure VII.14. The value that we get is almost identical to the experimental one, namely −0.021 C/m². This discussion shows that assigning the experimental value of [210] or the average theoretical value reported here to GaN is somehow misleading: −0.022 C/m² or −0.021 C/m² is not the spontaneous polarization of the perfect defectless GaN, it is rather the value associated with the different types of stacking fault of this material. Besides, we have stressed in Sec. V.3.8 that the true value of the spontaneous polarization of any wurtzite compound is the one referenced to the layered-hexagonal structure. As such, experimental measurements of P_{sp} for GaN should align with the theoretical value predicted by the hexagonal reference (~1.3 C/m²).

VII.4 Conclusion

In the previous chapters, we studied perfect wurtzite crystals, i.e. systems without crystalline defects that perturb their hexagonal symmetry. This ideal situation was changed in this chapter as we introduced two-dimensional defects called stacking faults. These are deviations from the hexagonal stacking sequence AaBb that form on the basal plane of the host wurtzite sample. We investigated how the presence of different types of stacking faults affects the atomic structure, electronic structure and electric polarization of wurtzite GaN and ZnO.

The intrinsic and extrinsic stacking faults were modelled using 20-atom 1×1×5 wurtzite supercells. Each stacking fault contains a specific number of cubic bonds as follows: one, two and three cubic bonds for the intrinsic type-I, intrinsic type-II and extrinsic stacking faults, respectively. The structural properties, namely the lattice constants a and c and the internal parameter u, were not affected by the stacking faults, their values are equal to the equilibrium properties of the ideal defect-free crystals. This is to be expected since these defects are merely small deviations of some atomic positions in the *xy*- or basal-plane which do not significantly change the crystalline structure. Different types of stacking faults have different lengths ℓ, which are related to the number of the corresponding cubic bonds.

A key parameter characterizing stacking faults is their formation energy E_f, defined as the minimum energy needed to create one of these defects within the material. Because of periodic boundary conditions, the result of computing this energy must always be divided by 2. The formation energy was calculated to be very low (in meV), with type-I stacking fault has the smallest value, followed by type-II and the extrinsic type. An important finding is that E_f is independent of the size of the supercell, the number of stacking faults in the supercell and their separation. The only factor that determines the value of the formation energy is the number of cubic bonds within each fault, which is always the same regardless the details of the supercell. We also found the energy difference between the wurtzite and zincblende polytypes for GaN and ZnO to be very close to the formation energy of type-I stacking fault. This result was explained by the fact that the wurtzite-zincblende phase transition involves the creation of one cubic bond (and hence one type-I stacking fault).

The next step was the calculation of the electronic band structure for the ideal and stacking-faults structures of both GaN and ZnO. The calculation was carried out twice using two exchange-correlation functionals: GGA alone and GGA+mBJ. The mBJ functional was employed in order to correct the band-gap underestimation predicted by GGA. Many quantities are extracted from the (mBJ) band structure, including the band gap E_g, conduction-band minimum E_C, valence-band maximum E_V, Fermi level E_F, conduction-band offset ΔE_C and valence-band offset ΔE_V. We showed that all stacking faults studied maintain a direct gap whose value is lower than that in the ideal structure. The stacking fault with the largest band gap is type-I, then type-II and finally the extrinsic type. The reported gap values of the defects were found to be between the limiting values of the wurtzite and zincblende phases.

The immediate consequence that arises from the lowering of the band gap is the formation of quantum-well-like region at the interface between the stacking faults and the rest of the

crystal. Such an interface can be considered as a zincblende (with stacking fault) and wurtzite (without stacking fault) interface. The conduction- and valence-band offsets measure the height of the quantum walls. The latter can capture charge carrier (holes and electrons) in the stacking-fault region. Electronic transitions from the conduction band to the valence band in this region produces photoluminescence radiations that can be detected experimentally. Since the gap is lower in the stacking-fault side of the interface, the wavelength of the photoluminescence emission line is longer than the one expected from the "ideal" side.

Using the Berry-phase approach, we were able to access the spontaneous polarization P_{sp}, interface polarization charge σ and piezoelectric constant e_{33} of the intrinsic and extrinsic stacking faults. The spontaneous polarization was computed with respect to the trigonal and hexagonal references, resulting in different values and trends. The magnitude of $P_{sp,T}$ referenced to the trigonal (or equivalently zincblende) structure deceases in going from type-I to type-II to extrinsic stacking fault. The reason of this behaviour is the similarity between the stacking faults and the zincblende (or trigonal) phase. Specifically, zincblende is not polarized, so the polarization associated with the defects (which have a local zincblende geometry) is weaker (in magnitude) than the polarization of the defect-free wurtzite material. On the other hand, it was observed that the magnitude of the spontaneous polarization $P_{sp,H}$ referenced to the layered-hexagonal structure has the opposite trend, i.e. it increases from type-I, type-II and the extrinsic type of stacking fault.

The second polarization property to be studied is the polarization charge that appears at the wurtzite/zincblende interface. For each stacking fault, the polarization charge equals the formal-polarization difference between the defect-free supercell and the supercell containing the stacking fault in question. We showed that for GaN and ZnO, the charge is maximum for the extrinsic fault, which is consistent with the values of the formal polarization used in the calculation of σ. In order to identify the influence of stacking faults on the piezoelectric response of wurtzite GaN and ZnO, we determined the (proper) piezoelectric coefficient by uniaxially straining the supercells of the ideal and defected configurations. The value of e_{33} decreases when the stacking faults are introduced to the materials, with the extrinsic type has the lowest value. The practical implication of this result is that a high density of stacking faults has a negative effect on the piezoelectric response (i.e. electromechanical conversion) of wurtzite compounds, indicating it is preferable for the piezoelectric devices to be made from wurtzite crystals whose stacking-faults density is as low as possible.

In addition to all the results listed above, we found a relation of proportionality between the physical properties and the number of cubic bonds associated with each type of stacking fault. This proportionality holds for the stacking-fault formation energy, band gap, spontaneous polarization, polarization charge and piezoelectric coefficient. Quantities that do not exhibit this proportionality are the band offsets and the effective masses, as they vary non-linearly with number of cubic layers. Taking all these results into consideration, we recommend the use of the values reported in this work in simulations involving basal stacking faults of wurtzite GaN and ZnO.

GaN is the only wurtzite material to date whose trigonal-referenced spontaneous polarization is measured directly. The measurement was done by employing the transition energies of excitons bound to the stacking faults in the crystal. The experimentalists established a formula that relates this energy and the polarization of each type of stacking faults, and the spontaneous polarization $P_{sp,T}$ of GaN is obtained as the average value of P_{sp} for all the faults. Here, we reproduced the experimental figure of -0.022 C/m² following basically the same protocol: using the Berry-phase method, we computed three values of P_{sp}, each value corresponds to a particular type of stacking fault. Averaging these polarizations led to the theoretical value -0.021 C/m², which we equated it to the spontaneous polarization of defect-free GaN. We emphasized that in this context, the experimental and theoretical values of the spontaneous polarization must be compared to the ones referenced to the trigonal or zincblende structures, not the layered-hexagonal phase. In this work, we demonstrated this method of determining $P_{sp,T}$ for GaN. However, we conjecture that the approach is applicable to any wurtzite crystal (i.e. also for AlN, InN, BeO or others) and probably also for other types of stacking faults (e.g. prism- and pyramidal- faults).

General conclusion

This thesis concerns the study of electric polarization of wurtzite crystals, with a special focus on group III-nitrides and II-oxides. Our choice of these materials is motivated by their critical relevance in the development of many modern technological applications. We have considered over the course of this work a wide expanse of topics, so we present here a summary of the principle results found in Part II of the thesis.

In Chapter IV, we have performed a theoretical study of the spontaneous polarization in wurtzite crystals based on density functional theory in combination with the Berry-phase theory of polarization. We have chosen to investigate this property for the III-nitrides and II-oxides. These are technologically significant materials and a fundamental understanding of their polarization effects is of central importance. Our results demonstrate that the trigonal structure allows a consistent determination of the spontaneous polarization of wurtzite compounds: the values obtained using this structure as a reference show an excellent agreement with the zincblende-based results reported in the literature. We have shown that the electronic and ionic parts of the spontaneous polarization are of opposite sign, with the electronic term has the largest effect, indicating that the strong polarization in these materials has its origin from the partial cancellation of the two terms. Also, the spontaneous polarization is found to follow a monotonous linear behaviour with the wurtzite internal parameter.

In Chapter V, we have presented a thorough analysis of the spontaneous and piezoelectric polarizations of wurtzite III-nitride alloys AlGaN, InGaN and InAlN. The calculation is done using density functional theory with the Berry-phase technique. The spontaneous polarization of the ternary alloys referenced to the layered-hexagonal structure is found to show linearity with composition, leading to the conclusion that this quantity obeys Vegard's law quite well, being very close to the average of the parent binary values at all concentrations x. This finding is in contrast with the trigonal/zincblende-based results, for which P_{sp} is characterized by a significant bowing. Additionally, we have explained how to eliminate the effect of the supercell dimensionality in order to make the spontaneous polarization a single-valued quantity. The piezoelectric polarization induced by a biaxial strain of AlGaN/GaN, InGaN/GaN and InAlN/GaN varies non-linearly with alloy composition and, contrary to the spontaneous polarization, its value depends on the selected polarization branch (i.e. it is a multi-valued quantity).

We have also examined the electric charge density generated by the polarization discontinuity in the quaternary alloy AlInGaN/GaN. Our results show that it is possible to reduce and even cancel the built-in electric fields within this system. This is achieved by taking advantage of the composition dependence of the interface polarization charge. Specifically, a careful choice of Al and In contents can lead to a zero net polarization charge, and hence to a zero field, making it possible to fabricate high-performance optoelectronic devices. Finally, we have presented our results of the polarization charge that builds up at the interface of

AlGaN/GaN, InGaN/GaN and InAlN/GaN, which found to be in good agreement with available experimental and theoretical data. These values can be used in the analysis and design of III-nitride nanostructures such as quantum wells and quantum dots.

In Chapter VI, we have performed a first-principles study of the structural and piezoelectric properties of wurtzite materials under uniaxial strain applied along the *c*-axis. Working with binary III-nitrides and II-oxides, we have shown that the application of compressive uniaxial strain to a wurtzite crystal increases its polarization and piezoelectric coefficient. Our results indicate a non-linear (roughly linear) increase of piezoelectric polarization (piezoelectric constant) with compressive uniaxial strain for both groups of materials. The internal parameter is found to increase rapidly with the applied strain, bringing the wurtzite crystals closer to the layered-hexagonal structure.

By studying the two contributions to the piezoelectric coefficient, we have demonstrated that it is the drastic increase in the strain-response of the internal parameter $du/d\varepsilon_3$ that leads to the increased piezoelectric effect in uniaxially-strained wurtzite systems. On the other hand, the Born effective charge Z^* is hardly affected by strain and thus does not contribute to the enhanced piezoelectricity.

In Chapter VII, we have presented the results of a systematic study of basal-plane stacking faults in wurtzite GaN and ZnO, obtained from DFT calculations using periodic supercells. Specifically, we have investigated the crystal structure, electronic structure and electric polarization of the intrinsic and extrinsic stacking faults. Such an investigation is of crucial importance since stacking faults are very common defects in real wurtzite materials. The overall message emerging from that work is that stacking faults affect most of the properties of GaN and ZnO to different extents, as summarized below.

From the structural relaxation, we found that stacking faults have a negligible influence on lattice parameters and atomic positions. The formation energies are quite low and increase in this order: type-I, type-II and extrinsic stacking fault. This ordering is consistent with the number of cubic bonds at each type of defect and with the wurtzite/zincblende energy difference. The band-structure calculation reveal that the band gap of stacking faults is smaller compared to that of the ideal wurtzite phase, which means that these defects act as quantum wells whose height is determined by the valence- and conduction-band offsets. These quantum wells act as a trap center for charge carriers and may lead to photoluminescence emission lines.

Both the trigonal-referenced spontaneous polarization and piezoelectric coefficient decrease in magnitude when the stacking faults are introduced within the studied materials. In contrast, the hexagonal-referenced spontaneous polarization increases. We found a trend of increasing polarization charge at the wurtzite/zincblende interface in going from type-I to type-II to extrinsic stacking faults. The investigated properties are found to be proportional to the number of cubic bonds for each stacking fault, in the sense that these properties vary almost linearly with this number.

Finally, we have reproduced the experimental value of the trigonal-referenced spontaneous polarization of wurtzite GaN. In order to do so, we calculate the spontaneous polarization for each type of stacking faults. This analysis lead to a value almost identical to the only reported experimental figure. Our theoretical approach is consistent with the experimental procedure, and can be used to determine $P_{sp,T}$ of other wurtzite crystals as well. We are not aware of any works where the spontaneous polarization of wurtzite stacking faults is reported. Indeed, the lack of such information was an important factor in motivating the present first-principles study.

Perspectives

The present thesis has addressed a number of topics related to polarization effects in wurtzite systems. Though many points have been considered, one important issue remain unexplored and open for future investigation, namely *ferroelectricity* in wurtzite crystals.

Next-generation wurtzite ferroelectrics:

A ferroelectric material has two stable polarization states that can be switched from one state into another by applying an electric field [44]. The polarization vector of convectional wurtzite crystals cannot be switched because the coercive electric field, which is the field needed to switch the polarization, is greater than the dielectric breakdown field [309]. When an insulating material undergoes a dielectric breakdown, it suddenly loses its dielectric properties (e.g. electric polarization) and becomes a conductor [310]. Thus, the occurrence of ferroelectricity requires the coercive field to be smaller than the dielectric breakdown strength [311].

Recent experimental and theoretical reports have shown that one way to achieve this is by engineering known wurtzite crystals via alloying, doping and straining. For example, adding scandium atoms (Sc) to wurtzite AlN and GaN flattens the energy surface, leading to a reduced energy barrier U_S against polarization switching and, consequently, reduced coercivity E_C [169,312,313] [note that U_S and E_C are proportional, see Eq. (I.13)]. For this reason, ternary wurtzite alloys and superlattices such as $Sc_xAl_{1-x}N$ and $Sc_xGa_{1-x}N$ are ferroelectric compounds with reversible polarization for moderate Sc contents x [167]. These next-generation ferroelectrics have the potential to extend the functionality of the III-nitrides to ferroelectric applications, for instance memory and information storage devices [314], where 1 and 0 bits are associated with "up" and "down" polarized states [315,316].

Nature of the paraelectric structure:

As explained in detail in Sec. I.4.3, the ferroelectric switching path passes by three key structures (*c.f.* Fig. I.4). These are the two wurtzite structures with opposite polarities**,** and the layered-hexagonal structure that serves as the intermediate paraelectric (non-polar) state [313]. We have introduced this structure to be used as a reference to calculate the spontaneous polarization in Chap. V. The internal parameter u (i.e. the anion-cation separation along the c-axis) of the hexagonal structure is 0.5. The switching mechanism of polarization in wurtzite systems involves moving the anions in opposite directions along the c-axis with the midpoint being u=0.5 [169,189,312]. In other words, the switching occurs when u=0.5.

The hexagonal (or hBN) structure plays the role of the paraelectric state for Sc-based wurtzite ferroelectrics like $Sc_xAl_{1-x}N$ and $Sc_xGa_{1-x}N$ [189]. It was revealed, however, that other wurtzite systems have different paraelectric structures in their ferroelectric switching pathway, such as the non-polar β-BeO phase for B-doped AlN (BAlN) [317], and the cubanite Fe_2CuS_3-type structure for mutinary wurtzite compounds such as Mg_2PN_3 and Zn_2TaN_3 [313].

Example of the ferroelectric III-nitride alloy ScAlN:

$Sc_xAl_{1-x}N$ stands out as the first material crystallizing in the wurtzite structure with ferroelectric behaviour. Since its discovery by Fichtner et *al*. in 2019 [189], it has attracted tremendous interest from both academia and industry due to its unique properties [318]. Following the recipe of Chapter V, we calculate the spontaneous polarization of wurtzite ScAlN with respect to the hexagonal reference. The alloy is modelled by a 1×1×4 (16-atom) wurtzite supercell. The results are plotted in Figure A (1) for Sc content in the range from 0 to 0.5 (beyond x= 0.5, the alloy is no longer stable in the wurtzite phase [284]). Overall, ScAlN exhibits a spontaneous polarization exceeding or approaching 1 C/m² and consistently decreases with increasing alloy composition x, a trend that agrees with other theoretical predictions and experimental measurements.

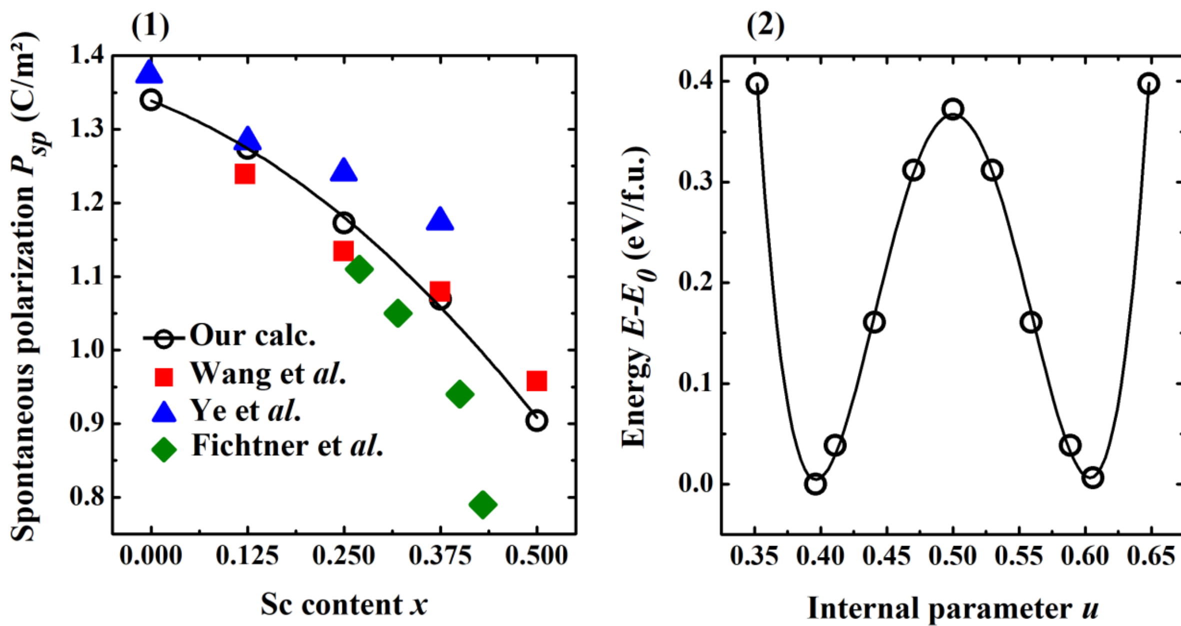

Figure A (1) Spontaneous polarization of $Sc_xAl_{1-x}N$ as a function of Sc concentration. Our results, obtained using Eq. (V.7), are represented by empty black spheres (the curve is a quadratic fit). The data point at x= 0 corresponds to pure AlN. Previous simulation values are extracted from the work of Wang et *al*. [169] (red squares) and Ye el *al*. [68] (blue triangles), and the experimental data points are taken from Fichtner et *al*. [189] (green diamonds). We note that the values of Fichtner et *al*. are actually those of the *remnant* polarization P_r, i.e. the polarization when the electric filed is zero, which coincides with the spontaneous polarization P_{sp}. (2) Energy per formula unit (f.u.) of $Sc_xAl_{1-x}N$ as a function of the internal parameter for Sc content x= 0.25. For ScAlN alloy, a formula unit is an Al-N or Sc-N "molecule" (for 16-atom supercell there are 8 formula units). The polar ferroelectric, non-polar paraelectric and anti-polar ferroelectric structures correspond to u= 0.382, 0.5 and 0.618, respectively. The polarization reverses its sign (orientation) from positive to negative (from up to down) once u passes 0.5. The curve is obtained by fitting the E-u data to a 4th degree polynomial. The energy of the two (minimum) ferroelectric states E_0 is set to zero. Note that the switching energy barrier is about 0.35 eV/f.u.

Figure A (2) shows our calculated double-well energy of wurtzite $Sc_{0.25}Al_{0.75}N$ as a function of the internal parameter. The alloy concentration x= 0.25 amounts to two Sc atoms replacing two of the eight Al atoms in a 16-atom wurtzite supercell. The internal parameter represents the ferroelectric distortion in this case, whose values are obtained by linear interpolation between the polar (wurtzite), non-polar (layered-hexagonal) and anti-polar (wurtzite) structures. The double well of Fig. A (2) is similar to the one shown in Fig. I.5 for perovskite $BaTiO_3$. The two energy minima at u= 0.382 and u= 0.618 represent degenerate ferroelectric states with opposite polarization. The saddle point at u= 0.5, which has zero polarization, corresponds to the paraelectric state.

The ferroelectric switching barrier is given by the total-energy difference between the wurtzite and hexagonal structures. For the specific case of $Sc_{0.25}Al_{0.75}N$, we obtain a barrier of 0.35 eV/formula unit (or 0.175 eV/atom). This result is in very good agreement with the work of Wang et *al*. who studied $Sc_{0.2}Al_{0.8}N$ (x= 0.2) [169]. The energy barrier of pristine AlN (i.e. for x= 0) is about 0.52 eV/f.u., which is higher than the barrier of $Sc_{0.25}Al_{0.75}N$ extracted from Fig. A (2). So alloying Sc with AlN really decreases the energy switching barrier and hence the coercive field, which ultimately makes the material ferroelectric prior to dielectric breakdown.

Collective versus individual switching:

Real ferroelectric materials are composed of many small regions called *ferroelectric domains*. The polarization within each domain has a uniform direction, but the polarization of different domains points in different directions [44]. Polarization switching is believed to occur via one of these two underlying mechanisms. First, every domain in the material undergoes a simultaneous reversal of polarization from one ferroelectric state to its opposite counterpart [49,313]. We call this process a *collective* switching. The ferroelectric double well for this mechanism is the one shown in Fig. A (2). It consists of one peak: two minima and one saddle point.

Second, the polarization of one domain switches first, then followed by the next domain and so on [49,313]. In this process, called *individual* switching, the polarization inversion propagates thorough the material like a wave. Interestingly, and in contrast to collective switching, the energy profile for the individual-switching process is characterized by a series of peaks associated with barriers to be overcome during switching of individual domains (see e.g. Refs. [49,309,313]). Both mechanisms are schematized in Figure B, where the material is modelled by a supercell consisting of four unit cells, each corresponds to a ferroelectric domain. The second mechanism usually involves the creation of *domain walls* followed by their translation [49]. In our context, a domain wall is an interface separating two domains with opposite polarization [44] [(the vertical dashed lines in Fig. B (2)].

It is now established that consecutive reversal of polarization via the switching of adjacent domains or unit cells (the second mechanism) is energetically more favourable than concurrent switching (the first mechanism) [49,313], which means that it is the most accurate and realistic description of the ferroelectric switching phenomenon. Most of the previous works are limited to collective switching, and ignores the presence and motion of domain walls. We intend to fill

this gap by modelling the individual switching in the framework of first-principles calculations. In order to so, we resort to the method explained in the seminal work of Ahmed et *al*. [49], whereby supercells are used to model the ferroelectric domains and walls [see Fig. B (2)]. This will allow us to compute the energy barrier for polarization reversal, the formation energy of the domain walls, the energy barrier for domain-wall motion and the associated coercive electric fields.

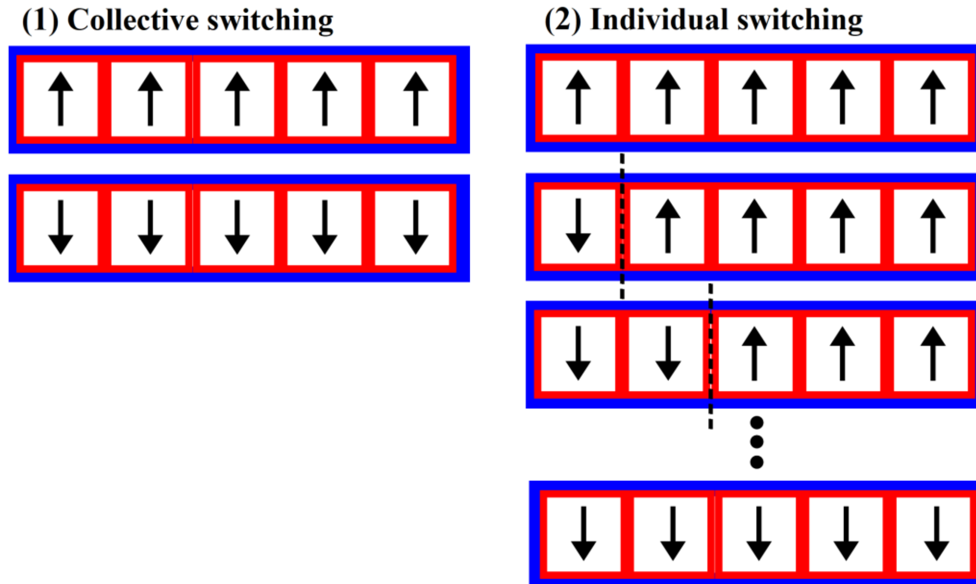

Figure B Schematics of (1) collective and (2) individual ferroelectric switching processes. For both panels, red rectangles illustrate ferroelectric domains (unit cells) and the arrows are polarization vectors of each domain. In collective switching, all polarization vectors flip from up to down together at the same time. But in the individual switching, the switching occurs via consecutive reversal of polarization in adjacent domains. The vertical dotted lines in (2) are domain walls that separates two domains with opposite polarities. The blue rectangle is a supercell model that captures the formation and motion of domain walls for the individual process (the collective process ignores the existence of domain walls). A major observation is that the energy barrier for individual switching is always lower in comparison to the collective mechanism. Quoting Ahmed et *al*. [49]: "This clearly favours the formation of domain walls and their successive propagation as a mechanism for ferroelectric switching within the first-principle framework as that process requires much lower energy to be overcome".

Ahmed et *al*. applied their method for investigating tetragonal $BaTiO_3$. It can however also be used to study other ferroelectric crystals, such as wurtzite $Sc_xAl_{1-x}N$, provided that the appropriate supercell is constructed. It is important to note that we have to construct two different supercells. The first one is used to model the alloy itself, e.g. a 16-atom 1×1×4 wurtzite supercell (shown as red rectangles in Fig B). The second supercell is built by repeating the first supercell horizontally in order to simulate the ferroelectric domains. This larger supercell is represented by the blue rectangle in Fig. B, and its dimension is 4×1×1, meaning there are 4 replicas of the smaller supercell along the *a*-axis. For the 16-atom red supercell, the blue one contains 64 atoms.

Ising, Bloch and Néel switching pathways:

An interesting question is on the so-called switching pathways. Ferroelectric materials are known to follow the *Ising*-type switching path, where the polarization vector flips itself from up to down (by 180°) without rotation, passing through zero polarization along the paraelectric structure [49,50] (see Fig. I.4). Many studies, however, have predicted the presence of *Bloch*- and *Néel*-type switching. In this case, the polarization vector rotates without vanishing [51]. Real materials show mixed character: while predominantly Ising-like, they also manifest some Bloch- and Néel-like character [51]. The three switching pathways are shown schematically in Figure C for the individual switching mechanism, in which the switching is realized by domain-wall motion. It is customary to classify domain walls by the nature of the switching pathway involved, so we have the Ising-, Bloch- and Néel-type domain walls.

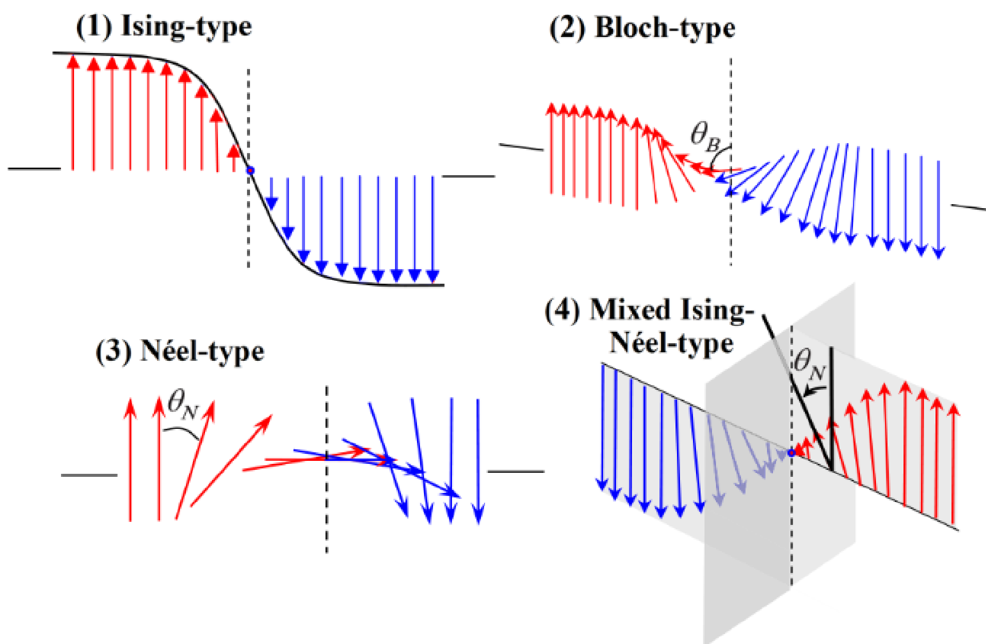

Figure C Schematics of three pure switching pathways: (1) Ising-type, (2) Bloch-type and (3) Néel-type, and one hybrid pathway: (4) mixed Ising-Néel-type. Ising switching allows only two possible polarization directions, namely up (P) and down ($-P$). In Bloch and Néel switching, the polarization vector rotates gradually between the two opposite polarities. The rotation takes place out of the plane of the polarization vector (Bloch) or in the plane of the polarization vector (Néel). It is found that the energy barrier for polarization rotation can be 2-3 times lower than the barrier associated with the flip of polarization (without rotation) [7]. Figure taken from Ref. [51].

Wurtzite-like ferroelectric XYZ compounds:

Another class of wurtzite crystals that support ferroelectricity is the ternary compounds with the general chemical formula XYZ [319]. These materials are natural ferroelectrics, and they crystallize in a wurtzite-like structure known as LiGaGe-type phase. Compared to traditional binary wurtzite compounds (GaN and ZnO, etc.), which have only one cation, these ternary systems contain two cations X and Y (Z is an anion). As such, the wurtzite structure in this case is characterized by two different internal parameters u and v [62,319]. There is also a layered-hexagonal variant for these new materials (ZrBeSi-type), which can be obtained from the wurtzite phase by putting the cations and anions on the same plane (i.e. u= 0.25 and v= 0.75) [62,319]. Figure D pictures the unit cell of both structures.

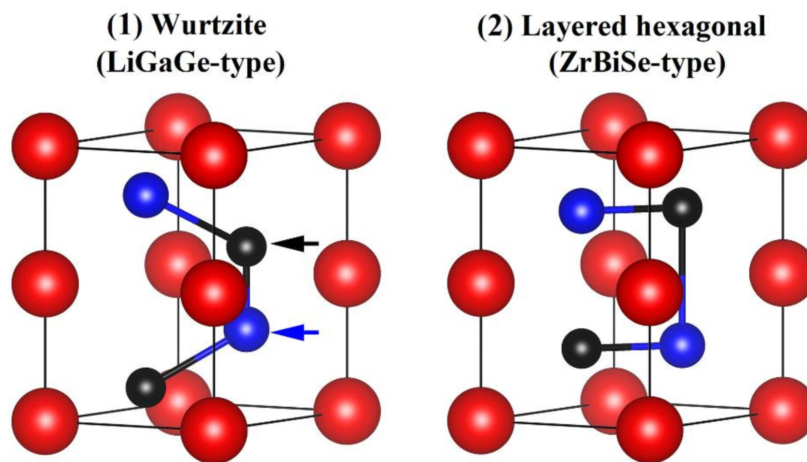

Figure D Unit cell of (1) wurtzite LiGaGe-type and (2) layered-hexagonal ZrBeSi-type structures for XYZ compounds. X, Y and Z atoms are indicated by red, blue and black spheres, respectively. Both structures are linked by the evolution of the two internal parameters from $u \neq 0.25$ and $v \neq 0.75$ (wurtzite) to $u = 0.25$ and $v = 0.75$ (layered hexagonal). The arrows point to the Y and Z atoms whose z fractional coordinates are given by the internal parameters u (blue arrow) and v (black arrow). The layered-hexagonal phase has two roles: (i) it serves as the reference structure to access the spontaneous polarization of the wurtzite system, and (ii) it can be used as the intermediate paraelectric (non-polar) state for polarization switching between the ferroelectric wurtzite states.

Bennett et *al*. [319] used first-principles methods to identify 17 ferroelectric compounds in the XYZ family with the wurtzite LiGaGe-type structure. Members of this class include LiBeP, NaMgAs and NaZnSb. These candidate ferroelectrics offer promise for the development of new high performance materials for practical applications. The researchers provided for these materials the structural parameters, band gap, energy barrier for collective switching and spontaneous polarization. In our future work we will access other polarization properties, namely the Born effective charges, the piezoelectric coefficients and coercive electric fields. Since such materials are ferroelectrics, the most immediate development will precisely concern understanding their ferroelectric behaviour. In this regard, we are going to assess the two switching mechanisms and the three switching pathways as in the case of ScAlN alloys.

References

[1] M.C. Sekhar, E. Veena, N. S. Kumar, K. C. B. Naidu, A. Mallikarjuna and D. B. Basha, "A review on piezoelectric materials and their applications", Cryst. Res. Technol. 2200130 (2023).

[2] R. Bansevičius, S. Telksnytė, G. Janušas and A. Palevičius, "Hybrid numerical-experimental investigation of two-degree-of-freedom piezoelectric positioning actuator", MECHANIKA 17, 182-186 (2011).

[3] E. Kioupakis, Q. Yan, and C. Van de Walle, "Interplay of polarization fields and Auger recombination in the efficiency droop of nitride light-emitting diodes", Appl. Phys. Lett. 101, 231107 (2012).

[4] P. Waltereit, O. Brandt, A. Trampert, H. T. Grahn, J. Menniger, M. Ramsteiner, M. Reiche, and K. H. Ploog, "Nitride semiconductors free of electrostatic fields for efficient white light-emitting diodes", Nature 406, 865 (2000).

[5] F. Zeng, J. X. An, G. Zhou, W. Li, H. Wang, T. Duan, L. Jiang, and H. Yu, "A comprehensive review of recent progress on GaN high electron mobility transistors: Devices, fabrication and reliability", Electronics 7, 12 (2018).

[6] D. Behrendt, S. Banerjee, J. Zhang, and A. M. Rappe, "Discovery of wurtzite solid solutions with enhanced piezoelectric response using machine learning", Phys. Rev. Mater. 8, 055406 (2024).

[7] J Cole, S J Ahmed, L Curiel, S Pichardo and O Rubel, "Marble game with optimal ferroelectric switching", J. Phys.: Condens. Matter 26 135901 (2014).

[8] Y. Wang, S.-L. Shang, H. Fang, Z.-K. Liu, and L.-Q. Chen, "First-principles calculations of lattice dynamics and thermal properties of polar solids", Npj Comput. Mater. 2, 16006 (2016).

[9] M. A. Caro, S. Zhang, T. Riekkinen, M. Ylilammi, M. A. Moram, O. Lopez-Acevedo, J. Molarius, and T. Laurila, "Piezoelectric coefficients and spontaneous polarization of ScAlN", J. Phys. Condens. Matter 27, 245901 (2015).

[10] Y. Zhou, B. Shen, T. Someya, H. Yu, J. Liu, H. Zhou, R. Zhang, Y. Shi, Y. Zheng and Y. Arakawa, "Investigation of the polarization-induced charges in modulation-doped $Al_xGa_{1-x}N$/GaN heterostructures through capacitance-voltage profiling and simulation", Jpn. J. Appl. Phys. 41 2531 (2002).

[11] Y. Zhang, I. P. Smorchkova, C. R. Elsass, S. Keller, J. P. Ibbetson, S. Denbaars and U. K. Mishra, "Charge control and mobility in AlGaN/GaN transistors: Experimental and theoretical Studies", J. Appl. Phys. 87, 7981–7987 (2000).

[12] R. D. King-Smith and D. Vanderbilt, "Theory of polarization of crystalline solids", Phys. Rev. B 47, 1651(R) (1993).

[13] R. Resta, "Theory of the electric polarization in crystals", Ferroelectrics 136, 51-55 (1992).

[14] M. V. Berry, "Quantal phase factors accompanying adiabatic changes", Proc. R. Soc. London Ser. A 392, 45 (1984).

[15] M. Posternak, A. Baldereschi, A. Catellani, and R. Resta, "Ab initio study of the spontaneous polarization of pyroelectric BeO", Phys. Rev. Lett. 64, 1777 (1990).

[16] C. Skierbiszewski, Z. R. Wasilewski, I. Grzegory and S. Porowski, "Nitride-based laser diodes by plasma-assisted MBE-From violet to green emission", J. Cryst. Growth 311, 1632 (2009).

[17] J. Casamento et al., “Perspectives and progress on wurtzite ferroelectrics: Synthesis, characterization, theory, and device applications”, Appl. Phys. Lett. 124, 080501 (2024).
[18] S. Arafin, X. Liu, and Z. Mi, “Review of recent progress of III-nitride nanowire lasers”, J. Nanophotonics 7, 074599 (2013).
[19] M. Z. Baten, S. Alam, B. Sikder, and A. Aziz, “III-nitride light-emitting devices”, Photonics 8, 10 (2021).
[20] A. Dobrinsky, G. Simin, R. Gaska and M. Shur, “III-nitride materials and devices for power electronics”, ECS Trans. 58, 129 (2013).
[21] Ü. Özgür, Ya. I. Alivov, C. Liu, A. Teke, M. A. Reshchikov, S. Doğan, V. Avrutin, S.-J. Cho and H. Morkoç, “A comprehensive review of ZnO materials and devices”, J. Appl. Phys. 98, 041301 (2005).
[22] Z. L. Wang, X. Y. Kong, Y. Ding, P. Gao, W. L. Hughes, R. Yang and Y. Zhang, “Semiconducting and piezoelectric oxide nanostructures induced by polar surfaces”, Adv. Funct. Mater. 14, 943 (2004).
[23] Y.-N. Xu and W. Y. Ching, “Electronic, optical, and structural properties of some wurtzite crystals”, Phys. Rev. B 48, 4335 (1993).
[24] A. E. Naclerio and P. R. Kidambi, “A review of scalable hexagonal boron nitride (h-BN) synthesis for present and future applications”, Adv. Mater. 35, 2207374 (2023).
[25] Y. Dou, R. G. Egdell, D. S. L. Law, N. M. Harrison and B. G. Searle, “An experimental and theoretical investigation of the electronic structure of CdO”, J. Phys.: Condens. Matter 10 8447(1998).
[26] C. E. Dreyer, A. Janotti, C. G. Van de Walle and D. Vanderbilt, “Correct implementation of polarization constants in wurtzite materials and impact on III-nitrides”, Phys. Rev. X 6, 021038 (2016).
[27] D. J. Griffiths, “Introduction to Electrodynamics”, Cambridge University Press, Cambridge (2017).
[28] M. F. Schubert et al., “Polarization-matched GaInN/AlGaInN multi-quantum-well light-emitting diodes with Reduced efficiency droop”, Appl. Phys. Lett. 93, 041102 (2008).
[29] C. Kittel, “Introduction to solid state physics”, John Wiley & Sons, New York (1996).
[30] G. Grosso and G. P. Parravicini, “Solid state physics”, Academic Press, Amsterdam (2014).
[31] R. M. Martin, “Comment on calculations of electric polarization in crystals”, Phys. Rev. B 9, (1974).
[32] R. Knight, “Physics for scientists and engineers: A strategic approach with modern physics”, Standalone Book, Pearson (2016).
[33] M. Sadiku, “Elements of Electromagnetics”, Oxford University Press, New York Oxford, (2018).
[34] O. Ambacher, B. Christian, M. Yassine, M. Baeumler, S. Leone and R. Quay, “Polarization induced interface and electron sheet charges of pseudomorphic ScAlN/GaN, GaAlN/GaN, InAlN/GaN, and InAlN/InN heterostructures”, J. Appl. Phys. 129, 204501 (2021).
[35] B.E. Foutz, O. Ambacher, M.J. Murphy, V. Tilak and L.F. Eastman, “Polarization induced charge at heterojunctions of the III–V nitrides and their alloys”, phys. stat. sol. (b) 216, 415 (1999).
[36] N. L. Adamski, C. E. Dreyer and C. G. Van de Walle, “Polarization properties at rocksalt/wurtzite oxide interfaces”, Phys. Rev. B 102, 201301(R) (2020).

[37] N. L. Adamski, C. E. Dreyer and C. G. Van de Walle, "Giant polarization charge density at lattice-matched GaN/ScN interfaces", Appl. Phys. Lett. 115, 232103 (2019).

[38] D. Vanderbilt and R. D. King-Smith, "Electric polarization as a bulk quantity and its relation to surface charge", Phys. Rev. B 48, 4442 (1993).

[39] J. Yang, "An introduction to the theory of piezoelectricity", Springer, Boston (2004).

[40] R. E. Cohen, "First-principles theories of piezoelectric materials", Springer, Berlin (2008) 471–492.

[41] M. Catti, Y. Noel and R. Dovesi, "Full piezoelectric tensors of wurtzite and zinc blende ZnO and ZnS by first-principles calculations", J. Phys. Chem. Solids 64, 2183 (2003).

[42] J. F. Nye, "Physical properties of crystals: Their representation by tensors and matrices", Oxford University Press, Oxfordshire, New York (1985).

[43] S. Jachalke, E. Mehner, H. Stöcker, J. Hanzig, M. Sonntag, T. Weigel, T. Leisegang and D. C. Meyer, "How to measure the pyroelectric coefficient?", Appl. Phys. Rev. 4, 021303 (2017).

[44] K. M. Rabe, C. H. Ahn, and J.-M. Triscone, "Physics of ferroelectrics: A modern perspective", Springer-Verlag, Berlin Heidelberg, (2007).

[45] M. A. Peña and J. L. G. Fierro, "Chemical structures and performance of perovskite oxides", Chem. Rev. 101, 1981-2017 (2001).

[46] B. Ravel ,E. A. Stern ,R. I. Vedrinskii and V. Kraizman, "Local Structure and the Phase Transitions of $BaTiO_3$", Ferroelectrics 206-207, 407-430 (1998).

[47] S. P. Beckman, X. Wang, K. M. Rabe and D. Vanderbilt, "Ideal barriers to polarization reversal and domain-wall motion in strained ferroelectric thin films", Phys. Rev. B 79, 144124 (2009).

[48] S. Ducharme, V. M. Fridkin, A. V. Bune, S. P. Palto, L. M. Blinov, N. N. Petukhova and S. G. Yudin, "Intrinsic ferroelectric coercive field", Phys. Rev. Lett. 84, 175 (2000).

[49] S. J. Ahmed, S. Pichardo, L. Curiel and O. Rubel, "First-principle modelling of the ferroelectric switching in $BaTiO_3$: concurrent switching versus domain wall motion", Modelling Simul. Mater. Sci. Eng. 22, 055014 (2014).

[50] M. Taherinejad, D. Vanderbilt, P. Marton, V. Stepkova and J. Hlinka, "Bloch-type domain walls in rhombohedral $BaTiO_3$", Phys. Rev. B 86, 155138 (2012).

[51] D. Lee, R. K. Behera, P. Wu, H. Xu, Y. L. Li, S. B. Sinnott, S. R. Phillpot, L. Q. Chen, and V. Gopalan, "Mixed Bloch-Néel-Ising character of 180° ferroelectric domain walls", Phys. Rev. B 80, 060102 (2009).

[52] A. F. Devonshire, "Theory of barium titanate", Phil. Mag. 40, 1040 (1949).

[53] Y. Zhang, J. Sun, J. P. Perdew and X. Wu, "Comparative first-principles studies of prototypical ferroelectric materials by LDA, GGA, and SCAN meta-GGA", Phys. Rev. B 96, 035143 (2017).

[54] H. H. Wieder, "Electrical behavior of barium titanatge single crystals at low temperatures", Phys. Rev. 99, 1161 (1955).

[55] S. Schulz, M. A. Caro, E. P. O'Reilly, and O. Marquardt, "Symmetry-adapted calculations of strain and polarization fields in (111)-oriented zinc-blende quantum dots", Phys. Rev. B 84, 125312 (2011).

[56] K. Momma and F. Izumi, "VESTA: a three-dimensional visualization system for electronic and structural analysis", J. Appl. Crystallogr. 41, 653 (2008).

[57] O. Madelung, U. Roessler and M. Schulz, "Landolt-Börnstein - Group III Condensed Matter", Springer (2001).

[58] T. Paskova, "Development and prospects of nitride materials and devices with nonpolar surfaces", phys. stat. sol. B 245 1011-1025 (2008).

[59] M. A. Caro, S. Schulz and E. P. O'Reilly, "Hybrid functional study of the elastic and structural properties of wurtzite and zinc-blende group-III nitrides", Phys. Rev. B 86, 014117 (2012).

[60] A. De and C. E. Pryor, "Predicted band structures of III-V semiconductors in the wurtzite phase", Phys. Rev. B 81, 155210 (2010).

[61] T. Mattila and A. Zunger, "Predicted bond length variation in wurtzite and zinc-blende InGaN and AlGaN alloys", J. Appl. Phys. 85, 160 (1999).

[62] F. Casper, C. Felser, R. Seshadri, C. Peter Sebastian and R. Pöttgen, "Searching for hexagonal analogues of the half-metallic half-Heusler XYZ compounds", J. Phys. Appl. Phys. 41, 035002 (2008).

[63] J. Piprek, "Nitride semiconductor devices: principles and simulation", Wiley (2007).

[64] S. Yu. Karpov, "Spontaneous polarization in III-nitride materials: crystallographic revision", Phys. Status Solidi C 7, 1841 (2010).

[65] K. Furuta, K. Hirata, S. A. Anggraini, M. Akiyama, M. Uehara and H. Yamada, "First-principles calculations of spontaneous polarization in ScAlN", J. Appl. Phys. 130, 024104 (2021).

[66] W. S. Yan, R. Zhang, X. Q. Xiu, Z. L. Xie, P. Han, R. L. Jiang, S. L. Gu, Y. Shi, and Y. D. Zheng, "Phenomenological model for the spontaneous polarization of GaN", Appl. Phys. Lett. 90, 182113 (2007).

[67] J. B. Neaton, C. Ederer, U. V. Waghmare, N. A. Spaldin and K. M. Rabe, "First-principles study of spontaneous polarization in multiferroic $BiFeO_3$", Phys. Rev. B 71, 014113 (2005).

[68] H. Ye et *al.*, "Experimental determination of giant polarization in wurtzite III-nitride semiconductors", J. Appl. Phys. 94, 3675. (2003).

[69] I. Vurgaftman and J. R. Meyer, "Band parameters for nitrogen-containing semiconductors", J. Appl. Phys. 94, 3675. (2003).

[70] R. R. Pelá, C. Caetano, M. Marques, L. G. Ferreira, J. Furthmüller and L. K. Teles, "Accurate band gaps of AlGaN, InGaN, and AlInN alloys calculations based on LDA-1/2 approach", Appl. Phys. Lett. 98, 151907 (2011).

[71] S. Zhang, W. Y. Fu, D. Holec, C. J. Humphreys and M. A. Moram, "Elastic constants and critical thicknesses of ScGaN and ScAlN", J. Appl. Phys. 114, 243516 (2013).

[72] S. H. Simon, "The Oxford solid state basics", University of Oxford (2013).

[73] G. Muziol, M. Hajdel, M. Siekacz, H. Turski, K. Pieniak, A. Bercha, W. Trzeciakowski, R. Kudrawiec, T. Suski and C. Skierbiszewski, "III-nitride optoelectronic devices containing wide quantum wells—unexpectedly efficient light sources", Jpn. J. Appl. Phys. 61, SA0801 (2021).

[74] M. Yamada, T. Mitani, Y. Narukawa, S. Shioji, I. Niki, S. Sonobe, K. Deguchi, M. Sano and T. Mukai, "InGaN-Based Near-Ultraviolet and Blue-Light-Emitting Diodes with High External Quantum Efficiency Using a Patterned Sapphire Substrate and a Mesh Electrode", Jpn. J. Appl. Phys. 41, L1431 (2002).

[75] L. K. Teles, J. Furthmüller, L. M. R. Scolfaro, J. R. Leite, and F. Bechstedt, "First-principles calculations of the thermodynamic and structural properties of strained $In_xGa_{1-x}N$ and $Al_xGa_{1-x}N$ alloys", Phys. Rev. B 62, 2475 (2000).

[76] I. Sayed and S. M. Bedair, "Quantum well solar cells: principles, recent progress, and potential", IEEE J. Photovolt. 9, 402 (2019).

[77] M. R. Krames, O. B. Shchekin, R. Mueller-Mach, G. O. Mueller, L. Zhou, G. Harbers, and M. G. Craford, "Status and Future of High-Power Light-Emitting Diodes for Solid-State Lighting", J. Disp. Technol. 3, 160 (2007).

[78] V. Fiorentini, F. Bernardini, F. D. Sala, A. D. Carlo and P. Lugli, "Effects of macroscopic polarization in III-V nitride multiple quantum wells", Phys. Rev. B 60, 8849 (1999).

[79] N. Grandjean, J. Massies and M. Leroux, "Self-limitation of AlGaN/GaN quantum well energy by built-in polarization field", Appl. Phys. Lett. 74, 2361–2363 (1999).

[80] T. Takeuchi, S. Sota, M. Katsuragawa, M. Komori, H. Takeuchi, H. A. H. Amano and I. A. I. Akasaki, "Quantum-confined stark effect due to piezoelectric fields in GaInN strained quantum wells", Jpn. J. Appl. Phys. 36, L382 (1997).

[81] J. J. Wierer Jr., A. J. Fischer, and D. D. Koleske, "The impact of piezoelectric polarization and nonradiative recombination on the performance of (0001) face GaN/InGaN photovoltaic devices", Appl. Phys. Lett. 96, 051107 (2010).

[82] Z. Q. Li , M. Lestradet, Y. G. Xiao and S. Li, "Effects of polarization charge on the photovoltaic properties of InGaN solar cells", Phys. Status Solidi A 208, 928-931 (2011).

[83] J. Xu et al., "Reduction in efficiency droop, forward voltage, ideality factor, and wavelength shift in polarization-matched GaInN/GaInN multi-quantum-well light-emitting diodes" , J. Appl. Phys. 107, 063102 (2010).

[84] W. Lee, M.-H Kim, D. Zhu, A. N. Noemaun, J. K. Kim and E. F. Schubert, "Growth and characteristics of GaInN/GaInN multiple quantum well light-emitting diodes", J. Appl. Phys. 107, 063102 (2010).

[85] D. P. Norton, Y. W. Heo, M. P. Ivill, K. Ip, S. J. Pearton, M. F. Chisholm and T. Steiner, "ZnO: growth, doping & processing", Mater. Today 7, 34 (2004).

[86] W. F. Brinkman, D. E. Haggan, and W. W. Troutman, "A history of the invention of the transistor and where it will lead us", IEEE J. Solid-State Circuits 32, 1858 (1997).

[87] M. J. Yang, F. Wang, C. H. Yang, B. R. Bennett and T. Q. Do, "A composite quantum well field-effect transistor", Appl. Phys. Lett. 69, 85 (1996).

[88] H. L. Störmer, R. Dingle, A. C. Gossard, W. Wiegmann and M. D. Sturge, "Two-dimensional electron gas at a semiconductor-semiconductor interface", Solid State Commun. 29, 705 (1979).

[89] O. Ambacher et al., "Two dimensional electron gases induced by spontaneous and piezoelectric polarization in undoped and doped AlGaN/GaN heterostructures", J. Appl. Phys. 87, 334 (2000).

[90] F. Roccaforte, G. Greco, P. Fiorenza and F. Iucolano, "An overview of normally-off GaN-based high electron mobility transistors", Material 12(10), 1599 (2019).

[91] H. Liu, J. Zhong, C. Lee, S. W. Lee et L. Lin, "A comprehensive review on piezoelectric energy harvesting technology: Materials, mechanisms, and applications", Appl. Phys. Rev. 5, 041306 (2018).

[92] N. S. Shenck and J. A. Paradiso, "Energy scavenging with shoe-mounted piezoelectrics", IEEE Micro 21, 30 (2001).

[93] N. Izyumskaya, Y.-I. Alivov, S.-J. Cho and H. Morkoç, "Processing, structure, properties, and applications of PZT thin films", Crit. Rev. Solid State Mater. Sci. 32, 111-202 (2007).

[94] Y. Li, K. Moon and C. P. Wong, "Electronics without lead", Science 308, 1419-1420 (2005).

[95] M. D. Maeder, D. Damjanovic,and N. Setter, “Lead Free Piezoelectric Materials”, J. Electroceram. 13, 385–392 (2004).

[96] A. V. Desai and M. A. Haque, “Mechanical properties of ZnO nanowires”, Sens. Actuators Phys. 134, 169 (2007).

[97] P. Feng, L. JingTing, Y. YuChao, W. XuBo and Z. Fei, “Giant piezoresponse and promising application of environmental friendly small-ion-doped ZnO”, Sci. China Technol. Sci.55, 421-436 (2012).

[98] S. Manna et al., “Enhanced piezoelectric response of AlN via CrN alloying”, Phys. Rev. Applied 9, 034026 (2018).

[99] A. Polian, M. Grimsditch and I. Grzegory, “Elastic constants of gallium nitride”, J. Appl. Phys. 79, 3343–3344 (1996).

[100] R. O. Jones, “Density functional theory: Its origins, rise to prominence, and future”, Rev. Mod. Phys. 87, 897 (2015).

[101] R. M. Martin. “Electronic Structure”, Cambridge University Press (2004).

[102] M. Born, and R. Oppenheimer, “On the quantum theory of molecules”, Annalen der Physik, 84, 457-484 (1927).

[103] R. M. Martin, L. Reining and D. M. Ceperley, “Interacting Electrons”, Cambridge University Press (2016).

[104] P. Reshma, P. Prasanth and K. M. Udayanandan, “The curse of dimensionality in physics”, Prog. Phys. 17, 203 (2021).

[105] P. Hohenberg and W. Kohn, “Inhomogeneous electron gas”, Phys. Rev. 136, B864 (1964).

[106] W. Kohn and L. J. Sham, “Self-consistent equations including exchange and correlation effects”, Phys. Rev. 140, A1133 (1965).

[107] A. J. Cohen, P. Mori-Sánchez and W. Yang, “Challenges for density functional theory”, Chem. Rev. 112, 289 (2012).

[108] J. P. Perdew, “Self-interaction correction to density-functional approximations for many-electron systems”, Phys. Rev. B 23, 5048 (1981).

[109] D. M. Ceperley and B. J. Alder, “Ground State of the electron gas by a stochastic method”, Phys. Rev. Lett. 45, 566 (1980).

[110] J. P. Perdew, “Generalized gradient approximation made simple”, Phys. Rev. Lett. 77, 3865 (1996).

[111] J. P. Perdew, “Density functional theory and the band gap problem”, Int. J. Quantum Chem. 28, 497 (1985).

[112] J. Heyd, G. E. Scuseria and M. Ernzerhof. “Hybrid functionals based on a screened Coulomb potential”, J. Chem. Phys. 118, 8207–8215 (2003).

[113] F. Tran and P. Blaha, “Accurate band gaps of semiconductors and insulators with a semilocal exchange-correlation potential”, Phys. Rev. Lett. 102, 226401 (2009).

[114] F. Tran, J. Doumont, L. Kalantari, A. W. Huran, M. A. L. Marques, and P. Blaha, “Semilocal exchange-correlation potentials for solid-state calculations: Current status and future directions”, J. Appl. Phys. 126, 110902 (2019).

[115] A. D. Becke and E. R. Johnson, “A simple effective potential for exchange”, J. Chem. Phys. 124, 221101 (2006).

[116] A. D. Becke, “Exchange holes in inhomogeneous systems: A coordinate-space model”, Phys. Rev. A 39, 3761 (1989).

[117] J. Wu et al., "Temperature dependence of the fundamental band gap of InN", J. Appl. Phys. 94, 4457–4460 (2003).
[118] S. Cottenier, "Density functional theory and the family of (L)APW-methods: a step-by-step introduction", 2002-2013 (2nd edition), ISBN 978-90-807215-1-7.
[119] J. C. Slater, "Wave Functions in a Periodic Potential", Phys. Rev. 51, 846 (1937).
[120] T. Loucks, "Augmented Plane Wave Method: A Guide to Performing Electronic Structure Calculations", W.A. Benjamin (1967).
[121] O. K. Andersen, "Linear methods in band theory", Phys. Rev. B 12, 3060 (1975).
[122] D. D. Koelling and G. O. Arbman, "Use of energy derivative of the radial solution in an augmented plane wave method: application to copper", J. Phys. F Met. Phys. 5, 2041 (1975).
[123] D. Singh, "Ground-state properties of lanthanum: Treatment of extended-core states", Phys. Rev. B 43, 6388 (1991).
[124] E. Sjöstedt, L. Nordström and D. J. Singh, "An alternative way of linearizing the augmented plane-wave method", Solid State Commun. 114, 15 (2000).
[125] P. Blaha, K. Schwarz, F. Tran, R. Laskowski, G. K. H. Madsen and L. D. Marks, "WIEN2k: An APW+lo program for calculating the properties of solids", J.Chem. Phys. 152, 074101 (2020).
[126] F. Nogueira, A. Castro, and M. A. L. Marques, "A tutorial on density functional theory", Springer, Berlin, Heidelberg, (2003).
[127] D. D. Johnson, "Modified Broyden's Method for accelerating convergence in self-consistent calculations", Phys. Rev. B 38, 12807 (1988).
[128] H. J. Monkhorst, "Special points for Brillouin-zone integrations", Phys. Rev. B 13, 5188 (1976).
[129] A. Togo, "First-principles phonon calculations with Phonopy and Phono3py", J. Phys. Soc. Jpn. 92, 012001 (2023).
[130] S. Curtarolo, G. L. W. Hart, M. B. Nardelli, N. Mingo, S. Sanvito and O. Levy, "The high-throughput highway to computational materials design". Nature Materials 12, 191-201 (2013).
[131] M. de Jong, W. Chen, H. Geerlings, M. Asta and K. A. Persson, "A database to enable discovery and design of piezoelectric materials", scientific Data volume 2, 150053 (2015).
[132] K. F. Garrity, "High-throughput first-principles search for new ferroelectrics", Phys. Rev. B 97, (2018).
[133] M. A. Caro, "Machine learning based modeling of disordered elemental semiconductors: understanding the atomic structure of a-Si and a-C", Semicond. Sci. Technol. 38, 043001 (2023).
[134] N.A. Spaldin, "A beginner's guide to the modern theory of polarization", J. Solid State Chem. 195, 2-10 (2012).
[135] R. Resta, "Macroscopic electric polarization as a geometric quantum phase", EPL 22 133 (1993).
[136] R. Resta and D. Vanderbilt, "Theory of polarization: A modern approach", Top. Appl. Phys. 105 (2007).
[137] D. Xiao, M.C Chang, and Q. Niu, "Berry phase effects on electronic properties", Rev. Mod. Phys. 82, 1959 (2010).
[138] D. J. Griffiths, "Introduction to quantum mechanics", Cambridge University Press, Cambridge (2018).

[139] W. B. Hodge, S. V. Migirditch and W. C. Kerr, “Electron spin and probability current density in quantum mechanics”, Am. J. Phys. 82, 681–690 (2014).

[140] D. Vanderbilt, “Berry-phase theory of proper piezoelectric response”, J. Phys. Chem. Solids 61, 147 (2000).

[141] S. J. Ahmed, J. Kivinen, B. Zaporzan, L. Curiel, S. Pichardo and O. Rubel, “BerryPI: A software for studying polarization of crystalline solids with WIEN2k density functional all-electron package”, Comput. Phys. Commun. 184, 647-651 (2013).

[142] J. Kuneš, R. Arita, P. Wissgott, A. Toschi, H. Ikeda and K. Held, “Wien2wannier: From linearized augmented plane waves to maximally localized Wannier functions”, Comput. Phys. Commun. 181, 1888 (2010).

[143] E. I. Blount, “Formalisms of Band Theory, in Solid State Physics”, Academic Press (1962).

[144] Y. Noel, C.M. Zicovich-Wilson, B. Civalleri, P.D. Arco and R.Dovesi, “Polarization properties of ZnO and BeO: An ab initio study through the Berry phase and Wannier functions approaches”, Phys. Rev. B: Condens. Matter Mater. Phys. 65, 14111 (2001).

[145] F. Bernardini and V. Fiorentini, “Polarization fields in nitride nanostructures: 10 points to think about”, Appl. Surf. Sci. 166, 23 (2000).

[146] W. Troy, M. Dutta and M. Stroscio, “Spontaneous polarization calculations in wurtzite II-oxides, III-nitrides, and SiC polytypes through net dipole moments and the effects of nanoscale layering”, Nanomaterials 11, 1956 (2021).

[147] A. D. Corso, M. Posternak, R. Resta and A. Baldereschi, “Ab initio study of piezoelectricity and spontaneous polarization in ZnO”, Phys. Rev. B 50, 10715 (1994).

[148] F. Bernardini, V. Fiorentini and D. Vanderbilt, “Spontaneous polarization and piezoelectric constants of III-V nitrides”, Phys. Rev. B 56, R10024 (1997).

[149] P. Gopal and N. A. Spaldin, “Polarization, piezoelectric constants, and elastic constants of ZnO, MgO, and CdO”, Journal of Elec Materi 35, 538–542 (2006).

[150] G. K. H. Madsen, P. Blaha, K. Schwarz, E. Sjöstedt and L. Nordström, “Efficient linearization of the augmented plane-wave method”, Phys. Rev. B 64, 195134 (2001).

[151] J. Ihm, “Total energy calculations in solid state physics”, Rep. Prog. Phys. 51, 105 (1988).

[152] F. D. Murnaghan, “The compressibility of media under extreme pressures”, J. Phys. Sci. 30 (9) 244-247 (1944).

[153] R. P. Feynman, “Forces in molecules”, Phys. Rev. 56, 340 (1939).

[154] K. Lawniczak-Jablonska, T. Suski, I. Gorczyca, N. E. Christensen, K. E. Attenkofer, R. C. C. Perera, E. M. Gullikson, J. H. Underwood, D. L. Ederer, and Z. Liliental Weber, “Electronic states in valence and conduction bands of group-III nitrides: Experiment and theory”, Phys. Rev. B 61, 16623 (2000).

[155] R.M. Hazen and L.W. Finger, “High-pressure and high temperature crystal chemistry of beryllium oxide”, J. Appl. Phys. 59, 3728 (1986).

[156] H. Karzel, W. Potzel, M. K¨offerlein, W. Schiessl, M. Steiner, U. Hiller, G. M. Kalvius, D. W. Mitchell, T. P. Das, P. Blaha, K. Schwarz and M. P. Pasternak, “Lattice dynamics and hyperfine interactions in ZnO and ZnSe at high external pressures”, Phys. Rev. B 53, 11425 (1996).

[157] A. M. Hofmeister, “Pressure derivatives of the bulk modulus”, J. Geophys. Res. Solid Earth 96, 21893 (1991).

[158] O. Ambacher, J. Majewski, C. Miskys, A. Link, M. Hermann, M. Eickhoff, M. Stutzmann,F. Bernardini, V. Fiorentini and V. Tilak, B. Schaff, and L. F. Eastman, “Pyroelectric properties of Al(In)GaN/GaN hetero- and quantum well structures”, J. Phys.: Condens. Matter 14, 3399 (2002).

[159] J. Lähnemann, U. Jahn, O. Brandt, T. Flissikowski, P. Dogan, and H. T. Grahn, “Luminescence associated with stacking faults in GaN”, J. Phys. D: Appl. Phys. 47, 423001 (2014).

[160] F. Bernardini, V. Fiorentini, and David Vanderbilt, “Accurate calculation of polarization-related quantities in semiconductors”, Phys. Rev. B 63, 193201 (2001).

[161] A. Malashevich and D. Vanderbilt, “First-principles study of polarization in $Zn_{1-x}Mg_xO$”, Phys. Rev. B 75, 045106 (2007).

[162] F. Bechstedt, U. Grossner and J. Furthmüller, “Dynamics and polarization of group-III nitride lattices: A first-principles study”, Phys. Rev. B 62, 8003 (2000).

[163] J. Jerphagnon and H. W. Newkirk, “Optical nonlinear susceptibilities of beryllium oxide”, Appl. Phys. Lett. 18, 245–247 (1971).

[164] A. Zoroddu, F. Bernardini, P. Ruggerone and V. Fiorentini, “First-principles prediction of structure, energetics, formation enthalpy, elastic constants, polarization, and piezoelectric constants of AlN, GaN, and InN: Comparison of local and gradient-corrected density-functional theory”, Phys. Rev. B 64, 045208 (2001).

[165] R. Resta, M. Posternak, and A. Baldereschi , “Towards a quantum theory of polarization in ferroelectrics: The case of $KNbO_3$”, Phys. Rev. lett. 70 (7), 1010-1013 (1993).

[166] S. Dall’Olio, R.Dovesi, and R. Resta, “Spontaneous polarization as a Berry phase of the Hartree-Fock wave function: The case of $KNbO_3$”, Phys. Rev. B 56, 10105 (1997).

[167] M. A. Moram and S. Zhang, “ScGaN and ScAlN: emerging nitride materials”, J. Mater. Chem. A 2, 6042 (2014).

[168] C. E. Dreyer, J. L. Lyons, A. Janotti and C. G. V. de Walle, “Band alignments and polarization properties of BN polymorphs”, Appl. Phys. Express 7, 031001 (2014).

[169] H. Wang, N. Adamski, S. Mu and C. G. Van de Walle, “Piezoelectric effect and polarization switching in $Al_{1-x}Sc_xN$”, J. Appl. Phys. 130, 104101 (2021).

[170] K. Liu, H. Sun, F. AlQatari, W. Guo, X. Liu, J. Li, C. G. T. Castanedo and X. Li, “Wurtzite BAlN and BGaN alloys for heterointerface polarization engineering”, Appl. Phys. Lett. 111, 222106 (2017).

[171] F. Bernardini and V. Fiorentini, “Nonlinear macroscopic polarization in III-V nitride alloys”, Phys. Rev. B 64, 085207 (2001).

[172] S. N. S. Nakamura, “GaN growth using GaN buffer layer”, Jpn. J. Appl. Phys. 30, L1705 (1991).

[173] N. Farrer and L. Bellaiche, “Properties of hexagonal ScN versus wurtzite GaN and InN”, Phys. Rev. B 66, 201203 (2002).

[174] M. A. Caro, S. Schulz and E. P. O’Reilly, “Theory of local electric polarization and its relation to internal strain: Impact on polarization potential and electronic properties of group-III nitrides”, Phys. Rev. B 88, 214103 (2013).

[175] S. T. Murphy, A. Chroneos, C. Jiang, U. Schwingenschlögl, and R. W. Grimes, “Deviations from Vegard’s law in ternary III-V alloys”, Phys. Rev. B 82, 073201 (2010).

[176] H. Angerer et al., “Determination of the Al Mole Fraction and the Band Gap Bowing of Epitaxial $Al_xGa_{1-x}N$ Films”, Appl. Phys. Lett. 71, 1504-1506 (1997).

[177] L. Görgens,O. Ambacher, M. Stutzmann, C. Miskys, F. Scholz, and J. Off, “Characterization of InGaN thin films using high-resolution x-ray diffraction” , Appl. Phys. Lett. 76, 577 (2000).

[178] T. Peng, J. Piprek, G. Qiu, J. O. Olowolafe, K. M. Unruh, C. P. Swann and E. F Schubert, “Band gap bowing and refractive index spectra of polycrystalline $Al_xIn_{1-x}N$ films deposited by sputtering”, Appl. Phys. Lett. 71, 2439 (1997).

[179] L. Dong and S. P. Alpay, “Polarization, piezoelectric properties, and elastic coefficients of $In_xGa_{1-x}N$ solid solutions from first principles”, J. Mater. Sci. 47, 7587–7593 (2012).

[180] C. Feng, C. Wei, B. Fang and H. Fan, “A deduction of the Hellmann-Feynman theorem”, Int. J. Theor. Phys. 59, 1396 (2020).

[181] F. Bernardini and V. Fiorentini, “Nonlinear behaviour of spontaneous and piezoelectric polarization in III–V nitride alloys”, Phys. Status Solidi A 190, 65 (2002).

[182] S.-H. Wei, L. G. Ferreira, James E. Bernard, and Alex Zunger, “Electronic properties of random alloys: Special quasirandom structures”, Phys. Rev. B 42, 9622 (1990).

[183] V. Ranjan, L. Bellaiche, and E. J. Walter, “Strained hexagonal ScN: A material with unusual structural and optical properties”, Phys. Rev. Lett. 90, 257602 (2003).

[184] S. Calderon , S. D. Funni and E. C. Dickey, “Accuracy of local polarization measurements by scanning transmission electron microscopy”, Microscopy and Microanalysis 28, 2047–2058 (2022).

[185] S. Calderon, J. Hayden, S. M. Baksa, W. Tzou, S. Trolier-McKinstry, I. Dabo, J.-P. Maria and E. C. Dickey, “Atomic-scale polarization switching in wurtzite ferroelectrics”, Science 380,1034-1038(2023).

[186] K. Hasegawa, T. Shimizu, T. Ohsawa, I. Sakaguchi, and N. Ohashi, “Full polarization reversal at room temperature in unsubstituted AlN”, Appl. Phys. Lett. 123, 192903 (2023).

[187] D. Wang, D. Wang, S. Yang and Z. Mi, “Rethinking polarization in wurtzite semiconductors”, Appl. Phys. Lett. 124, 263502 (2024).

[188] M. Yassine, A. Yassine, A. Nair, B. Sundarapandian, N. Afshar, L. Kirste, S. Fichtner and O. Ambacher, “Modeling of polarization reversal-induced interface sheet charge in wurtzite-type AlScN/GaN heterostructures”, J. Appl. Phys. 135, 155702 (2024).

[189] S. Fichtner, N. Wolff, F. Lofink, L. Kienle and B. Wagner, “AlScN: A III-V semiconductor based ferroelectric”, J. Appl. Phys. 125,114103 (2019).

[190] D. Wang et *al*., “Ferroelectric YAlN grown by molecular beam epitaxy”, Appl. Phys. Lett. 123, 033504 (2023).

[191] A. Konishi, T. Ogawa, C. A. J. Fisher, A. Kuwabara, T. Shimizu, S. Yasui, M. Itoh, and H. Moriwake, “Mechanism of polarization switching in wurtzite-structured zinc oxide thin films”, Appl. Phys. Lett. 109, 102903 (2016).

[192] H. Moriwake, A. Konishi, T. Ogawa, K. Fujimura, C. A. J. Fisher, A. Kuwabara, T. Shimizu, S. Yasui, and M. Itoh, “Ferroelectricity in wurtzite structure simple chalcogenide”, Appl. Phys. Lett. 104, 242909 (2014).

[193] H. Amano, N. Sawaki, I. Akasaki and Y. Toyoda, “Metalorganic vapor phase epitaxial growth of a high quality GaN film using an AlN buffer layer”, Appl. Phys. Lett. 48, 353 (1986).

[194] J.-M. Wagner and F. Bechstedt, “Properties of strained wurtzite GaN and AlN: Ab initio studies”, Phys. Rev. B 66, 115202 (2002).

[195] H. K. Cho, J. Y. Lee, G. M. Yang and C. S. Kim, "Formation mechanism of V defects in the InGaN/GaN multiple quantum wells grown on GaN layers with low threading dislocation density", Appl. Phys. Lett. 79, 215 (2001).

[196] F. Mouhat and F.-X. Coudert, "Necessary and sufficient elastic stability conditions in various crystal systems", Phys. Rev. B 90, 224104 (2014).

[197] D. Holec, M. Fri´ak, J. Neugebauer and P. H. Mayrhoferb, "Trends in the elastic response of binary early transition metal nitrides", Phys. Rev. B 85, 064101 (2012)

[198] I. R. Shein, V. S. Kiĭko, Yu. N. Makurin, M. A. Gorbunova and A. L. Ivanovskiĭ, "Elastic parameters of single-crystal and polycrystalline wurtzite-like oxides BeO and ZnO: Ab initio calculations", Phys. Solid State 49, 1067 (2007).

[199] M. Jamal, M. Bilal, I. Ahmad, and S. Jalali-Asadabadi, "IRelast package", J. Alloys Compd. 735, 569-579 (2018).

[200] T. Kawabe, "Perceptual properties of the Poisson effect", Front. Psychol. 11, (2021).

[201] G. N. Greaves, A. Greer, R. Lakes, and T. Rouxel, "Poisson's ratio and modern materials" Nat. Mater. 10(11), 823-37 (2011).

[202] A. Nakajima, Y. Sumida, M. H. Dhyani, H. Kawai and E. M. S. Narayanan, "High density two-dimensional hole gas induced by negative polarization at GaN/AlGaN heterointerface", Appl. Phys. Express 3, 121004 (2010).

[203] O. Ambacher, J. Smart, J. R. Shealy, N. G. Weimann, K. Chu, M. Murphy, W. J. Nhaff, L. F. Eastman, R. Dimitrov, L. Wittmer, M. Stutzmann, W. Rieger, and J. Hilsenbeck, "Two-dimensional electron gases induced by spontaneous and piezoelectric polarization charges in N- and Ga-face AlGaN/GaN heterostructures", J. Appl. Phys. 85, 3222 (1999).

[204] S. H. Park, Y. E. Pak, C. Y. Park, D. Mishra, S. H. Yoo, Yong. Cho, M. B. Shim, and S. Kim, "Quaternary AlInGaN/InGaN quantum well on vicinal c-plane substrate for high emission intensity of green wavelengths", J. Appl. Phys. 117, 185707 (2015).

[205] D. Xiao, K. W. Kim, S. M. Bedair, J. M. Zavada, "Design of white light-emitting diodes using InGaN/AlInGaN quantum-well structures", Appl. Phys. Lett. 84, 672–674 (2004).

[206] V. Adivarahan, A. Chitnis, J. P. Zhang, M. Shatalov, J. W. Yang, G. Simin, M. Asif Khan, R. Gaska, and M. S. Shur, "Ultraviolet light-emitting diodes at 340 nm using quaternary AlInGaN multiple quantum wells", Appl. Phys. Lett. 79, 4240–4242 (2001).

[207] F. Wu, H. Sun, I. A. Ajia, I. S. Roqan, D. Zhang, J. Dai, C. Chen, Z. C.Feng, and X. Li, "Significant internal quantum efficiency enhancement of GaN/AlGaN multiple quantum wells emitting at ~350 nm via step quantum well structure design", J. Phys. D: Appl. Phys. 50, 245101 (2017).

[208] M. A. Caro, S. Schulz, S. B. Healy, and E. P. O'Reilly, "Built-in field control in alloyed c-plane III-N quantum dots and wells", J. Appl. Phys. 109, 084110 (2011).

[209] M.-H. Kim, M. F. Schubert, Q. Dai, J. K. Kim, E. F. Schubert, J. Piprek, and Y. Park, "Origin of efficiency droop in GaN-based light-emitting diodes", Appl. Phys. Lett. 91, 183507 (2007).

[210] J. Lähnemann, O. Brandt, U. Jahn, C. Pfüller, C. Roder, P. Dogan, F. Grosse, A. Belabbes, F. Bechstedt, A. Trampert and L. Geelhaar, "Direct experimental determination of the spontaneous polarization of GaN", Phys. Rev. B 86, 081302(R) (2012).

[211] M. Feneberg, M. F. Romero, M. Roppischer, C. Cobet, N. Esser, B. N. K. Thonke, M. Bickermann, and R. Goldhahn, "Anisotropic absorption and emission of bulk (1-100) AlN", Phys. Rev. B 87, 235209 (2013).

[212] A. S. Barker and M. Ilegems, “Infrared lattice vibrations and free-electron dispersion in GaN”, Phys. Rev. B 7, 743 (1973).

[213] O. Madelung, “Semiconductors: Data Handbook”, Springer, Berlin-Heidelberg, (2004).

[214] S. Arulkumaran, T. Egawa, H. Ishikawa and T. Jimbo, “Characterization of different-Al-content $Al_xGa_{1-x}N$/GaN heterostructures and high-electron-mobility transistors on sapphire”, J. Vac. Sci. Technol. B 21, 888–894 (2003).

[215] N. Susilo, M. Schilling, M. Narodovitch, H.-H. Yao, X. Li, B. Witzigmann, J. Enslin, M. Guttmann, G. G. Roumeliotis, M. Rychetsky, “Precise determination of polarization fields in c-plane GaN/$Al_xGa_{1-x}N$/GaN heterostructures with capacitance–voltage measurements”, Jpn. J. Appl. Phys. 58, SCCB08 (2019).

[216] I. P. Smorchkova, C. R. Elsass, J. P. Ibbetson, R. Vetury, B. Heying, P. Fini, E. Haus, S. P. DenBaars, J. S. Speck, and U. K. Mishra, “Polarization-induced charge and electron mobility in AlGaN/GaN heterostructures grown by plasma-assisted molecular-beam epitaxy,” J. Appl. Phys. 86, 4520 (1999).

[217] S. K. Davidsson, M. Gurusinghe, T. G. Andersson, and H. Zirath, “The influence of composition and unintentional doping on the two-dimensional electron gas density in AlGaN/GaN heterostructures,” J. of Electron. Mater. 33, 440 (2004).

[218] H. M. Ng, R. Harel, S. N. G. Chu, and A. Y. Cho, “The effect of built-in electric field in GaN/AlGaN quantum wells with high AIN mole fraction”, J. Electron. Mater. 30, 134 (2001).

[219] L. Jia, E. T. Yu, D. Keogh, P. M. Asbeck, P. Miraglia, A. Roskowski, and R. F. Davis, “Polarization charges and polarization-induced barriers in $Al_xGa_{1-x}N$/GaN and $In_yGa_{1-y}N$/GaN heterostructures”, Appl. Phys. Lett. 79, 2916 (2001).

[220] Q. Li, S. J. Xu, M. H. Xie, S. Y. Tong, X. H. Zhang, W. Liu, and S. J. Chua, “Strong screening effect of photo-generated carriers on piezoelectric field in $In_{0.13}Ga_{0.87}N$/$In_{0.03}Ga_{0.97}N$ quantum wells,” Jpn. J. Appl. Phys. 41, L1093 (2002).

[221] Y. D. Jho, J. S. Yahng, E. Oh, and D. S. Kim, “Measurement of piezoelectric field and tunneling times in strongly biased InGaN/GaN quantum wells,” Appl. Phys. Lett. 79, 1130 (2001).

[222] C. Y. Lai, T. M. Hsu, W.-H. Chang, K.-U. Tseng, C.-M. Lee, C.-C. Chuo, and J.-I. Chyi, “Direct measurement of piezoelectric field in $In_{0.23}Ga_{0.77}N$/GaN multiple quantum wells by electrotransmission spectroscopy,” J. Appl. Phys. 91, 531 (2002).

[223] D. Turchinovich, P. Uhd Jepsen, B. Monozon, M. Koch, S. Lahmann, U. Rossow, and A. Hangleiter, “Ultrafast polarization dynamics in biased quantum wells under strong femtosecond optical excitation,” Phys. Rev. B 68, 241307 (2003).

[224] R. A. Wolf and S. Trolier-McKinstry, “Temperature dependence of the piezoelectric response in lead zirconate titanate films”. J. Appl. Phys. 95, 1397–1406 (2004).

[225] N. Yasuda, T. Banno, K. Fujita, H. Ohwa, M. Matushita, Y. Yamashita, M. Iwata, and Y. Ishibashi, “Pressure dependence of piezoelectric properties of a Pb $(Mg_{1/3}Nb_{2/3})O_3$-$PbTiO_3$ binary system single crystal near a morphotropic phase boundary”. J. Phys.: Condens. Matter 18, 7659 (2006).

[226] Y.-R. Wu, R. Shivaraman, K.-C. Wang and J. S. Speck, “Analyzing the physical properties of InGaN multiple quantum well light emitting diodes from nano scale structure”, Appl. Phys. Lett. 101, 083505 (2012).

[227] P. M. McBride, Q. Yan and C. G. Van de Walle, "Effects of In Profile on simulations of InGaN/GaN multi-quantum-Well light-emitting diodes", Appl. Phys. Lett. 105, 083507 (2014).

[228] D. A. Aldahiry, D. A. Bajaba, N. M. Basalamah and M. M. Ahmed, "Piezoelectric transducer as an energy harvester: A review", Yanbu J. Eng. Sci. 19, 30 (2022).

[229] J. Li, L. Fang, B. Sun, X. Li, and Sung H. Kang, "Review—Recent progress in flexible and stretchable piezoresistive sensors and their applications", J. Electrochem. Soc 167, 037561 (2020).

[230] L. Wang, C. Wang, Y. Wang, A. Quan, M. Keshavarz, B.P. Madeira, H. Zhang, C. Wang, and M. Kraft, "A Review on Coupled Bulk Acoustic Wave MEMS Resonators", Sensors 22, 3857 (2022).

[231] M. Cardona, "Semiconductors under uniaxial strain", phys. stat. sol. (b) 198, 5 (1996).

[232] V. Kolomoet, V. Ermakov, L. Panasyuk, S. Fedosov, B. Orasgulyev, and P. Nazarchuk, "Application of high uniaxial strain methods for semiconductor parameter determination", Physica B 417, 46–48 (2013).

[233] H. D. Hochheimer, F. Widulle, J. T. Held, G. Strehl, R. T. Kotitschke, and A. R. Adams, "Study of semiconductor lasers under simultaneous uniaxial stress and hydrostatic pressure", High Press. Res. 18, 41-48 (2000).

[234] V. Stankevič, Č. Šimkevičius, S. Balevičius, N. Žurauskienė, P. Cimmperman, A. Abrutis, and V. Plaušinaitienė, "Uniaxial stress influence on electrical conductivity of thin epitaxial lanthanum-strontium manganite films", Thin Solid Films 540, 194-201 (2013).

[235] G. Yang, S. F. Liu, W. Ren, and B. K. Mukherjee, "Effects of uniaxial stress on the piezoelectric, dielectric, and mechanical properties of lead zirconate titanate piezoceramics", Ferroelectrics 262, 207-212 (2001).

[236] K. R. Talley, R. Sherbondy, A. Zakutayev, and G. L. Brennecka. "Review of high-throughput approaches to search for piezoelectric nitrides", J. Vac. Sci. Technol. A 37, 060803 (2019).

[237] N. Gogneau, N. Jamond, P. Chrétien, F. Houzé, E. Lefeuvre, and M. Tchernycheva, "From single III-nitride nanowires to piezoelectric generators: New route for powering nomad electronics", Semicond. Sci. Technol. 31, 103002 (2016).

[238] R. K. Pandey, J. Dutta, S. Brahma, B. Rao, and C. Liu, "Review on ZnO-based piezotronics and piezoelectric nanogenerators: aspects of piezopotential and screening effect", J. Phys. Mater. 4, 044011 (2021).

[239] A. E. Romanov, T. J. Baker, S. Nakamura, and J. S. Speck, "Strain-induced polarization in wurtzite III-nitride semipolar layers", J. Appl. Phys. 100, 023522 (2006).

[240] P. -Y. Prodhomme, A. B. Wakata, and G. Bester, "Nonlinear piezoelectricity in wurtzite semiconductors", Phys. Rev. 88, 121304(R) (2013).

[241] J.-M. Wagner and F. Bechstedt, "Properties of strained wurtzite GaN and AlN: Ab initio studies", Phys. Rev. B 66, 115202 (2002).

[242] K. Kobayashi, "Electronic and lattice properties of layered hexagonal compounds under anisotropic compression: a first-principles study", Mater. Trans. 46, 1094-1099 (2005).

[243] P. Gopal, N.A. Spaldin, and U. V. Waghmare, "First-principles study of wurtzite-structure MnO", Phys. Rev. B 70, 205104 (2004).

[244] K. Shimada, "First-principles determination of piezoelectric stress and strain sonstants of wurtzite III–V nitrides", Jpn. J. Appl. Phys. 45, L358 (2006).

[245] Z. Wang, J. Zhao, Y. Gao and Y. Zhang, "First-principle studies on the influence of anisotropic pressure on the physical properties of aluminum nitride", Mater. Res. Express 4, 016303 (2017).
[246] F. Tasnádi, B. Alling, C. Höglund, G. Wingqvist, J. Birch, L. Hultman and I. A. Abrikosov, "Origin of the anomalous piezoelectric response in wurtzite $Sc_xAl_{1-x}N$ alloys", Phys. Rev. Lett. 104, 137601 (2010).
[247] R. Resta, "Dynamical charges in oxides: Recent advances", J. Phys. Chem. Solids 61, 153-157 (2000).
[248] R. H. Lyddane, R. G. Sachs and E. Teller, "On the polar vibrations of alkali halides", Phys. Rev. 59, 673 (1941).
[249] X. Gonze and C. Lee, "Dynamical matrices, Born effective charges, dielectric permittivity tensors, and interatomic force constants from density-functional perturbation theory", Phys. Rev. B 55, 10355 (1997).
[250] J. A. Sanjurjo, E. López-Cruz, P. Vogl and M. Cardona, "Dependence on volume of the phonon frequencies and the Ir effective charges of several III-V semiconductors", Phys. Rev. B 28, 4579 (1983).
[251] A. S. Barker, Jr. and M. Ilegems, "Infrared lattice vibrations and free-electron dispersion in GaN", Phys. Rev. B 7, 743 (1973).
[252] R. M. Martin, "Piezoelectricity", Phys. Rev. B 5, 1607 (1972).
[253] S. Massidda, R. Resta, M. Posternak, and A. Baldereschi, "Polarization and dynamical charge of ZnO within Different One-Particle Schemes", Phys. Rev. B 52, R16977(R) (1995).
[254] T. J. Flack, B. N. Pushpakaran, and S. B. Bayne, "GaN technology for power electronic applications: a review", J. Electron. Mater. 45, 2673-2682 (2016).
[255] H. A. A. Abdul Amir, M. A. Fakhri, A. A. Alwahib, "Review of GaN optical device characteristics, applications, and optical analysis technology", Mater. Today: Proc. 42, 2815-2821 (2021).
[256] Ü. Özgür, D. Hofstetter, and H. Morkoç, "ZnO devices and applications: a review of current status and future prospects", Proc. IEEE 98, 1255-1268 (2010).
[257] F. Glas, J.-C. Harmand, and G. Patriarche, "Why does wurtzite form in nanowires of III-V zinc blende semiconductors?", Phys. Rev. Lett. 99, 146101 (2007).
[258] J. Bao, D. C. Bell, and F. Capasso, "Optical properties of rotationally twinned InP nanowire heterostructures", Nano Lett., Vol. 8, 836 (2008).
[259] D. Spirkoska, J. Arbiol, A. Gustafsson, S. Conesa-Boj, F. Glas, I. Zardo, M. Heigoldt, M. H. Gass, A. L. Bleloch, S. Estrade, M. Kaniber, J. Rossler, F. Peiro, J. R. Morante, G. Abstreiter, L. Samuelson, and A. Fontcuberta i Morral, "Structural and optical properties of high quality zinc-blende/wurtzite GaAs nanowire heterostructures", Phys. Rev. B 80, 245325 (2009).
[260] H. J. Joyce, J. Wong-Leung, Q. Gao, H. Hoe Tan, and C. Jagadish, "Phase perfection in zinc blende and wurtzite III−V nanowires using basic growth parameters", Nano Lett. 10, 908-915 (2010).
[261] C. F. Lin, H. C. Cheng, G. C. Chi, M. S. Feng, J. D. Guo, J. M. Hong, and C. Y. Chen, "Growth and characterizations of GaN on SiC substrates with buffer layers", J. Appl. Phys. 82, 2378–2382 (1997).
[262] W. A. Melton and J. I. Pankove, "GaN growth on sapphire", J. Cryst. Growth 178, 168-173 (1997).

[263] YS. Park, YS. Jeon, KO. Jeon, BA. Kang, KS. Hwang, JH. Jeong, and YH. Lee, "Epitaxial growth of ZnO thin films on SiC prepared by chemical solution deposition", Mater. Res. Soc. Symp. Proc. 957, 1014 (2006).
[264] N. Takahashi, K. Kaiya, T. Nakamura, Y. Momose, and H. Yamamoto, "Growth of ZnO on sapphire (0001) by the vapor phase epitaxy using a chloride source", Jpn. J. Appl. Phys. 38, L454 (1999).
[265] G. Naresh-Kumar, D. Thomson, Y. Zhang, J. Bai, L. Jiu, X. Yu, Y. P. Gong, R. M. Smith, T. Wang, and C. Trager-Cowan, "Imaging basal plane stacking faults and dislocations in (11-22) GaN using electron channelling contrast imaging", J. Appl. Phys. 124, 065301 (2018).
[266] G. Dhanaraja, M. Dudley, D. Bliss, M. Callahan, and M. Harris, "Growth and process induced dislocations in zinc oxide crystals", J. Cryst. Growth 297, 74-79 (2006).
[267] N. Li, S. Labat, S. J. Leake, M. Dupraz, J. m. Carnis, T. W. Cornelius, G. Beutier, M. Verdier, V. Favre-Nicolin, T. U. Schü lli, O. Thomas, Jl Eymery, and MI. Richard, "Mapping inversion domain boundaries along single GaN wires with Bragg coherent X-ray imaging", ACS Nano 14, 10305−10312 (2020).
[268] Y. Z. Liu , H. T. Yuan , Z. Q. Zeng , X. L. Du , X. D. Han , Q. K. Xue, and Z. Zhang, "Inversion domain boundary in a ZnO film", Philos. Mag. Lett. 87, 687-693 (2007).
[269] K. Suzuki, M. Ichihara, and S. Takeuchi, "High-resolution electron microscopy of extended defects in wurtzite crystals", Jpn. J. Appl. Phys. 33, 1114 (1994).
[270] B. Lia, H. Liu, X. Lu, L. Kang, Y. Sheng, and A. Xiong, "Atomic configurations of basal stacking faults and dislocation loops in GaN irradiated with Xe^{20+} ions at room temperature", Appl. Surf. Sci. 486, 15-21 (2019).
[271] D. Gerthsen, D. Litvinov, Th. Gruber, C. Kirchner, and A. Waag, "Origin and consequences of a high stacking fault density in epitaxial ZnO layers", Appl. Phys. Lett. 81, 3972-3974 (2002).
[272] S. -H. Lim and D. Shindo, "High Resolution electron microscopy of stacking faults in heteroepitaxial $ZnO/LiTaO_3$", Microscopy 51, S165 (2002).
[273] H. Blank, P. Delavignette, R. Gevers, and S. Amelinckx, "Fault structures in wurtzite", phys. stat. sol. B 7, 747–764 (1964).
[274] B. Li, P.F. Yan, M.L. Sui, and E. Ma, "Transmission electron microscopy study of stacking faults and their interaction with pyramidal dislocations in deformed Mg", Acta Mater. 58, 173-179 (2010).
[275] X. L. Guo, J. H. Choi, H. Tabata, and T. Kawai, "Fabrication and optoelectronic properties of a transparent ZnO homostructural light-emitting diode", Jpn. J. Appl. Phys., 40, L177 (2001).
[276] B. Yin, Z. Wu, and W.A. Curtin, "Comprehensive first-principles study of stable stacking faults in hcp metals", Acta Mater. 123, 223-234 (2017).
[277] Y. Yan, G. M. Dalpian, M. M. Al-Jassim, and S. H. Wei, "Energetics and electronic structure of stacking faults in ZnO". Phys. Rev. B 70, 193206 (2004).
[278] W. Rieger, R. Dimitrov, D. Brunner, E. Rohrer, O. Ambacher, and M. Stutzmann, "Defect-related optical transitions in GaN", Phys. Rev. B 54 17596–602 (1996).
[279] K. Dovidenko, S. Oktyabrsky, and J. Narayan, "Characteristics of stacking faults in AlN thin films", J. Appl. Phys 82, 4296 (1997).
[280] C. Stampfl and C. G. Van de Walle, "Energetics and electronic structure of stacking faults in AlN, GaN, and InN". Phys. Rev. B 57, R15052 (1998).

[281] I. G. Batyrev, W. L. Sarney, T. S. Zheleva, C. Nguyen, B. M. Rice, and K. A. Jones, "Dislocations and stacking faults in hexagonal GaN", Phys. Status Solidi A 208, 1566-1568 (2011).

[282] S. Takeuchi and K. Suzuki, "Stacking fault energies of tetrahedrally coordinated crystals", Phys. Stat. Sol. (a) 171, 99 (1999).

[283] A. Nakamura, E. Tochigi, R. Nagahara, Y. Furushima, Y. Oshima, Y. Ikuhara, T. Yokoi, and K. Matsunaga, "Structure of the basal edge dislocation in ZnO", Crystals 8, 127 (2018).

[284] S. Zhang, D. Holec, W. Y. Fu, C. J. Humphreys, and M. A. Moram, "Tunable optoelectronic and ferroelectric properties in Sc-based III-nitrides", J. Appl. Phys. 114, 133510 (2013).

[285] A. Mokadem, M. Bouslama, O. Benhelal, A. Assali, M. Ghaffour, Z. Chelahi Chikr, K. Boulenouar and A. Boubaia, "Investigation of the electron structure of ZnO by the GGA and mBJ calculations associated with the characterization techniques AES and EELS", Int. J. Mod. Phys. B 28, 1450078 (2014).

[286] R. Dingle, D. D. Sell, S. E. Stokowski, and M. Ilegems, "Absorption, reflectance, and luminescence of GaN epitaxial layers", Phys. Rev. B 4, 1211 (1971).

[287] D. Vogel, P. Krüger, a nd J. Pollmann, "Ab initio electronic-structure calculations for II-VI semiconductors using self-interaction-corrected pseudopotentials", Phys. Rev. B 52, R14316 (1995).

[288] M. Ghosh, S. Ghosh, M. Seibt, K. Y. Rao, P. Peretzkic, and G. M. Raoa, "Ferroelectric origin in one-dimensional undoped ZnO towards high electromechanical response", CrystEngComm 18, 622-630 (2016).

[289] Y. T. Rebane, Y. G. Shreter, and M. Albrecht, "Stacking faults as quantum wells for excitons in wurtzite GaN", phys. stat. sol. (a) 164, 141 (1997).

[290] P. Corfdir, C. Hauswald, J. K. Zettler, T. Flissikowski, J. Lähnemann, S. Fernández-Garrido, L. Geelhaar, H. T. Grahn, and O. Brandt, "Stacking faults as quantum wells in nanowires: Density of states, oscillator strength, and radiative efficiency", Phys. Rev. B 90, 195309 (2014).

[291] M. Albrecht, S. Christiansen, G. Salviati, C. Zanotti-Fregonara, Y. T. Rebane, Y. G. Shreter, M. Mayer, A. Pelzmann, M. Kamp, K. J. Ebeling, M. D. Bremser, R. F. Davis, and H. P. Strunk, "Luminescence related to stacking faults in heterepitaxially grown wurtzite GaN", Mat. Res. Soc. Symp. Proc. 468, 293–298 (1997).

[292] M. Schirra, R. Schneider, A. Reiser, G. M. Prinz, M. Feneberg, J. Biskupek, U. Kaiser, C. E. Krill, K. Thonke, and R. Sauer, "Stacking fault related 3.31-eV luminescence at 130-meV acceptors in zinc oxide", Phys. Rev. B 77, 125215 (2008).

[293] S. Yang, C. C. Kuo, W.-R. Liu, B. H. Lin, H.-C. Hsu, C.-H. Hsu, and W. F. Hsieh, "Photoluminescence associated with basal stacking faults in c-plane ZnO epitaxial film grown by atomic layer deposition", Appl. Phys. Lett. 100, 101907 (2012).

[294] N. Armakavicius et al., "Electron effective mass in GaN revisited: New insights from terahertz and mid-infrared optical Hall effect", APL Mater. 12, 021114 (2024).

[295] W. M. Chen, N. T. Son, E. Janzén, D. M. Hofmann and B. K. Meyer, "Effective masses in SiC determined by cyclotron resonance experiments", Phys. Status Solidi A 162, 79 (1997).

[296] A. M. Witowski, K. Pakuła, J. M. Baranowski, M. L. Sadowski and P. Wyder, "Electron effective mass in hexagonal GaN", Appl. Phys. Lett. 75, 4154 (1999).

[297] M. D. M. Drechsler, D. M. H. D. M. Hofmann, B. K. M. B. K. Meyer, T. D. T. Detchprohm, H. A. H. Amano and I. A. I. Akasaki, “Determination of the conduction band electron effective mass in hexagonal GaN”, Jpn. J. Appl. Phys. 34, L1178 (1995).

[298] M. R. Filip, C. Verdi and F. Giustino, “GW band structures and carrier effective masses of $CH_3NH_3PbI_3$ and hypothetical perovskites of the type $APbI_3$: A=NH_4, PH_4, AsH_4, and SbH_4”, J. Phys. Chem. C 119, 25209 (2015).

[299] C. E. Dreyer, A. Janotti and C. G. Van de Walle, “Effects of strain on the electron effective mass in GaN and AlN”, Appl. Phys. Lett. 102, 142105 (2013).

[300] W. Setyawan and S. Curtarolo, “High-throughput electronic band structure calculations: Challenges and tools”, Comput. Mater. Sci. 49, 299 (2010).

[301] A. Kokalj, “XCrySDen—a new program for displaying crystalline structures and electron densities”, J. Mol. Graph. Model. 17, 176 (1999).

[302] C. Freysoldt, B. Grabowski, T. Hickel, J. Neugebauer, G. Kresse, A. Janotti, and C. G. Van de Walle, “First-principles calculations for point defects in solids”, Rev. Mod. Phys. 86, 253 (2014).

[303] L.-W. Wang, L. Bellaiche, S.-H. Wei and A. Zunger, “Majority representation of alloy electronic states”, Phys. Rev. Lett. 80, 4725 (1998).

[304] O. Rubel, A. Bokhanchuk, S. J. Ahmed, and E. Assmann, “Unfolding the band structure of disordered solids: From bound states to high-mobility Kane fermions”, Phys. Rev. B 90, 115202 (2014).

[305] F. Bernardini and V. Fiorentini, “Macroscopic polarization and band offsets at nitride heterojunctions”, Phys. Rev. B 57, R9427(R) (1998).

[306] J. A. Majewski and P. Vogl, “Polarization and band offsets of stacking faults in AlN and GaN”. MRS Internet J. Nitride Semicond. Res., 10.1557 (1998).

[307] N. Gogneau, N. Jamond, P. Chrétien, F. Houzé, E. Lefeuvre, and M. Tchernycheva, “From single III-nitride nanowires to piezoelectric generators: New route for powering nomad electronics”, Semicond. Sci. Technol. 31, 103002 (2016).

[308] R. K. Pandey, J. Dutta, S. Brahma, B. Rao, and C. Liu, “Review on ZnO-based piezotronics and piezoelectric nanogenerators: aspects of piezopotential and screening effect”, J. Phys. Mater. 4, 044011 (2021).

[309] Y. Shimomura, S. Ohno, K. Hayashi and H. Akamatsu, “Quadruple-well ferroelectricity and moderate switching barrier in defective wurtzite α-Al_2S_3: A first-principles study”, Npj Comput. Mater. 11, 38 (2025).

[310] C. Kim, G. Pilania and R. Ramprasad, “From organized high-throughput data to phenomenological theory using machine learning: The example of dielectric breakdown”, Chem. Mat. 28, 1304–1311 (2016).

[311] C.-W. Lee, N. U. Din, K. Yazawa, G. L. Brennecka, A. Zakutayev and P. Gorai, “Emerging materials and design principles for wurtzite-type ferroelectrics”, Matter 7, 1644-1659 (2024).

[312] T. Mikolajick, S. Slesazeck, H. Mulaosmanovic, M. H. Park, S. Fichtner, P. D. Lomenzo, M. Hoffmann and U. Schroeder, “Next generation ferroelectric materials for semiconductor process integration and their applications”, J. Appl. Phys. 129, 100901 (2021).

[313] C.-W. Lee, K. Yazawa, A. Zakutayev, G. L. Brennecka and P. Gorai, “Switching it up: New mechanisms revealed in wurtzite-type ferroelectrics”, Sci. Adv.10, eadl0848 (2024).

[314] J. F. Scott, C. A. Paz de Araujo, “Ferroelectric memories”, Science 246, 1400-1405 (1989).

[315] Y. Arimoto and H. Ishiwara, “Current status of ferroelectric random-access memory”, MRS Bull. 29, 823 (2004).

[316] Y. Kato, T. Yamada and Y. Shimada, “0.18- m nondestructive readout FeRAM using charge compensation technique”, IEEE Trans. Electron Devices 52, 2616 (2005).

[317] Z. Liu, X. Wang, X. Ma, Y. Yang and D. Wu, “Doping effects on the ferroelectric properties of wurtzite nitrides”, Appl. Phys. Lett. 122, (2023).

[318] F. Yang, “Physics of ferroelectric wurtzite $Al_{1-x}Sc_xN$ thin films”, Adv. Electron. Mater. 11, 2400279 (2025).

[319] J. W. Bennett, K. F. Garrity, K. M. Rabe and D. Vanderbilt, “Hexagonal ABC Semiconductors as Ferroelectrics”, Phys. Rev. Lett. 109, 167602 (2012).